Modelling the effects of aquatic plant growth and management on the hydraulics of a chalk stream.

Adam Graeme Sutcliffe

Thesis submitted in partial fulfilment

of the requirements of the degree of Doctor of Philosophy

Queen Mary, University of London

2014

I, Adam Graeme Sutcliffe, confirm that the research included within this thesis is my own work or that where it has been carried out in collaboration with, or supported by others, that this is duly acknowledged below and my contribution indicated. Previously published material is also acknowledged below.

I attest that I have exercised reasonable care to ensure that the work is original, and does not to the best of my knowledge break any UK law, infringe any third party's copyright or other Intellectual Property Right, or contain any confidential material.

I accept that the College has the right to use plagiarism detection software to check the electronic version of the thesis.

I confirm that this thesis has not been previously submitted for the award of a degree by this or any other university.

The copyright of this thesis rests with the author and no quotation from it or information derived from it may be published without the prior written consent of the author.

Signature:

Date: 26th September 2014

Abstract

One of the major factors affecting flood conveyance in small to medium-sized water courses is the growth of aquatic plants. In-stream vegetation increases the resistance to flow, giving higher flood levels for a given discharge and leading to greater incidence of over-bank flooding. This thesis is focused on vegetation, characteristic of a chalk stream. Here, vegetation management is as much for the provision and maintenance of habitat as for flood risk. In order to balance these two demands, new tools are required which enable sound estimates of both flood conveyance and changes in habitat suitability. To this end, a three-dimensional hydraulic model is developed for a typical chalk stream.

A novel methodology for modelling the impact of in-stream vegetation on river flow hydraulics is developed using the double-averaged Navier-Stokes equations. This is implemented within general purpose computational fluid dynamics software and tested using field measurements taken during both summer and autumn, before and after vegetation management. The model performs well when compared to field measurements of flow velocity and turbulent kinetic energy.

Results show that the complex three-dimensional morphology of *Ranunculus spp* is shown to have a key role in energy loss and a marked impact on the distribution of flow velocities and turbulent kinetic energy. Vegetation management is discussed in terms of its effect on flow velocity, turbulent kinetic energy, flow depth, conveyance capacity and in-channel habitat. A sensitivity analysis shows the importance of rigorous data collection and guidance is provided as to which measurements have the greatest influence on calibrated model parameters. Finally, possible implications of the findings of this study for conveyance estimation methodologies and the management of aquatic vegetation are provided.

Acknowledgements

Firstly, I would like to thank my supervisors Ponnambalam Rameshwaran, Pam Naden and Geraldene Wharton for all their guidance, patience and support over the past years. They have always been willing to bounce ideas back and forth and spend time reviewing endless drafts. I must thank Pam and Ramesh in particular for their specialist advice relating to the hydraulic modelling undertaken, without which this study would not have been possible. I would also like to acknowledge the Natural Environment Research council (NERC), the main sponsors of this work (grant number NE/H525346/1). NERC have also provided me with access to the facilities and expertise at the Centre for Ecology and Hydrology, Wallingford which has been my main place of study during this project.

In the field, I am indebted to a number of willing volunteers including Jon Kelvin, Peter Scarlett, Ponnambalam Rameshwaran, Nathalie Binding, Fran Mallion, and Pauline Harvey. Their hours of help in all weathers made fieldwork an often enjoyable task.

I must thank my long suffering family and friends for all their care, support, generosity and patience throughout this sometimes torturous journey. In particular, my parents Yvonne and Stuart, grandma Margery, partner Jennie and her parents Sue and Malcolm have all been sources of unwavering support. To all of them I am eternally grateful. Also, Jane, I cannot thank you enough for helping me find the confidence to face the final steps of this humongous task. Finally, to all those who keep asking, yes it is finally finished!

Table of contents

List of Tables

List of Figures

Notation

A	channel cross sectional area	(m^2)
A_c	characteristic area of vegetation	(m^2)
A_p	area of cross section occupied by vegetation	(m^2)
A_{px}	projected area of gravel in the *x* direction per unit volume	(m^2m^{-3})
A_{sg}	surface area of gravel per unit volume	(m^2m^{-3})
A_{sv}	total wetted surface area per unit volume of vegetation	(m^2m^{-3})
B^{SA}	proportion of the surface area of a reach containing vegetation	(m^2)
B^{V}	volumetric blockage	(m^3)
B^{X}	proportion of a cross section blocked by macrophyte growth	(m^2)
C	Chezy coefficient	($m^{-1/2}s$)
C_d	drag coefficient	
C_e	edge shape coefficient for ADCP measurement	
$C_{dg}S_{fg}$	bulk drag coefficient for gravel	
$C_{dv}S_{fv}$	drag coefficient for vegetation	
C_{fg}	skin friction coefficient for gravel	
C_{fv}	skin friction coefficient for vegetation	
d_m	depth of the estimated region for ADCP measurement	(m)
f	Darcy-Weisbach friction factor	($m^{-1/2}s$)
F_i	total drag force per unit volume	(Nm^{-3})
F_{gx}	total gravel drag force per unit volume in the *x* direction	(Nm^{-3})
F_{vx}	total vegetation drag force per unit volume in the *x* direction	(Nm^{-3})
g	acceleration due to gravity	(ms^{-2})
g_i	acceleration due to gravity in the *i* direction	(ms^{-2})

H	total water depth	(m)
h	vegetation canopy height	(m)
K	permeability of a porous medium	
$\langle k \rangle$	spatially averaged turbulent energy	(Jkg^{-1})
L	distance from bank to first subsection of an ADCP measurement	(m)
n	Manning's coefficient	($m^{-1/3}s$)
n_b	base value of n for a straight, uniform, smooth channel i.e. boundary resistance	($m^{-1/3}s$)
n_1	a correction factor for the effect of surface irregularities	($m^{-1/3}s$)
n_2	a value for variations in shape and size of the channel cross section	($m^{-1/3}s$)
n_3	a value for obstructions	($m^{-1/3}s$)
n_4	the Manning value for vegetation	($m^{-1/3}s$)
P_k	production of turbulent kinetic energy	
p	pressure	(Pa)
p_a	atmospheric pressure	(Pa)
p_f	pressure at the model free surface	(Pa)
Q	discharge	(m^3s^{-1})
Q_{10}	flow equalled or exceeded 10% of the time	(m^3s^{-1})
Q_{95}	flow equalled or exceeded 95% of the time	(m^3s^{-1})
Q_e	estimated discharge of unmeasured ADCP regions	(m^3s^{-1})
q	discharge	(m^3s^{-1})
R	hydraulic radius	(m)
S	the extent of the water-bed interface bounded by the averaging domain	
S_0	bed slope	
S_f	sheltering factor due to the proximity of other gravel/vegetation elements	

t	time	(s)
U	average streamwise velocity	(ms^{-1})
u	streamwise velocity	(ms^{-1})
u'	streamwise velocity fluctuations	(ms^{-1})
u_*	shear velocity	(ms^{-1})
u_x	streamwise velocity	(ms^{-1})
u_y	lateral velocity	(ms^{-1})
u_z	vertical velocity	(ms^{-1})
$\overline{u}_D$	time mean Darcy velocity	(ms^{-1})
u'_i	fluctuating velocity in the x_i direction	(ms^{-1})
$\bar{u}_i$	time averaged velocity in the x_i direction	(ms^{-1})
$\langle \bar{u}_i \rangle$	time space averaged velocity in the x_i direction	(ms^{-1})
$\widetilde{\overline{u_i}}$	spatially averaged velocity in the x_i direction	(ms^{-1})
ν	kinematic viscosity	(m^2s^{-1})
v'	lateral velocity fluctuations	(ms^{-1})
V_0	total volume of the averaging domain	(m^3)
V_f	fluid only volume within the averaging domain	(m^3)
V_m	mean velocity in first/last subsection of ADCP measurement	(ms^{-1})
$\nu_{\tau\phi}$	turbulent eddy viscosity	(m^2s^{-1})
w'	vertical velocity fluctuations	(ms^{-1})
Z^+	normal distance to the wall	
z_0	bed elevation	(m)
α	function of reach sinuosity	
Γ	secondary flow parameter	
$\hat{\gamma}$	semivariance	

∂_{ij}	Kronecker delta function	
$\langle\varepsilon\rangle$	spatially averaged dissipation of turbulent energy	
η_k	efficiency of the production of turbulent kinetic energy	
η_ε	efficiency of the dissipation of turbulent kinetic energy	
κ	von Karman constant	
λ	dimensionless eddy viscosity	
ρ	fluid density	(kgm^{-3})
τ_{zx}	*C*artesian Reynolds stress in the *x* direction on the plane perpendicular to the *z* direction	(Nm^{-2})
τ_{xy}	Cartesian Reynolds stress in the *y* direction on the plane perpendicular to the *x* direction	(Nm^{-2})
ϕ	space-time porosity	
ϕ_T	local time porosity	
ϕ_{V_m}	local space porosity	
φ	projection of shear stress onto the plane due to Catersian coordinate system	

Chapter 1. Introduction

The Pitt Review (Pitt, 2008) was commissioned to assess what lessons could be learnt from the summer floods of 2007. The review highlighted the management of aquatic vegetation as a key area of concern, as many respondents blamed the high water levels on the presence of vegetation in river channels. There were also concerns that the presence of vegetation meant that flood waters did not recede as quickly as they might otherwise have done (Pitt, 2008). Increased temperatures are predicted under most climate change scenarios (IPCC, 2007) and there is evidence that the global hydrological cycle is intensifying as the planet warms (Huntington, 2006) leading to increasingly heavy precipitation (Groisman *et al.*, 2004) and more frequent and intense convective storms during summer (IPCC, 2007). These factors are expected to increase flood risk across England and Wales, with over 4 million people and properties in excess of £200 billion currently at risk (Foresight: Future Flooding Study, 2004; Wilby *et al.*, 2008). For example, using the HadRM3H Regional Climate Model, Bell *et al.* (2009) predict increases in flood frequency throughout much of the UK by the 2080s with changes in peak flows across the country varying by as much as 100%. Increases in temperature, along with increased levels of dissolved CO_2, may also lead to higher rates of photosynthesis in submerged aquatic vegetation (IPCC, 2007), with the potential for plant growth rates to increase as a result.

Aquatic vegetation, often termed macrophytes in the ecological literature, occurs predominantly in river environments which are relatively shallow, physically stable, rich in nutrients and have limited hydrodynamic energy. The presence of vegetation in streams generally increases the hydraulic resistance of the channel and it has been suggested that between 45 and 58% of channel resistance can be

attributed to vegetation alone (Graeme and Dunkerley, 1993; Sellin and van Beesten, 2004). This increased resistance leads to lower mean channel velocity and, thus, higher flow levels for a given discharge, potentially leading to greater incidence of over-bank flooding. Hence, the coincidence of high levels of growth of aquatic vegetation and increasing frequency and intensity of summer convective storms is an area of concern.

Aquatic vegetation has, thus, been traditionally viewed as a nuisance and, as a result, has historically been extensively managed in the form of cutting. In England and Wales, the Environment Agency currently spends around £8m a year on vegetation cutting. However, it has also been increasingly recognised that vegetation can increase bank stability, act as erosion control, attenuate floods and improve the quality of the aquatic habitat (Brookes and Shields, 1996; Defra, 2005; Liu et al., 2008, Gurnell, 2014). For example, the chalk streams of southern and eastern England are acknowledged as priority habitats at both the UK (UK Biodiversity Action Plan) and European (EU Habitats Directive) level. Vegetation is also important in maintaining and improving ecological status under the EU Water Framework Directive. Hence, there must be increased efforts through interdisciplinary approaches such as ecohydraulics (Leclerc *et al*, 1996; Maddock *et al*., 2013) to develop holistic management solutions that aid habitat conservation and good ecological status, whilst maintaining adequate flood defence.

Estimating the conveyance (i.e. the amount of water that a river channel can transfer downstream without overtopping the banks) of vegetated rivers is, therefore, an important component of flood management and a range of approaches are currently in use. In 2001, the Environment Agency commissioned a research project to define actions for reducing uncertainty in river flood conveyance estimation. Key

gaps in knowledge were identified relating to the parameterisation of vegetation roughness (Samuels et al., 2002). The main outcome of this project was the Conveyance and Afflux Estimation System (CES-AES), providing conveyance estimation for natural and engineered river systems. An estimate of uncertainty due to the effects of vegetation is also included. Flows are predicted using a depth integration of the Reynolds Averaged Navier-Stokes equation at specified sections along a watercourse (McGahey *et al*., 2008). The methodology is underpinned by the Shiono-Knight method (Shiono and Knight, 1988; 1990; 1991). The CES-AES uses a boundary unit roughness value similar to that of Manning's *n* applied at the section of interest, derived from a literature review of over 700 studies. The inclusion of the effects of vegetation roughness in the CES-AES, particularly with reference to results collected for field cases using the River Habitat Survey (Environment Agency, 2003) and how these effects vary seasonally and following cutting, represents a major advance in conveyance modelling.

Despite this advance with respect to the inclusion of vegetation in practical conveyance estimation methods, it is clear from the literature that the effect of vegetation on flow is much more fundamental and complex than can be simply represented by a change in channel roughness (Rameshwaran and Shiono, 2007). Many have advocated that there is a need for an increased understanding of the reduction in mean velocity and turbulence production induced by vegetated regions due to their fundamental significance for flood conveyance estimation (e.g. Naden et al., 2006, Sand-Jensen and Pedersen, 1999).

Energy losses due to aquatic vegetation occur at a variety of scales ranging from the leaf scale to the patch scale. These combine with blockage to form an overall vegetative resistance. The study of the effect of aquatic vegetation on flow

velocity in the field of hydraulics has predominantly been limited to small-scale process studies, often in the laboratory (e.g. Nepf, 1999; Nepf and Vivoni, 2000; Carollo *et al*., 2002; Ghisalberti and Nepf, 2002, 2004, 2006), with little consideration of the broader scale implications of natural vegetation at the scale of a river reach. From field studies, however, we know that the spatial distribution and morphology of plant patches is complex, three dimensional and responds to changes in flow (e.g. Sand-Jensen, 2003; Sand-Jensen, 2005; Sukhodolov, 2005; Green, 2005; Stazner *et al*., 2006).

In light of the importance of aquatic vegetation from both the flood conveyance and habitat perspectives, the overall aim of this research was to explore how the representation of aquatic vegetation in hydraulic models can be improved. The study focused on the vegetation characteristic of a chalk stream, a priority habitat under the UK Biodiversity Action Plan and EU Habitats Directive. Here, vegetation management is as much for the provision and maintenance of habitat as for flood risk. In order to balance these two demands, new tools are required which enable sound estimates of both flood conveyance and changes in habitat suitability. To this end, a three-dimensional hydraulic model was developed for a typical chalk stream – the River Lambourn, near Boxford, Berkshire, UK. Such an approach is in its infancy, particularly with regard to non reed-like plants and a patchy pseudo-braided flow environment (Dawson and Robinson, 1984). Hence, the study addressed a key gap in understanding the role that the spatial morphology and structure of aquatic vegetation plays in the overall hydraulic resistance of natural river channels.

A review of the current understanding of aquatic vegetation, its effects on flow velocity at a range of scales and its representation in hydraulic models is

undertaken in Chapter 2. The methodology adopted in this study, a three dimensional hydraulic model, is introduced in Chapter 3 along with a description of the field site on the River Lambourn. Field data required to construct the hydraulic model are presented in Chapters 4-6. Model construction is addressed in Chapter 7. Model performance and results for seasonal variation in vegetation structure and the impact of vegetation cutting are presented in Chapter 8. The effects of vegetation cutting are assessed with regards to reach scale changes in flow velocity, water depth and conveyance capacity. A sensitivity analysis of the results with respect to the data used to construct the model is presented in Chapter 9. Finally, the implications of the findings of this study, along with recommendations for further research, are provided in Chapter 10.

Chapter 2. Effects of aquatic vegetation on flow

This chapter reviews the current literature relating to the effect of aquatic vegetation on river flow velocities. Firstly, a description of the morphology of aquatic vegetation, how it grows and its management, is given. Following this, a discussion of the effect of vegetation on velocity profiles and the three dimensional velocity field is undertaken along with a review of current understanding of the conversion of mean flow energy into turbulent kinetic energy in vegetated flows. The representation of vegetation within one dimensional, quasi-two dimensional, two dimensional and three dimensional hydraulic models is discussed. Finally, the overall aim of this study, along with the specific research questions addressed, is outlined.

2.1. What is aquatic vegetation?

Aquatic vegetation and macrophytes are interchangeable terms which refer to those plant species occurring within aquatic environments. Vegetation can take varying forms such as emergent, submerged, free-floating (rooted), amphibious and mosses amongst others, identified by the River Habitat Survey (Environment Agency, 2003). Aquatic vegetation both affects and responds to fluvial processes, and as such is often considered to be a 'river system engineer' (sensu Jones *et al*., 1994; Gurnell, 2014). Vegetation also provides important habitat for a range of species including invertebrates and fish (Haslam, 1978; Hearne and Armitage, 1993; Baattrup-Pedersen *et al.*, 2002; Mainstone and Parr, 2002; Hatton-Ellis *et al*., 2003; Old *et al*., 2014). Frequent management of aquatic vegetation takes place to satisfy both flood conveyance and habitat needs. This section outlines the forms of aquatic vegetation, its growth and its management.

2.1.1. Forms

There are many species of aquatic vegetation, however, these can be classified into a number of common forms or 'morphotypes' (Gurnell *et al*., 2010; Frostick *et al*., 2011). The River Habitat Survey in the UK (Environment Agency, 2003) recognises nine common morphotypes, examples of which are shown in Table 2.1.1. Common locations of such species over a channel cross section are shown in Figure 2.1.1. The location of these morphotypes in the UK varies, for example mountain streams are dominated by liverworts, lichens and mosses whilst lowland streams are dominated by a range of emergent and submerged vascular plants (Baattrup-Pedersen *et al*., 2006).

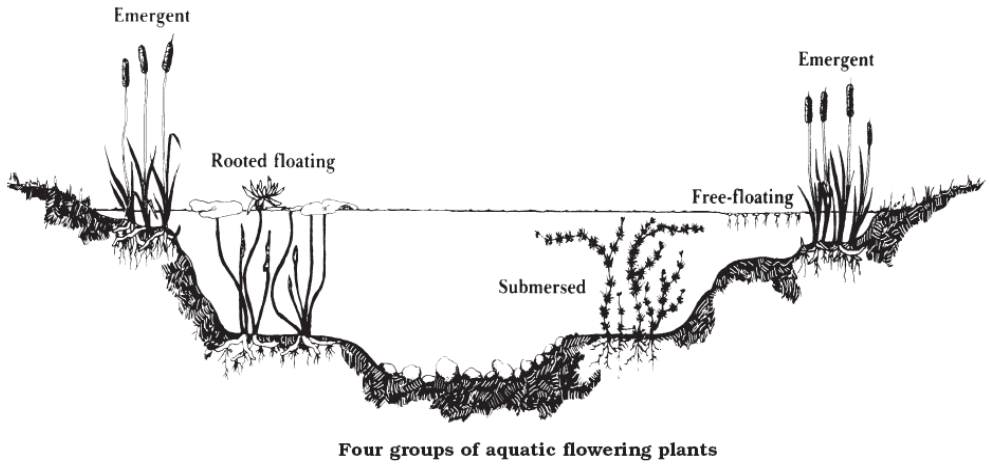

Figure 2.1.1: Example of four groups of commonly occurring aquatic plants and their distribution over a cross section (Managing Iowa Fisheries, 2009).

Plant morphology describes the dimensions of a plant (e.g. its stem length and leaf area), its volumetric characteristics (e.g. leaf volume, stem volume and stem spacing) and the area of the plant presented to the flow (i.e. its frontal and lateral projected area).

Table 2.1.1: Vegetation morphotypes identified in the River Habitat Survey (Environment Agency, 2003).

Morphotype	Example species	Photograph
Liverworts/mosses/lichens	*Scapania*	 Source: Environment Agency (2003).
Emergent reeds/sedges/rushes/grasses/ Horsetails	*Sparganium erectum*	 Source: Liffen *et al* (2013)
Emergent broad leaved herbs	*Veronica becabunga*	 Source: Environment Agency (2003).
Submerged broad leaved	*Nuphar lutea*	 Source: Environment Agency (2003).

Morphotype	Example species	Photograph
Floating-leaved (rooted)	*Ranunculus penicillatus* subsp. *pseudofluitans* var. *pseudofluitans*	 Source: A. Sutcliffe (2014).
Free-floating	*Lemna* spp.	 Source: Environment Agency (2003).
Amphibious	*Catabrosa aquatica*	 Source: Environment Agency (2003).

The attributes of aquatic plants in terms of dimensions and volume can be defined using a number of descriptors. These include stem spacing, biomass and Leaf Area Index (LAI). Stem spacing relates to the density of vegetation and may be indicative of whether a plant acts upon flow at the stem scale or whether, at a high stem density, the stems interact with each other necessitating their consideration as a patch (e.g. Nepf, 1999; Schindler *et al*, 2003; Chen *et al*., 2012). Plant biomass has been used to demonstrate temporal and seasonal variation in plant growth and how

this relates to water levels (e.g. Vereecken *et al*., 2006; O'Hare *et al*., 2010) and plant drag (e.g. Sand-Jensen, 2008). Vereecken *et al*. (2006) used biomass as a measure to assess the effect on vegetation of eight different vegetation cuts with associated changes in water level and conveyance capacity. Leaf Area Index (LAI) is defined as the ratio of total upper leaf surface area divided by the bed surface area over which the vegetation grows (Gacia *et al*., 1999) and is used as a metric to compare canopy structure between species. Leaf area can also be used in relation to plant resistance when expressed as a total wetted surface area per unit volume (e.g. Fathi-Moghadam and Kouwen., 1997; Naden *et al*., 2004).

The overall morphology of a plant in relation to its effect on flow is often described by a characteristic area (e.g. frontal area, lateral projected area or total wetted surface area) with important implications for characterising flow resistance due to vegetation (Sand-Jensen, 2003; 2005; Green, 2005a; Sukhodolov, 2005; Statzner *et al*., 2006). This overall morphology varies in response to changes in flow velocity. Increasing flow velocities lead to an increase in physical and mechanical stresses on aquatic plants due to increased drag forces (Haslam, 1978; Riis and Biggs, 2003). In response to this increasing drag force, many species have the ability to adapt their morphology to reduce their susceptibility to drag (Sand-Jensen, 2003; Sand-Jensen, 2005; Sukhodolov, 2005; Green, 2005d; Statzner et al., 2006; O'Hare et al, 2007; Franklin *et al*., 2008; Liffen *et al*., 2013). The ability of a plant to reconfigure is largely governed by its biomechanical traits, especially its bending and tensile properties (Neumier, 2005; Miler *et al*., 2012). Emergent species such as *Sparganium erectum* do not streamline and exhibit remarkable strength enabling them to resist uprooting and breakage (Liffen *et al*., 2011). More generally however,

plants adopt a streamlined profile, bending in order to reduce the drag exerted upon them (Sand-Jensen and Pedersen, 1999; Green, 2005d).

The bending angle of a plant in flow is an important determinant of plant drag (Sand-Jensen, 2003) as it represents the way the plant reconfigures (sensu Vogel, 1994) and responds to stress (Puilajon *et al*., 2005; Puilajon and Bornette, 2013). Sand-Jensen (2003) assessed the response of five common aquatic species (*Vallisneria natans*, *Limnopholia aquatic*, *Myriophyllum tuberculatum* and *Hygrophilia corymbosa*) to increasing flow velocity. The bending angle for all species was observed to increase with increase in flow velocity (Figure 2.1.2). Sand-Jensen (2003) concluded that increasing flexibility leads to greater reconfiguration but there was no clear pattern in the relationship between the flexibility of the five plants and the drag they experienced.

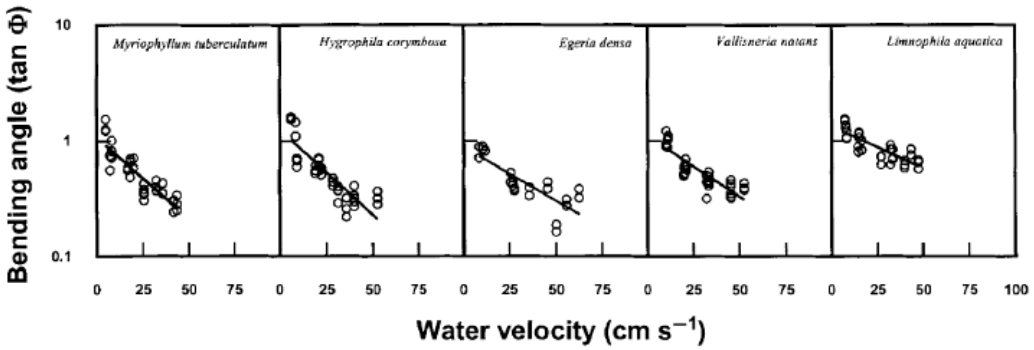

Figure 2.1.2: Increasing bending angle for increasing flow velocity for five aquatic species (Sand-Jensen, 2003).

Other studies (e.g. O'Hare *et al*., 2007; Siniscalchi and Nikora, 2012) have also assessed the bending angle for *Ranunculus* spp in response to flow. O'Hare *et al.* (2007) placed a single patch of *Ranunculus* in a flume and increased the flow velocity from $0.1ms^{-1}$ to $0.5ms^{-1}$. As the flow velocity was increased, the plant bent and attained a more horizontal position close to the channel floor. Siniscalchi and

Nikora (2012) observed differing responses of *Ranunculus* dependent on the time of year. Their results indicated that at low velocities the drag force on the plant was mainly due to the interaction of the flow with the leaves, with more significant contribution from the stems occurring at higher velocities. During the growing season, *Ranunculus* has leaves distributed along its entire length as opposed to just towards the tip of the stems during winter. As such, a different response to increases in flow velocity was found during the summer period.

2.1.2.Growth

The growth of aquatic vegetation has been shown to exhibit high seasonality (e.g. Wright *et al*., 1982; Ham *et al*., 1982; Franklin, 2007). This is in response to the physical stream environment in which it exists (Baattrup-Pedersen and Riis, 1999). The physical environment limits the growth of aquatic vegetation in response to changes in discharge and velocity, light availability, substrate and nutrient availability (Franklin, 2007). The tolerance of vegetation species to these different flow environments has been shown to be a key determinant of aquatic vegetation distribution in rivers (Haslam, 1978).

Several species of aquatic vegetation grow in scattered clumps across the channel (Green, 2005a) whilst other species (e.g. *Rorippa nasturtium aquaticum*) are limited to the channel margins. Where species grow in scattered clumps, they produce environments which can be referred to as 'pseudo-braided' (Dawson and Robinson, 1984). Such structured environments have been observed by Green (2005a); Cotton *et al*. (2006); Naden *et al*. (2006); Wharton *et al*. (2006); Nikora *et al*. (2008); Bal *et al*. (2011); Schoelynck *et al.* (2011) and Luhar and Nepf (2013). The existence of this structure forces flow to divert around and, in some cases, under vegetation patches. This diversion of flow has important implications for the three

dimensional velocity field and local flow velocity gradients, which result from low velocities within plant patches and associated acceleration around them (Green, 2005a). This has been demonstrated in the field by Naden *et al*. (2006); Cotton *et al*. (2006) and Wharton *et al*. (2006). Cotton *et al*. (2006), for example, demonstrated how *Ranunculus* stands divert flow between vegetation patches (Figure 2.1.3) on the River Frome at Pallington. Changes in macrophyte spatial coverage throughout the growing season were shown to result in changes to the dominant flow path through the studied reach.

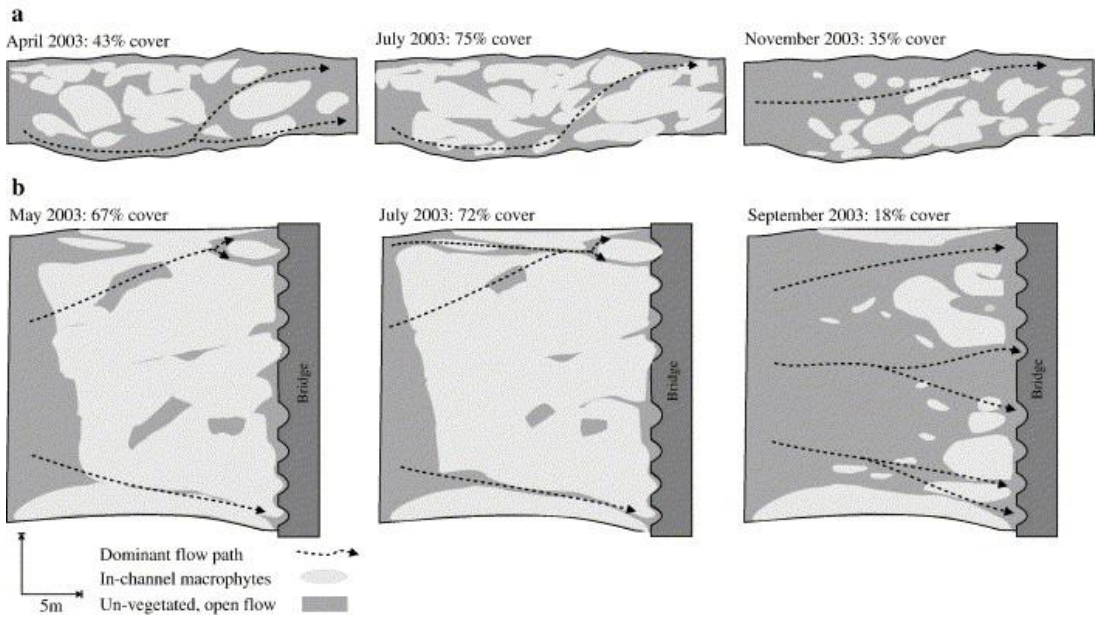

Figure 2.1.3: Flow diversion between patches of *Ranunculus* spp. and how this varies seasonally (Cotton *et al*., 2006).

Both the species morphology and its 'patchy' arrangement are important considerations when analysing the effects of aquatic vegetation on flow. Although the 'patchy' arrangement of aquatic vegetation has been highlighted in the literature (Green, 2005a; Cotton *et al*., 2006; Naden *et al.*, 2006; Wharton *et al*., 2006; Nikora *et al*., 2008; Bal *et al.*, 2011; Schoelynck *et al.*, 2011), a detailed understanding of its effects on flow properties at the reach scale is yet to be undertaken.

2.1.3.Management

Extensive and frequent vegetation cuts take place on rivers dominated by aquatic vegetation in order to maintain their key functions including flood water conveyance and ecological habitat (Baattrup-Pedersen and Riis, 2004; Nikora *et al*., 2008). Whether to cut or not to cut aquatic vegetation is a highly contested subject (Old *et al*., 2014). The most common methods of vegetation management are manual and mechanical cutting (Wade, 1994). Manual cutting entails selective removal of vegetation patches and is usually applied to reaches managed as natural fisheries or those with high ecological status. Mechanised cutting provides a more rapid approach to vegetation removal and is often used for channel clearance for flood defence and navigation purposes (Wade, 1994). It has been suggested by some researchers that a more appropriate approach to vegetation management is to manage the causes of high levels of aquatic vegetation growth, namely unnaturally low shading of rivers and high nutrient levels (Dawson, 1978; Swales, 1982). It has also been suggested that, if not managed through cutting, the biomass of aquatic vegetation would be lower (Dawson, 1976) and therefore wash out naturally (Ham *et al*., 1982). Franklin (2007) suggests that this would be the case due to the feedbacks that exist between plant growth and flow velocity. However, such washout may cause blockage of watercourses, necessitating careful assessment of such an approach for flood conveyance purposes.

In chalk streams, the management of aquatic vegetation often produces the largest change in water levels over a short time period in a given water year. The change in water levels following a vegetation cut, reported to be as high as a 28% reduction in flow depth (Old *et al*., 2014), demonstrate the effectiveness of vegetation cuts in the short term for mitigating against flood risk. Vereecken *et al.*

(2006) also observed an effective fall in water levels for various patterns of vegetation cuts. A vegetation cut impacts on both conveyance capacity and distribution of flow velocities and their magnitude. Old *et al.* (2014) observed an increase in conveyance capacity following a vegetation cut on the River Lambourn of up to 141% with a corresponding increase in mean depth-averaged velocity of 158%. In rivers affected by abstraction and in dry years, however, macrophytes may be required to maintain water levels (Hearne and Armitage, 1993). A balance is, therefore, required to protect in-stream habitats.

Changes in flow velocity following a vegetation cut have both direct and indirect effects on macrophyte growth. Direct effects include uprooting caused by increased flow velocities (Madsen *et al*., 2001) whereas indirect effects can include changes in sediment characteristics (Madsen *et al*., 2001; Riis and Biggs, 2003; Franklin *et al*., 2008; Warren *et al*., 2009). The management of vegetation has also been shown to result in a decrease in species diversity (Baattrup-Pedersen *et al*., 2002). Slow recovery from cuts can also occur when large amounts of vegetation are removed (Franklin, 2007). Vegetation cuts have also been shown to have direct impacts on invertebrate (e.g. Dawson *et al*., 1991) and fish (Swales, 1982) populations. Impacts on invertebrates include direct loss when attached to macrophytes (e.g. Dawson *et al*., 1991; Wright, 1992) whilst fish populations are sensitive to changes in physical habitat (i.e. increased velocities and lower depth) the effect of which can be assessed using physical habitat metrics (e.g. PHABSIM; Bovee, 1982).

Finally, aquatic vegetation exerts an important control on sediment dynamics, particularly sediment trapping and retention (Sand-Jensen, 1998; Cotton et al., 2006; Wharton et al., 2006: Heppell et al., 2009; O'Hare *et al*., 2011; Gurnell, 2014; Gibbs

et al., 2014). Patches of aquatic vegetation are significant storage areas for fine sediment including organic matter (e.g. Clarke and Wharton, 2001). The act of cutting vegetation exposes fine sediment to increased flow which can flush out fine sediment and help to maintain clean gravels (Wharton *et al*., 2006). Dependent on the extent of cutting, the resulting distribution of flows and fine sediments following management also has important ecological implications resulting from an increased diversity of in-stream habitats (Sand-Jensen and Pedersen, 1999; Cotton *et al*., 2006).

Best practice guidelines when undertaking vegetation cuts is summarised in several publications (e.g. Wheeldon, 1993, Mainstone, 1999) along with guidance from the Environment Agency, Natural England and various angling/wildlife associations. The potential impact of vegetation management on ecological habitats has led to advice from the Environment Agency to only cut vegetation where necessary. For example, the River Avon is only cut in response to flood risk to multiple properties or damage to infrastructure (Old *et al*., 2014).

2.2. How does aquatic vegetation affect flow?

The complex morphology of aquatic vegetation described in the previous section has a marked impact on flow velocity. In this section literature relating to the affect of aquatic vegetation on velocity profiles, the three dimensional velocity field, and the production of turbulent kinetic energy is reviewed.

2.2.1. Effect of vegetation on velocity profiles

In Section 2.1.1, a number of broad types of aquatic vegetation were identified which vary in height above the channel bed, depending on their morphology. Work by Sand-Jensen and Mebus (1996), Sand-Jensen (1998) and Sand-Jensen and Pedersen (1999) demonstrated that flow within vegetation patches does not conform to a logarithmic velocity profile. However, much of the evidence for the effect of vegetation of varying morphologies on velocity profiles (i.e. how flow velocity changes with increasing height above the channel bed) comes from flume experiments. Such experiments essentially consider a uniform two dimensional distribution of aquatic vegetation. Initial work (e.g. Pasche and Rouvé, 1985; Tsujimoto *et al*., 1992; Shimizu and Tsujimoto, 1994; Nepf, 1999; Stone and Shen, 2002; Schindler *et al.*, 2003; Ghisalberti and Nepf, 2004; James *et al*., 2004) assessed the effect of aquatic vegetation on velocity profiles using groups of cylinders of the same height and diameter at a regular spacing. Rigid cylinders are often used as surrogates for natural arrangements of plants as their diameter and spatial arrangement can be varied to replicate stem arrangements in natural patches. Investigations relating to rigid cylinders were mainly focused on emergent vegetation. More recently, a range of plant surrogates (e.g. rods with strips, plastic strips, plastic foliage, and artificial plants scaled to the flume dimensions) have also been used to assess the effect of aquatic vegetation on velocity profiles for a range of morphologies, flexible or rigid. The range of approaches used to assess the effects of aquatic vegetation in the laboratory are summarised in Table 2.2.1.

Table 2.2.1: Laboratory approaches to the study of aquatic vegetation. Studies are grouped by the type of plant used.

Reference	Type of plant	Purpose
Pasche and Rouvé (1985)	Artificial rods	Flow resistance on floodplains
Tsujimoto *et al*. (1992)	Artificial rods	Effect on flow of aquatic vegetation.
Tsujimoto and Shimizu (1993)	Artificial rods	Effect on flow of aquatic vegetation.
Nepf (1999)	Artificial rods	Stem density effects on drag and flow resistance
Stone and Shen (2002)	Artificial rods	Stem density effects on drag and flow resistance
Schindler *et al.* (2003)	Artificial rods	Stem density effects on drag and flow resistance
Ghisalberti and Nepf (2004)	Artificial rods	Stem density effects on drag and flow resistance
James *et al*. (2004)	Artificial rods	Stem density effects on drag and flow resistance
Nepf and Ghisalberti (2008).	Artificial rods with strips	Assessment of flow structures.
Nepf and Vivoni (2000)	Artificial rods with strips	Assessment of flow structures.
Ghisalberti and Nepf (2002)	Artificial rods with strips	Assessment of flow structures.
Ghisalberti and Nepf (2006)	Artificial rods with strips	Assessment of shear layer structures over flexible canopies.
Carollo *et al*. (2002)	Natural grass mat	Observation of velocity profile over natural grasses.
Huai *et al.* (2009)	Artificial grass mat.	Observation of velocity profile over flexible artificial grasses.

Reference	Type of plant	Purpose
Naden et al. (2004)	Transplanted natural stand of Ranunculus spp.	Measurement of flow velocities through a natural vegetation patch.
Järvelä (2002)	Scaled natural plants.	Characterisation of flow resistance.
Wilson and Horrit (2002)	Natural grass mat.	Flow over natural grasses of various depths.
Chen et al. (2013)	Artificial rods.	PIV observation of flow over vegetation patches.
Fathi-Moghadam et al. (2011).	Artificial plastic plants.	Characterisation of hydraulic resistance of flexible plants.
Hui and Hu (2010)	Plastic emergent grasses.	Study of drag coefficients related to aquatic vegetation.
Li *et al*. (2014)	Submerged and emergent plastic vegetation.	Study of flow through combined submerged and emergent vegetation.
Rhee *et al*. (2008).	Natural vegetation.	Measurement of hydraulic resistance in open channel flows.

Analysis of the literature in Table 2.1.1 reveals there are three characteristic velocity profiles associated with the presence of emergent or submerged vegetation which differ from the expected logarithmic profile associated with open channel flow (Figure 2.2.1); (i) flow retarded within vegetation where the depth ratio declines towards the emergent limit (H/*h* = 1) (Figure 2.2.1a); (ii) an S-Shaped profile with low velocity within vegetation, an inflection point above which flow is logarithmic and a region of high constant velocity (Figure 2.2.1b); and (iii) a double maxima velocity profile where flow accelerates both above and below vegetation (Figure 2.2.1c). For emergent vegetation where the depth ratio H/*h* tends towards a value of

1, Nepf and Vivoni (2000) identify a velocity profile where vegetation drag remains mainly constant throughout the water depth with correspondingly low flow velocities.

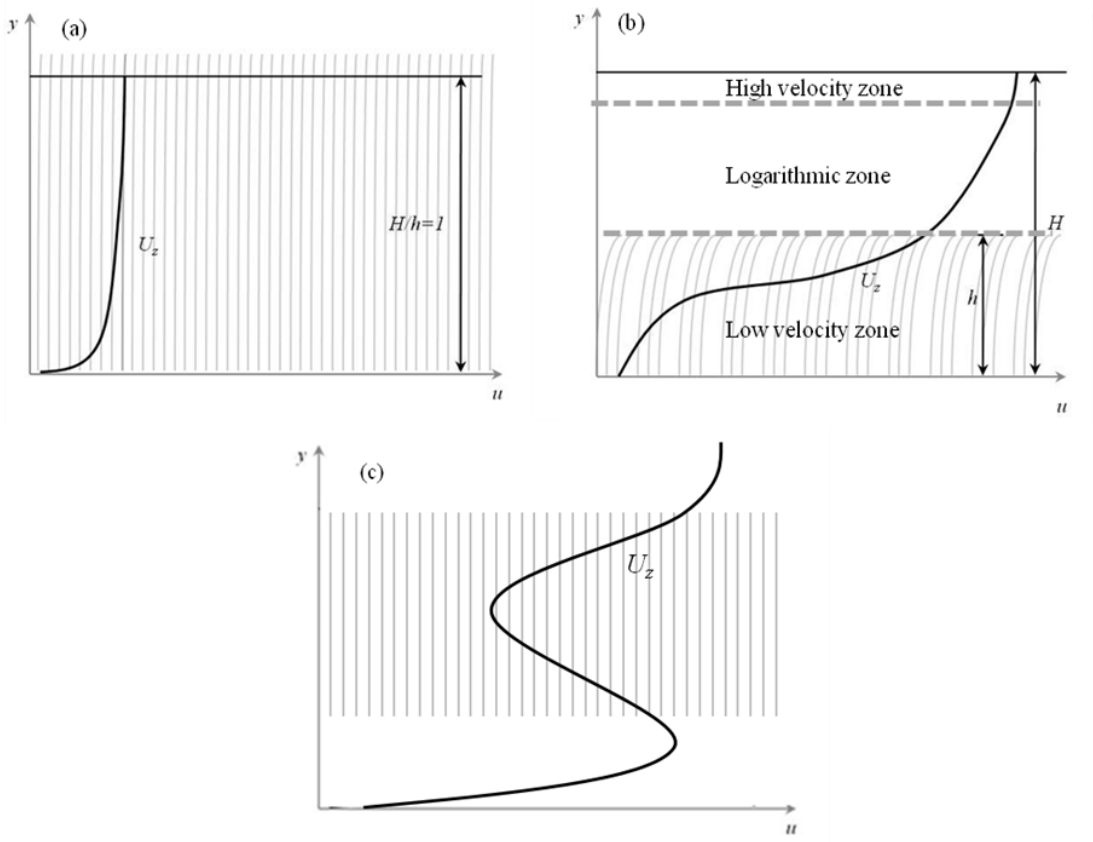

Figure 2.2.1: Velocity profiles in the presence of vegetation (a) After Nepf and Vivoni (2000). Profile produced when the depth ratio declines toward the emergent limit (H/h =1). H = total water depth; h = canopy height; U_z = streamwise velocity profile. (b) After Carollo et al. (2002). Characteristic 's-shape' velocity associated with the presence of flexible, submerged vegetation first identified by Kouwen et al. (1969). (c) After Wilson *et al*. (2003) double maxima velocity profile where vegetation is suspended above the channel bed.

Where the depth ratio decreases from the emergent limit, Carollo et al. (2002) identified an S-shaped profile. Similar work has been performed by Ghisalberti and Nepf (2002). Here, the low velocity zone, where horizontal momentum exchange

occurs, and the high velocity zone, where vertical momentum exchange occurs, were identified as being separated by a mixing layer. The mixing layer is a confined region of shear containing an inflection point. Figure 2.2.2 illustrates this type of velocity profile using a mixing layer analogy.

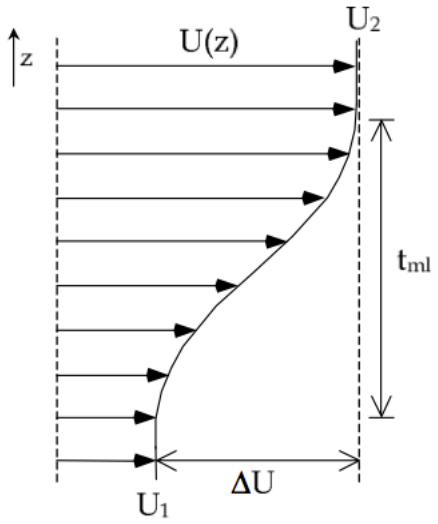

Figure 2.2.2: Representation of a velocity profile using a mixing layer analogy. U_1 and U_2 = low and high stream velocities respectively, U = mean velocity, $\Delta U = U_1 - U_2$ and t_{ml} is the mixing layer thickness.

Ghisalberti and Nepf (2002) postulate that the velocity profile of a mixing layer (i.e. a hyperbolic tangent) could be used to closely approximate those found in vegetated flows. Laboratory experiments for a range of flow scenarios (Figure 2.2.3) show reasonable agreement between the hyperbolic tangent of a mixing layer and observed velocity profiles.

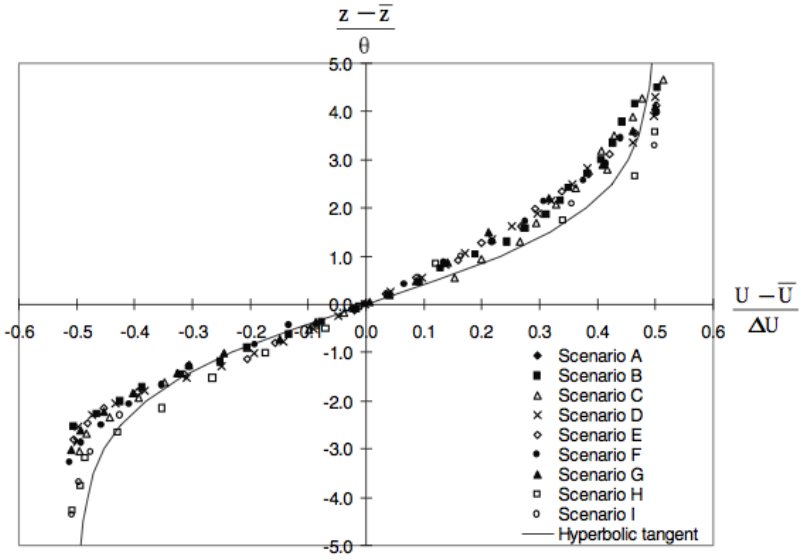

Figure 2.2.3: Results of the experiment performed by Ghisalberti and Nepf (2002).

Finally, plants with relatively rigid stems that are bare near to the bed but from which flexible branches and leaves (i.e. fronds) grow further up in the water column (i.e. *Berula erecta*) have been observed to exhibit a flow velocity profile with a near-bed flow maxima in addition to a flow maxima at the top of a vegetation canopy (e.g. Wilson *et al*. 2003). Wilson *et al*. (2003) postulate that this occurs due to the additional surface area of the fronds significantly increasing the momentum absorbing area of the plant causing a decrease in the flow velocity within the fronds.

2.2.2.Effect of vegetation on the 3D velocity field

Velocity profile characterisation which takes place in laboratories relies on conditions of uniform flow, uniform vegetation and a fully developed boundary layer. Conversely, in natural rivers, macrophytes grow in distinct patches within the channel and result in velocity profiles that are highly variable and depend on the spatial organisation and structure of plant stands as discussed in Section 2.1.2. So far

we have considered the case for a uniform plant distribution. Very little consideration has been given to channels with scattered blocks of plants, i.e. those with a spatially structured environment. Field studies have demonstrated that the spatial distribution of vegetation controls flow velocities in three dimensions (Marshall and Westlake, 1990; Watts and Watts, 1990; Sand-Jensen and Mebus, 1996; Sand-Jensen, 1998; Sand-Jensen and Pedersen, 1999; Gurnell *et al*., 2006; Naden *et al*., 2006, Green, 2005a; Green, 2006; Wharton *et al*., 2006; Liffen et al, 2011; Old *et al*, 2014).

Flow measurements throughout patches of aquatic macrophytes in Danish streams (Sand-Jensen and Mebus, 1996; Sand-Jensen, 1998; Sand-Jensen and Pedersen, 1999), specifically *Callitriche cophocarpa*, *Elodea Canadensis* and *Sparganium emersum*, showed that velocity profiles differed dependent on their location within a plant patch. Using measurements undertaken with a hot wire anemometer, Sand-Jensen and Mebus (1996) demonstrated that logarithmic velocity profiles did not exist within vegetation patches and steep velocity gradients existed above vegetation patch surfaces. Measurements of flow velocities at the patch scale have also been undertaken in UK streams (Green, 2005a; Wharton *et al*., 2006). Green (2005a) showed that the structure of flow changed throughout a single patch of *Ranunculus*, with high velocity gradients occurring at the patch margins due to the retardation of flow within the plant (Figure 2.2.4).

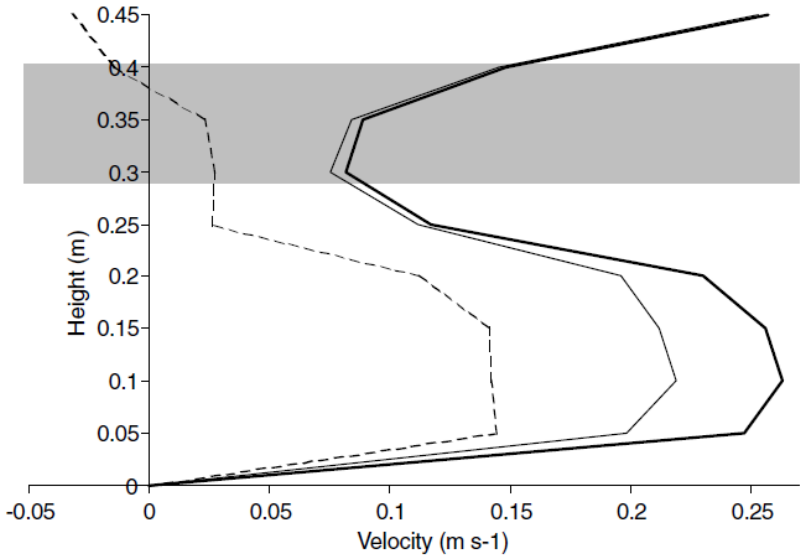

Figure 2.2.4: Flow profiles through a patch of *Ranunculus* at 3.5m from the root Green (2005a). The location of the plant in the vertical profile is highlighted in grey.

Limited point measurements of velocity within and around patches of *Ranunculus* were undertaken on the Bere Stream at Snatford Bridge (Wharton *et al*., 2006). Profiles outside the patch followed the more typical logarithmic form. Profiles within the patch indicated a high degree of spatial variability in velocity, similar to the results of Green (2005a). The differences in the profiles within the stand were attributed to the morphological characteristics of the plant.

Field measurements taken over entire channel cross sections demonstrate that the effect of vegetation on a velocity profile is entirely dependent on location in relation to the plant (Marshall and Westlake, 1990; Watts and Watts, 1990; Sukhodolova, 2004; Naden *et al*., 2006; Old *et al*., 2014). Naden *et al*. (2006), for example, observed differing velocity profiles over a cross section when aquatic vegetation is present (Figure 2.2.5). During May 2011 (black circles), profile 1a is directly downstream of a dense patch of *Sparganium emersum* with a clear retardation of velocity with flow diverted into the centre of the channel. For the same

profile in September 2001 (black triangles), vegetation within in the centre of the channel diverts the flow towards the bank giving a significant increase in flow velocity. Profile 1d in September 2001 shows an S-Shaped profile, attributed by Naden *et al*. (2006) to the presence of plant leaves in the centre of the profile.

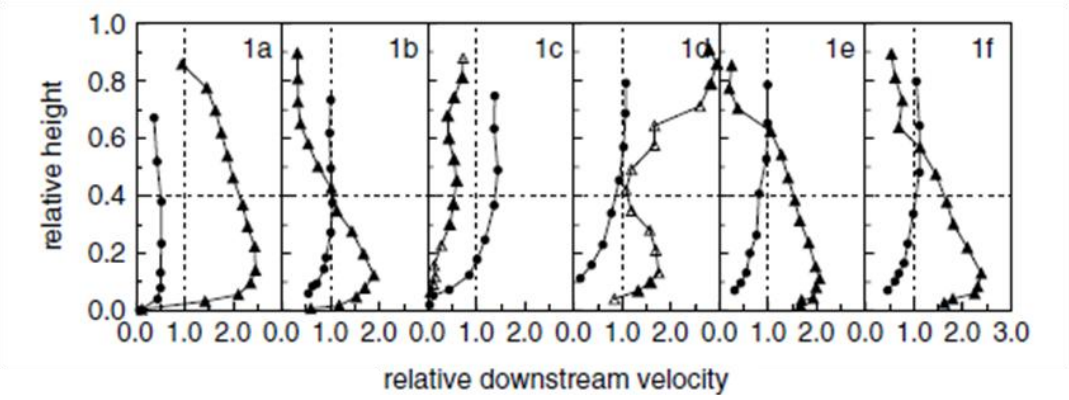

Figure 2.2.5: Relative downstream velocity for seven vertical velocity profiles at a cross section of the River Blackwater (Naden *et al*., 2006). Vegetated data in May 2001 are denoted by circles. Unvegetated data in September 2001 are denoted by triangles.

Finally, measurements at the reach scale (e.g. Franklin, 2007) demonstrate the effect that the presence of aquatic vegetation has on the distribution of flow velocities (Figure 2.2.6). The distribution of *Ranunculus* can be seen to have a marked impact on the distribution of depth-averaged velocity. Where the cover class for *Ranunculus* is highest, for example between 3 and 7 metres cross stream (Figure 2.2.6a), there is a corresponding reduction in velocity (Figure 2.2.6b). Two patches of *Ranunculus* are evident, with a space between the two patches represented by a low cover of *Ranunculus* between 7 and 8 metres cross stream. Where this occurs, there is an acceleration in flow and high velocities between 2 and 13 metres downstream (Figure 2.2.6b).

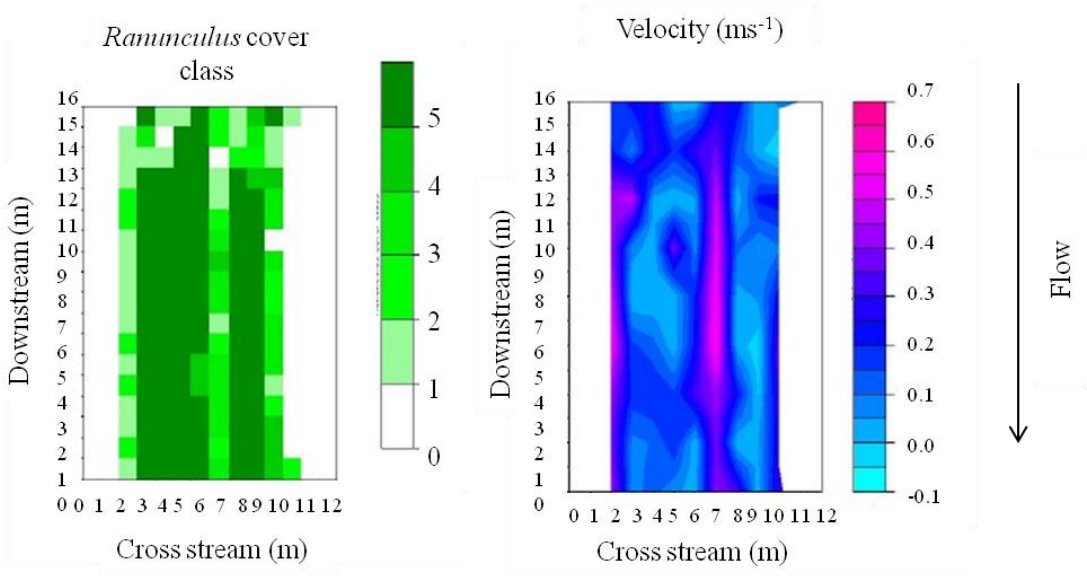

Figure 2.2.6: Spatial variation in velocity characteristics for high *Ranunculus* spp. cover at Dunsford Mill, River Kennet (Franklin, 2007). Dense cover is represented by darker shades of green.

2.2.3. Effect of vegetation on turbulence

As well as changing the distribution of downstream velocity (Section 2.2.1 and Section 2.2.2) the overall effect of vegetation on flow is a reduction in velocity and consequent increase in flow depth. This reduction of mean flow energy arises from its conversion into turbulent kinetic energy. Much of our understanding of this conversion has come from laboratory studies (e.g. Ghisalberti and Nepf, 2009; Nepf and Vivoni, 2000; Lopez and Garcia, 2001; Ghisalberti and Nepf, 2002; Schindler *et al*., 2003; Ghisalberti and Nepf, 2005; White and Nepf, 2007; Zong and Nepf, 2011). There are three main mechanisms for generating turbulent kinetic energy; (i) stem wake effects; (ii) shear zones around vegetation canopies and (iii) waving of flexible plant forms.

Using rigid cylinders, Nepf (1999) demonstrated that blockage by vegetation led to the generation of stem wakes downstream. Schindler *et al*. (2003) undertook detailed measurements of such stem wakes using Particle Imaging Velocimetry

(PIV) for two arrays of rigid cylinders of different densities. Results taken at 30% of the flow depth demonstrated that, at the lower density, stem wakes are clearly separated (Figure 2.2.7). At higher densities, stem wakes interfere with each other producing an area of low velocities surrounded by an area of faster flow. Work by Zong and Nepf (2011) demonstrated that wake formation downstream of a porous body has an entirely different behaviour to that behind a bluff body such as a solid cylinder. Here, the wake length was found to vary with the porosity of the patch. These areas of low velocity surrounded by areas of faster flow contribute to the formation of highly turbulent regions surrounding vegetation patches.

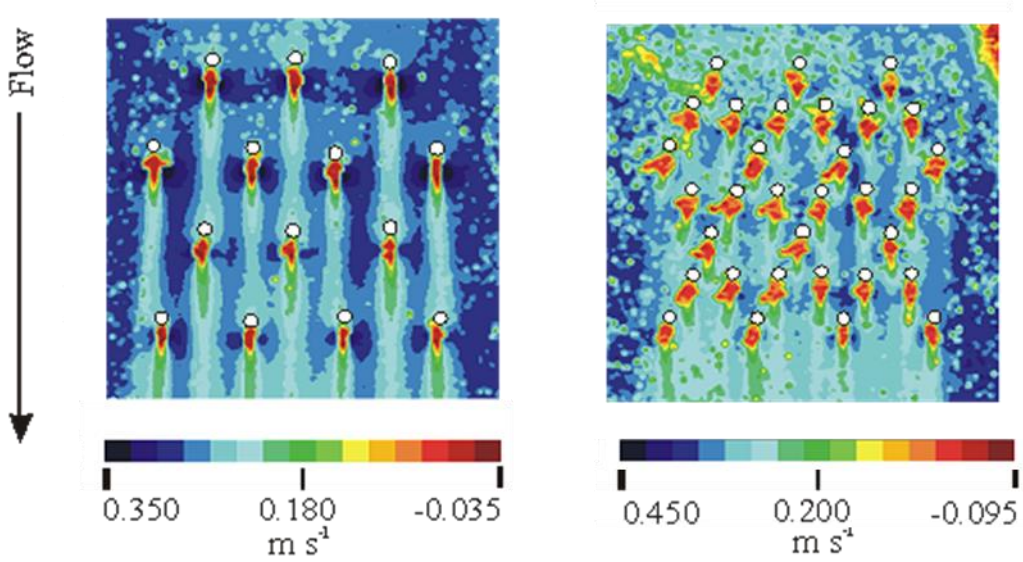

Figure 2.2.7: Time-averaged downstream velocity at 30% of flow depth using PIV from Schindler *et al*., 2003

Steep flow velocity gradients generated around vegetation patches define shear zones which are another key mechanism in the generation of turbulent kinetic energy (Ghisalberti and Nepf, 2004; Ghisalberti and Nepf, 2006; Nepf and Ghisalberti, 2008; Ghisalberti and Nepf, 2009). When flow encounters a vegetation patch, it accelerates over the patch surface generating a shear zone between the faster

flow above the patch and the slower flow within (Ghisalberti and Nepf, 2006; Nepf and Ghisalberti, 2009). This region has been demonstrated to be the location of the maximum values for turbulent kinetic energy and Reynolds stress values (Sand-Jensen and Pedersen, 1999; Folkard, 2011). Again, the nature of the specific plant morphology has been shown to be key, with different flow profiles and turbulence characteristics depending on the morphology of the plant (Wilson *et al*., 2003).

Although much of the literature provides us with helpful insights into turbulence production mechanisms, there is little in the way of turbulence data within and around real plants in natural channels, and their mechanisms of turbulence production remain relatively unexplored (Naden et al., 2006). Sand-Jensen and Pedersen (1999) investigated turbulence and vertical velocity gradients using hot-wire anemometry (30Hz) in the vicinity of and within the canopies of four macrophyte species to evaluate how canopies influenced velocity gradients and shear forces on the surface of the plants and stream bed. It was observed that turbulence increased in proportion to the mean flow velocity, however the slope of the relationship changed with location outside and inside the canopy suggesting that the morphology and movement of the plants influenced the intensity of turbulence. Green (2005a) observed similar results, however the validity of results is questionable due to the relatively low frequency of measurement (10Hz) employed by the electromagnetic current meter used to measure the in-stream velocities. Turbulence intensities were also calculated for the velocity profiles shown in Figure 2.2.5 for a cross-section on the River Blackwater by Naden *et al*. (2006) (Figure 2.2.8).

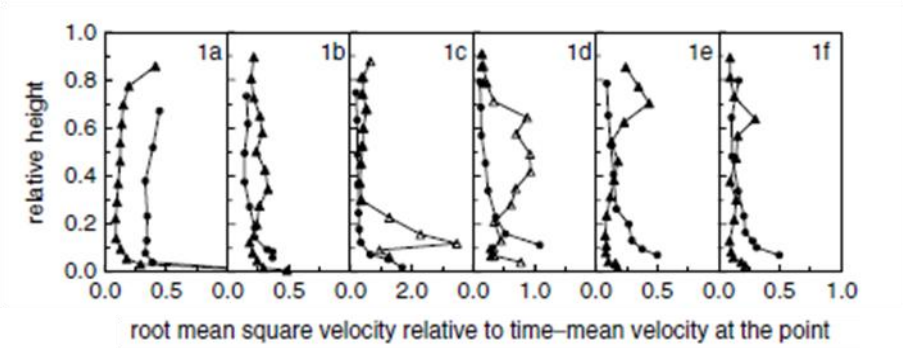

Figure 2.2.8: Turbulence intensity profiles calculated by Naden et al. (2006). Profiles for May 2001 are denoted by circles, profiles for September 2001 are denoted by triangles.

The profiles for May (represented by the circles) have a form typical of cases where the dominant source of turbulent kinetic energy (TKE) is the interaction of the flow with the river bed. Turbulence intensity is highest close to the bed and reduces exponentially to an almost constant value. In September (represented by the triangles) nearly all profiles show an increase in turbulence intensity at some point higher up the profile, dependent on the location that the measurement was taken relative to the stem and leaves.

Finally, the presence of the inflection point between the low flow velocity and high flow velocity zones in the mixing layer analogy proposed by Ghisalberti and Nepf (2002) (Figure 2.2.3) is argued to make the flow susceptible to Kelvin-Helmholtz instability near the top of the canopy. This instability generates large coherent vortices within the mixing layer which Ghisalberti and Nepf (2002; 2004; 2006) claim are the cause of the progressive waving motion often observed for aquatic plants known as monami (Ackerman and Okubo, 1993). It has also been suggested that extent of plant waving due to monami is related to plant biomechanical properties which control flow-vegetation interactions (Py *et al* 2006; de Langre et al, 2008; Nikora, 2009).

2.3.How can we represent aquatic vegetation in hydraulic models ?

Hydraulic models are either one dimensional (1D), quasi-two dimensional, two dimensional or three dimensional. Aquatic vegetation is represented differently in each approach dependent on the model assumptions. A review of each approach is provided along with a discussion of the suitability of the approach in light of the flume and field evidence presented in Section 2.2.

2.3.1. Traditional 1D methods

One dimensional approaches to reach-scale flows are common and are likely to remain so where the reach of interest is a length in the order of ten times (or greater) the channel width due to computational needs (Lane and Ferguson, 2005). Where a river reach is described by a cross-section of an area A with an average velocity of U, the discharge of the river at that cross section can be evaluated using $Q=AU$. Both U and A vary throughout the length of a river reach. Using these basic parameters in conjunction with an appropriate consideration of hydraulic resistance or bed roughness such as Manning's n, Chezy's C or the Darcy-Weisbach friction factor f, predictions can be made relating solely to flow velocity in the downstream direction. There is general agreement that measures of hydraulic resistance depend on: parameters of flow such as Reynolds number; bed material; bed forms; channel forms; and vegetation geometry. The ability to quantify all of the above for modelling purposes is a long-standing problem in hydraulic research.

The presence of aquatic vegetation in streams increases the hydraulic resistance of the channel (Kouwen, 1992; Wu *et al*., 1999) and up to 45% of total channel resistance can be attributed to vegetation alone (Graeme and Dunkerley,

1993). The term hydraulic resistance describes the net effect of all forms of flow resistance on the mean flow velocity and is fundamental to ascertaining the relationship between flow depth and total discharge. Hydraulic resistance is commonly expressed in terms of Manning's *n* and is calculated using Equation 2.3.1:

$$n = \frac{R^{2/3} S_0{}^{1/2}}{U}$$

2.3.1

where *n* is Manning's roughness coefficient, *R* is hydraulic radius (m), S_0 represents the channel slope and *U* is mean water velocity (ms^{-1}). Under the assumption of uniform flow conditions, the bed slope is the same as the slope of the water surface slope. However, in natural channels, the water depth varies. Hence, the slope of the water surface is commonly used to represent the channel slope S_0 in the Manning equation. The use of Manning's *n* dominates the literature on vegetative resistance (Dawson and Robinson, 1984; Bakry *et al*., 1992; Sellin and van Beesten, 2004; Fisher and Dawson, 2003; Green, 2006; Naden *et al*., 2006; Wilson, 2007; Rhee *et al.*, 2008; O'Hare *et al.*, 2010b; Bal *et al.*, 2011; Fathi-Moghadam *et al*., 2011; Li *et al*., 2014) due to its ease of use and perceived ability to indicate the net effect of all factors creating channel resistance. However, based purely on the original formula, what is actually calculated refers to a boundary roughness in the presence of a logarithmic velocity profile (see Gioia and Bombardelli, 2002 for a theoretical explanation). This is not applicable to the entire water column, especially in vegetated channels, and hence in most cases this approach is employed incorrectly.

Empirical studies into the effects of aquatic vegetation on hydraulic resistance have been conducted for many years, reflecting the recognition of its

importance in fluvial research (e.g. Chow, 1959, Bache and MacAskill, 1984). The Cowan method for estimating Manning's n, for example, includes a vegetation correction factor as shown below (2.3.2):

$$n_{tot} = (n_b + n_1 + n_2 + n_3 + n_4)m \qquad 2.3.2$$

where n_{tot} is the overall value of Manning's *n* coefficient, n_b is a base value of *n* for a straight, uniform, smooth channel (i.e. boundary resistance), n_1 is a correction factor for the effect of surface irregularities, n_2 is a value for variations in shape and size of the channel cross section, n_3 is a value for obstructions, n_4 is the value for vegetation and *m* is a correction factor for the meandering of the channel. Values for Manning's *n* have been shown to vary seasonally due to the presence of macrophytes during summer periods (e.g. Gurnell and Midgley, 1994, Dawson and Robinson, 1984, Watson, 1987, Bakry *et al*., 1992; Fisher and Reeve, 1994, Fisher and Dawson, 2003; Sellin and van Beesten, 2004; Naden *et al*., 2006; Franklin, 2007; O'Hare *et al*., 2010b). Naden *et al*. (2006), for example, observed a threefold increase in Manning's *n* that could be attributed to the growth of *Sparganium emersum* in the River Blackwater.

Alternative approaches to incorporating resistance due to aquatic vegetation in a 1D hydraulic model have been proposed using the idea of a blockage factor (Kouwen *et al*., 1969; Fisher, 1992; Carollo *et al*., 2005; Green, 2005c). There are three primary types of blockage factor: B^X defined as the proportion of one or several cross sections blocked by macrophyte growth; B^{SA} defined as the proportion of the surface area of a reach containing vegetation; and B^V which defines the volumetric blockage. Green (2005c) concluded that B^{SA} provides the most appropriate measure of blockage due to aquatic vegetation. Using the proportion of

cross sectional area occupied by vegetation, Kouwen et al. (1969) derived the relationship:

$$\sqrt{8/f} = \frac{U}{u_*} = C_1 ln\left(\frac{A}{A_p}\right) + C_2$$

2.3.3

where U is the cross sectional mean velocity; u_* is shear velocity; A is total cross sectional area of the flow; A_p is the cross sectional area occupied by vegetation and C_1 and C_2 are coefficients dependent on vegetation properties. Tests revealed that this relationship approximates experimental data reasonably well. Carollo et al. (2005), based upon similar considerations, derived the relationship (2.3.4):

$$\sqrt{8/f} = \frac{U}{u_*} = A_0 \left(\frac{H}{h_s}\right)^{\alpha_1} \left(\frac{u_* h_s}{v}\right)^{\alpha_2} \left(\frac{l_p}{h_s}\right)^{\alpha_3}$$

2.3.4

where A_0 is a coefficient depending on vegetation density; v is the kinematic viscosity; l_p is the plant shoot length, h_s is the bent height of the plant, H is the total water depth, f is the Darcy-Weisbach friction factor, u_* is the shear velocity and α_1, α_2 and α_3 are empirical exponents.

Evidence in the literature presented in Sections 2.1 and 2.2 demonstrated that aquatic vegetation cannot be considered as a bed roughness value such as Manning's n. Vegetation occupies either part of or the whole depth of flow and has a clear effect on velocities throughout the vertical profile. Although one dimensional hydraulic models have been shown to have some applicability to vegetated rivers, the

predictions they provide are based on unsound principles when considering the three dimensional effect vegetation has on flow velocity.

2.3.2.Quasi 2D models

Quasi two dimensional (2D) hydraulic models are again concerned with predictions of downstream mean velocity. However, such methods include additional terms to correct for the effects of two dimensional flow. Quasi 2D methods have been developed to allow the lateral distribution of depth-averaged velocity and bed shear stress to be predicted in non-vegetated cases (e.g. Shiono and Knight, 1991; Wark *et al.*, 1990; Wormleaton,1996; Lambert and Sellin, 1996; Ervine *et al.*, 2000, Abril and Knight, 2004; van Prooijen *et al.*, 2005). The method has since been expanded upon to include the effects of vegetation in the Conveyance and Afflux Estimation System (CES-AES) (e.g. McGahey *et al*., 2006, McGahey *et al*., 2008; McGahey *et al*., 2009) and the Mike 11 quasi 2D hydraulic model (e.g. Kourgialas and Karatzas, 2011). The CES-AES is underpinned by the Shiono-Knight method (1988; 1990; 1991) and subsequent evolutions of this (e.g. McGahey *et al*., 2006; 2008; 2009). The flow mechanisms represented within the CES-AES are shown in Figure 2.3.1.

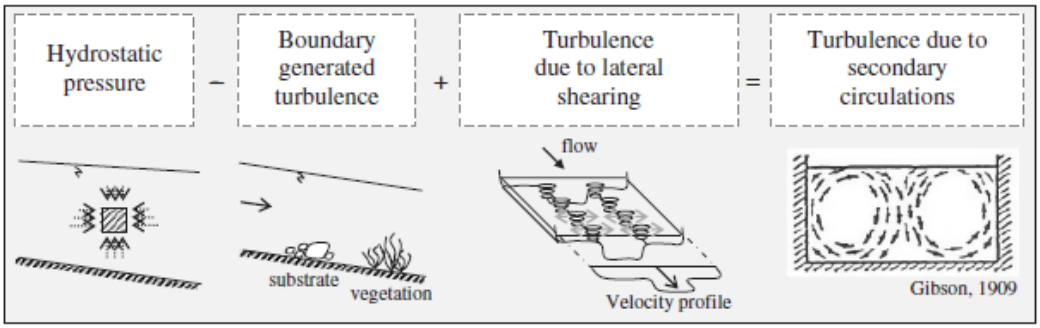

Figure 2.3.1: Example flow mechanisms represented in the CES-AES.

The flow mechanisms in Figure 2.3.1 are represented in equation form as (2.3.5)

$$ghS_0 - \frac{\varphi f q^2}{8h^2} + \frac{\delta}{\delta y}\lambda q h \left(\frac{f}{8}\right)^{1/2} \frac{\delta}{\delta y}\left(\frac{q}{h}\right)$$

$$= \alpha\Gamma + (1-\alpha)C_{uv}\frac{\delta h}{\delta y}$$

2.3.5

where g is the gravitational acceleration (ms^{-2}), h is the local depth (m), S_o is the reach averaged bed slope, y is the lateral distance across the channel cross section, φ is the projection of the shear stress onto the plane due to choice of the Cartesian coordinate system; α is a function of the reach sinuosity and q the flow rate (m^3s^{-1}). Equation 2.3.5 contains four calibration coefficients; the dimensionless eddy viscosity λ, the secondary flow parameter Γ , the coefficient of meandering C_{uv} and the local friction factor f, derived from a user input value of unit roughness n_1. Values of n_1 are notionally associated with a representative depth of flow of 1m, typical of UK rivers (McGahey *et al*., 2009). The unit roughness n_1 is comprised of three component values: vegetation n_{veg}, surface material n_{sur}, and irregularities n_{irr} e.g. urban trash and is evaluated from (2.3.6):

$$n_1 = \sqrt{{n_{veg}}^2 + {n_{sur}}^2 + {n_{irr}}^2}$$

2.3.6

Roughness values for each component are based on a literature review of over 700 references. The parameter n_{veg} of interest in this study is informed by the species type, time of year relating to growth and includes the ability to specify any

management which takes place through cutting. Specification of cuts, however, is limited to specifying the date and percentage of vegetation removed.

Rameshwaran and Shiono (2007) also adopted the Shiono-Knight method to investigate the feasibility of simulating straight compound flows with vegetated floodplains. Vegetation drag force terms and blockage effects were specified as additional momentum sink terms in the Shiono-Knight method. A similar approach to roughness as adopted in the CES-AES was also trialled. Rameshwaran and Shiono (2007) found that the CES-AES overestimated bed shear stress as the water depth was increased. They concluded that a single equivalent roughness approach as adopted in the CES-AES could lead to considerable error when estimating bed shear stress where channel roughness is dominated by vegetative drag.

Quasi 2D approaches represent an improvement when compared to a 1D approach, with momentum transfers such as momentum shearing and secondary circulations accounted for directly in the model equations. However, vegetation which clearly has a three dimensional structure throughout the water depth (Section 2.1. and 2.2) is still represented using a parameter designed to represent boundary roughness only. Hence, the effect of the complex three dimensional morphology of aquatic vegetation on the flow velocity field and energy losses will not be represented fully in the methodology.

2.3.3. 2D models

Two dimensional (2D) hydraulic models simulate downstream and lateral depth-averaged flows. The TELEMAC-2D (Galland *et al.*, 1991; Herveout and Van Haren, 1996) modelling system is one of the main standard codes in 2D hydraulic modelling. TELEMAC-2D has been used to assess the effects of submerged (Sun *et al*., 2010) and emergent (Horrit and Bates, 2002; Sun *et al*., 2010) vegetation on

floodplains. TELEMAC-2D solves the 2D shallow water equations, also known as the Saint-Venant or depth-averaged, equations of free surface flow (Hervouet, 2007; Sun *et al*., 2010):

$$\frac{\partial H}{\partial t} + \frac{\partial}{\partial x}(HU) + \frac{\partial}{\partial y}(HV) = 0$$

2.3.7

$$\frac{\partial U}{\partial} + \frac{\partial U^2}{\partial x} + \frac{\partial}{\partial y}(UV) = -g\frac{\partial Z}{\partial x} + F_x + \frac{1}{H}\mathrm{div}\left((v_e + v_m)H\overrightarrow{\mathrm{grad}}\mathrm{U}\right)$$

2.3.8

$$\frac{\partial V}{\partial} + \frac{\partial V^2}{\partial x} + \frac{\partial}{\partial y}(V^2) = -g\frac{\partial Z}{\partial x} + F_y + \frac{1}{H}\mathrm{div}\left((v_e + v_m)H\overrightarrow{\mathrm{grad}}\mathrm{V}\right)$$

2.3.9

where *t* is time *x* and *y* are longitudinal and lateral directions, *z* is free-surface elevation, *U* and *V* are depth-averaged longitudinal and lateral velocities, *H* is flow depth, *g* is acceleration due to gravity, F_x and F_y are forces per unit volume in the *x* and *y* directions and v_e and v_m are the depth-averaged turbulent and kinetic eddy viscosities respectively. Within the 2D shallow water equations, vegetation is often represented by parameterising F_x and F_y as (Hervouet, 2007):

$$F_x = -\frac{u}{\cos(\alpha)}\frac{gn^2}{h^{4/3}}\sqrt{u^2 + v^2}$$

$$F_y = -\frac{v}{\cos(\alpha)}\frac{gn^2}{h^{4/3}}\sqrt{u^2 + v^2}$$

2.3.10

Again, when we consider the evidence presented in Sections 2.1 and 2.2, the use of Manning's *n* to represent vegetation is limited as vegetation is not solely confined to the channel boundary. To counteract this, Sun *et al*. (2010) introduced additional drag terms to the 2D shallow water equations in order to represent the complex interaction of flow with vegetation. However, the resulting predicted velocity is depth integrated and, therefore, does not allow an assessment of how the flow varies throughout the depth, something which has been shown to be key when considering the three dimensional flow distribution discussed in Section 2.2.2.

2.4. 3D modelling approaches

So far, the representation of vegetation in hydraulic models using one dimensional and two dimensional approaches has been considered. Such approaches have serious limitations when considering the complex morphology of aquatic vegetation (Section 2.1) and evidence from various laboratory and field experiments (Section 2.2). The need for an increased understanding of complex processes occurring in vegetated rivers has led to a shift in focus to three dimensional hydraulic models. These solve for velocities in three dimensions and include use of the Reynolds-averaged Navier-Stokes equations, Large Eddy Simulation and the double-averaged Navier-Stokes equations. Here, a review of the principles behind three-dimensional hydraulic models is provided along with a description of how vegetation is represented within them.

To simulate time-averaged turbulent flow in three dimensions at a point, the time-averaged Navier-Stokes equations, also known as the Reynolds equations or Reynolds averaged Navier-Stokes equations (RANS) are used. The RANS equations

take the following form for steady state flow (Rameshwaran *et al*., 2011) (Equation 2.4.1 and Equation 2.4.2):

$$\frac{\partial \overline{u_i}}{\partial x_i} = 0$$

2.4.1

$$\bar{u}_j \frac{\partial_{\overline{u_i}}}{\partial x_i} = g_i - \frac{1}{\rho}\frac{\partial \bar{\rho}}{\partial x_i} + \frac{\partial}{\partial x_j}\left(v\frac{\partial \bar{u}_i}{\partial x_j} - \overline{u'_i u'_j}\right)$$

2.4.2

where *i* and *j* are the standard tensor notation indicating two out of the three *x*, *y* and *z* coordinate directions, $\bar{u}_i$ is the time-averaged velocity component in the x_i direction and u'_i is the fluctuating part of the velocity where the instantaneous velocity is decomposed as $u_i = \bar{u}_i + u'_i$, ρ is the density, *p* is the pressure, g_i is the gravity force per unit volume and $-\overline{u'_i u'_j}$ is the turbulent Reynolds stress where the over bar indicates time-averaged variables. In order to predict flows over complex boundaries such as aquatic vegetation and gravel beds, the mesh for a RANS model needs to be of a suitable scale to resolve the complex flows which occur. The mesh resolution required to describe the complex nature of aquatic vegetation, particularly at the reach scale, is so small (i.e. millimetre scale) as to be computationally unfeasible with current computing technology.

Another approach to 3D modelling which can accommodate the interaction of aquatic vegetation with flow is large eddy simulation (LES). Here the evolution of large-scale turbulent motions, such as those that occur within and around aquatic vegetation, can be resolved and directly simulated (Ingham and Ma, 2005). The LES

equations are derived from the Navier-Stokes equations by the application of a filter (Keylock *et al*. 2005). LES modelling of aquatic vegetation mostly takes place at the stem scale (e.g. Cui and Neary, 2002; 2008; Neary *et al*., 2012). Neary *et al*. (2012) for example modelled various arrays of wooden dowels using LES with results comparing favourably to measurement undertaken using a laser Doppler velocimeter of the same experiment by Liu *et al*. (2008). LES has the potential to increase our understanding of flow processes at the finest of scales. However, due to the fine grid scale needed, in the case of vegetation a scale small enough to resolve flow processes occurring at the leaf scale, its computational needs are extraordinarily high (Ingham and Ma, 2005) therefore precluding its use for predicting flows at the reach scale.

The limitations of the use of the RANS and LES approaches necessitated the development of a practical methodology which could incorporate vegetation in three dimensional hydraulic models. This led to the development of the double-averaged Navier-Stokes equations (DANS). The term double averaging results from the method of averaging over both time and space. The development of the double averaging methodology stems from work by atmospheric scientists to describe flow within and above terrestrial forest canopies (e.g. Wilson and Shaw, 1977; Raupach and Shaw, 1982; Finnigan, 1985). In the DANS method, the RANS equations are integrated over space and supplemented with measures of porosity related to gravel roughness elements and vegetation (Nikora *et al*., 2007a). Because of the spatial averaging, additional terms arise in the model equations to represent form-induced stresses and form and viscous drag. Through the use of spatially-averaged parameters to describe both gravel roughness elements and aquatic vegetation, the DANS methodology allows us to adopt a model resolution whose dimensions are

such that they can be applied at the reach scale and do not cause computational or numerical problems.

Aquatic vegetation can be represented within a DANS model by modifying the volume porosity of each computational cell. This accounts for the morphology of aquatic vegetation at the patch scale (Naden *et* al., 2004; Rameshwaran and Naden, 2012). To account for processes that occur at a sub-grid scale within the DANS model, drag due to aquatic vegetation elements is usually parameterised using a drag force approach (Naot *et al*., 1996; Nepf, 1999; Naden *et al*., 2004; Rameshwaran and Naden, 2012; Rameshwaran *et al*., 2014). The parameterisation of drag due to aquatic vegetation has been studied extensively in the literature, usually using arrays of wooden dowels to represent vegetation (e.g. Shimizu and Tsujimoto, 1993; Naot *et al*., 1996; López and García, 2001). The conventional drag force equation takes the form:

$$F_d = -\frac{1}{2}\rho C_d A_c |\langle \bar{u}_i \rangle| \langle \bar{u}_i \rangle \qquad 2.4.3$$

where F is the drag force, C_d is the drag coefficient, A_c is the characteristic area of the vegetation and $|\langle \bar{u}_i \rangle|$ is the resultant time-space averaged velocity. The parameterisation of drag is key for numerical modelling of vegetated flows. There is much debate surrounding the selection of an appropriate measure of the characteristic area A_c (Fathi-Maghadam and Kouwen, 1997; Sand-Jensen, 2003, Sand-Jensen, 2005, Sukhodolov, 2005, Green, 2005b, Statzner et al., 2006). A range of measures exist, such as the vegetation frontal area, its planform area or the total wetted surface area, with the choice of characteristic area impacting on the value of drag coefficient needed (Sukhodolov, 2005). Fathi-Maghadam and Kouwen (1997)

conducted experiments on pine and cedar tree saplings and branches for emergent conditions. They found that in flexible vegetation there was a considerable area of foliage hidden behind the frontal areas that also absorbs momentum in addition to the plant projected area. Wilson *et al.* (2003) argue, therefore, that the momentum absorbing area should be based on a total foliage area in the flow direction per unit volume.

The application of the DANS methodology to flows through natural aquatic vegetation is in its infancy, although studies are displaying a level of success (e.g. Naden *et al*., 2004; Rameshwaran and Naden, 2012). Initial work by Naden *et al.* (2004) demonstrated the applicability of the DANS method when modelling flow through a single patch of *Ranunculus* spp. Measured flow profiles were well replicated by the model. Rameshwaran and Naden (2012) applied the DANS model to a vegetated reach of the River Blackwater, Hampshire. Flow variables were solved using the double-averaged equations. Vegetation patches in the model reach were located explicitly within the computational grid and spatially-averaged vegetation parameters applied within each grid cell occupied by vegetation. Using this approach, the measured free surface profile on the River Blackwater, Hampshire was replicated; something not possible with the equivalent RANS approach.

2.5.Summary and research questions

A review of the literature has shown that aquatic vegetation has a complex three dimensional morphology and grows in a patchy structure within rivers (Section 2.1). Approaches to assessing the impact of vegetation on flow velocity in the laboratory (section 2.2.1) are generally based on an assumption that vegetation height is uniform and distributed evenly throughout any experimental setup. Field studies

which assess the three dimensional distribution of flow velocities (Section 2.2.2) show the importance of recognising the effect of the distribution of vegetation both over a cross section and throughout the flow depth. Turbulence studies (Section 2.2.3) also support these findings in that aquatic vegetation has been shown to have a significant effect on the distribution of turbulent kinetic energy and location of shear zones.

The study of the three dimensional effect of aquatic vegetation on flow velocities and associated energy losses are crucial to our understanding of the effects of vegetated flow. Once the effects of these processes are understood, they can be parameterised and incorporated into conveyance modelling with more accurate predictions of flood levels and bed shear stress a likely result. The understanding of how flow velocity and turbulence is distributed in vegetated reaches is also important for in-stream habitats.

The representation of aquatic vegetation within hydraulic models has historically been limited to a roughness parameter such as Manning's *n* particularly within 1D and quasi-2D approaches. Researchers (e.g. Sun *et al*., 2010) have attempted to address this by using two dimensional hydraulic models with additional drag terms to capture the complex interactions of vegetation on flow. However, the use of 1D, quasi-2D or 2D approaches cannot capture the effect of the complex three-dimensional morphology of vegetation on the flow velocity field. This has been demonstrated here (section 2.2.2) to be crucial to understanding the effects of vegetation on flow. Three-dimensional hydraulic models are therefore required in order to accurately assess the effect of vegetation on river flow. There has been recent focus in the literature on the DANS approach which allows the representation

of aquatic vegetation in such models. However, the method is still in its early stages, particularly when considering non-reed like, spatially distributed plant patches.

This study therefore addressed a key gap in understanding the role that the spatial morphology and structure of aquatic vegetation plays in the overall hydraulic resistance of natural river channels. Given that vegetated flow is three dimensional in structure and there is need for realism at the field reach scale, a three dimensional hydraulic approach using the DANS equations was employed. The specific research questions addressed were:

- RQ1 – How can the representation of aquatic vegetation within three-dimensional hydraulic models be improved?
- RQ2 – What is the sensitivity of a three-dimensional hydraulic model containing aquatic vegetation to model inputs and parameter values?
- RQ3 – What is the impact of vegetation management on hydraulics?

Chapter 3. Methodological framework and field site

The case for a three-dimensional modelling approach using the double-averaged Navier-Stokes equations (DANS) has been presented in Chapter 2 (Section 2.4). In this chapter, the DANS equations are introduced along with a description of how they were applied in this study. The nature of three-dimensional hydraulic modelling is complex and detailed datasets are required to construct the model. Thus, the study was focused on a single river reach. The study site, the CEH River Lambourn Observatory, is introduced in Section 3.3 and the modelled reach is described in Section 3.4. Finally, the field sampling strategy and data collection methods adopted in this thesis to address the research questions set out in Chapter 2 (section 2.5) is presented (section 3.5).

3.1.Governing equations

For this study, a three-dimensional hydraulic model was constructed using the double-averaged (i.e. in both space and time) Navier-Stokes (DANS) equations. In previous work, three-dimensional river flow has generally been modelled using the Reynolds-averaged Navier-Stokes equations (Section 2.4) with a suitable turbulence closure scheme (Pedras and de Lemos, 2001; de Lemos, 2006). However, due to the multi-scale property of flows in a natural river with a gravel-bed boundary and complex vegetation structure, the issue of spatial averaging needs to be addressed (Nikora, 2009; Nikora *et al*., 2013). Hence in natural rivers at the reach scale it is most appropriate to use the DANS equations (Section 2.4).

The fundamental variables required to describe a river flow are the pressure and velocity of the fluid flow. If the flow is assumed to be incompressible and Newtonian then these variables can be calculated using the Continuity and Navier-

Stokes equations which are based on the principles of conservation of mass and momentum. Hence, the DANS equations consist of the double-averaged Continuity equation and the double-averaged Navier-Stokes equations which ensure both mass and momentum are conserved. The continuity equation in its basic form is given as:

$$\frac{\partial \rho}{\partial t} + \frac{\partial \rho u_i}{\partial x_i} = 0$$

3.1.1

where ρ is the fluid density, u_i is the instantaneous velocity in the x_i direction and *t* is time. If we assume that fluid density is constant, the double-averaged form of the continuity equation can be obtained as (Nikora *et al*., 2013):

$$\frac{\partial \phi_{V_m} \langle \phi_T \rangle}{\partial t} + \frac{\partial \phi_{V_m} \langle \phi_T \overline{u}_i \rangle}{\partial x_i} = 0$$

3.1.2

where ϕ_{V_m} is the volume porosity and ϕ_T is the local time porosity.

The Navier-Stokes equation in its basic form is:

$$\frac{\partial u_i}{\partial t} + \frac{\partial u_i u_j}{\partial x_j} = g_i - \frac{1}{\rho}\frac{\partial p}{\partial x_i} + \frac{\partial}{\partial x_j}\left(v \frac{\partial u_i}{\partial x_j}\right)$$

3.1.3

where *i* and *j* are the standard tensor notation indicating two out of the three *x*, *y* and *z* coordinate directions, g_i is acceleration due to gravity, *p* is the pressure and *v* is the kinematic viscosity. The following double-averaged momentum equation is obtained for the general case of a mobile boundary with vegetation as (Nikora *et al*., 2013):

$$\underbrace{\frac{\partial \phi_{Vm}\langle \phi_T \bar{u}_i \rangle}{\partial t}}_{1} + \underbrace{\frac{\partial \phi_{Vm}\langle \phi_T \rangle \langle \bar{u}_i \rangle \langle \bar{u}_j \rangle}{\partial x_j}}_{2}$$

$$= \underbrace{\phi_{Vm}\langle \phi_T g_i \rangle}_{3} - \underbrace{\frac{1}{\rho}\frac{\partial \phi_{Vm}\langle \phi_T \bar{p} \rangle}{\partial x_i}}_{4} - \underbrace{\frac{\partial \phi_{Vm}\left\langle \phi_T \overline{u_i' u_j'} \right\rangle}{\partial x_j}}_{5} - \underbrace{\frac{\partial \phi_{Vm}\left\langle \phi_T \tilde{\bar{u}}_i \tilde{\bar{u}}_j \right\rangle}{\partial x_j}}_{6} + \underbrace{\frac{\partial}{\partial x_j}\left(\phi_{Vm}\left\langle \phi_T \nu \overline{\frac{\partial u_i}{\partial x_j}} \right\rangle \right)}_{7}$$

$$\underbrace{- \frac{\partial \phi_{Vm}\left\langle \phi_T \tilde{\bar{u}}_i \right\rangle \langle \bar{u}_j \rangle}{\partial x_j}}_{8} \underbrace{- \frac{\partial \phi_{Vm}\left\langle \phi_T \tilde{\bar{u}}_j \right\rangle \langle \bar{u}_i \rangle}{\partial x_j}}_{9} + \underbrace{F_i}_{10}$$

3.1.4

where t is time, $\langle \bar{u}_i \rangle$ is the time-space averaged velocity and $\tilde{\bar{u}}_i$ is the spatially varying part of the time-averaged velocity where the instantaneous velocity is decomposed as $u_i = \langle \bar{u}_i \rangle + \tilde{\bar{u}}_i + u'_i$ in the x_i direction and u'_i is the temporally fluctuating part of the velocity, and

$$F_i = \frac{1}{\rho}\frac{1}{V_0}\overline{\iint_{S_{int}} \bar{p} n_i dS}^{S} - \frac{1}{V_0}\overline{\iint_{S_{int}} \left(\nu \frac{\partial \bar{u}_i}{\partial x_j} \right) n_j dS}^{S}$$

where V_0 is the total volume of the averaging domain, S is the extent of the water-bed interface bounded by the averaging domain, and n_i is the outward (i.e. into the fluid) vector normal to the bed surface. Angle brackets denote the spatial (volume) averaged variables and overbars indicate time-averaged variables. In Equation 3.1.4, the first two terms represent local and convective accelerations, respectively. The third term is the gravity term; the fourth term is the pressure gradient; the fifth, sixth

and seventh terms are contributions from turbulent ($\langle\phi_T\overline{u'_i u'_j}\rangle$), form-induced ($\langle\phi_T\widetilde{\overline{u}}'_i\widetilde{\overline{u}}'_j\rangle$) and viscous fluid stresses, respectively; the eighth and ninth terms represent momentum fluxes (stresses) due to potential correlations between the local time porosity and time-averaged velocities; and the tenth term represents both pressure and viscous drag (Nikora *et al*., 2013).

For this study, it was assumed that the movement of the bed material and vegetation within the flow domain are insignificant when compared to the cell size of the mesh. Hence, spatial correlation between the local time porosity and time-averaged flow parameters (terms eight and nine in Equation 3.1.4) can be neglected. Equations 3.1.2 and 3.1.4 can also be simplified for steady state flows to (Nikora *et al*., 2013; Rameshwaran *et al*., 2011; Rameshwaran and Naden, 2012; Rameshwaran *et al*., 2014):

$$\frac{\partial\phi\langle\overline{u}_i\rangle}{\partial x_i} = 0$$

3.1.5

$$\underbrace{\phi\langle\overline{u}_j\rangle\frac{\partial\langle\overline{u}_i\rangle}{\partial x_j}}_{1} = \underbrace{g_i}_{2} - \underbrace{\frac{1}{\rho}\frac{\partial\phi\langle\overline{p}\rangle}{\partial x_i}}_{3} + \underbrace{\frac{\partial}{\partial x_j}\phi\left(\nu\left\langle\frac{\partial\overline{u}_i}{\partial x_j}\right\rangle - \left\langle\overline{u'_i u'_j}\right\rangle - \left\langle\widetilde{\overline{u}}_i\widetilde{\overline{u}}_j\right\rangle\right)}_{4} + \underbrace{F_i}_{5}$$

3.1.6

where ϕ is the space-time porosity ($\phi = \phi_{Vm}\langle\phi_T\rangle$).

3.1.1. Treatment of turbulent and form-induced stresses

The fourth term of Equation 3.1.6 describes the contributions from turbulent ($-\langle\overline{u'_i u'_j}\rangle$) and form-induced ($-\langle\widetilde{\overline{u}}'_i\widetilde{\overline{u}}'_j\rangle$) stresses. The term for turbulent stresses arises from the time averaging of the original Navier-Stokes equations and is known as the Reynolds stress tensor. In practice, it represents the effects of turbulence on the fluid flow. The overbar denotes a time average and the dash represents the fluctuating part of the turbulent velocity. As the turbulent stresses are not known *a priori*, the double-averaged Navier-Stokes equations (Equations 3.1.5 & 3.1.6) are not closed unless a model is provided which relates the Reynolds stress tensor to the global mean property of the flow in a consistent fashion (Ingham and Ma, 2005). Hence, there is a need to apply an appropriate turbulence closure model to the DANS equations to allow them to be solved.

In this study the turbulent Reynolds stresses $-\langle\overline{u'_i u'_j}\rangle$ are calculated using the spatially averaged $\langle k-\varepsilon\rangle$ turbulence model (Pedras and de Lemos, 2001; de Lemos, 2006):

$$-\phi\left\langle\overline{u'_i u'_j}\right\rangle = \nu_{t\phi}\left(\frac{\partial\phi\langle\overline{u}_i\rangle}{\partial x_j}+\frac{\partial\phi\langle\overline{u}_j\rangle}{\partial x_i}\right)-\frac{2}{3}\phi\langle k\rangle\delta_{ij} \qquad 3.1.7$$

where $\langle k\rangle$ is the spatially-averaged turbulent kinetic energy, δ_{ij} is the Kronecker delta function and $\nu_{t\phi}$ is the turbulent eddy viscosity of the porous medium. The turbulent eddy viscosity can be expressed in the same way as the Kolmogorov-Prandtl expression as:

$$\nu_{t\phi} = c_\mu \frac{\langle k \rangle^2}{\langle \varepsilon \rangle}$$

where $\langle \varepsilon \rangle$ is the spatially-averaged turbulent dissipation rate and c_μ is a constant.

Pedras and de Lemos (2001) and de Lemos (2006) suggest that for a porous medium, the spatially-averaged turbulent energy $\langle k \rangle$ and turbulent dissipation rate $\langle \varepsilon \rangle$ can be determined from the spatially-averaged $\langle k - \varepsilon \rangle$ turbulence model equations:

$$\phi \langle \bar{u}_i \rangle \frac{\partial \langle k \rangle}{\partial x_i} = \frac{\partial}{\partial x_i} \left[\left(\nu + \frac{\nu_{t\phi}}{\sigma_k} \right) \frac{\partial \phi \langle k \rangle}{\partial x_i} \right] + P_k + G_k - \phi \langle \varepsilon \rangle$$

3.1.8

$$\phi \langle \bar{u}_i \rangle \frac{\partial \langle \varepsilon \rangle}{\partial x_i} = \frac{\partial}{\partial x_i} \left[\left(\nu + \frac{\nu_{t\phi}}{\sigma_\varepsilon} \right) \frac{\partial \phi \langle \varepsilon \rangle}{\partial x_i} \right] + \frac{\langle \varepsilon \rangle}{\langle k \rangle} \left[c_{1\varepsilon} P_k + c_{2\varepsilon} \left(G_k - \phi \langle \varepsilon \rangle \right) \right]$$

3.1.9

where $c_{1\varepsilon}$, $c_{2\varepsilon}$, σ_k, and σ_ε are empirical constants and P_k is the production of turbulent kinetic energy. G_k is a proposed parameterisation of the extra transport and production rates arising from solid material within the integration volume and is defined as (de Lemos, 2006) as:

$$G_k = c_k \phi \langle k \rangle |\bar{u}_D| / \sqrt{K}$$

3.1.10

where c_k is the turbulence model constant, $\bar{u}_D$ is the time mean Darcy velocity vector and K is the permeability of the porous medium.

Shimizu and Tsujimoto (1993) and Naot *et al*. (1996) however, suggest that when using the conventional drag force equation in cases of flow within roughness layers or vegetation that the dissipation rate ε should be parameterised as:

$$\phi\langle\bar{u}_i\rangle\frac{\partial\langle\varepsilon\rangle}{\partial x_i}=\frac{\partial}{\partial x_i}\left[\left(\nu+\frac{\nu_{t\phi}}{\sigma_\varepsilon}\right)\frac{\partial\phi\langle\varepsilon\rangle}{\partial x_i}\right]+\frac{\langle\varepsilon\rangle}{\langle k\rangle}\left[c_{1\varepsilon}\left(P_k+G_\varepsilon\right)-c_{2\varepsilon}\phi\langle\varepsilon\rangle\right]$$

3.1.11

where G_ε represents the additional contribution arising from the material within the integration volume. When modelling flow through aquatic vegetation, Rameshwaran *et al*. (2011) suggest that the spatially-averaged turbulence model takes the form of Equations 3.1.8 and 3.1.11. Given the lack of evidence to the contrary, the closure coefficients for the spatially-averaged turbulence model are assumed to take the same values as those in the standard $k-\varepsilon$ turbulence model where $c_{1\varepsilon}=1.44$, $c_{2\varepsilon}=1.92$, $c_\mu=0.09$, $\sigma_k=1.0$, and $\sigma_\varepsilon=1.3$ (Rodi, 2000). The extra terms G_k and G_ε can be parameterised as (Shimuzi and Tsujimoto, 1993; Naot *et al*., 1996; Rameshwaran *et al*., 2011):

$$G_k=\eta_k F_i\langle\bar{u}_i\rangle;\ G_\varepsilon=\eta_\varepsilon F_i\langle\bar{u}_i\rangle$$

3.1.12

where η_k is the efficiency of the production of turbulent kinetic energy and η_ε is the efficiency of the dissipation of turbulent kinetic energy. There is little agreement on the parameterisation of, or the values of, η_k and η_ε (Table 3.1.1). Independent values were proposed by Shimizu and Tsujimoto (1993), however Naot *et al*. (1996) and López and García (2001) both argue that η_ε has to be dependent on the value of η_k in order to maintain equilibrium between the production and dissipation of turbulent

kinetic energy. Work by Naot *et al*. (1996) parameterised drag due to vegetation at the sub-grid scale. In their approach, l is the turbulence length scale and l_v is the roughness reference length, which are given by:

$$l = \frac{{c_\mu}^{3/4} k^{3/2}}{\kappa\varepsilon} \text{ and } l_v = 0.5D\sqrt{\frac{s}{D}} \qquad 3.1.13$$

where s is the averaged spacing of roughness elements ($s = 1/\sqrt{N}$), N is the roughness element density and D is the averaged width of the frontal projected area of the roughness elements in each layer.

Table 3.1.1: Values for the efficiency coefficients η_k and η_ε in the literature.

Efficiency coefficient η_k	Efficiency coefficient η_ε	Source
0.07	0.16	Shimizu and Tsujimoto (1993)
0.07	$\eta_\epsilon = \frac{c_{2\varepsilon}\eta_k}{c_{1\epsilon}}\frac{l}{l_v}$	Naot *et al*. (1996)
1.00	$\eta_\epsilon = \frac{c_{2\varepsilon}\eta_k}{c_{1\varepsilon}}$	López and García (2001)

There is no agreed approach in the literature to the representation of these additional turbulence terms for the production and dissipation of turbulent energy at the sub-grid scale. Furthermore, the dominant generating mechanism for turbulence around plant patches is the steep velocity gradients between faster flows around patches and the slower velocities within (Section 2.2.3) which is explicitly represented in the model. Investigation of any additional sub-grid terms were hence beyond the scope of this study, and G_k and G_ε were set to zero.

Form-induced stress is a product of spatial averaging, just as the Reynolds stress is a product of time averaging. In studies adopting the DANS method, form-induced stresses are usually neglected as they are considered to be much smaller than the Reynolds stress (Manes *et al.*, 2008). Furthermore, equations for the form-induced stresses are not yet available in the literature. Hence, in this study, the form-induced stresses are ignored. Any effects of these are captured implicitly by the calibrated bulk drag coefficients for gravel (Section 7.2) and vegetation (Section 7.6).

3.1.2. Treatment of the drag term F_i

Within the DANS methodology, roughness at scales smaller than the model mesh is accounted for using spatially-averaged parameters which describe the blockage due to small-scale roughness elements, i.e. the gravel bed or vegetation elements (e.g. stems and leaves). In this study, drag terms are needed within the model that relate to the gravel bed and the vegetation.

The drag force which relates to the gravel bed is approximated using (Nikora et al., 2007b; 2013) and Rameshwaran et al. (2011):

$$F_{gx} = -\frac{1}{2} C_{dg} S_{fg} A_{px} |\langle \bar{u}_i \rangle| \langle \bar{u}_x \rangle \qquad F_{gy} = -\frac{1}{2} C_{dg} S_{fg} A_{py} |\langle \bar{u}_i \rangle| \langle \bar{u}_y \rangle$$

$$F_{gz} = -\frac{1}{2} C_{fg} A_{sg} |\langle \bar{u}_i \rangle| \langle \bar{u}_z \rangle$$

3.1.14

where $C_{dg}S_{fg}$ is the bulk drag coefficient, S_{fg} is a sheltering factor arising from the proximity of other roughness elements, C_{fg} is the skin friction coefficient of the

surface of the gravel roughness elements, A_{px} and A_{py} are the averaged frontal streamwise and lateral projected areas of the gravel surface per unit volume, A_{sg} is the averaged surface area of the roughness elements per unit volume and $|\langle \bar{u}_i \rangle|$ is the resultant time-space averaged velocity. F_{gx} and F_{gy} are assumed to be proportional to the pressure drag in the longitudinal and lateral flow directions whilst the vertical component is assumed to be proportional to the skin friction and surface area of the gravel (cf. Rameshwaran *et al.*, 2011). The skin friction coefficient, C_{fg}, in this study was set at 0.005, the value for surfaces similar to rough concrete (French, 1985). The bank material was assumed to consist of the same material as the bed. The parameterisation of drag due to gravel roughness elements within the DANS necessitates a layer by layer description of porosity (ϕ), averaged projected area in the streamwise and lateral directions and the gravel surface area, A_{px}, A_{py}, and A_{sg} respectively. The collection and processing of data relating to the gravel roughness elements can be found in Sections 4.3. and 4.4.

In the DANS model, plants are assumed to act as a complex porous canopy as in the atmospheric literature (Wilson and Shaw, 1977; Raupach and Shaw, 1982; Finnigan, 1985). At the stem and leaf scale, the drag force is mainly due to the frictional drag which is proportional to the surface area A_{sv} of the individual plant elements. Hence the momentum absorbing area per unit volume A_{sv} was defined as the wetted surface area of the plant elements per unit volume (cf. Fathi-Maghadan and Kouwen, 1997; Naden *et al.*, 2004). The drag force which relates to the vegetation elements is, thus, parameterised as (Naot *et al.*, 1996; Nepf, 1999):

$$F_{vx} = -\frac{1}{2} C_{dv} S_{fv} A_{sv} |\langle \bar{u}_i \rangle| \langle \bar{u}_z \rangle \qquad F_{vy} = -\frac{1}{2} C_{dv} S_{fv} A_{sv} |\langle \bar{u}_i \rangle| \langle \bar{u}_y \rangle$$

$$F_{vy} = -\frac{1}{2} C_{fv} A_{sv} |\langle \bar{u}_i \rangle| \langle \bar{u}_z \rangle$$

3.1.15

where $C_{dv}S_{fv}$ is the bulk drag coefficient, S_{fv} is a sheltering factor arising from the proximity of other plant elements, C_{fv} is the skin friction coefficient of the surface of the vegetation elements, A_{sv} is the averaged surface area of the vegetation elements per unit volume and $|\langle \bar{u}_i \rangle|$ is the resultant time-space averaged velocity. The description of vegetation within the 3D CFD model comprises two datasets; (i) data relating to the three-dimensional shape of vegetation patches to allow the location of the vegetation within the model mesh to be described explicitly and (ii) data to inform the vegetation parameters in the drag equation of the model. An explanation of the data collection and processing relating to vegetation can be found in Chapter 6.

3.2.Solving the DANS equations

In order to solve the DANS equations, a solution domain is needed which takes the form of a boundary-fitted model mesh. The domain is defined by the flow boundaries (i.e. inlet, outlet and water surface) and the channel topography. The construction of the model mesh is described in Section 7.l.3. This section provides a description of the model boundary conditions, solution method, and convergence criteria.

3.2.1. Boundary conditions

The governing partial differential equations presented in section 3.1 can only be solved for a particular problem when boundary conditions are specified. The model inlet is the upstream boundary of the modelled reach. Here, the value of mean streamwise velocity is prescribed, determined from field measurements (described in Section 5.2). In subsequent runs, the fully developed flow variables from simulated results are prescribed. At the model outlet, the downstream boundary of the model, the pressure $\bar{p}$ is fixed to be the atmospheric pressure on the water surface determined by the water depth. The water depth at the outlet was recorded using staff gauge boards, a description of which can be found in Section 5.3. The fully developed flow condition is applied where $\partial\langle\bar{u}_i\rangle/\partial n = \partial\langle k\rangle/\partial n = \partial\langle\varepsilon\rangle/\partial n = 0$, where *n* is the outward (i.e. into the fluid) unit vector normal to the outlet plane. At the water surface which is assumed to be planar in the initial run and determined from field measurements (Section 5.3), the velocity normal to the surface $(\bar{u}_z)$ is set to zero and the normal gradients of $\langle\bar{u}_x\rangle$, $\langle\bar{u}_y\rangle$, $\langle\bar{u}_z\rangle$, $\langle k\rangle$ and $\langle\varepsilon\rangle$ are set to zero. At the channel boundary, i.e. the bed and the banks, the generalised version of the standard log-law function (Launder and Spaulding, 1974) is applied in order to calculate the skin friction of the individual gravel elements:

$$\frac{U}{u_*} = \frac{1}{\kappa} ln(EZ^+)$$

3.2.1

with

$$E = \begin{cases} 8.6, & Re_* < 3.7 \\ f(Re_*), & 3.7 \leq Re_* \leq 100 \\ 29.7/Re_*, & Re_* > 100 \end{cases}$$

3.2.2

where E is a roughness parameter, Re_* ($= U_* k_s / v$ where k_s is the equivalent sand roughness height) is the particle Reynolds number and Z^+ is the non-dimensional wall distance given by $Z^+ = U_* Z / v$ where U_* is the shear velocity, Z is the normal distance to channel boundary and v is the kinematic viscosity. Here, local turbulence equilibrium is also assumed in order to specify values for k and ε (Rodi, 1993):

$$k = \frac{{U_*}^2}{\sqrt{c_\mu}};\ \varepsilon = \frac{{U_*}^3}{\kappa Z}$$

3.2.3

3.2.2. Numerical algorithm and solution sequence

The American Society of Mechanical Engineers *Journal of Fluids Engineering* editorial policy statement regarding the control of numerical accuracy (September 1993 vol.115, p399) along with the additional comments of Lane *et al*. (2005) are used as the minimum criteria for numerical modelling. The solution method and satisfaction of these criteria follows.

To solve the governing partial differential equations for steady state flow, the general purpose finite-volume code Phoenics (CHAM, 2013) was used. The conservation equations can be written in the same differential form as:

$$\frac{\partial}{\partial x_i}\left(\rho\phi\overline{u_i}\varphi - \Gamma_\phi \frac{\partial \phi\varphi}{\partial x_i}\right) = S_\varphi$$

3.2.4

where φ is the variable depending on the equation considered, Γ_ϕ is the diffusion coefficient of the variable φ, and S_φ is the source term in the equation. The discretised finite volume formulations are obtained by integrating Equation 3.2.4 over each computational cell within the model. The model employs the staggered

grid approach. The approximation of the convection term is handled using the Hybrid Differencing Scheme (HYBRID) and is second order accurate (Spalding, 1972). HYBRID switches between the central differencing scheme and upwind differencing scheme depending on the cell Peclet number. Pressure-velocity coupling within the model is achieved using the SIMPLEST algorithm (Spalding, 1980). The discretised equations are solved with a Stone-based extension of a tri-diagonal solver (Stone, 1968).

Convergence of simulations was deemed to have been achieved when mass is balanced to within 0.1%, for each solved variable the residual error is reduced to 0.1%, and the spot value has settled down to an almost constant value. An example of the model dialogue illustrating this is shown in Figure 3.2.1.

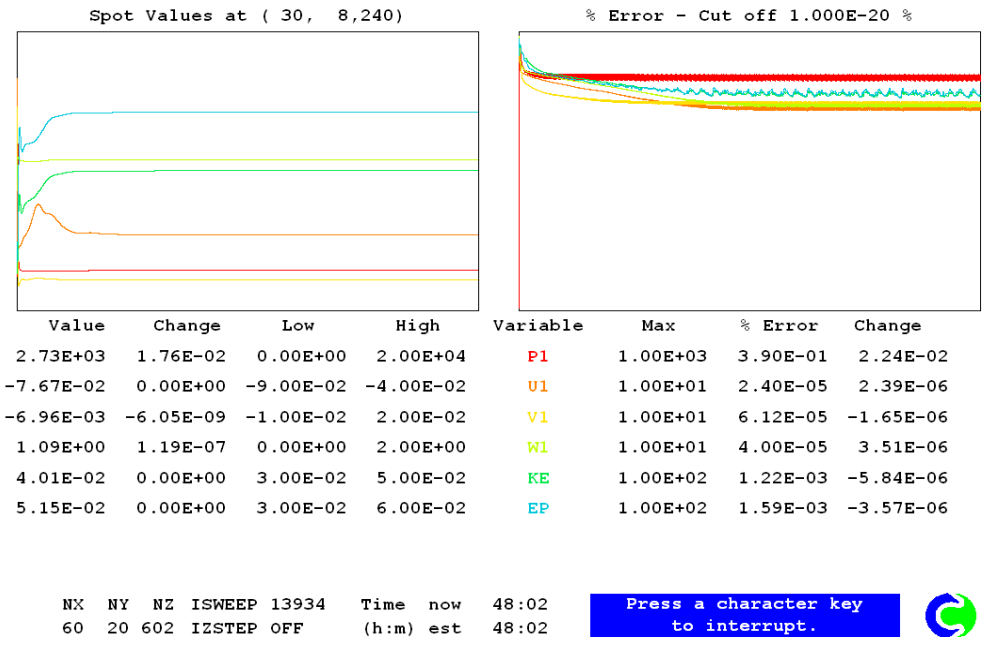

Figure 3.2.1: Model dialogue used to assess convergence. The left screen displays the spot values at a location within the model mesh. The right screen displays the residual error.

Following an initial simulation, the free-surface treatment of Rameshwaran and Naden (2004b) was applied in which the position of the fixed lid is adjusted based on the predicted pressure at the water surface:

$$\Delta h = \frac{p_f - p_a}{\rho g} \qquad 3.2.5$$

where Δh is the adjustment required, p_f is the pressure at the surface and p_a is the atmospheric pressure. Where pressure on the fixed lid is greater than the atmospheric pressure, this represents super-elevation of the water surface. Where the pressure is less than atmospheric, this represents a depression in the water surface. Using this information, an appropriate adjustment to the height of the fixed lid is undertaken and a revised model mesh is generated. Following re-gridding, the model simulation is restarted with the prior steady-state solution as initial variables to accelerate convergence. The procedure was repeated until the differences between the surface and atmospheric pressure were reduced to less than 1×10^{-3}.

To satisfy ASME guidelines, grid convergence was examined over three mesh different resolutions (Section 7.3) using the method outlined by Roache (1994). This is used to demonstrate that the solution of the simulation is mesh independent and relatively free of numerical error. Finally, the performance of the model is assessed in Chapter 8 by comparing model results to measurements undertaken in the field (Section 5.4).

3.3. Field site selection and description

The CEH Lambourn Observatory was chosen as a suitable site for this work for several reasons. It is typical of chalk streams in the UK and has the advantages of (i)

seasonal vegetation growth with a diversity of plant types dominated by *Ranunculus penicillatus* subsp. *pseudofluitans* var. *pseudofluitans*., (ii) a weed management regime that can be manipulated for experimental purposes, (iii) long-term data since 2008 on vegetation growth and river discharge to set the work into context, (iv) ease of access; and (v) permission to install equipment. This section provides details of the site, including available background data collected by CEH between 2009 and 2012, and the strategy adopted for detailed data collection to support the modelling approach taken here.

The CEH River Lambourn Observatory (Figure 3.3.1) comprises a 600m reach of river which varies in width between 7m and 12m and 9.7 hecatares of associated water meadows at Boxford, Berkshire (NGR SU429722) (Figure 3.3.2).

Figure 3.3.1: Aquatic vegetation at the CEH River Lambourn Observatory. Photograph taken looking downstream, May 2011.

The site represents one of the most pristine chalk stream environments within England and the reach is dominated by aquatic vegetation. Predominant in-stream

species at the site include: *Ranunculus penicillatus* subsp. *pseudofluitans* var. *pseudofluitans*, *Berula erecta* and *Callitriche obtusangula*. Riparian vegetation in the form of trees keeps the upper region of the Observatory in shade throughout the day, whereas the lower reach is largely open. Marginal vegetation present at the site includes *Rorippa nasturtium aquaticum*, *Sparganium emersum* and *Myosotis scorpiodies*. Previous studies have focused on the vegetation characteristic of the site. Wright *et al*. (1982) observed the seasonal growth and die-back of macrophyte communities on the River Lambourn whilst Franklin (2007) identified the feedback relationships which occurred between *Ranunculus* spp. and flow velocity. He also observed that the effect of vegetation management following an aggressive cut on the River Lambourn significantly extended the re-colonisation time of *Ranunculus* at the site.

The management of vegetation at the CEH River Lambourn Observatory is undertaken by, and in accordance with advice from, the downstream river keeper, whose main aim is to maintain fish habitat to promote a natural trout fishery. Aquatic vegetation is cut up to three times per year depending on vegetation growth and flow levels, in order to meet legal obligations with regards to conveyance capacity (Pepper and Rickard, 2009). Previous research on the effect of vegetation cuts on the River Lambourn (Old *et al*., 2014) quantified a wide range of coincident physical and chemical impacts on both the in-stream and riparian environments. Measurements undertaken clearly demonstrated how vegetation cuts increase conveyance through reduced resistance and increased flow velocities whilst lowering the water depth.

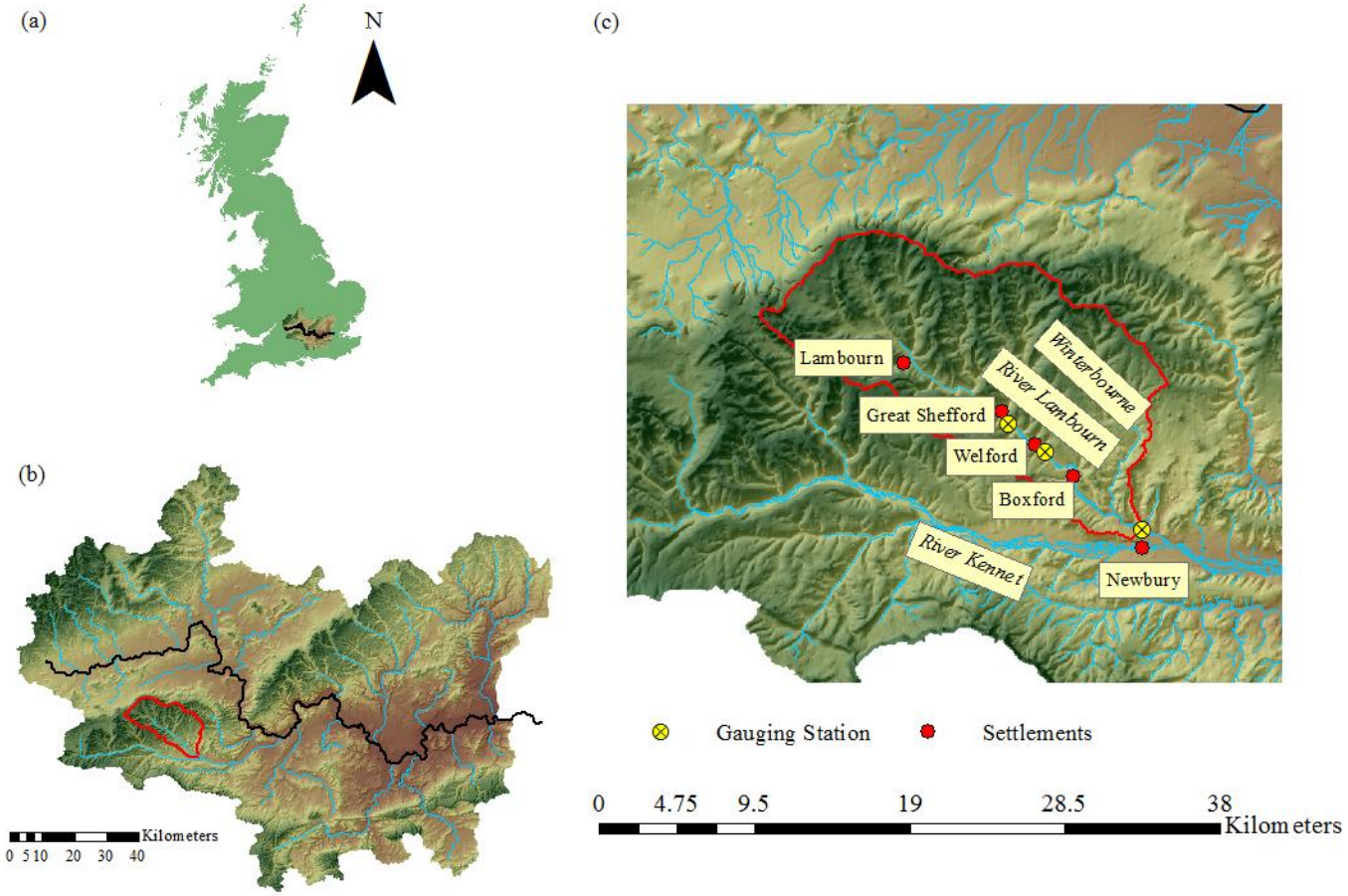

Figure 3.3.2: : Location of the Lambourn catchment within (a) The Thames basin within the United Kingdom; (b) The Lambourn catchment within the Thames basin; (c) The Lambourn catchment displaying selected local settlements and the location of the Environment Agency gauging stations at East Shefford, Welford and Shaw, listed in order moving downstream from Great Shefford.

The River Lambourn is a tributary of the River Thames. The catchment geology is comprised of Chalk (Upper Cretaceous) underlain by a thin layer of Upper Greensand (Lower Cretaceous) (Aldiss and Royse, 2002). The Chalk is overlain by Palaeogene deposits and superficial drift from the Quaternary period (Allen *et al*., 2011). Alluvial deposits line the valley bottoms. The bed material of the River Lambourn Observatory is typically gravel with a D_{84} of 32.3mm and a standard deviation of 8.8mm (Baker, 2010). However, in the lower reach of the Observatory, deposition of fine sediment is prominent.

Gauging stations are located at three points in the Lambourn catchment: at East Shefford, Welford and Shaw (Figure 3.3.2). Mean annual rainfall for the Lambourn catchment at Chieveley, Berkshire, during the study period (2009-2012) was 1918mm (UK Meteorological Office, 2014). Flow statistics for the catchment above the Environment Agency gauging station at Shaw, Berkshire, are shown in Table 3.3.1. The Base Flow Index of 0.97 indicates that the flow is largely controlled by the chalk aquifer in the catchment, the groundwater regime of which was monitored by the British Geological Survey during the Lowland Catchment Research (LOCAR) programme (e.g. Adams *et al*., 2003; Gooddy, *et al*., 2006; Mullinger *et al*., 2007).

Table 3.3.1: Flow statistics for the River Lambourn at Shaw, Berkshire. Data are taken from the National River Flow Archive (NRFA, 2012). Data refer to the period between 1962 and 2012. Data shown are the mean flow, the Q_{10} high flow threshold (flow equalled or exceeded 10% of the time), the Q_{95} low flow threshold (flow equalled or exceeded 95% of the time) and the Base Flow Index.

Mean flow (m^3s^{-1})	Q_{10} Discharge (m^3s^{-1})	Q_{95} Discharge (m^3s^{-1})	Base Flow Index
1.728	2.930	0.757	0.97

For context, Figure 3.3.3 shows the variation of discharge, stage and vegetation cover between March 2009 and March 2012. Figure 3.3.3a shows the variation in discharge at Boxford, estimated from the Shaw gauging station (P. Rameshwaran 2013, pers.comm). In general, the trend of the estimated discharges at Boxford broadly follows that of the measured monthly discharges at the site. Griffiths *et al*. (2006) demonstrated that flow is dominated by input from the Chalk aquifer and is largely unaffected by abstraction. This is reflected by the minimum flow generally being recorded in October when groundwater levels are at their lowest. Groundwater recharge following precipitation during winter leads to a peak in flow between February and April each year. During the period studied, mean flow on the River Lambourn generally decreased. However, as of winter 2012, flows have recovered with record high flows at the Observatory being recorded.

Figure 3.3.3b shows the variation in river level, measured at the upstream end of the Observatory reach. River levels on the Lambourn are closely related to the growth in aquatic vegetation. Vegetation cover (Figure 3.3.3c) is shown for the dominant species *Ranunculus*. Surveys were undertaken at four cross sections established by CEH at the site; XS2, XS3, XS4 and XS5. XS2 and XS5 are located in areas of sparse over-hanging vegetation cover, whereas XS3 and XS4 are located in shaded areas. Data were collected by Peter Scarlett (CEH Wallingford) and are presented here with his kind permission. Peaks in aquatic vegetation cover occurred during the period May to August each year (2009 to 2011). Vegetation cuts, highlighted in blue and red, produced the greatest step-change in water level seen during the water year.

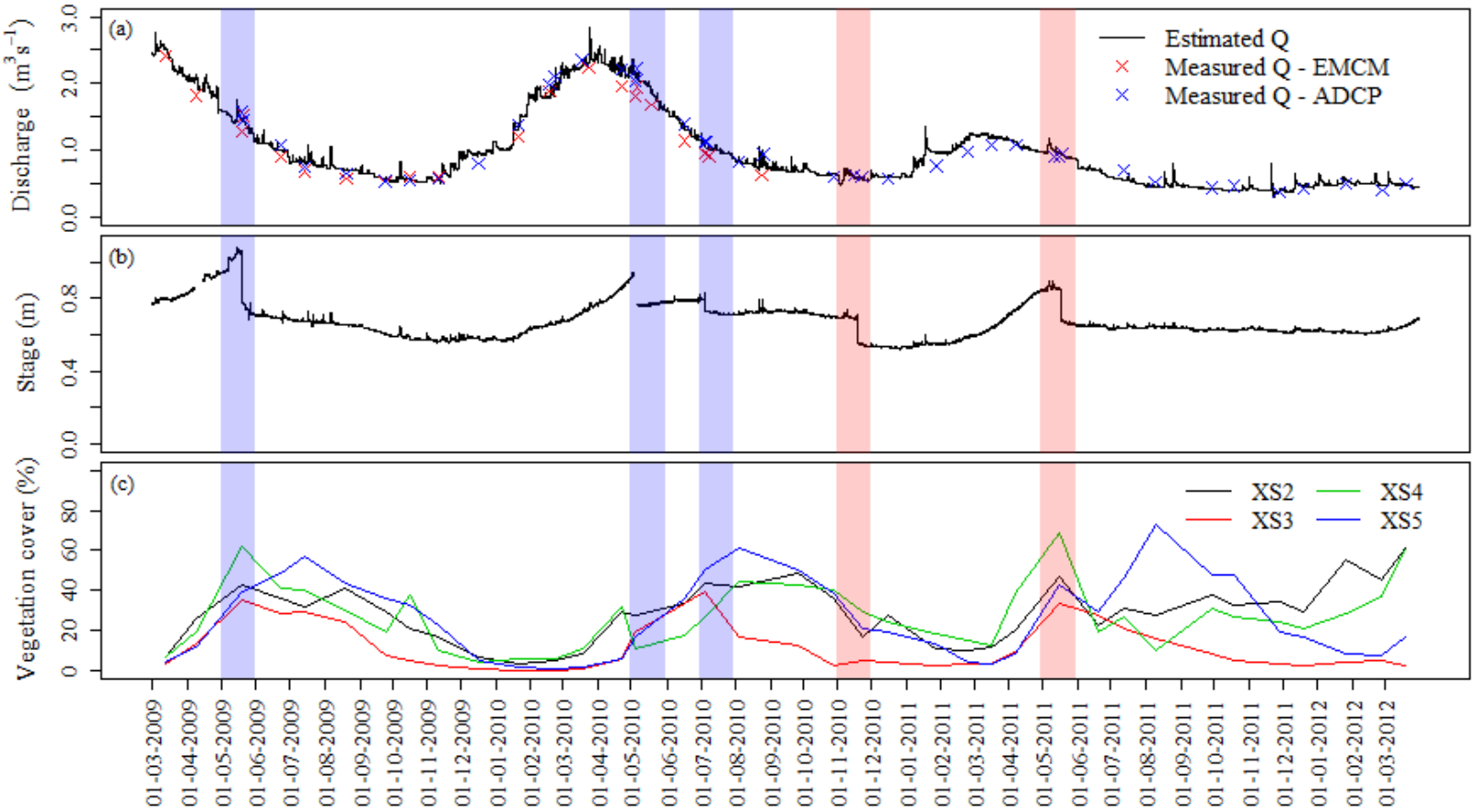

Figure 3.3.3: Flow and vegetation data at Boxford between March 2009 and March 2012 for; (a) Estimated discharge and monthly measured discharge using EMCM and ADCP; (b) River stage and (c) Percentage vegetation cover. Blue and red shading represents periods during which vegetation cuts have taken place. Red shading represents the two sampled vegetation cuts in this study.

3.4. Modelled reach

An experimentally manageable reach of the CEH River Lambourn Observatory was selected for study (Figure 3.4.1).

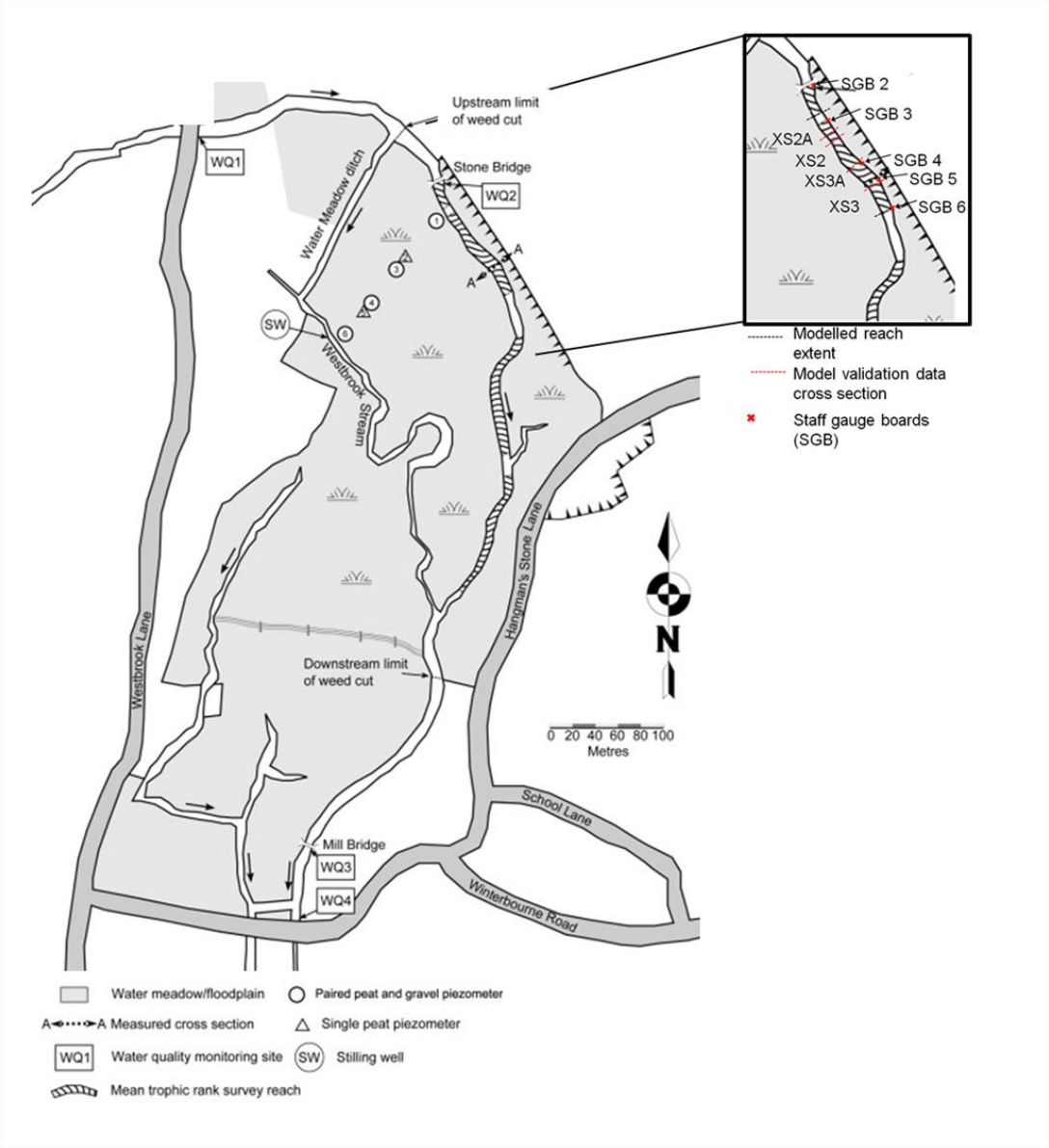

Figure 3.4.1: Map of the CEH River Lambourn Observatory. Inset displays experimental reach. Map adapted from Old *et al*. (2014).

The reach chosen for measurements had a total length along the channel centreline of 137m. The selection of the experimental reach was largely driven by

the presence of a two-arch stone bridge at the upstream end of the site. Immediately downstream of the bridge, scouring ensured that a deep and largely vegetation free cross section was maintained. This allowed detailed measurement of flow using an acoustic Doppler current profiler (ADCP) to define the flow conditions at the reach inlet. The ADCP requires no vegetation to be present due to the interference this causes to acoustic backscatter. This is discussed further in Chapter 5. The downstream limit of the experimental reach was governed by the location of a deep bend which was not accessible for surveying purposes. Hence, the end of the reach was set at the nearest staff gauge board to this bend (SGB6).

Four cross sections were established for the purpose of undertaking measurements relating to the validation of the 3D hydraulic model: XS2A, XS2, XS3A and XS3. XS2 and XS3 had already been used since 2008 by CEH for the measurement of vegetation cover and the measurement of flow for the purpose of ascertaining river discharge (XS2). The two additional cross sections were located in an area of deep water (XS2A) and at the widest cross section within the experimental reach (XS3A) in order to capture data for the full range of channel morphology.

3.5. Field survey strategy

To address the research questions set out in Section 2.5, five cases of differing vegetation cover were considered: a minimum vegetation case necessary to calibrate the bulk drag coefficient for the gravel bed, and a further four cases with substantial vegetation cover for two different growth stages (November and May), pre and post cutting.

Ideally, in order to calibrate the bulk drag coefficient for the gravel $C_{dg}S_{fg}$ (equation 3.1.14), a case with no vegetation in the channel was needed. This did not occur during the study on the River Lambourn therefore the case where the vegetation cover in the channel was at its minimum was used. The percentage cover of *Ranunculus* was assessed using data from a quadrat survey over two transects (XS2 and XS3; see Figure 5.4.8) within the experimental reach. The extent of *Ranunculus* is at its lowest during January and February when vegetation occupies less than 5% of the channel area. Hence, during January and February, Manning's *n* may be used to assess the overall roughness of the channel. During the study period (2010-2012), data provided by CEH Wallingford showed that the minimum value for Manning's *n* (0.038), calculated from flow measurements at XS2, occurred on the 22nd February 2010. Hence, flow data associated with this date were used for the calibration of $C_{dg}S_{fg}$.

The period 2009-2012 was characterised by low flows (Figure 3.3.3) and only two weed-cuts were undertaken. However, these provided the opportunity to characterise both the effect of weed management and the seasonal variation in vegetation growth. The November 2010 cut was undertaken along the channel thalweg, leaving only vegetation within the riparian zones. The aim of the cut was to flush out excess silt from the reach in order to leave clean gravel for the fish spawning season the following spring, whilst leaving a sufficient amount of riparian vegetation as refugia habitat for fish during potentially high winter flows. Cutting commenced shortly after sunrise on 18th November 2010 and was completed the following evening. An estimated 61% of in-channel vegetation was removed. Cutting was performed over no more than 1/3rd the total channel width in line with Environment Agency guidelines.

A second cut was performed on the 18th May 2011, where an estimated 35% of vegetation was removed, timed to coincide with the flowering of *Ranunculus*. The purpose of this Spring cut was to increase the diversity of in-channel habitat within the river for the fish species present at the site. The vegetation was removed in clear cut channels in the upper part of the study reach, and on a patch-wise basis in the lower part. Again, Environment Agency guidelines were followed with respect to the width of channel cleared of vegetation.

3.6. Summary

This chapter has outlined the modelling methodology. The three-dimensional approach using the DANS equations was described. The criteria for numerical modelling adhered to in this study and an outline description of the datasets necessary to construct the model have been provided. Secondly, the field site at which the study took place, the CEH River Lambourn Observatory, Berkshire, UK was described. The experimental reach represented within the model and the location for field data collection was introduced, along with its catchment context. Longer term monitoring data from the Lambourn Observatory was presented to provide the background for this study. Finally, the field sampling strategy used to characterise variations in vegetation and flow seasonally has been outlined along with a description of the nature and extent of the two vegetation cuts which were surveyed.

Chapter 4. Defining the physical boundaries of the model

A key issue when undertaking hydraulic modelling of rivers is the representation of multi-scale roughness, which ranges from broad-scale roughness, i.e. channel topography, through bedforms to grain-scale roughness i.e. individual particles which make up the river bed (e.g. Nicholas, 2001; Lawless and Robert, 2001; Lane *et al.,* 2002; Lane *et al.,* 2004; Nicholas, 2005, Carney *et al.,* 2006; Nikora *et al.,* 2007; Rameshwaran *et al.,* 2011; Nikora *et al*., 2013). These different elements of roughness do not map well onto the sort of simple mesh required for hydraulic modelling, as different scales of mesh would be required.

If using a RANS approach (see Section 2.4), broad scale channel topography and large bedforms (e.g. channel bars) can be represented using a single mesh. However, at scales smaller than this, e.g. small bedforms and gravel clusters, the mesh resolution needed to resolve such roughness is too fine for practical use due to the enormous data requirements and computational demands (e.g. Lane *et al.,* 2004; Hardy *et al*., 2005; 2007). Small scale roughness is, therefore, represented in a RANS approach using a roughness function. Where a roughness function is used, e.g. the law of the wall (Launder and Spalding, 1974), the mesh size imposes a limit on the roughness parameter k_s of 29.7Z, where Z is the normal distance between the centre of the bottom cell and the wall. Values of k_s above this are meaningless and, from a numerical modelling perspective, it is not possible to increase the size of the bottom cell to accommodate a larger k_s as the non-dimensional criterion for the application of the wall function ($30 < Z^+ < 300$ where $Z^+ = U_* Z/\nu$) is not satisfied. Studies have also shown that use of k_s in a RANS approach cannot match the measured free surface of a gravel bed river (Rameshwaran and Naden, 2012).

Consequently, in this study, an approach using a double averaging methodology, DANS, was preferred. The DANS approach has the significant advantage that roughness due to the broad-scale topography and large bedforms are accounted for explicitly in the model mesh, whilst roughness at scales smaller than this are accounted for using spatially-averaged parameters describing the blockage and drag of these small-scale roughness elements (Lane *et al.*, 2004; Carney *et al*., 2006; Nikora *et al.*, 2007, Rameshwaran *et al*., 2011; Nikora *et al*., 2013). These parameters include porosity, frontal projected area, lateral projected area, and element surface area. These parameters were determined in this study from field measurements.

The broad-scale reach topography was collected using an integrated differential GPS (DGPS) and total station surveying system, which allowed data collection to an accuracy of ±5cm. Post-processing of the topography dataset, was undertaken using an adaptation of the kriging methodology outlined by Legleiter and Kyriakidis (2008). Data to describe the gravel-bed microtopography were collected using a physical profiler with a 0.25m by 0.25m footprint with data recorded to an accuracy of 1mm. The data were detrended using a LOESS model (Cleveland, 1979) to remove the two dimensional trend of the gravel bed, and parameters of projected area, surface area and porosity calculated. Fifteen samples were processed in order to provide the spatially-averaged roughness parameters required by the DANS approach. This chapter describes the data collection and post-processing for both the channel topography and the gravel-bed micro-topography.

4.1.Channel topography – data collection

Three dimensional hydraulic modelling of rivers requires a specification of topographic information comparable with the mesh resolution (Lane et al., 2002), often within the range 0.001-0.5m, although resolving roughness to a scale of 0.001m is not practical for hydraulic model applications due to the huge computational effort required, as previously explained. The lack of data at a similar scale to the mesh resolution has been identified as a major limitation upon the successful validation of hydraulic model applications to gravel-bed rivers (Lane et al., 1999). As such a need for high resolution 3D topographic data rather than data collected at widely-spaced cross sections, commonly used for 1D models such as HEC-RAS, is apparent. In this study, the topographic data were used to build a Digital Elevation Model (DEM) to represent the channel bathymetry at the resolution of the model mesh.

The main factors affecting the accuracy of the resulting DEM are the accuracy, density and distribution of the source data (Liu et al., 2007). It is generally accepted that an increased number of points leads to a more accurate DEM (Lane et al., 1994; 1998; Heritage et al., 2009). Typical point densities using various methods of topographic survey are given in Table 4.1.1.

Table 4.1.1: Comparison of point densities obtained using various topographic survey methods found in the literature.

Reference	Method	Density (pts m^{-2})	Survey scale
Lane *et al*. (1994)	Ground based survey	1.2-1.7	Reach
Brasington *et al.* (2000)	Ground based survey	1.0-3.2	Reach
Liu *et al*. (2007)	LiDAR	0.037	Catchment
Smith *et al.* (2012)	Terrestrial laser scanning	$2.2x10^6$	Patch

The need for an increased number of points has propagated the use of remote sensing techniques in the gathering of topographic source data. Such techniques include the use of LiDAR (e.g. Kinzel *et al*., 2008; Hilldale and Raff, 2008; Mandlburger *et al*., 2009; Legleiter, 2012), digital photogrammetry (e.g. Chandler et al., 2002) and terrestrial laser scanning (TLS) (e.g. Milan *et al.*, 2007; Heritage and Milan, 2009; Hodge *et al*., 2009; Smith *et al.*, 2012). The use of an acoustic Doppler current profiler coupled to Real Time Kinematic (RTK) GPS systems for high resolution data collection has also been noted (Wilson *et al.*, 1997).

However, remote sensing approaches are limited due to a number of factors: dependence of data collection on line of sight (not always possible due to riparian vegetation); length of time required to process that data; and high equipment cost. The accuracy of remote sensing methods, particularly in the vertical dimension, is also reported by Brasington et al. (2003) to be much lower (e.g. RMSE ± 0.21m) than in traditional ground-survey methods such as RTK GPS (e.g. RMSE ± 0.052m). Thus, due to their high level of accuracy (Casas et al., 2006), ground-based

techniques are often used in preference to remote sensing techniques for surveys at the reach scale (Brasington et al., 2000; Legleiter and Kyriakidis, 2008).

Historically, ground-based surveys have been undertaken on a cross section by cross section basis (Schäppi et al., 2010). This is possibly a legacy of hydraulic geometry where information for the analysis of river channel morphology was provided by analysing one or a number of channel cross sections through time. Such data provide key information required for 1D hydraulic models. However, these approaches led to an over emphasis on cross-sectional variation in morphology at the expense of downstream variation. Points over a cross-section were generally separated by 0.1 to 0.5m and points in the downstream by 5 to 20m (Lane et al., 1994).

When spaced closer together (<5m), data from cross sections have been used to produce DEMs (Milan *et al.*, 2001; Heritage *et al.*, 2009). Heritage *et al*. (2009) found that DEM error is strongly influenced by the position of survey points relative to the morphology being surveyed. Hence the survey method employed is critical. Compared to LiDAR data, the greatest vertical error was found in DEMs generated from cross-sectional data. Data collected by taking into account morphological outlines, cut banks, breaks of slope, and inclusion of spot heights on uniform surfaces reduces DEM error significantly (Heritage *et al*., 2009). It is therefore desirable to select a sampling strategy that both optimises the time taken to collect the data and the spatial density/morphological detail required.

Given the large amount of riparian vegetation at the River Lambourn site, remote sensing approaches were not suitable for this study. Furthermore, ground-based surveys generally provide a higher vertical accuracy and are much quicker to perform and post-process than remote sensing approaches. Recent technological

advances in ground-based survey have facilitated rapid topographic data capture due to the automation of previously manual procedures. Robotised total stations and differential GPS have increased the speed and resolution of ground surveys. In this study, an integrated total station and differential GPS (DGPS) system was used to collect the topographic data. The system provided a number of advantages, allowing a balance between survey resolution and duration: (i) data were collected in National Grid coordinates which allowed comparison to aerial photographs of the River Lambourn; (ii) if line of sight was lost at any point, the system was able to switch from optical to GPS data collection which greatly reduced the time spent refocusing the total station on the optical sight when obscured by riparian vegetation; (iii) and station set up time was greatly reduced due to the presence of the integrated GPS. This removed the need to relocate ground control markers at the start of each day of surveying. However, there is still need for a balance between spatial resolution and duration of the survey (Rumsby et al., 2008) and a suitable sampling strategy had to be devised to allow the collection of important topographical features at an appropriate spatial resolution for the model. This strategy is described in Section 4.1.1.

4.1.1.Topographic Survey Method

Points were surveyed using an integrated surveying system comprising a Trimble S3 total station and R8 GNSS DGPS system with real-time VRS NOW corrections. Station set-up was performed using three control points that encompassed the site area. Each point was surveyed using a 180-epoch GPS measurement that was then back-sighted to the total station location using an optical measurement. Coupled with the known location of the nearest OS National Grid correction transmitter using the

VRS-NOW function (a real time data correction function onboard the surveying equipment), this allowed the standard deviation for northing, easting and elevation to be assessed. The required standard deviation for each component was 0.05m or less for the station set-up procedure to be accepted. If this was not achieved, the set-up was repeated. For the collection of points, a hybrid between the approach to river bed survey suggested by Heritage *et al*. (2009) and a cross-sectional approach was undertaken. To ensure a suitable grid resolution, points were collected over the experimental reach at a cross-stream and downstream interval of approximately 0.5m. The decision to adopt the cross-sectional approach at a resolution of 0.5m was taken to ensure data were collected at an appropriate spatial resolution to account for morphological variation whilst also keeping the survey time to a reasonable duration. A cross-sectional approach was used to ensure that complete coverage of the channel was achieved. To augment these points, morphological features such as bank break lines and in-channel breaks of slope were surveyed in much greater detail by increasing the point density of the survey in these locations. This was undertaken with the aim of reducing the error of the resulting DEM. The distribution of points collected during the topographical survey is shown in Figure 4.1.1. The average point density of the survey was calculated to be 2.6 points per square metre, a value within the range given by Brasington *et al.* (2000) for a similar survey on the River Feshie (Table 4.1.1).

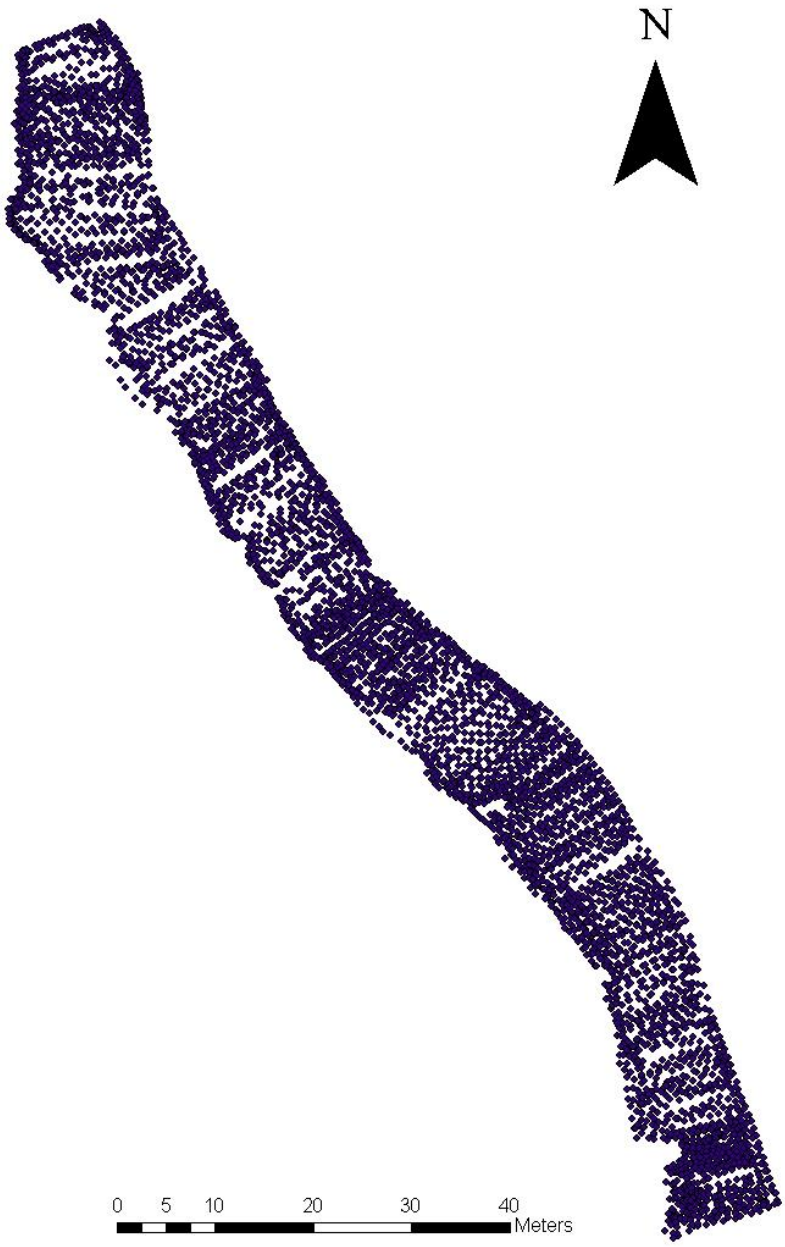

Figure 4.1.1: Distribution of points in the topographic survey of the River Lambourn at Boxford (April 2010)

4.2. Channel topography – data processing

The topography data were converted to a digital elevation model at the resolution of the model mesh to define the channel bathymetry. The accuracy of the resulting DEM may be influenced by the interpolation algorithm used (Heritage *et al*, 2009). Two main methods have been applied successfully to fluvial data: triangulated irregular networks (TINs) (e.g. Brasington *et al*, 2000; Milan *et al*, 2007; Rumsby *et al*, 2008) and kriging (e.g. Nicholas *et al*, 2003; Fuller *et al*, 2003). It has been found, however, that the choice of interpolation strategy is not as important as survey strategy as discussed above (Heritage *et al*, 2009).

In this study, kriging was the interpolation method chosen. Carter and Shankar (1997) advocated the use of kriging to derive statistically optimal predictions of bed elevation from irregular survey data. Several advantages of this approach were cited: (i) predictions are based on the semivariogram (a statistical model of spatial structure fitted to the data); (ii) the kriging system is constructed to minimize the variance of the prediction errors while ensuring that they are unbiased and (iii) the error variance provides an indication of uncertainty associated with each prediction. The key advantage of kriging is that the average spatial variability of the data is integrated into the interpolation process (Reed *et al*, 2004; Legleiter and Kyriakidis, 2008; Meadows, 2010).

Kriging is derived from regionalised variable theory. The method depends on expressing the spatial variability of a given variable in order to make predictions of that variable at unsampled locations (Oliver and Webster, 1990). The main assumption behind the kriging method is that of stationarity. This means that statistical properties do not depend on exact spatial locations and that correlation between any two points depends only on the vector which links them.

River channel bathymetry data violates the assumption of stationarity made during the kriging procedure (Carter and Shankar, 1997). Due to the geometry of the channel, trends are present in both the cross-stream and downstream direction. This means that differences would be expected between the elevation values of points at the top of the bank and channel centre, and points upstream and downstream within the reach. The variance which results from these differences is dependent on location within the channel, not just the separation distance. This non-stationarity means that variance always increases with distance. It is therefore important to remove these trends prior to kriging.

4.2.1. Channel bathymetry generation method

The generation of the bathymetry model was undertaken using a method similar to that of Legleiter and Kyriakidis (2008). Here, survey data are first transformed from Cartesian (x,y) coordinates into a channel centred (n,s) coordinate system. The coordinate transformation was undertaken using algorithms outlined by Legleiter and Kyriakidis (2007) and based upon the generalised algorithms of Merwade *et al.*(2005) and Goff and Nordfjord (2004). The coordinate transformation is required as kriging weights depend on data-to-data and data-to-unknown covariance values (i.e. distances). An appropriate channel-centred distance metric must, therefore, be used to model the variogram and compute covariances. Kriging should be performed within a frame of reference that allows for unambiguous identification of along versus cross-channel anisotropy (Legleiter and Kyriakidis, 2008). The conversion from (n,s) coordinates to (*x,y*) was undertaken using an algorithm developed for ArcGIS by Dr Venkatesh Merwade (University of Texas) (Merwade *et al*., 2005).

Trends present in the data which violate the assumption of stationarity in kriging are removed and the resulting data kriged using the ordinary kriging method. Following kriging, the trends are replaced and data converted from the (n,s) coordinate system back to Cartesian coordinates. There are two ways of dealing with the cross-sectional trend present in the survey data. The first (Method 1) is to consider the surveyed data as a whole, removing the cross-sectional trend using a LOESS model. The second (Method 2) is to treat the bed and bank as separate datasets. In this latter approach, following trend removal, the bed data are kriged and the height of the top bank is determined using either a linear or LOESS fit to the surveyed data. Both methods were applied to the data in order to find the best representation of the channel bathymetry. The two methods were carried out using a variety of packages (MATLAB, R, ArcGIS). Work completed in MATLAB was made possible by the kind provision of code by Dr. Carl Legleiter (University of Wyoming). The workflow developed to process the data is shown in Figure 4.2.1.

Kriging was undertaken using a frame of reference which is fitted to the channel itself. An orthogonal curvilinear coordinate system defined by a streamwise axis (s) aligned with the channel centreline and a transverse axis aligned normal to this (n). This axis system has been widely used to describe flow and sediment transport processes in meandering rivers (e.g. Smith and Maclean, 1984; Nelson *et al,*. 2003). The resulting coordinate system is right-handed, i.e. s increases positively downstream and n is positive towards the left-bank. The resultant space is hereafter referred to as the (n,s) space.

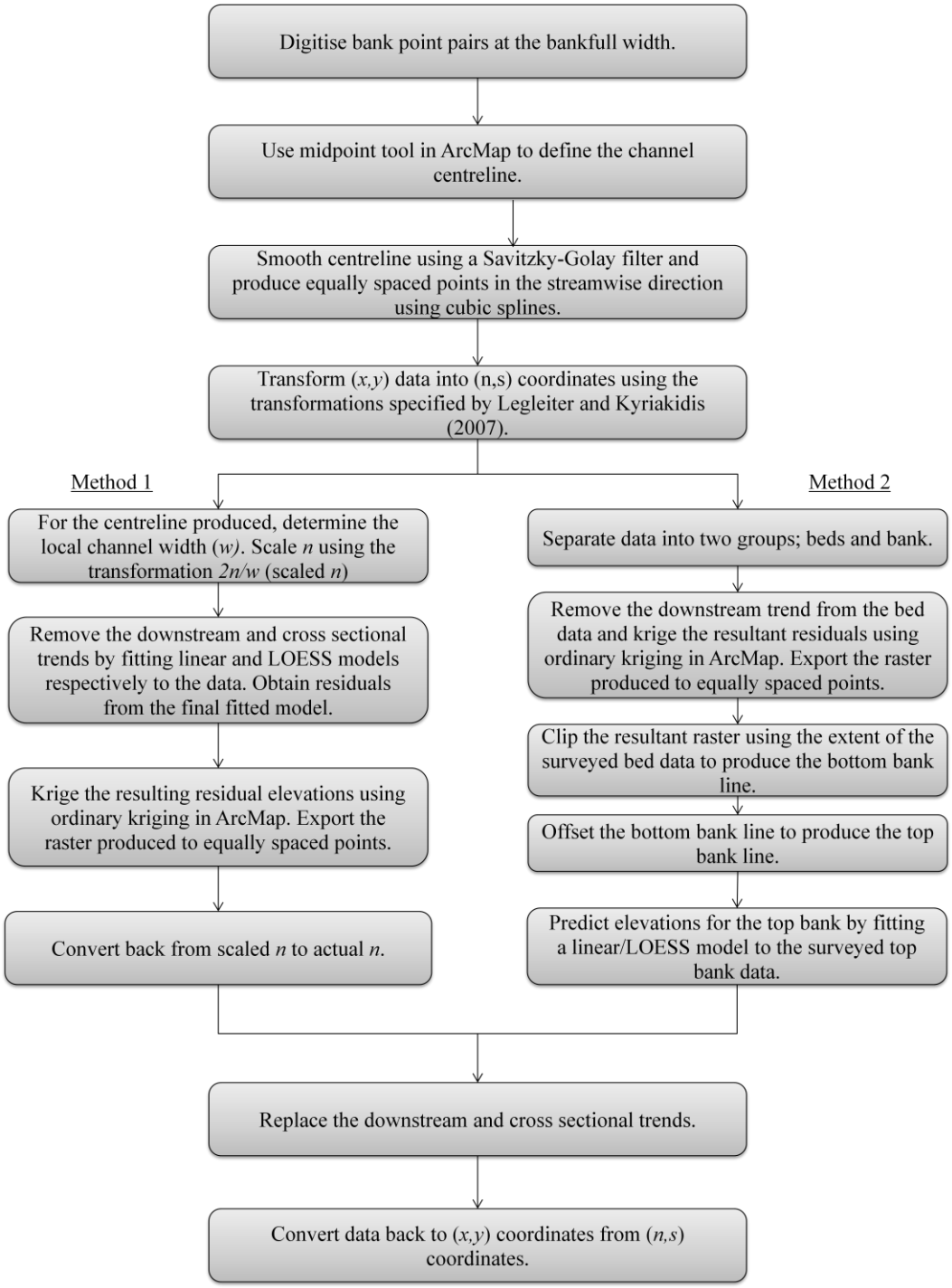

Figure 4.2.1: Workflow for the generation of bathymetry models adapted from that developed by Legleiter and Kyriakidis (2008).

To undertake the transformation, bank points were digitised from the extent of the surveyed data, the result is shown in Figure 4.2.2. Centreline points were defined by selecting a point on one bank, another on the opposite bank, and then

creating a point at the midpoint of the cross-section using the midpoint editing tool in ArcGIS.

Figure 4.2.2: Centreline definition of the River Lambourn. Points were digitised along the bank (circles) and the midpoints of bank pairs were determined (triangles).

Next, the digitised centreline was discretised into a number of equally spaced points in the streamwise direction at an interval of 0.1 m. The resultant centreline was smoothed using a Savitzky-Golay filter (Hamming, 1983). Derivation of a

smoothed centreline is important as subsequent steps in the transformation involve derivatives which tend to amplify point-to-point variation in the centreline trace (Fagherazzi *et al.*, 2004; Legleiter and Kyriakidis, 2007). A number of parameters were required for the discretisation of the centreline:

- Number of times for the Savitzky-Golay filter to be applied (*f*);
- Order of the polynomial fitted to the centreline (*p*);
- The number of points included in the search window (*m*);
- The number of discretised points required (based upon the cumulative centreline distance) (*N*);
- The search distance (set slightly greater than the greatest plausible channel width).

The effect of varying *f*, *p* and *m* was examined. The number of discretised points was set to produce equally spaced points of 0.1 m over a cumulative distance of 145 m along the centreline (*N*=1450). The search distance was set at 15 m. When varying a particular parameter, the other parameters were set at the midpoint of the range of values being explored. The range of values of the parameters is shown in Table 4.2.1. Figure 4.2.3 illustrates the effect of varying these parameters.

Table 4.2.1: Values input and varied to the centreline smoothing algorithm

Parameter	Values
Number of times filter applied (*f*)	1,2,3,4,5
Order of the polynomial fitted (*p*)	2,3,4
Window size (*m*)	3,5,7,9,11
Output number of centreline points (N)	1450

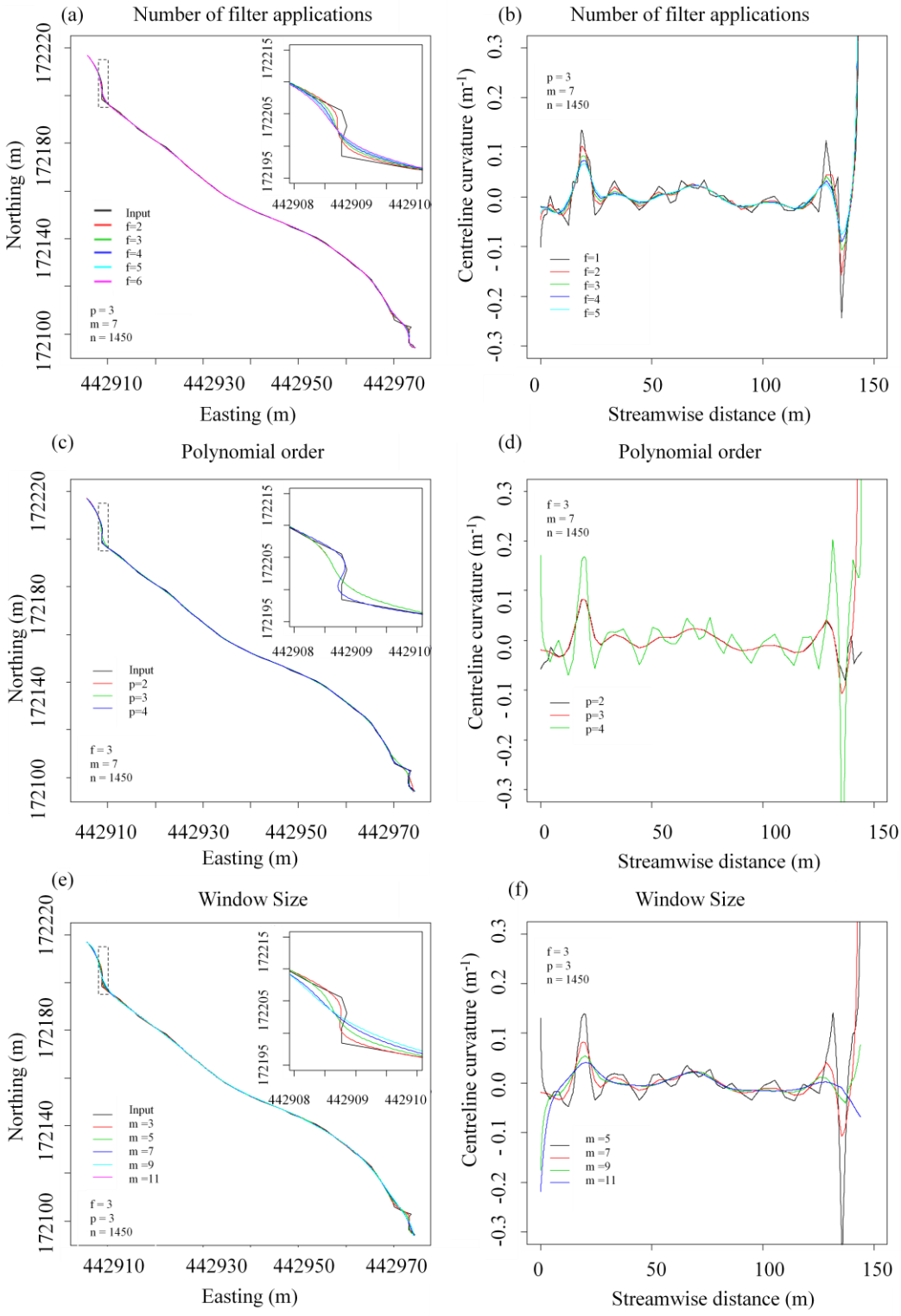

Figure 4.2.3: Sensitivity of centreline definition (left column) and curvature (right column) to filter parameters

Figure 4.2.3a and Figure 4.2.3b illustrate that two applications of the filter do not provide sufficient smoothing of the centreline. Where f = 2, the resulting centreline still follows the input centreline from the digitisation of the aerial photograph, represented in black (Figure 4.2.3a) and the curvature of the centreline shows a high degree of noise (Figure 4.2.3b). A third application of the filter (f = 3) reduces the noise in the fitted centreline, with higher values of f having relatively little effect. The opposite is true when selecting which order of polynomial to represent the centreline (Figure 4.2.3c and Figure 4.2.3d). Here, higher order polynomials fit closely to the digitised centreline, an effect which is not desired. As a result, higher order polynomials produce a centreline with a large amount of noise in the fitted curvature (Figure 4.2.3c). The cubic function was selected as producing the best representation of the centreline as a balance between the desired smoothed centreline and that digitised from the aerial photograph. Finally, the effect of the window size was considered. With an increasing window size, channel centreline curvature is reduced (Figure 4.2.3f). No further reduction in curvature is noted beyond m = 9.

On the basis of these results, values of f = 3, p = 3 and m = 9 were chosen as the optimal parameters for the Savitzky-Golay filter for the River Lambourn. Values in the literature for a channel of similar curvature have been quoted as f = 3, p = 3 and m = 7 (Legleiter and Kyriakidis, 2007). It is important to note that the assignment of values for the filter is dependent on site characteristics such as the width and sinuosity of the channel (Legleiter and Kyriakidis, 2007).

4.2.2. Trend removal

Trend removal was undertaken using two different approaches, as outlined in Figure 4.2.1. In Method 1, the bed and banks are treated as the same dataset and the trends in both the cross stream and downstream directions are removed. To ensure a consistent application of trend removal in the cross-stream direction, the distance from the smoothed centreline was scaled by the local width, determined by calculating the distance from each centreline point to a digitised bank line in ArcGIS. The resulting relationship between local width (w) and distance along the centreline (s) is shown in Figure 4.2.4.

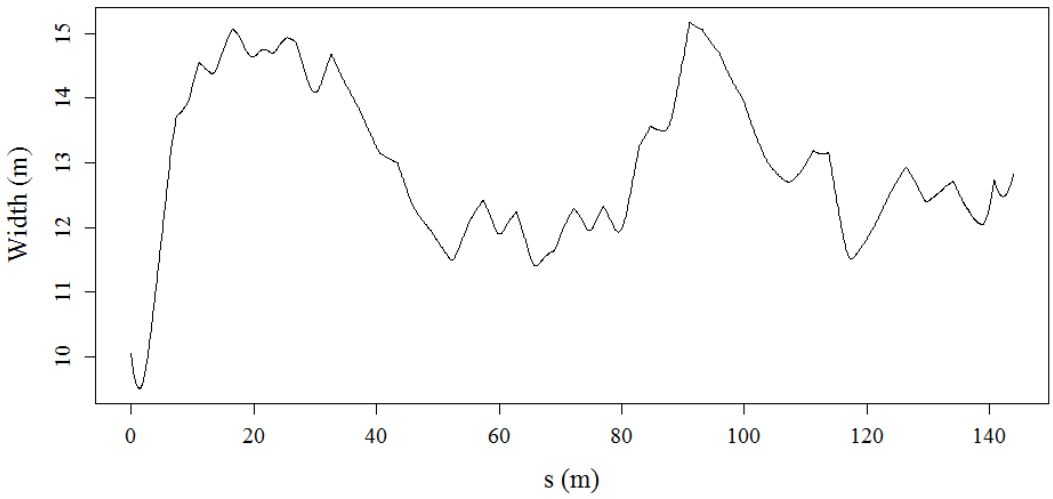

Figure 4.2.4: Relationship between local width and distance along the centreline (s).

In order to remove the cross-sectional trend, the data were scaled by the local width using a transformation of $2n/w$ The effect of this transformation is shown in Figure 4.2.5. The transformation removed some of the scatter in the data in the region above z = 90.5m caused by the variation in width along the channel.

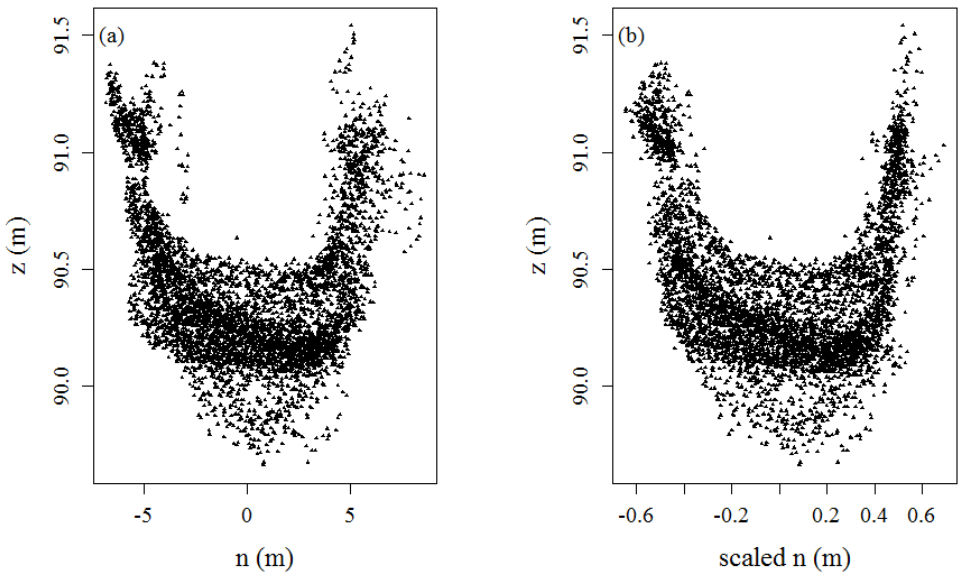

Figure 4.2.5: Effect of transforming the data by scaling n by the local width.

In Method 2, the bed and banks were treated as separate datasets. Bed and bank data were identified using information assigned to each point when the data was surveyed (Figure 4.2.6).

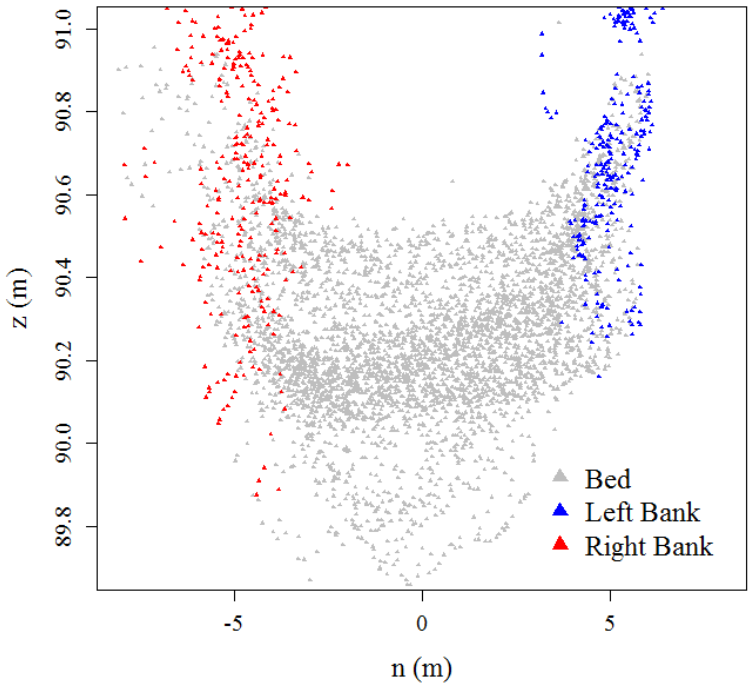

Figure 4.2.6: Decomposition of surveyed data into bed and bank components.

The first trend removed was the downstream channel slope. A linear model was fitted to the data in the form $z = ms + c$ where m and c are the slope and intercept respectively. For Method 1, the data and the fitted model, as well as the data with the trend removed, are shown in Figure 4.2.7.

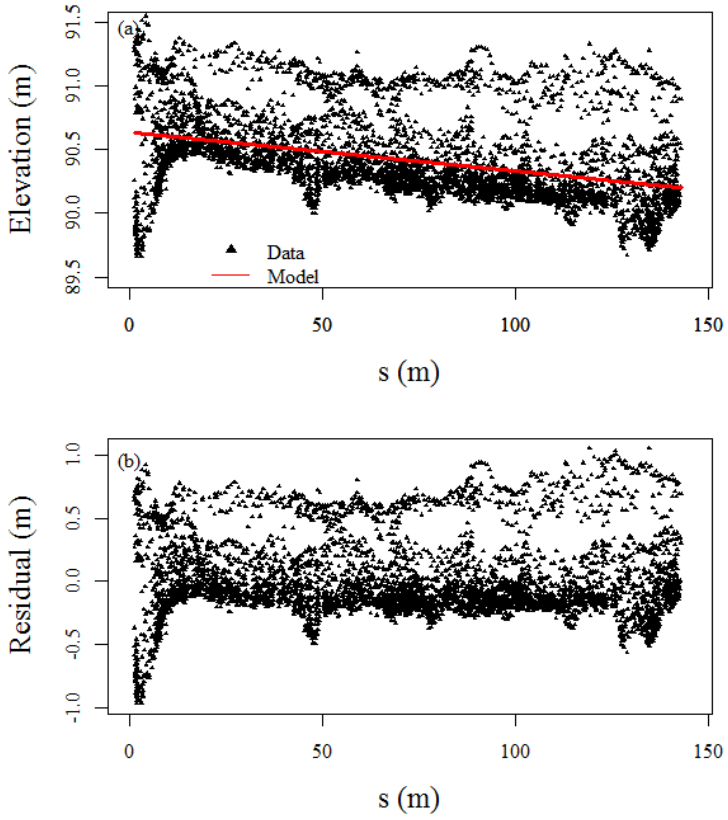

Figure 4.2.7: (a) Fitting of a linear model to remove the downstream trend from the data; (b) data with trend removed.

To remove the cross-sectional trend, a LOESS model was then fitted to the data. To explore possible trend lines, the value of the span for the model was adjusted between 0.2 and 1. The results of this analysis (Figure 4.2.8) show that a span level (α) of 0.2 attempts to fit the model closely to the data provided but bends over at the edges of the channel. Values of α closer to 1 provide a much smoother representation of the trend. To assess which value of α was most suitable for the River Lambourn,

the equivalent number of parameters included in the model and residual standard error were also analysed (Figure 4.2.9).

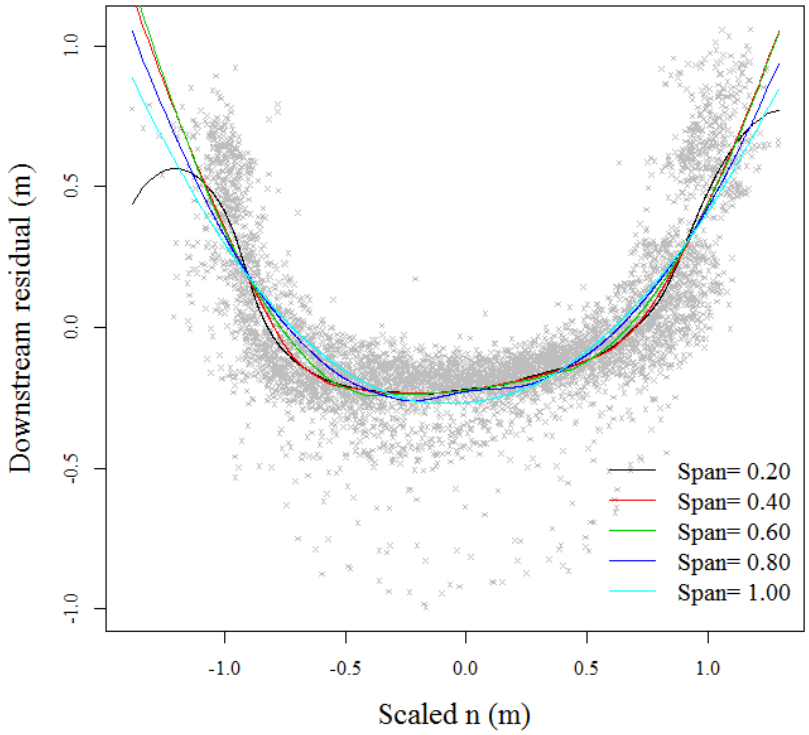

Figure 4.2.8: Effect of varying the value of the LOESS span on the model fitting to the data.

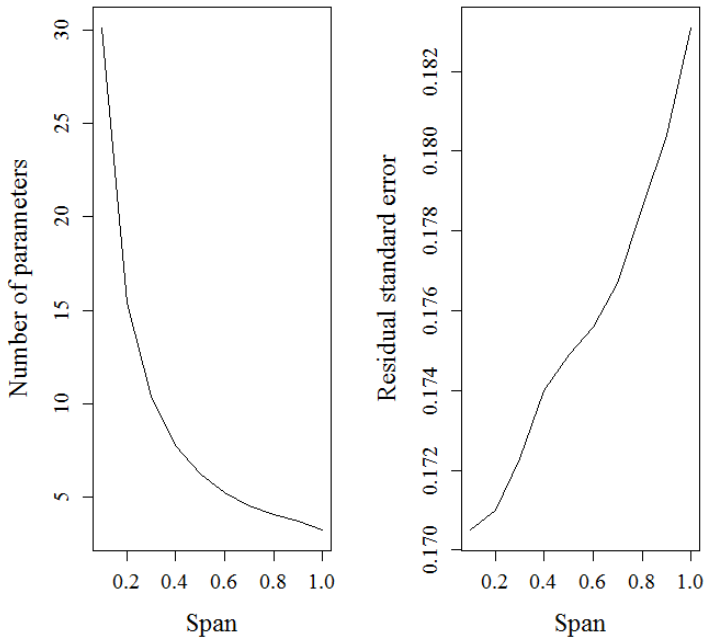

Figure 4.2.9: Analysis of the effect of varying the value of α on the equivalent number of parameters in the LOESS model and the residual standard error.

For a value of α of between 0 and 0.2, there is a tight fit to the measured data resulting in low values of the residual standard error (RSE). Values of α between 0.4 and 0.6 have increased values of RSE (0.175 α = 0.6), with the error increasing greatly beyond an α value of 0.8 as the fit becomes more smooth. To select between a value of α of 0.4 or 0.6, the equivalent number of parameters was considered, which is similar to degrees of freedom for an Ordinary Least Squares regression. In order to limit the degrees of freedom to five or less, i.e. to avoid a fit which corresponds too closely to the original data, whilst maintaining a low RSE value a value of α of 0.6 was selected. Again, the residuals of the model were obtained to assess the success of trend removal from the data (Figure 4.2.10).

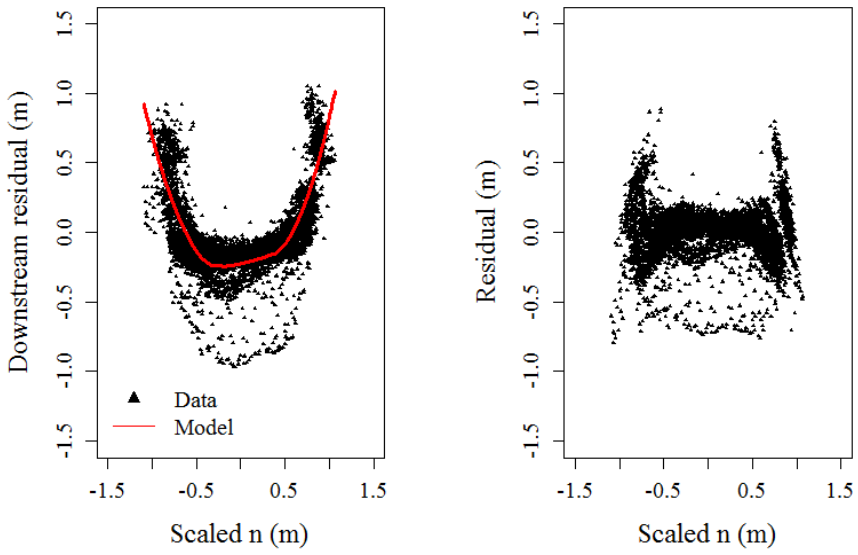

Figure 4.2.10: (a) Final fitted LOESS model and (b) the resultant residuals

The trend fitted using the LOESS model with a value of α = 0.6 displays a reasonable fit to the data. The scatter below the fitted model line results from the deeper area of the channel adjacent to the stone bridge. The final residual values display no significant trend. The very high variability in the data at the lower and upper ranges of scaled *n* results from the variation in the shape of the banks.

In Method 2, when considering the bed and bank data as separate datasets, trend removal in the cross-sectional direction and scaling by the local width was not performed. Downstream trend removal for the bed data in this case is shown in Figure 4.2.11. Treatment of the banks is outlined in Section 4.2.5 .

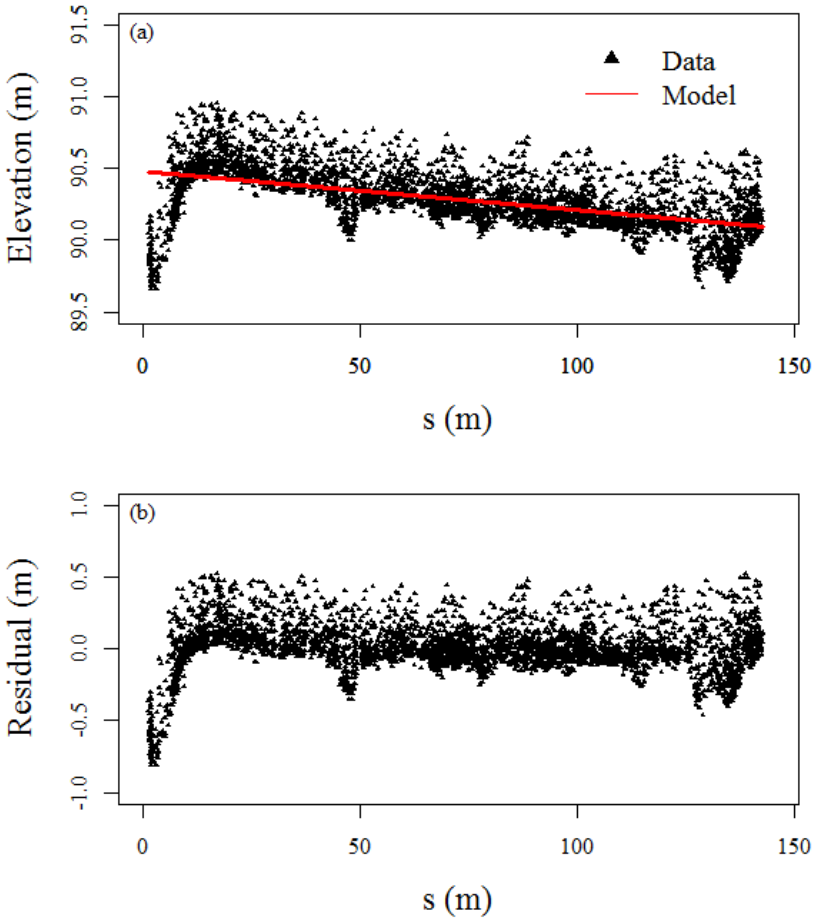

Figure 4.2.11: (a) Fitting of a linear trend to remove the downstream trend from the data. (b) data with trend removed.

4.2.3. Ordinary kriging of residuals

The detrended datasets from both Methods 1 and 2 were interpolated using the method of ordinary kriging. The spatial structure of the data is expressed using a semivariogram which provides a measure of the variance of the differences between the surveyed points as a function of distance or 'lag'. The variance of the differences

is expressed using semi-variance, defined as half the expected distance between two values and estimated using:

$$\hat{\gamma}(\boldsymbol{h}) = \frac{\mathbf{1}}{\mathbf{2}} \cdot \frac{\mathbf{1}}{\boldsymbol{n}(\boldsymbol{h})} \sum_{\boldsymbol{i}=\mathbf{1}}^{\boldsymbol{n}(\boldsymbol{h})} \left(\boldsymbol{z}(\boldsymbol{x_i} + \boldsymbol{h}) - \boldsymbol{z}(\boldsymbol{x_i})\right)^2$$

4.2.1

where $\hat{\gamma}$ is semi-variance as a function of the lag distance h, n is the number of observation pairs separated by h used in each summation and z is the random variable at location x_i. The semivariogram is the semi-variance plotted against lag distance (Figure 4.2.12).

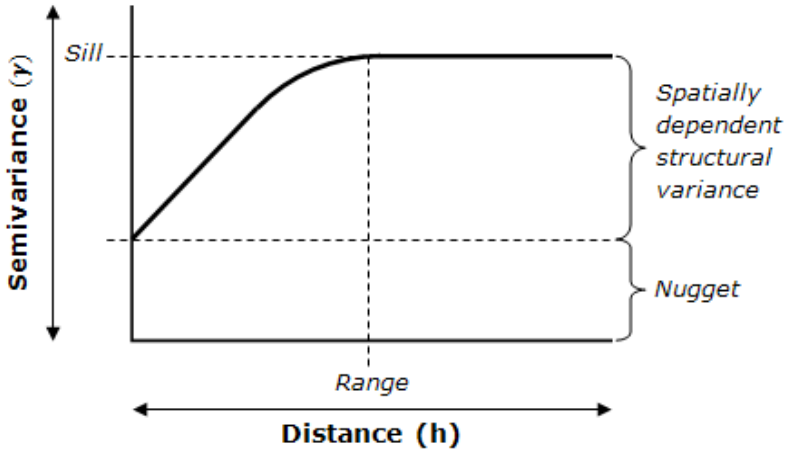

Figure 4.2.12: Example semivariogram with key components highlighted (Meadows, 2010)

The three key components of the semivariogram are the range, nugget and sill. These parameters describe the spatial structure of the data. The range indicates the distance at which the data are no longer spatially dependent. The maximum level of semi-variance is known as the sill and this represents an estimate of the total

variance of the population. It is important to recognise, however, that the semi-variogram produced during the kriging procedure will never reach a constant sill (Carter and Shankar, 1997). Lastly, the nugget gives the difference value as the distance between two points tends to zero. This represents the spatially-independent variance. To produce the most accurate semivariogram for the kriging procedure, the lag interval was specified manually. As the data were not on a regular grid, the lag interval was set to the average separation distance between nearest neighbours (Isaaks and Srivastava, 1989; Webster and Oliver, 2001). For the topography data collected for the experimental site at the Lambourn Observatory, the average distance between nearest neighbours (lag size) was found to be 0.32m. The number of lags was specified so that when multiplied by the lag size it did not exceed half the length of the widest channel cross-section (Johnston *et al.*, 2001), in this case 11m. The semivariograms produced for both Method 1 and Method 2 are shown in Figure 4.2.13 and their associated parameters in Table 4.2.2.

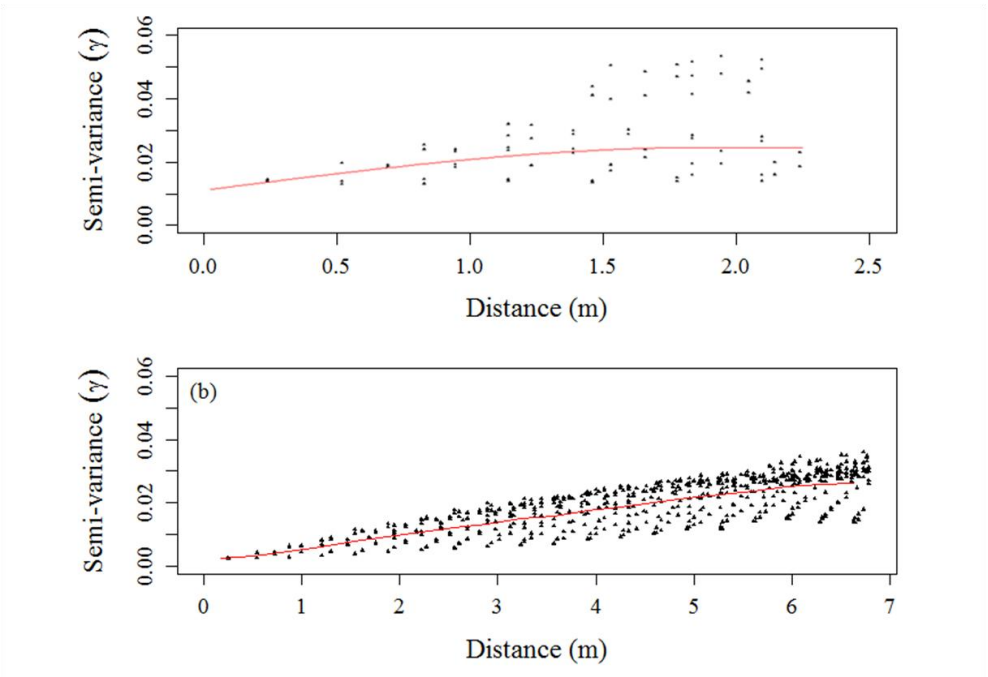

Figure 4.2.13: Semivariogram modelled from (a) Method 1 de-trended bed and bank data; (b) Method 2 detrended bed data.

For Method 1 (Figure 4.2.13a), high scatter is apparent at a distance of 1.5m. This results from including the bank data in the kriging. As the difference in height between bed and bank points is high, semivariance is high. Conversely, for Method 2 (Figure 4.2.13b), scatter in the region below the sill is much lower. Furthermore, fewer points are considered for the semivariogram derived for Method 1 as fewer lags are required to cover the scaled width due to the width scaling. This occurs as, although the lag size remains approximately equal in each method, the overall width of the channel has been reduced due to scaling and hence requires a smaller number of lags to cover the scaled width.

Table 4.2.2: Kriging parameters used to model the semi-variogram for Methods 1 and 2

Parameter	Method 1 Bed and banks	Method 2 Bed only
Range	2.24	6.8
Nugget	0.014	0.003
Lag Size	0.32	0.34
Number of lags	7	20
Sill	0.029	0.026

The values of the parameters used to model the semi-variogram reflect the difference in approaches used. Where width scaling has been used in Method 1, the range is smaller than for Method 2 which only considers the bed data. The average distance, or lag size, between nearest neighbours remains broadly the same, as is to be expected. The value for the nugget is lower in Method 2. The nugget represents the difference between two points, in this case the predicted residual, as the distance between them tends towards zero. This would suggest that the difference between

the residual heights of two points is lower in Method 2. The similar sill values suggest that the overall variation in each dataset is of a comparable magnitude.

Following kriging, a rectangular grid of predicted elevations was produced in the (n,s) coordinate system. To delineate the area of interest for each approach, this area was clipped in ArcGIS. Clipping was performed with the top bank lines for Method 1 and the bottom bank lines for Method 2.

4.2.4. Generation of top bank lines for Method 2

In Method 2, top bank lines were not produced by kriging as only the bed data were considered. Surveying of true top bank lines on the River Lambourn was problematic due to the high density of riparian vegetation. Top bank lines were, therefore, surveyed as close to the true top bank as possible. To enable a more appropriate prediction of the bank slope, the bottom bank line obtained from the clipped kriged grid was offset by 0.7m. The value of 0.7m was chosen as this represented the median distance between the surveyed top and bottom bank lines for the experimental reach. Although the median differed for the left and right banks (0.78m and 0.70m respectively), the difference was negligible compared to the width of the channel and the smaller of the two distances was chosen so as to treat both banks equally.

Initially, a linear model was fitted to the surveyed bank-top data for each bank of the River Lambourn (Figure 4.2.14). The difference in slope between banks reflects the different bank morphology. The true right bank is fairly uniform in nature with a large step change from the floodplain to the river bed. This is shown by relatively small scatter in the data. The true left bank, however, varies in morphology along the reach. This influences the slope of the linear regression fitted to the data.

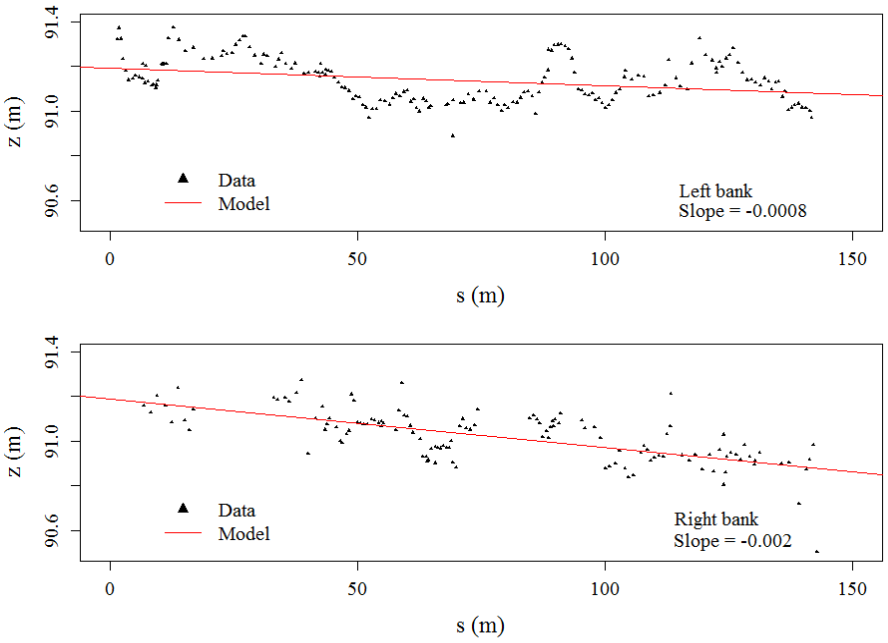

Figure 4.2.14: Linear model fitted to surveyed bank top data for left and right banks.

The resulting linear models were used to predict the bank-top elevation for each of the values of *s* on the smoothed bank lines. To check whether the bank generated was representative of that surveyed on the Lambourn, the maximum and minimum bank heights of each bank were obtained from the surveyed data. At these locations, the predicted height from the linear model was also obtained. Bank angles calculated from surveyed data compared to the predicted bank angle for the true left bank (Table 4.2.3) show that the use of a linear trend to predict the bank top height is inappropriate.

Table 4.2.3: Comparison of measured and predicted bank angles for the true left bank

Location	Measured bank angle (^{o})	Predicted bank angle (^{o})
Left bank maximum	37.50	26.50
Left bank minimum	21.04	36.60

The difference between the angles in both cases is large, approximately 10 and 15 degrees, respectively. This arises from the fact that the distance between the fitted trend and the surveyed data in many locations is quite large (up to 0.3m) (Figure 4.2.14). The use of a LOESS model looked to address this (Figure 4.2.15). Again an analysis of the angles was undertaken (Table 4.2.4).

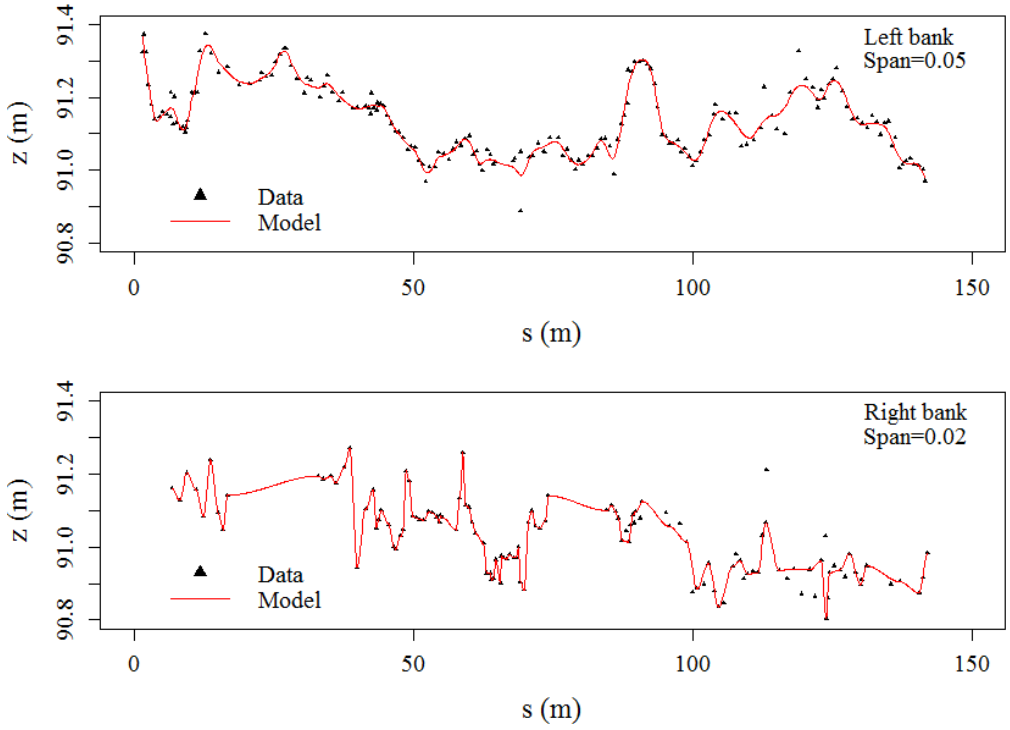

Figure 4.2.15: LOESS model fitted to surveyed bank top data for left and right banks.

Table 4.2.4: Comparison of measured and predicted bank angles for the true left bank

Location	Measured bank angle (^{o})	Predicted bank angle (^{o})
Left bank maximum	37.50	35.67
Left bank minimum	21.04	27.69

Using the LOESS model, the difference between the actual and predicted angles for the minimum and maximum heights along the left bank was reduced to approximately 2 and 6 degrees respectively. This represents a large improvement which can be attributed to the close fit to the surveyed data provided by the LOESS model. Due to this reduction in difference, bank heights in the final topographic model are predicted using the LOESS model in order to minimise the difference in angle between surveyed and predicted data.

4.2.5. Results of bathymetry generation

The final step in the generation of bathymetry data for the reach was the conversion back into Cartesian coordinates (Figure 4.2.1). For Method 1, scaled *n* was first transformed back to actual *n*. Results for both the trend and residual components as well as the final predicted elevation model, for both Methods 1 and 2 are shown in Figure 4.2.16. The final model was formed of the kriged residuals with the appropriate trends replaced. In the second approach where only the bed data were kriged, the banks are included as generated using the procedure described in Section 4.2.4.

For Method 1, trend removal using the LOESS approach on both the bed and bank data (Figure 4.2.16a), the trends removed appear sensible. The residuals that are interpolated reveal morphological features within the channel, with three deep pools apparent at the points labelled A, B and C. Following kriging, it is important that the morphological variation apparent in the residual plot is maintained. Although the pools are maintained in the final prediction, a large amount of the morphological variation has also been removed. The dominant channel shape in this approach is driven by the fitted LOESS trend.

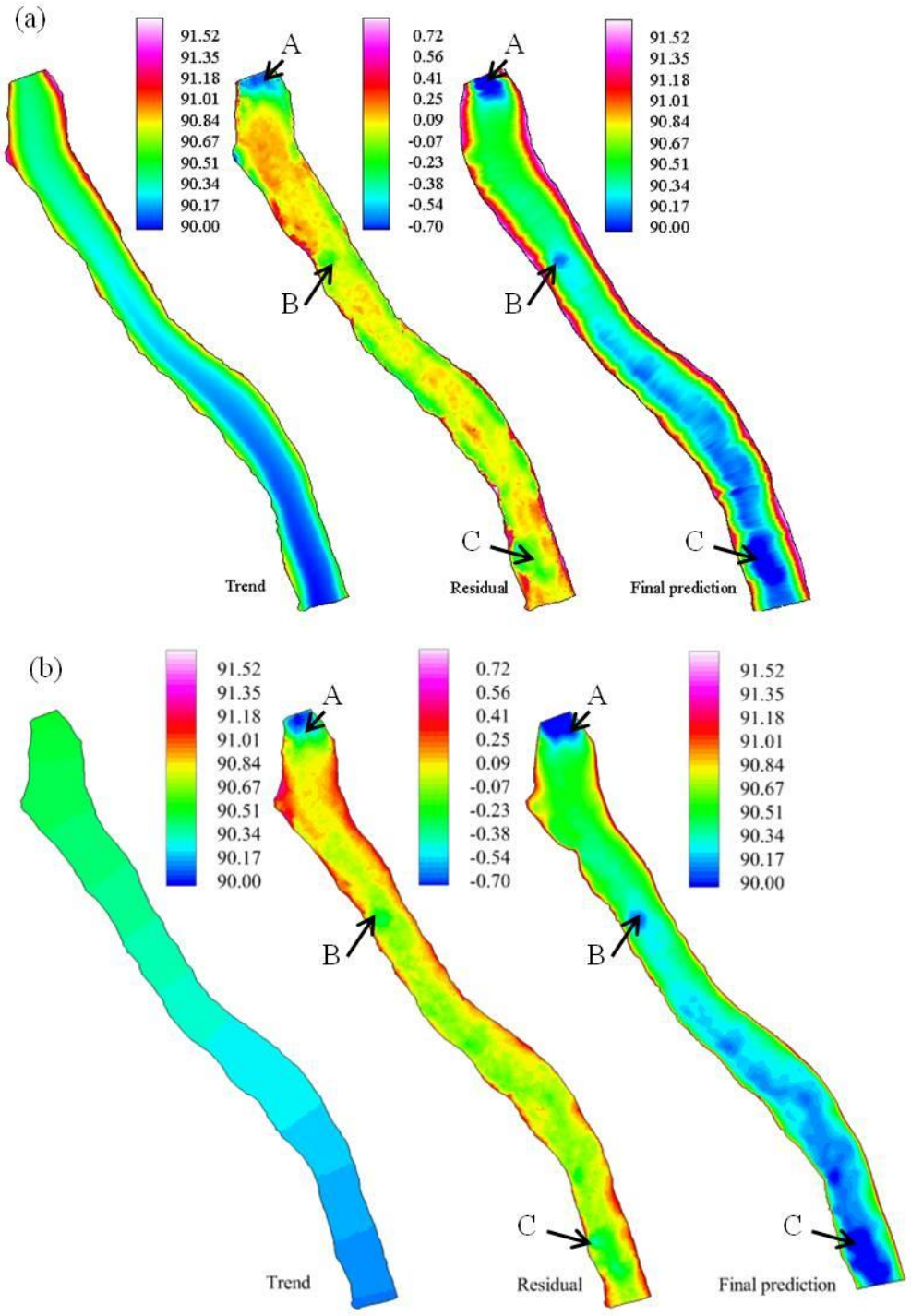

Figure 4.2.16: Decomposition of data into trend and residual components and final predicted elevation model for (a) Method 1; (b) Method 2. Bed elevations and residual heights are given in metres.

In Method 2, only the bed data were used in the kriging analysis. The same morphological features at A, B and C can be identified following the removal of the downstream trend (Figure 4.2.16b). Following kriging, features throughout the channel are better defined than in Method 1. Hence the advantage of Method 2 is that morphological variation within the channel is maintained, rather than being dominated by the channel shape.

When comparing the two approaches, there is also a clear difference in the bank slopes. Method 1 attributes the banks with a gradual slope defined by the LOESS model fitted to the data. In Method 2, the banks are much steeper, representing the true bank slope much more accurately.

4.2.6. Discussion

To further assess the results of the kriging using both approaches, measured data for two cross-sections along the reach were compared with the predictions (Figure 4.2.17). The data for these cross sections were collected independently of the topographic data.

The evidence in Figure 4.2.17 suggests that the use of a LOESS model to remove a general cross-sectional trend from the data is inappropriate in this case. Although the bed is predicted reasonably well, data in the near bank region is smoothed and the angle between the bank and the bed is not well represented.

When using Method 2, the banks are still not totally accurate; however, the results are a large improvement on Method 1. For cross-section 2 (XS2), data are predicted well for the majority of the channel width. However, the channel is marginally narrower in this area. A similar situation is observed for cross-section 3 (XS3) where data in the near bank regions deviates from the measured data. In this case the predicted channel is larger than that measured.

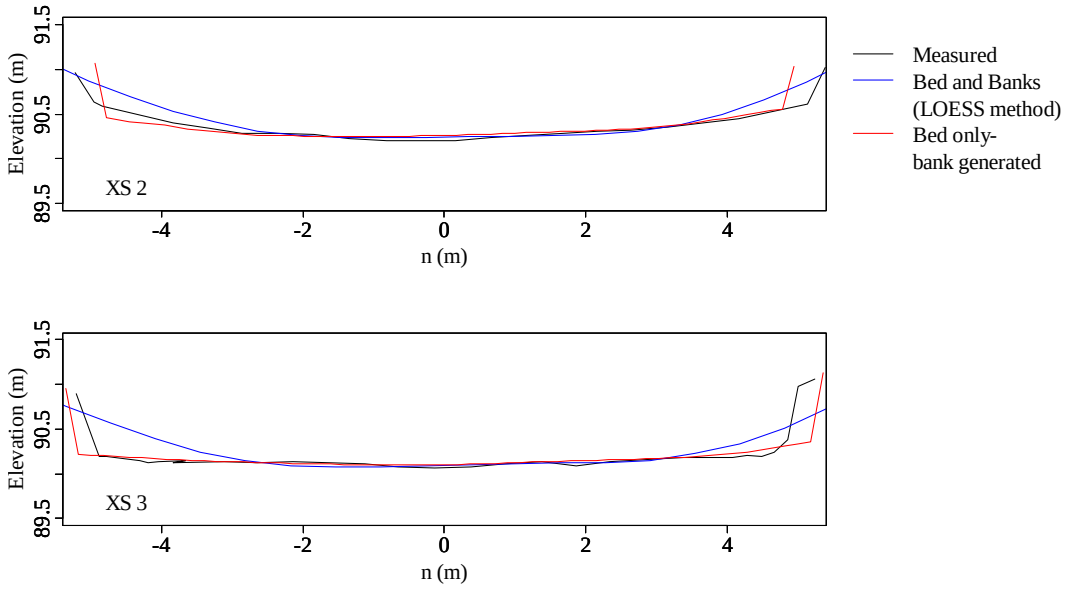

Figure 4.2.17: Comparison of predicted data against measured data for two cross-sections within the Lambourn study reach. Black lines represent measured data. Blue lines represent cross section predictions using the LOESS trend removal approach. Red lines represent cross section predictions using the bed only kriging and bank top generation approach.

The percentage difference in cross sectional area between the measured data and the predicted cross sections (Table 4.2.5) shows that Method 1 seriously overestimates the cross sectional area while Method 2 underestimates the area by only between 6.39 and 8.18%. A large proportion of the difference in predicted and measured area occurs near the top bank. This area is largely removed when generating the model mesh, as cross sections are cut at the intersection of the water surface with the bank. This effect is explored further in Chapter 7.

Table 4.2.5: Comparison of predicted and measured cross-sectional areas for two cross-sections.

Method	Cross section	Measured Area (m^2)	Predicted Area (m^2)	Percentage difference (%)
1	XS2	7.51	10.31	37.28
1	XS3	8.56	11.76	37.38
2	XS2	7.51	7.03	6.39
2	XS3	8.56	9.26	8.18

To analyse how the constructed DEM performs at the reach scale overall, the predicted and measured values of elevation for the surveyed data points were analysed. Data were compared to a 1:1 line as the assumptions of a linear regression were not met. The results for Method 1 (Figure 4.2.18a) display very high scatter around the 1:1 line. This is reflected with a Spearman rank correlation coefficient of 0.411. Points to the right hand side of the 1:1 line are bank points. Method 2 (Figure 4.2.18b) gives much better agreement of the predictions with measured data, and a Spearman rank correlation coefficient of 0.987. This suggests that Method 2 in which the surveyed data were separated into two groups (bed and banks) is the appropriate method to achieve an accurate topographic representation from the measured data using kriging. Hence, Method 2 was used to generate the bathymetry model of the experimental reach.

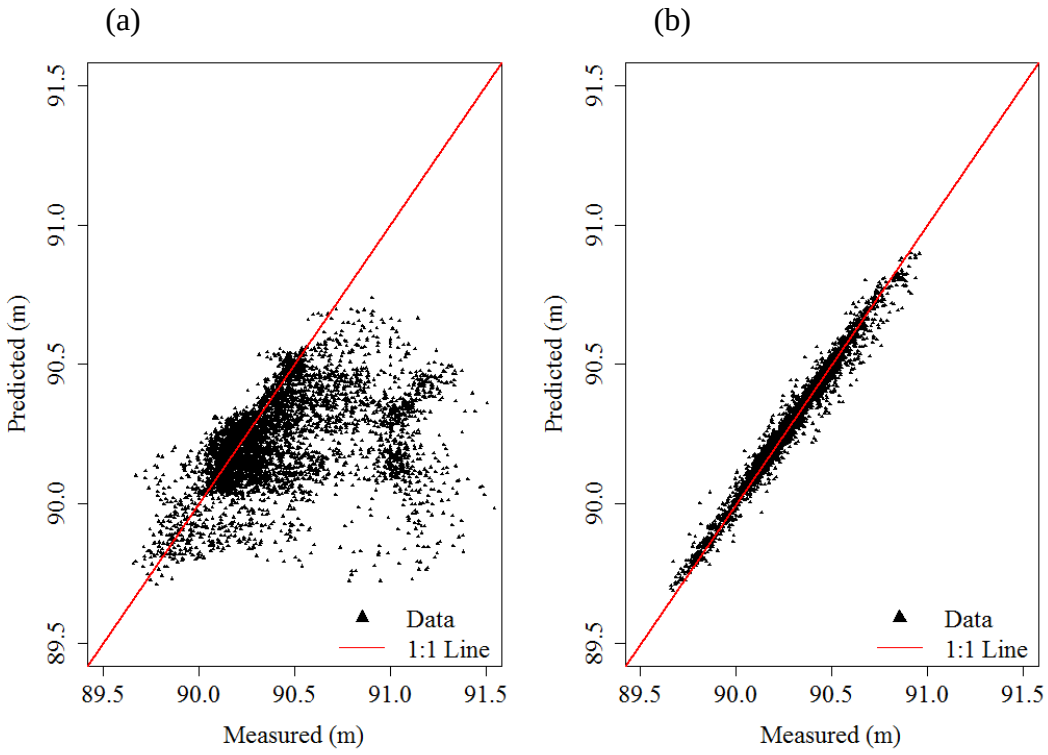

Figure 4.2.18: Comparison of kriged predictions against the measured data from the River Lambourn for (a) Method 1; (b) Method 2.

4.3.Gravel-bed microtopography – data collection

To enable the parameterisation of grain-scale roughness within the model, it was necessary to collect data pertaining to the structure of the gravel bed of the River Lambourn. For the purposes of the DANS model, the measurement technique must have a high enough resolution to describe the bed microtopography in enough detail to create a digital elevation model of the physical surface and allow calculation of the physical properties of porosity, averaged streamwise and lateral frontal projected areas and surface areas (cf. McMillan and Brasington, 2007; Rameshwaran *et al.*, 2011).

Bed microtopography data in this study were collected using a physical profiler, illustrated in Figure 4.3.1. The physical profiler was chosen in preference to alternative methods such as Terrestrial-Laser Scanning or stereo pair photogrammetry. Terrestrial-Laser Scanning was rejected due to high instrument cost whereas the need for intensive post-processing precluded the selection of stereo pair photogrammetry. The frame was positioned over a patch of unobscured gravel and driven into the bed using spikes installed on the legs of the frame. The frame was then levelled using a bubble mounted on the frame. Once level, pins were pushed down onto the bed surface. Care was taken to rest the pins on the gravel surface rather than forcing them into gaps between gravel particles, or into the bed. Once the pins were resting on the gravel surface, the height of each pin above the frame was recorded on millimetre scale graph paper to record the bed surface microtopography. The data were collected to a spatial resolution of 0.01m over an area of 0.0625m^2 with a vertical accuracy of 0.005m.

Figure 4.3.1: Physical profiler in situ on the River Lambourn. (a) Frame facing upstream. (b) Top down view of exposed gravel surveyed by the frame.

In order to obtain representative data for the experimental reach, areas throughout the reach were selected for measurement to give a total of fifteen samples. Care was

taken to ensure a wide spread of locations throughout the reach including both the channel margins and thalweg. Data were collected during two sampling periods, November 2010 and July 2011: This was to ensure that samples surveyed were representative of areas that may have previously been obscured due to macrophyte cover.

4.4. Gravel-bed microtopography – data processing

Post-processing of the bed microtopography data was undertaken in order to remove any two dimensional trends in the overall bed slope which might obscure the grain-scale properties of the bed. This then provided a dataset from which the parameters of gravel projected area in the streamwise and lateral direction, gravel surface area and gravel porosity could be calculated for use in the drag equations within the DANS model.

Common methods to perform trend removal in the literature include the use of a moving filter (e.g. Smart et al. 2002) or the fitting of a linear or higher degree polynomial trend to the data (e.g. Clifford *et al*. 1992; Marion *et al*. 2003). Smart et al. (2002), for example, used a moving filter of size $1.25D_{90}$ to determine the spatial extent of the trends to be removed from the data. Although it is possible to use many different sizes of a moving filter, a presupposition of the structure of the surface is then imposed on the trend analysis. This is something which is not desirable. Clifford *et al.* (1992) developed a method which obtained a consistent measure of bedform amplitude. To achieve this, the overall trend of the bed elevation was represented by a low order polynomial (normally first order). Individual elements of the bed roughness were then defined between successive upward crossings of the fitted trend line. This ‘zero crossing’ analysis in conjunction with fractal analysis of

bed elevations allowed the identification of roughness properties within wavelength classes defined as grain and form scale by the fractal bands (Clifford *et al*., 1992). Marion *et al*. (2003), however, de-trend the data in both the lateral and streamwise directions (i.e. a 2D trend removal) to remove spatial bias in the datasets arising from any change in the sediment bed slope underneath the measurement frame used. In this study a 2D trend removal technique was applied using a LOESS model in order to remove the trends in the downstream and lateral directions and leave only the bed microtopography.

4.4.1. Porosity of surface gravel layer

Many ways of calculating the porosity of gravel beds are presented in the literature (Aberle, 2006, 2007; Aberle and Koll, 2004; Nikora et al., 1998, 2001, 2007b; Rameshwaran *et al*., 2011, Rameshwaran and Naden, 2012). Nikora *et al*. (1998, 2001, 2007b), Aberle and Koll (2004), Aberle (2006), Rameshwaran *et al* (2011) and Rameshwaran and Naden (2012) undertake point or laser measurements of gravel bed surfaces in both flumes and natural streams. Nikora *et al*. (1998, 2001, 2006b), Aberle and Koll (2004) and Aberle (2006) conclude that there is a correction required for estimates of Φ as the lowest porosity obtained using points measurements ($\Phi = 0$) does not represent the material porosity of the bed. In reality, Φ tends towards the material porosity below at the minimum roughness height, not zero (Aberle, 2007, Nikora *et al*., 2007b).

In this study, it is the porosity of the surface gravel at the interface between the river bed and the water column which is required, i.e. the roughness layer (Figure 4.4.1). It is the effect of roughness on flow processes occurring at this scale (i.e. sub-grid scale) which must be represented within the DANS equations as it is not possible to represent such small scale roughness within the model mesh (e.g. Lane *et*

al., 2004; Carney *et al.*, 2006; Nikora *et al.*, 2007b, Rameshwaran *et al.*, 2011; Nikora *et al.*, 2013). The method for determining the porosity of this layer is described in Section 4.4.3

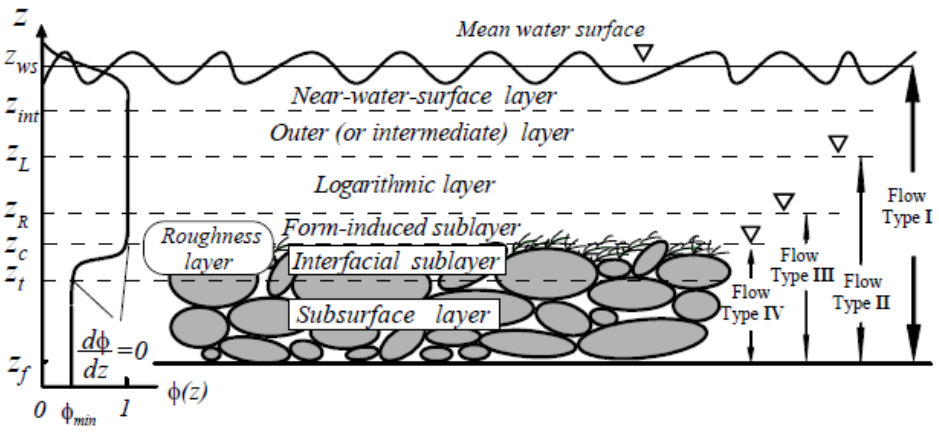

Figure 4.4.1: Relationship between porosity and water depth (Nikora et al., 2007).

4.4.2. Reference area of gravel beds

For the calculation of the area measures (projected and surface areas) it is important to consider the flow over roughness crests. McLean and Nikora (2006) highlight that flow modelled using a DANS approach is highly sensitive to gravel roughness geometry. To capture flow processes occurring at the gravel scale, i.e. at scales less than that of the model mesh, within the DANS model, the full range of grain scale roughness was used in the calculation of representative projected and surface areas for the River Lambourn.

4.4.3. Method

In order to remove the trend in bed slope in both the downstream and lateral directions from the bed microtopography data, a polynomial trend surface was constructed for each of the samples collected from the experimental reach of the

River Lambourn. A 2D polynomial trend surface, fitted using a LOESS model, was chosen in preference to a linear trend in order to remove both cross-stream and downstream trends. For this analysis, the span α was set at 0.25, the dimension of the point frequency frame. An example of a LOESS model fitted to a scatter plot of collected gravel roughness heights in two dimensions is shown below. Figure 4.4.2a shows gravel roughness protrusions above the LOESS trend; Figure 4.4.2b shows data below the fitted model.

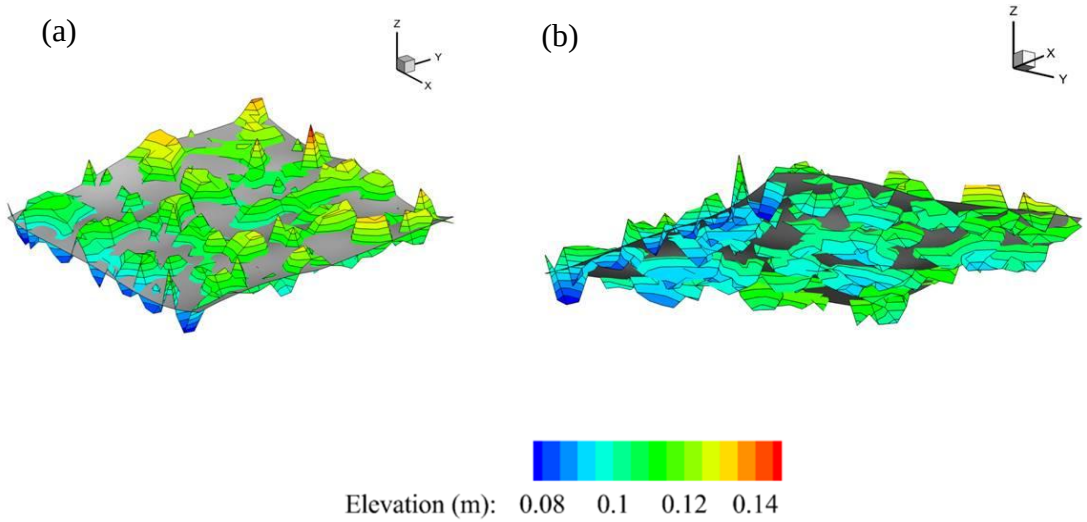

Figure 4.4.2: Example of LOESS model (grey) fitted to surveyed grain scale roughness data. (a) data above fitted model. (b) data below fitted model.

The LOESS function was applied using the statistical environment R. The function took each individual elevation point from the data and fitted the LOESS model to produce a smoothed value of elevation (Z) and the difference between this and the original value (i.e. the residual). The residuals for all 15 samples are shown in Figure 4.4.3.

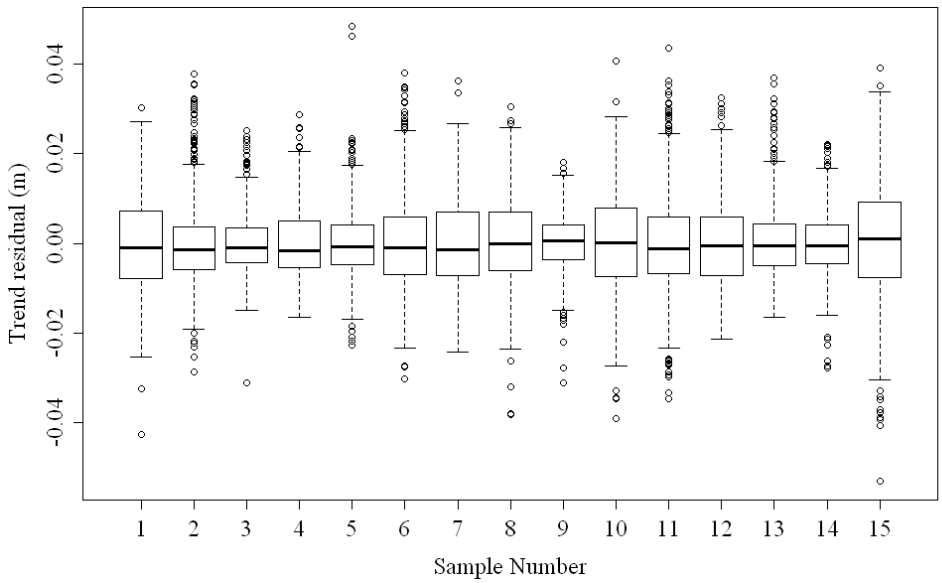

Figure 4.4.3: LOESS model residuals for each gravel sample surveyed on the River Lambourn. Boxes represent the inter-quartile range. Outliers are defined as values which fall outside 1.5 times the inter-quartile range

The outliers represent large peaks and troughs in the surveyed data. Hence, these values were removed from the data and replaced with ±1.5 times the inter-quartile range, dependent on whether the outlier was positive or negative. The minimum residual value was assumed to represent the fully blocked bed. This value was set to zero, with all other points in the sample adjusted accordingly. This resulted in a range of gravel heights of between 0.031m (sample 9) and 0.067m (sample 15). As the majority of heights are below 0.05m, five layers of 0.01m in thickness were used to represent the gravel microtopography in the model. Consequently, sample 15 with a range of 0.067m was adjusted by setting values greater than 0.05m to have a value of 0.05m Contour plots showing the height variation following trend and outlier removal for all 15 samples are shown in Figure 4.4.4.

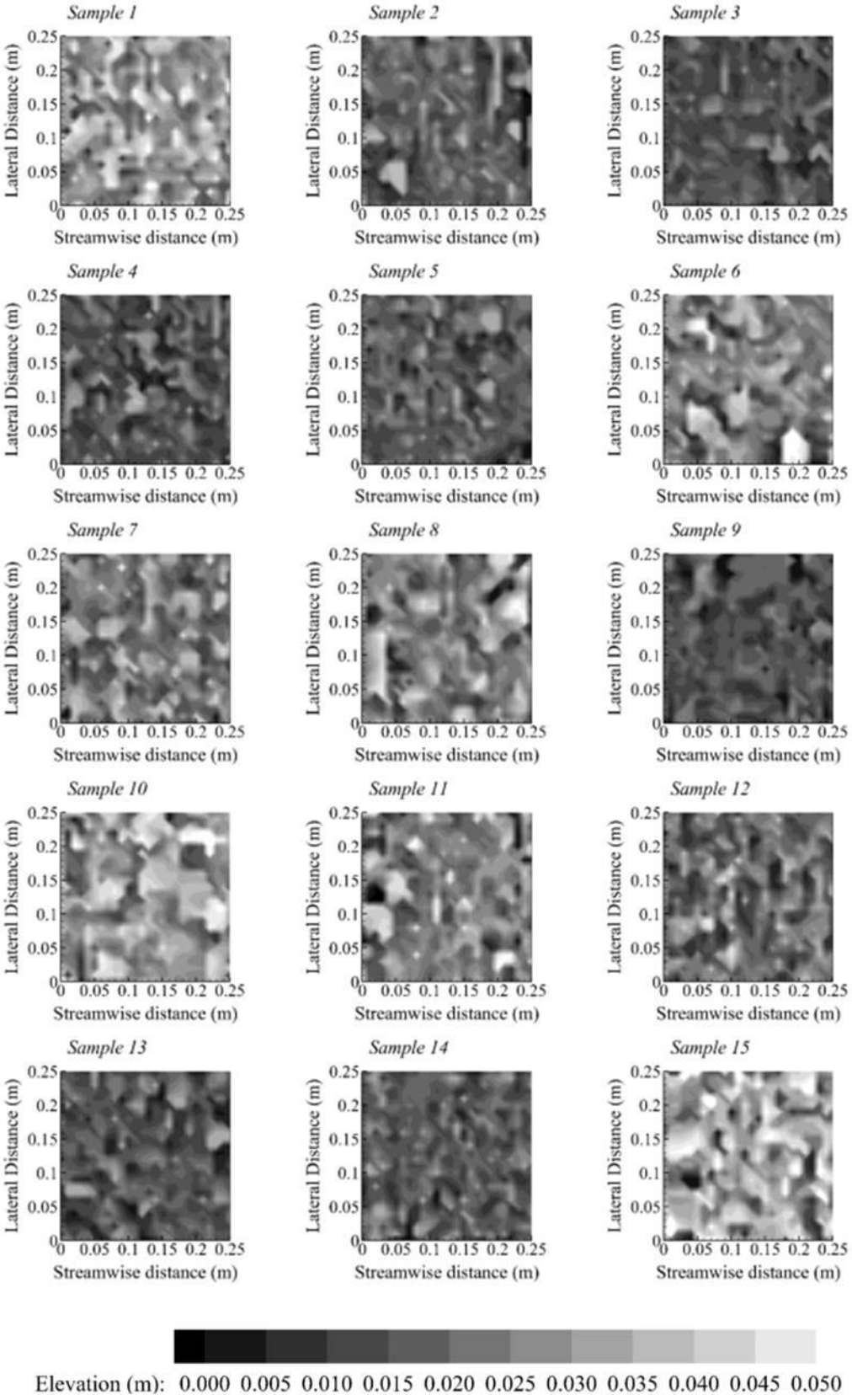

Figure 4.4.4: Bed microtopography for all samples following trend and outlier removal

The parameters of porosity, projected area (streamwise and lateral) and surface area were then calculated on a layer by layer basis. Porosity was determined as follows. For each row of points collected by the physical profiler, the space between two rods was designated as a cell of 0.01m wide and 0.01m long. The height of the gravel in this cell following trend and outlier removal was then used to determine the volume of gravel in that layer. For example, if the gravel height at a location is 0.022m, the first layer of 0.01m is fully occupied, the second layer is also fully occupied and the third layer is occupied by a height of 0.002m. Using this approach the total volume of gravel was calculated for each layer and the fluid fraction determined as 1 minus the gravel volume. The porosity of the layer is then determined by

$$\phi = \frac{V_f}{V_0}$$

4.4.1

where V_f and V_0 are the fluid only volume and the total volume of the averaging domain respectively.

The projected area of the roughness elements used represents the total area per unit volume which interacts with the flow. Projected area is approximated as the area of the gravel presented to the flow for each individual roughness element, an approach used previously by Rameshwaran *et al*. (2011). An example of the projected area calculation for one profile of a single sample is shown in Figure 4.4.5. Again, this was calculated on a layer by layer basis. Where gravel was exposed to flow in each cell (highlighted in red in Figure 4.4.5) the height of the gravel particle was multiplied by the cell width. This was repeated for each cell in the layer and

then summed to get the total projected area in each layer. To convert from area to area per unit volume, the resultant projected areas were divided by the volume of each layer based on the size of sampling frame (0.25m x 0.25m).

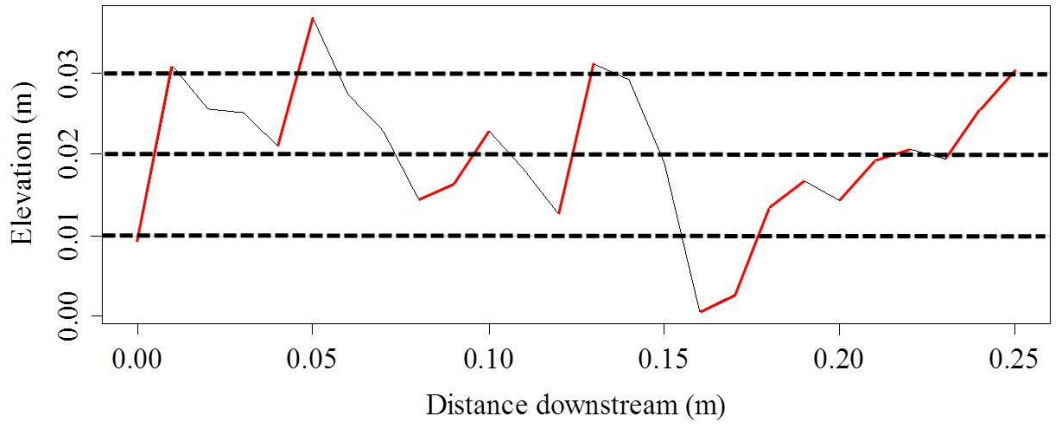

Figure 4.4.5: Example surveyed gravel profile on the River Lambourn. Areas used to determine projected area are highlighted in red. Dashed lines indicate the layers the sample was divided into to determine porosity, projected area and surface area.

Gravel surface area was calculated for the entirety of the roughness profile shown in Figure 4.4.5. For each cell, the height of the gravel tip was determined and multiplied by the cell size (0.01m) to provide the surface area. These were summed on a layer by layer basis and converted to surface area per unit volume in the same manner as the projected area.

4.4.4.Results

The relationships between each of the parameters and the height above the fully blocked bed are shown in Figure 4.4.6. Parameters were determined for five layers of 0.01m in height. Five layers were chosen as this was the maximum practical number of layers for representing the micro-topography within the model mesh.

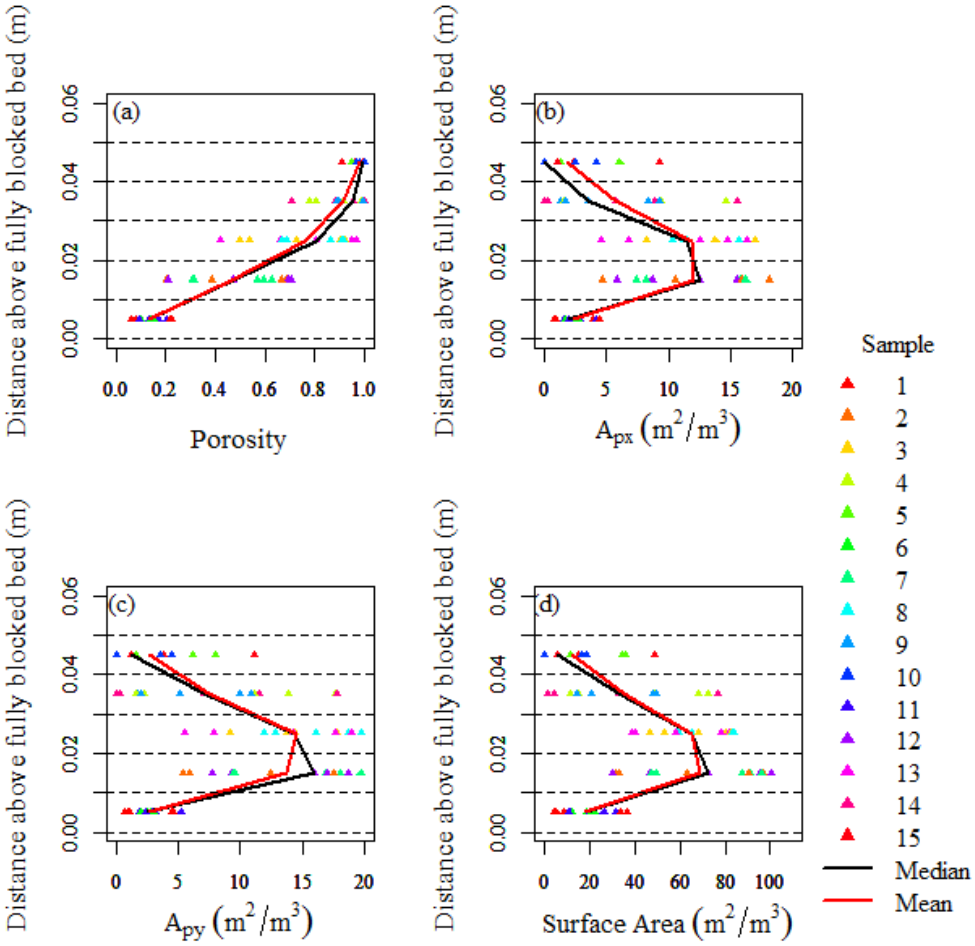

Figure 4.4.6: Relationship between height above a fully blocked bed and bed roughness parameters (a) porosity; (b) streamwise projected area; (c) lateral projected area; (d) surface area. Mean and median values are indicated for comparison.

The mean porosity, streamwise and lateral projected area and surface area were used to represent the grain scale topography within the model (Table 4.4.1). The mean was chosen in preference to the median as porosity values in the layer 0.04-0.05m often equalled 1, biasing the median towards this value.

Table 4.4.1: Mean parameters of porosity, streamwise and lateral projected area, and surface area

	Porosity	Streamwise projected area A_{px} (m^2m^{-3})	Lateral projected area A_{py} (m^2m^{-3})	Surface area A_s (m^2m^{-3})
0.00-0.01	0.134	2.281	2.688	18.159
0.01-0.02	0.471	11.550	13.663	68.677
0.02-0.03	0.765	12.289	14.505	65.210
0.03-0.04	0.917	6.446	7.506	34.893
0.04-0.05	0.980	2.172	2.646	12.424

4.4.5. Discussion

When assessing the relationship between porosity and the height above a fully blocked bed (Figure 4.4.6a), a similar relationship is found to that of Nikora *et al* (2007b) (Figure 4.4.1). The values of porosity, projected area in the streamwise and lateral directions and surface area are of a similar magnitude to those presented by Rameshwaran *et al*. (2011) and Rameshwaran and Naden (2012) for samples collected on the River Blackwater. Here, parameters were determined for four layers of 0.01m in thickness. Porosity values for layers one to four are quoted as 0.13, 0.60, 0.92 and 0.99. Projected areas are quoted as 1.65, 12.03, 13.33 and 2.13 m^2m^{-3}in the streamwise direction and 1.98, 15.08, 14.81 and 2.50 m^2m^{-3} in the lateral direction; surface areas as 13.83, 77.52, 76.61 and 15.33m^2m^{-3}.

Overall, projected areas of gravel on the River Blackwater in the streamwise and lateral directions are of a similar magnitude within each layer, a trend which can also be observed for the River Lambourn in Table 4.4.1. Trends in both porosity and projected areas are similar when moving through the gravel layer for both rivers. Values of projected area increase at first, reach a peak at approximately 0.035m

above the bed and decrease towards the surface of the gravel layer. Values of porosity increase gradually when moving away from the bed.

4.5. Conclusions

This chapter has explained the data that were collected to enable the construction of the physical boundaries of the 3D hydraulic river model. Two components of the data collection were considered: the reach scale topography measurements using a topographical survey; and the gravel-bed microtopography measurements necessary to inform the formulation of bed roughness. The methods used to post-process both datasets and the results of this post-processing have also been presented.

With regards to the reach scale topography, the following conclusions can be drawn. The conversion of the data into the (n,s) coordinate system aided in the interpolation of the data onto a rectilinear grid, a key advantage when using kriging. However, the method using a LOESS model to remove the cross-sectional trend from the data was unsuccessful. The topography produced was dominated by this trend. As a result, the channel bathymetry was over-smoothed, cross-sectional areas for test sections were seriously over-estimated, and bed elevation predictions were both highly scattered when compared to measured data.

The alternative method in which bed and bank data were separated prior to processing worked well. Here, only a downstream trend was removed from the data prior to kriging. Evidence (Figure 4.2.16b) showed that this method maintains a good representation of morphological variation, and provides reasonably accurate predictions of measured elevations (Figure 4.2.18). The prediction of the top bank height using a LOESS model allowed for a more accurate representation of the bank

angle compared to a linear model with the result that cross-sectional area was only marginally overestimated in the two test sections.

Minimising error resulting from measurement and interpolation is key to producing a good representation of channel bathymetry for use in hydraulic modelling. Not only does this minimise errors when undertaking numerical modelling but it can also help reduce the occurrence of convergence problems resulting from topographic anomalies. Experience in this study has shown that, where possible, top and bottom bank lines should be surveyed to high resolution and accuracy. This enables the clear definition of bank slope when generating a bathymetric model.

When considering the gravel-bed microtopography, overall, the grain scale roughness is well represented in this case using five layers of 0.01m in thickness. A range of gravel roughness heights was found in the fifteen samples taken. This shows a clear need for a large number of spatially distributed samples, to be taken in order to characterise the gravel roughness at a reach scale. Derived model parameters are similar to those found in other studies.

Chapter 5. Defining model boundary conditions and model validation

This chapter describes the datasets collected in order to define the model boundary conditions, specifically the model inlet and outlet conditions and the upper boundary (i.e. water surface or depth), and to validate the model. The timing of these measurements for each field campaign is summarised. For each dataset, the collection procedure is described, followed by a description of any necessary post processing.

The collection of data to define the model inlet condition was undertaken using a Teledyne RD Instruments Streampro acoustic Doppler current profiler (ADCP) which is specifically designed for use in small to medium sized watercourses. Measurements were taken at the deepest non-vegetated cross section upstream of the experimental reach on the River Lambourn. Following collection, data were processed using guidelines provided by the equipment manufacturer and were compared to discharge values from two Environment Agency gauging stations at Welford and Shaw (see Figure 3.3.2), provided by the National River Flow Archive (NRFA), for quality control.

Water depth data for the study reach were collected by installing permanent staff gauge boards along the reach. These data were used to define the initial fixed lid for the model and the water depth at the model outlet.

Model validation data comprised three datasets: (i) velocity data collected using an acoustic Doppler velocimeter (ADV) to enable validation of both 3D velocity and turbulence values in areas between plant patches; (ii) electromagnetic current meter (EMCM) measurements to enable validation of 2D velocities both around and within plant patches; (iii) measurements of the local water surface to enable validation of the modelled free surface for each of the four vegetated cases.

5.1. Chronology of detailed measurements

Data relating to vegetation cover at a cross section and river stage were collected on a monthly basis by CEH Wallingford throughout the three year period of interest (Section 3.3) for contextual information. The chronology of detailed data collection for the November 2010 and May 2011 field campaigns is shown in Table 5.1.1 and Table 5.1.2, respectively. Dates for the measurements relating to vegetation (Chapter 6) are also given. ADCP data relating to the minimum vegetation case (Section 3.5) were collected on 22nd February 2010.

Table 5.1.1: Field sampling chronology for the November 2010 field campaign.

Dataset collected	Date collected	
Vegetation survey	10/11/2010	Before cut
Acoustic Doppler current profiler (ADCP)	15/11/2010	
Stageboard readings	15/11/2010	
Free surface	16/11/2010	
Acoustic Doppler velocimeter (ADV)	16/11/2010	
Electromagnetic current meter (EMCM)	16/11/2010	
Day of vegetation cut – 18th November 2010		
Free surface after cut	22/11/2010	After cut
ADCP	22/11/2010	
Stageboard readings	22/11/2010	
ADV	23/11/2010	
EMCM	23/11/2010	
Vegetation survey	24/11/2010	
Vegetation shape and structure	25/11/2010 – 30/11/2010	

Table 5.1.2: Field sampling chronology for the May 2011 field campaign.

Dataset collected	Date collected	
Vegetation survey	12/05/2011	Before cut
ADV	16/05/2011	
Free surface	17/05/2011	
ADCP	17/05/2011	
Stageboard readings	17/05/2011	
EMCM	17/05/2011	
Day of vegetation cut – 18th May 2011		
Free surface after cut	19/05/2011	After cut
ADV	19/05/2011	
ADCP	20/05/2011	
Stageboard readings	20/05/2011	
EMCM	20/05/2011	
Vegetation survey	23/05/2011	
Vegetation shape and structure	24/05/2011 – 31/05/2011	

5.2. Model inflow conditions

River discharge is required as the basic inflow condition for the model. Measurements were undertaken using an ADCP. The use of an ADCP (Figure 5.2.1a) was preferred to other flow measuring equipment due to its operational efficiency in determining discharge (Muste et al., 2004b). Other methods, such as acoustic Doppler velocimetry or the use of electromagnetic current meters, were rejected. In order to rigorously define the model inflow condition using an ADV or EMCM, a number of vertical profiles over a cross section, with a high number of point measurements per vertical profile, would be required. In the case of both the ADV and EMCM this would take a number of hours. The ADCP, however,

measures up to thirty points per vertical profile simultaneously, enabling a much more rapid determination of discharge.

5.2.1.ADCP measurements

The ADCP uses sound to measure water velocity by measuring the Doppler shift frequency. The Doppler principle is applied by bouncing an ultrasonic sound pulse off small particles of sediment and other materials, often referred to as backscatterers that are present even in water which appears clear to the eye (Simpson, 2001). More detailed background on the principles of ADCPs can be found in Gordon (1996), Simpson (2001) and Mueller and Wagner (2009).

Figure 5.2.1: Vessel mounted ADCP as deployed on the River Lambourn (Photograph taken 16th November 2010).

Two deployment methods are commonly used for ADCPs: the moving boat method and the section by section method. The moving boat method (Simpson, 2001) is commonly used to obtain a rapid estimate of discharge and involves the ADCP constantly measuring the velocity profile and depth along a given track. As velocity data collected is instantaneous, multiple crossings are required in order to

produce a reliable estimate of discharge. Section by section measurement (Huang, 2012) involves splitting a cross section at intervals and fixing the ADCP at these locations. Velocity data are then collected for a fixed sampling period, usually around 180 seconds (Gunawan *et al*, 2010) in order to provide a time-averaged velocity for the calculation of discharge. The ADCP, deployed in section by section mode, has the ability to simultaneously measure up to 30 points in a given depth profile, a distinct advantage when compared to the time intensive ADV and EMCM methods. Discharge is then calculated for subsections of a channel using the velocity and depth data. A total discharge is then provided when measurements at all subsections are completed. An immediate estimate of the uncertainty of the discharge measurement is also given using a relative standard uncertainty model (Huang, 2012) allowing the data collected to be quality controlled.

In this study, a total of five ADCP datasets were collected. The measurement protocol used in both approaches was that supplied by the manufacturer, Teledyne RD Instruments. In order to facilitate these measurements, a fixed cross-section was established approximately 30 metres upstream of the experimental reach of the River Lambourn used in the model. This location was the deepest cross section available and was usually free of vegetation. These criteria were fundamental to the effective deployment of the ADCP. Measurements cannot be undertaken in vegetated areas due to interference with the acoustic signal and sufficient flow depth is required beneath the sensor to produce reliable estimates of discharge. The permanent cross section ensured that data were collected at a consistent location for all measurement campaigns. During May 2010, a pulley system was installed to improve data reliability. The minimum vegetation case in February 2010 (Section 3.5) was undertaken using the moving boat method. These data pre-dated both the upgrade to

the ADCP and the system to improve the boat path and are, therefore, less reliable than subsequent data. The section by section approach was adopted following the upgrade to the ADCP in May 2010, and was used to collect four further datasets for the two main field campaigns in November 2010 and May 2011.

5.2.2.ADCP discharge calculation

The terms bin, ensemble and blanking distance are used extensively when considering discharge calculation using ADCP data, and can be defined as:

(i) Bin: a single measurement in a vertical profile.

(ii) Ensemble: a collection of measurements taken for one vertical profile, i.e. a collection of bins.

(iii) Blanking distance: Regions of the measured cross section which are not measured due to limited depth or acoustic interference.

The calculation of discharge by an ADCP differs depending on the method employed, i.e. moving boat or section by section. When using the moving boat approach, a velocity vector cross product is obtained for each depth bin in a vertical velocity profile. This is then integrated over the water depth and then integrated by time over the entire cross section (Simpson, 2001). The section by section approach is similar to that adopted if using a conventional current meter (Huang, 2012). Here, the ADCP is stationed at a number of subsections across the channel and measurements of velocity and depth are taken. The discharge of these subsections can be obtained using the equation $Q = AU$ and all subsections are summed to provide a measurement of discharge for the cross section. In particular, it is important to highlight that there is a need to estimate discharge in certain areas of the cross section (Figure 5.2.2). These areas are:

(i) The top of the cross section due to the blanking distance and depth (draft) of the transducer;

(ii) The bottom of the cross section due to side lobe interference;

(iii) The edges of the cross section due to the blanking distance and limited depth.

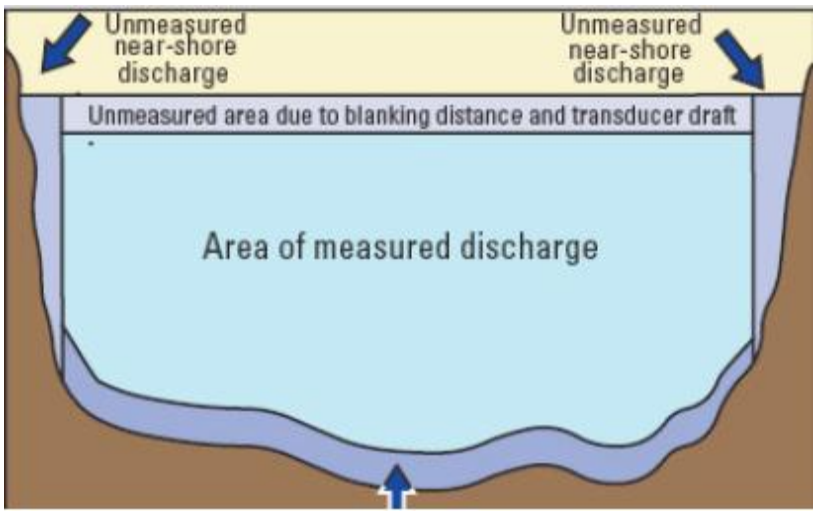

Figure 5.2.2: Unmeasured areas of cross section (Simpson, 2001).

The software used to collect the discharge for the moving boat approach, WinRiverII, and the section by section approach, Section by Section Pro (hereafter referred to as SxS Pro for brevity), estimate discharge in these regions in the following manner. At the channel margins, due to the size of the float the sensor is mounted upon, the minimum distance from the bank the sensor can be placed is 0.25m. This provides the width of the first subsection, the discharge of which can then be estimated using the formula (Simpson, 2001):

$$Q_e = C_e V_m L d_m \qquad 5.2.1$$

where:

C_e = edge shape coefficient (0.91 for rectangular banks)

V_m = mean water velocity in the first/last subsection

L = distance from the shore to the first subsection (0.25m)

d_m = depth of the estimated region.

The discharge in the top and bottom unmeasured regions also has to be estimated. Simpson (2001) examined the effect of using various different methods to estimate discharge in the top and bottom regions (e.g. logarithmic and general power law), but found that the noisy nature of ADCP profile data resulted in estimates which were unrealistic. A method using the $1/6^{th}$ power law (Chen, 1989) was found to robustly reject noise in ADCP data and hence was the most appropriate for use in discharge estimation. The full derivation can be found in Simpson and Oltmann (1993). An example application to the data collected in this study for the May 2011 after cut case is shown in Figure 5.2.3. Once discharge for the unmeasured regions has been estimated, the total river discharge can be estimated by summing the discharges from the estimated regions and that obtained from measured data.

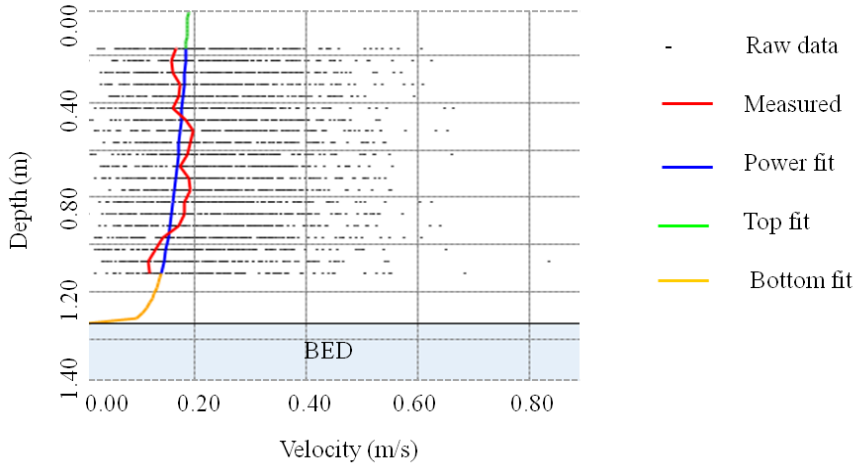

Figure 5.2.3: Example of power law fitting to the average measured profile within SxS Pro. Data taken from the May 2011 after cut case.

5.2.3.Minimum vegetation case – February 2010

The dataset for the minimum vegetation case was gathered by traversing the ADCP over the established cross-section using stiff wire. Discharge was calculated using the moving boat method.

Four crossings of the channel were needed to provide a measurement of discharge (Mueller and Wagner, 2009). The data from these crossings were initially processed in WinRiverII (RD Instruments, 2009). Due to the data collection method employed, only three transects were selected as being reliable and the criterion for the difference between discharges was relaxed from 5% to 8%. The discharges for these cross sections as displayed in WinRiverII are shown in Figure 5.2.2. The average discharge for these transects, 2.191m^3s^{-1}, was used as the model input for the February 2010 minimum vegetation case.

Transect	Start Bank	# Ens.	Start Time	Total Q m^3/s	Delta Q %
Boxford _22_02_10003	Right	62	12:08:21	2.103	-4.03
Boxford _22_02_10004	Left	59	12:09:48	2.368	8.06
Boxford _22_02_10005	Right	64	12:10:53	2.103	-4.03
Average		61		2.191	0.00
Std Dev.		3		0.153	6.98
Std./| Avg.|		0.05		0.07	0.00

Figure 5.2.4: Example of discharge filtering undertaken in WinRiverII. "# Ens" refers to the total number of ensembles for that transect.

5.2.4.Improved method of data collection

To improve the data collection and ensure that the data collected were reliable and repeatable, it was important to ensure that the ADCP followed a consistent transect across the river during each set of measurements. Stiff wire was insufficient to maintain this and a rope and pulley system was devised (Figure 5.2.5). The system was installed on two permanent concrete bases to allow consistent relocation between measurements. The system proved to be highly effective in ensuring the ADCP measurements did not deviate from the selected cross section. Prior to using the rope and pulley system, the variation of the boat course, given in local northings and eastings, can be seen in Figure 5.2.6a. The data show high variation in positioning both within and between crossings. The improvement following the installation of the rope and pulley system is shown in Figure 5.2.6b. The difference in angle between the north displacement axis and the ADCP crossing between the two datasets can be attributed to the installation of a compass on board the ADCP in September 2010. With the rope and pulley system (Figure 5.2.6b), there is a greater consistency of data collection with only a small difference in location. Consistent start and end points for the cross section are obtained along with a straightened course.

Figure 5.2.5: ADCP deployment using rope and pulley system on the River Lambourn.

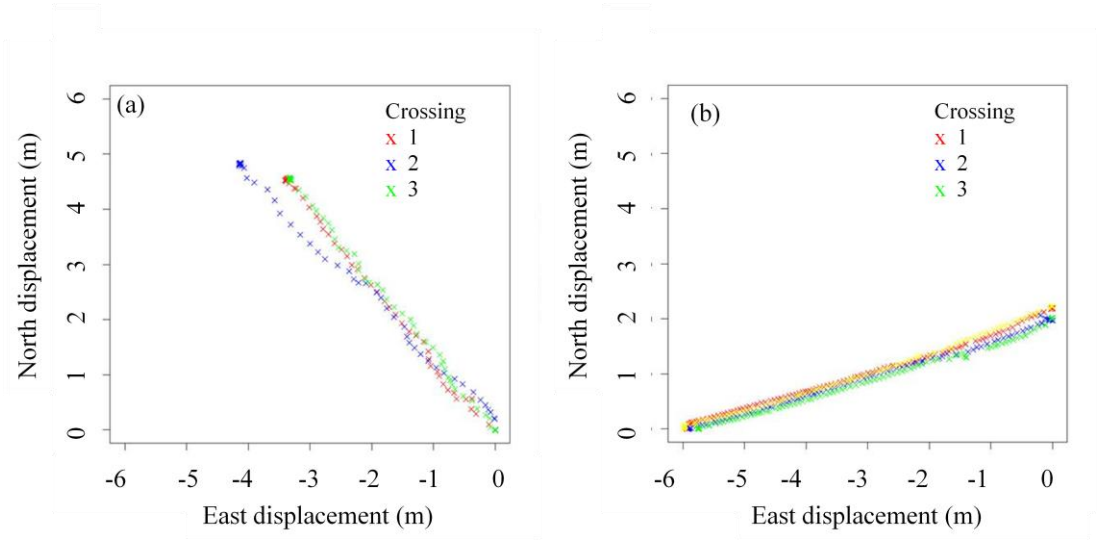

Figure 5.2.6: (a) local grid coordinates of ADCP crossing data prior to deployment using the rope and pulley system (February 2010). (b) local grid coordinates obtained when ADCP is deployed with the rope and pulley system (October 2010).

5.2.5. November 2010 and May 2011 data collection

The measurement protocol outlined by the manufacturer was used to collect data for each measurement campaign (RD Instruments, 2009). It is important to note that the onboard compass requires calibration before each measurement. Compass calibration was performed by placing the ADCP in a still area of the channel. The ADCP is then

rotated slowly 360^{o} around its axis with angle errors recorded by SxS Pro. Calibration was deemed to have been achieved when the mean angle error was less than 1^{o}. Data collected in November 2010 were collected at intervals over the cross section of 0.50m, whilst data collected in May 2011 were refined to an interval of 0.25m in order to reduce uncertainty attributable to a limited number of vertical profiles. The effect of this refinement is shown in Table 5.2.1. In all cases, 30 points were collected in the vertical profile.

Table 5.2.1: Effect of reduction of measurement interval on overall uncertainty.

Case	Interval (m)	Uncertainty (%)
November 15th 2010	0.50	4.63
November 22nd 2010	0.50	5.01
May 17th 2011	0.25	2.57
May 20th 2011	0.25	2.74

Work by Gunawan *et al*. (2010) demonstrated that the minimum sampling time for a stationary measurement using a StreamPro ADCP is approximately 180 seconds. This was determined by analysing the mean streamwise velocity for periods of 1, 180 and 300 seconds. After 180 seconds, the mean streamwise velocity and its standard deviation become almost constant suggesting that the velocity can be considered as stationary beyond this sampling time. As such, the sampling time in this study was increased to 200 seconds to ensure an accurate time-averaged discharge for each sub-section of the inlet cross section.

5.2.6. November 2010 and May 2011 data processing

Recent research has developed a variety of methods for processing data obtained from ADCP deployments, with the development of software an area of particular focus (e.g. Muste *et al.*, 2004a,b; Dinehart and Burau, 2005; Le Coz *et al.*, 2007; Szupiany *et al.*, 2007; Gunawan *et* al., 2010; Kim and Muste, 2012; Parsons *et al*., 2013). However, software for post-processing of section by section data is currently limited to that provided by the manufacturer. Hence, data post-processing undertaken for this study was undertaken using SxS Pro (RD Instruments, 2010).

Data were screened for instantaneous measurements which may lead to incorrect estimation of discharge. Such data points were identified by first examining the velocity contour plot provided by SxS Pro and secondly the measured velocity profile for each vertical for data which should be screened. Assessment of the initial results from SxS Pro (Figure 5.2.7) allowed the initial identification of bins which most likely contained erroneous data. This was mainly performed for the edges of the channel and at the bottom of the measured region. Bins which differ markedly in velocity from neighbouring bins such as the channel margins in Figure 5.2.7a, c and d are identified by the difference in colour to surrounding bins. Where such differences occur, the measured velocity profile was examined to assess whether data screening was required. Two examples of suspected outliers are shown in Figure 5.2.8, both taken from the 17th May 2011 case (Figure 5.2.7c).

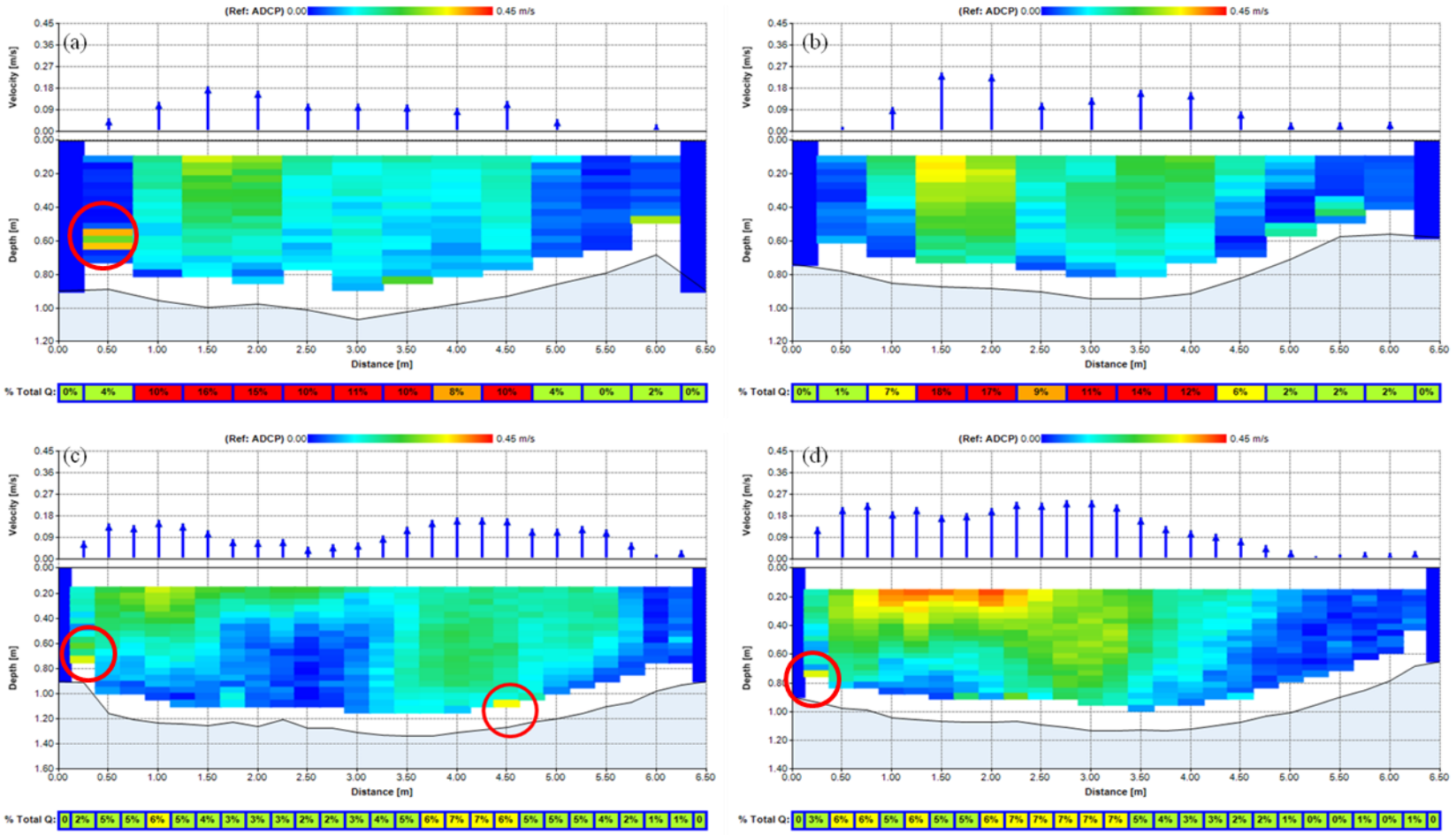

Figure 5.2.7: Plots from SxS Pro showing velocity vector distribution (top plot) and velocity contour plot (bottom plot) for; (a) November 15th 2010 before cut, (b) November 22nd 2010 after cut, (c) May 17th 2011 before cut with and (d) May 20th 2010 after cut datasets. % Total Q refers to the percentage of total discharge for each sub-section. Red circles highlight suspected erroneous data

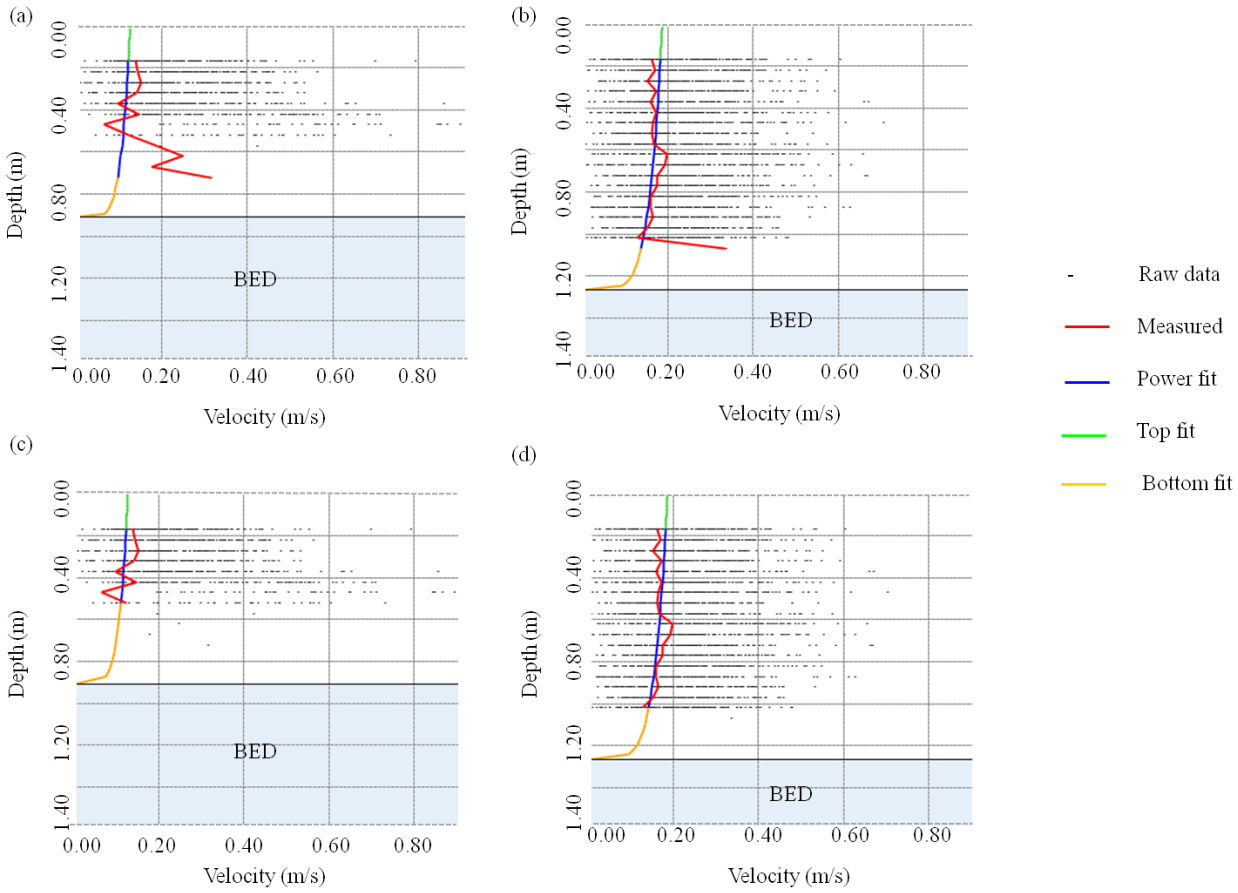

Figure 5.2.8: Example of two velocity profiles where outliers may occur; (a) 0.25m from left bank, (b) 4.50m from left bank. (c) and (d) show the same profiles following processing.

In each case where anomalies were suspected to have occurred, the raw measurements were examined. For most bins, a large number of instantaneous measurements were recorded. However, near the channel bed the number of measurements decreases due to the effect of the bed on the acoustic signal (Section 5.2.2). In the case of the measurement in Figure 5.2.8a taken near the left bank four bins needed to be screened due to the lack of measurements at these depths. The lack of measurements creates uncertainty as to whether these measurements are representative of the flow velocity, or merely represent acoustic anomalies. For the measurement taken in Figure 5.2.8b, only one measurement existed in the bin closest to the channel bed which led to a significant departure from the trend of the average measured profile.

Screening of such values was undertaken within SxS Pro. The program screens values before discharge is calculated from measured mean velocities and top and bottom discharge estimates. To achieve this, a threshold number of measurements are set for each bin. If the number of measurements in a bin is smaller than this threshold the bin is marked as bad and is removed from the discharge estimation (RD Instruments, 2009). During data collection this value is set as one. A value of one ensures all data collected is returned. To undertake data screening, this value is increased iteratively until bins containing outlier velocity data are removed. Table 5.2.2 shows the number of iterations required for each case. The iterations have the effect of increasing the number of measurements per bin required before a bin is deemed acceptable. The velocity profiles following post processing are shown in Figure 5.2.8c and Figure 5.2.8d. This shows that, in both cases, the anomalies identified are no longer included in the fitting of the measured average velocity

profile. The average measured profile is now limited to bins which contain a minimum number of measurements identified using the criteria in Table 5.2.2.

Table 5.2.2: Number of good measurements required for a valid measurement per bin.

Case	Number of measurements
November 15th 2010	5
November 22nd 2010	4
May 17th 2011	4
May 20th 2011	11

The effect of this post-processing on the contour plot, initially shown in Figure 5.2.7, is shown in Figure 5.2.9. Bins at the channel margins that were identified as possibly containing erroneous data in Figure 5.2.7a, c and d are of particular interest for comparison. For example, processing undertaken for the May 17th 2011 before-cut case (Figure 5.2.9c) results in these measurements being discounted. However, for the November 15th 2010 before-cut case (Figure 5.2.9a) and May 2011 after-cut case (Figure 5.2.9d) these values remain as sufficient data were collected to determine that these velocities were representative of flow occurring in this region for that particular date.

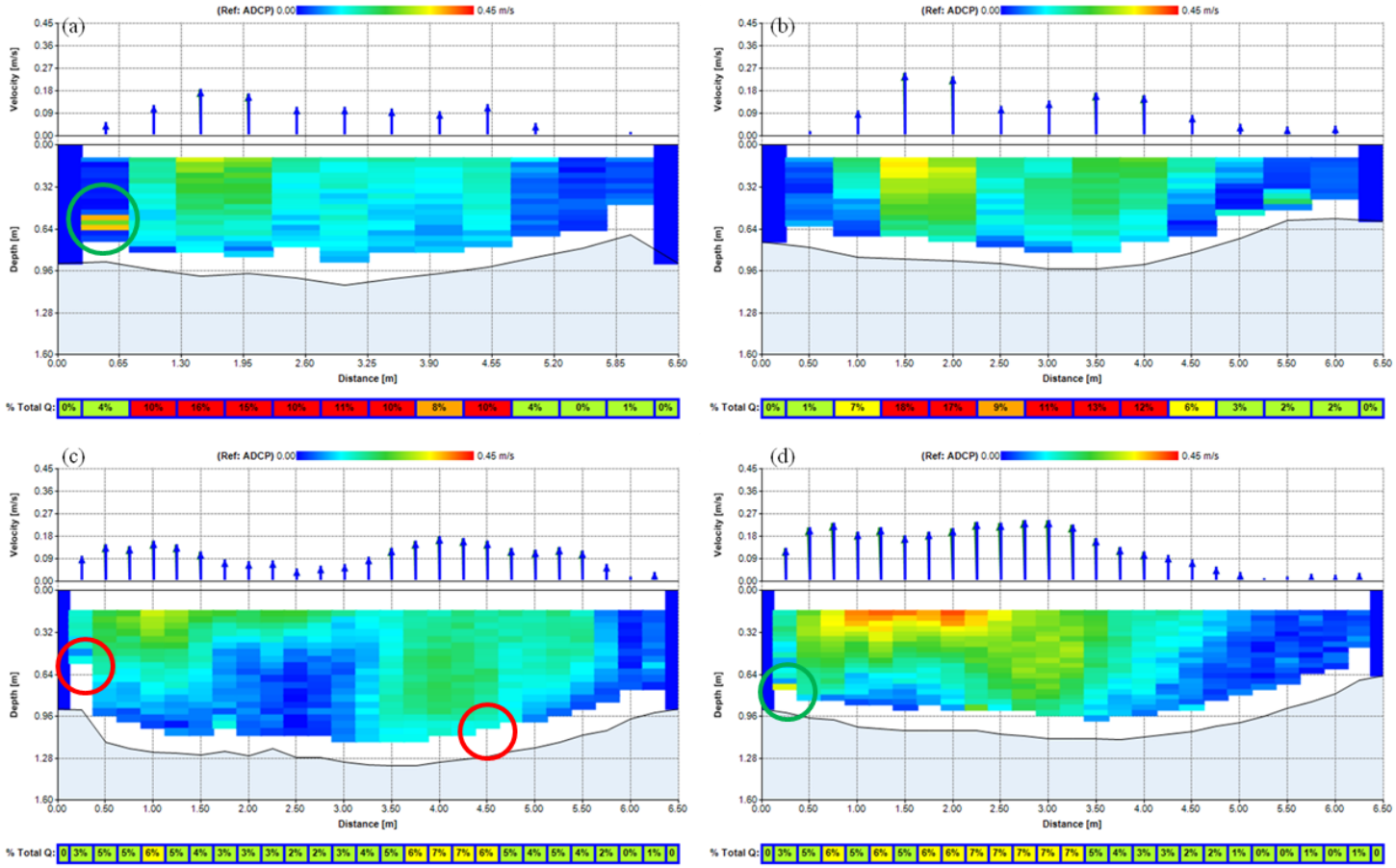

Figure 5.2.9: Plots from SxS Pro showing post-processed velocity vector distribution (top plot) and velocity contour plot (bottom plot) for; (a) November 15th 2010 before cut, (b) November 22nd 2010 after cut, (c) May 17th 2011 before cut and (d) May 20th 2010 after cut datasets. Red circles show where erroneous data have been removed. Green circles show where suspected erroneous data have been accepted.

5.2.7. Quality assurance of discharge values

The resulting values for discharge calculated from the collected data, following post-processing, are shown in Table 5.2.3. Values of discharge collected using the moving boat method in WinRiverII are included for comparison. An independent check of gauged daily discharge was performed using the Environment Agency flow gauging stations at Welford and at Shaw, around 1.5 kilometres upstream and 5 kilometres downstream from Boxford respectively. Both gauging stations are compound crump weirs, the most common type of flow gauging weir in use providing highly accurate measures of discharge. Their use in vegetated rivers, however, requires upstream maintenance of aquatic vegetation which if not performed may limit their accuracy (Rickard *et al*., 2003). There were no reported issues for either gauging station on the dates of interest. The potential impact of groundwater recharge on measurements is highlighted for both weirs (NRFA, 2014). Discharge values from Shaw were scaled using the catchment area ratio between Boxford and Shaw ($162km^2/234km^2$) in order to account for differences in drainage area between the two locations. Data from Welford were not scaled due to the station's proximity to the site at Boxford. The discharge measured for the February 2010 case is also included.

Table 5.2.3: Values of Q measured using SxS compared to moving boat approach (Q_{WR}) and those measured at EA gauging stations at Welford and Shaw ($Q_{Welford}$/ Q_{Shaw}). Flow duration percentiles are quoted based on the Shaw gauging station.

Case	Q_{sxs}	Q_{WR}	$Q_{Welford}$	Q_{Shaw}	Flow duration percentile
February 22nd 2010	-	2.191	1.580	1.349	Q15
November 15th 2010	0.557	0.619	0.456	0.647	Q99
November 22nd 2010	0.603	0.605	0.457	0.631	Q99
May 17th 2011	0.841	0.912	0.812	0.969	Q89
May 20th 2011	0.946	0.942	0.796	0.941	Q85

The flow during February 2010 was high (Q15) due to input from the chalk aquifer following groundwater recharge. Flows during November 2010 and May 2011 (Q85-Q89) fall within the normal baseflow range. For the before and after cut datasets, there is a slight variation in discharge before and after the cut, however this is to be expected when considering the discharges were measured around three days apart (Section 5.1). Discharge measured in February 2010 using WinRiverII is overestimated, the reasons for which are unclear. Discharge calculated using SxS Pro compared to the gauging station at Welford is, in general, over estimated. Discharge calculated using SxS Pro compared to the gauging station at Shaw is, in general, under estimated. Differences between the measurements reported at the gauging stations and those calculated in SxS Pro may result from the either the data collection method or local groundwater upwelling or downwelling (e.g. Grapes *et al*., 2004). Crump weirs estimate discharge based upon measurement of the upstream and downstream water level. The ADCP, however, undertakes site specific measurements of flow velocity and depth to determine discharge. An independent check of the method was performed by comparing discharge measurements calculated in SxS Pro to those calculated using the moving boat method in WinRiverII, measured on the same day. A slight variation in values can be observed, with values calculated in SxS Pro generally marginally lower (between 0.3 to 11.1%) than those calculated in WinRiverII.

Overall the measurements of discharge undertaken using SxS Pro were deemed to be of acceptable quality when considering their low overall uncertainty (5% or lower) (Table 5.2.1), their similarity to the closest flow gauging station at Welford and their similarity to measurements undertaken using the moving boat method in WinRiverII (Table 5.2.3)

5.3.Fixed lid and model outlet

To measure the reach scale water surface slope and, thus, water depth necessary for the model outlet condition and the initial fixed lid (the upper boundary of the model), four D50 staff gauge boards (SGB) complying to BS 3680 Part 7 (Figure 5.3.1) were installed along the 110m reach at the locations shown in Figure 3.3.1. The height of each board above Ordnance Datum was surveyed using the integrated surveying system (Section 4.1). This allowed rapid measurement of the free-surface to be undertaken monthly. Readings were taken by eye, and recorded to the nearest centimetre. Staff gauge board readings for each modelled case are shown in Figure 5.3.2.

Figure 5.3.1: Staff gauge board installation on the River Lambourn (Photograph taken February 2014).

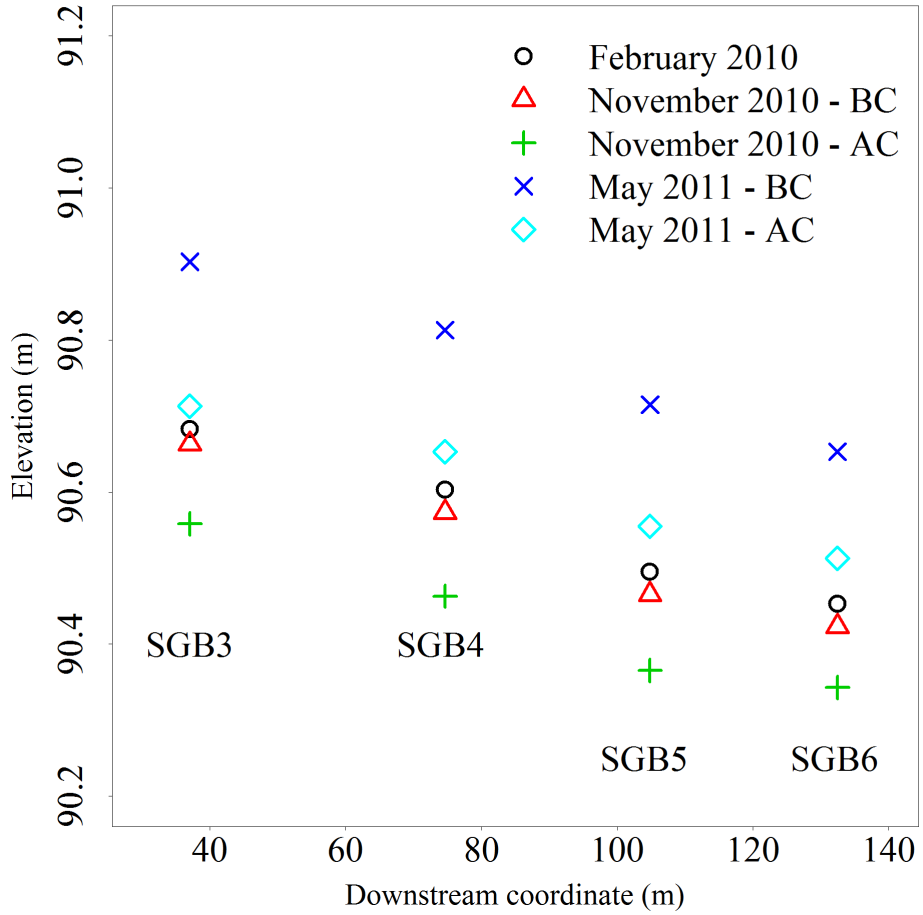

Figure 5.3.2: Staff gauge board readings for modelled cases. BC and AC refer to before cut and after cut respectively. SGB refers to staff gauge board reference.

5.4.Model validation data

A basic requirement of the scientific method is the need to demonstrate that a theory (or in this case a model) provides a good representation of reality. The validation of hydraulic models tests model output against those observed in reality (Mulligan and Wainwright, 2004) and is based upon the premise that when a model fails to predict data which is collected independently, then a component, or components of the model are incorrect (Luis & McLaughlin, 1992; Beven, 2001). Equally, however, when model predictions are correct the model is still not necessarily valid. This is

due to the fact that it is possible for an invalid model to provide adequate representations of some aspects of reality (Lane et al., 2005).

Commonly, validation of hydraulic models takes place through the traditional technique of field and ground-based measurement (Horrit, 2005). This is often undertaken in one of two ways. The first is through the use of flow measurements using either an acoustic Doppler velocimeter (ADV) (e.g. Lane et al., 1999) or an electromagnetic current meter (EMCM) (e.g. Nicholas and Sambrook-Smith, 1999). In order to validate the streamwise and cross-stream velocities predicted by the model, an EMCM was used to collect, on average, a total of fifteen profiles per vegetation case distributed throughout the modelled reach. These were supplemented by ADV data in order to compare model predictions with measurements of turbulent kinetic energy. For the ADV, a maximum of eleven profiles were collected per case. The combination of the EMCM and ADV allowed a detailed coverage of the reach both before and after vegetation cuts. A third validation dataset, consisting of water surface elevations measured using the integrated surveying system, was collected to validate model predictions of the water surface.

5.4.1.Acoustic Doppler velocimeter data

Acoustic Doppler velocimetry makes use of the Doppler frequency shift of emitted acoustic signals after reflection by particles suspended in channel flow. Detailed theory regarding the ADV can be found in Lane *et al*. (1998), however the principle is broadly the same as that of the ADCP where the water velocity is measured using the Doppler shift principle (Section 5.2.1). Consideration was given to the setting of the expected velocity range, maximum velocity and water temperature values. Each has a significant bearing on the accuracy of the collected data, especially where the goal of the measurements is to quantify turbulence. Two ADV sampling strategies

were employed. For the November 2010 field campaign, ADV measurements were undertaken at random point locations in non-vegetated regions of the channel. Due to equipment malfunction, only five profiles were collected during this period, one before the cut and four following cutting.

For the May 2011 campaign, a series of four cross sections with between two and three verticals in each was defined. These allowed ADV measurements both before and after the vegetation cut to be taken in the same location to enable comparisons before and after a vegetation cut as well as to validate the model. A larger number of profiles were collected during this period, with eight profiles collected before the cut and eleven collected following the cut. The determination of the location of the profiles was driven by the locations of plant patches across the cross section. Profiles were taken both in non-vegetated regions and in close proximity to vegetation patches. Where profiles were close to vegetation patches, care was taken to ensure no plant leaves or filaments passed through the sampling volume whilst measurements were taking place. The locations of ADV measurements within the channel for each case are shown in Figure 5.4.1.

Measurements were carried out using a Nortek acoustic Doppler velocimeter, providing velocities in three dimensions sampling at a frequency of 25Hz. The sampling volume was $0.346cm^3$ located 5.8cm below the instrument. The equipment was deployed in downward looking mode and held in place using a wading rod which was similar in design to that of Lane *et al.* (1998) as shown in Figure 5.4.2.

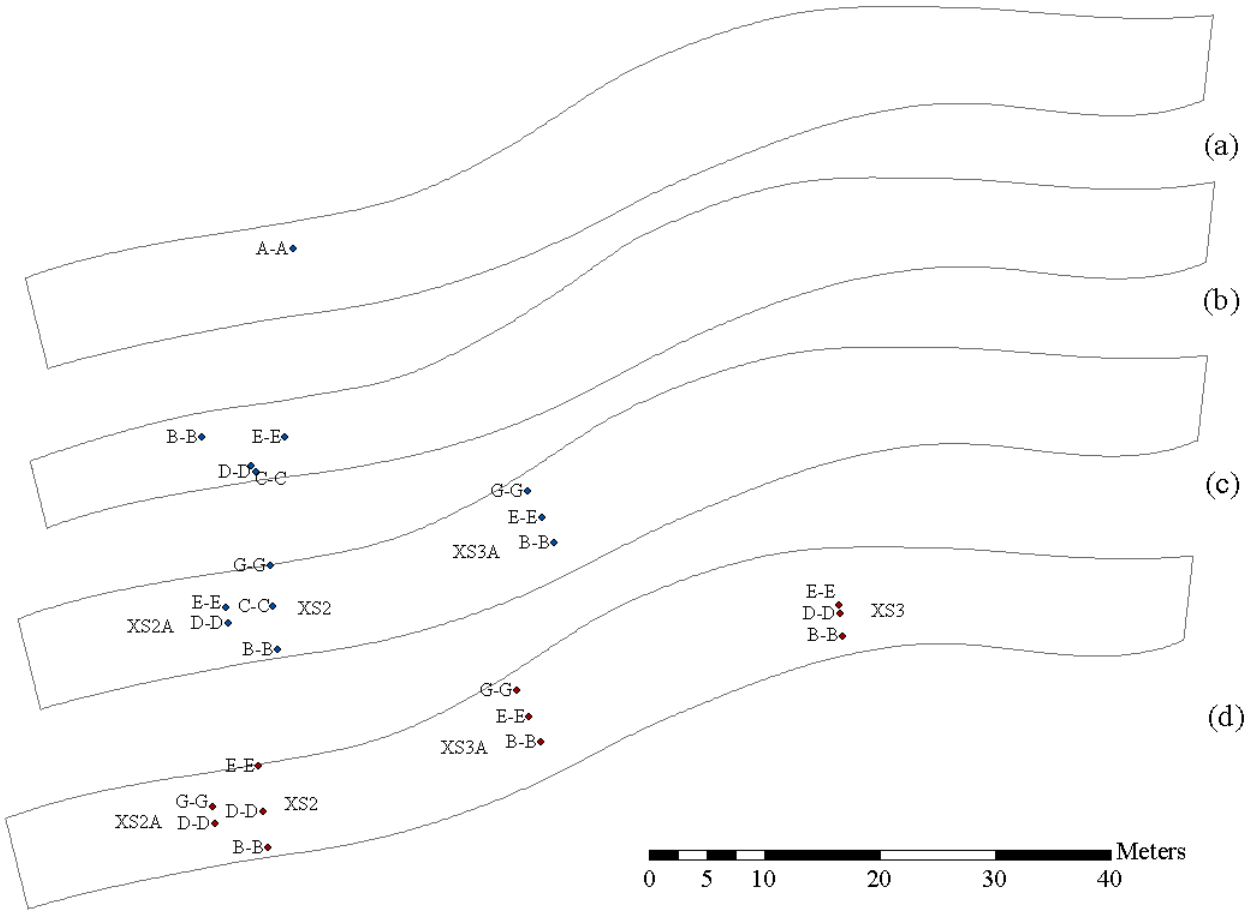

Figure 5.4.1: Location of ADV measurements in the experimental reach for (a) November 2010 before cut; (b) November 2010 after cut; (c) May 2011 before cut and (d) May 2011 after cut.

(a)

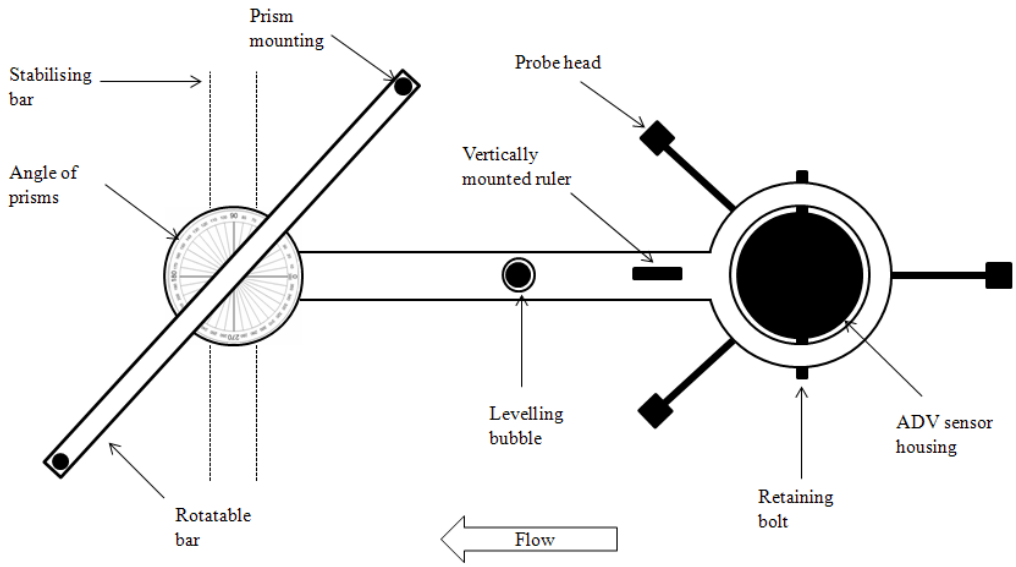

(b)

Figure 5.4.2: (a) Schematic representation of ADV deployment (based upon Lane et al., 1998); (b) Field deployment of the ADV (Photograph taken May 2011) .

The wading rod incorporated a levelling bubble to ensure the instrument was held horizontally, two prisms mounted on a cross beam which were surveyed using the integrated surveying system so the location and orientation of the probe was known and a graduated scale on the rod so to allow vertical positioning of the instrument. The wading rod and the operator were positioned downstream of the sensor at all times to ensure the flow being measured was not disturbed. The first measurement was taken at the closest point to the bed which did not exhibit interference from the boundary, determined to be a height of 0.05m. Subsequent measurements were taken at intervals of 0.05m for the first three measurements, then every 0.10m thereafter. Measurements were taken over a three minute period to provide sufficient accuracy for computing turbulence characteristics (Sukhodolov, 1998), nearly double that recommended as the minimum sampling effort required for low standard errors suggested by Buffin-Belanger and Roy (2005).

5.4.2.ADV data processing

The accuracy of mean flow measurement using an ADV has been reported to be high; in some cases within 1% (e.g. Lohrmann *et al.*, 1995; Voulgaris and Trowbridge, 1998). However, there is a need for considerable post-processing of the data to take place to ensure quality. The steps applied in this study to process ADV data are outlined in Figure 5.4.3.

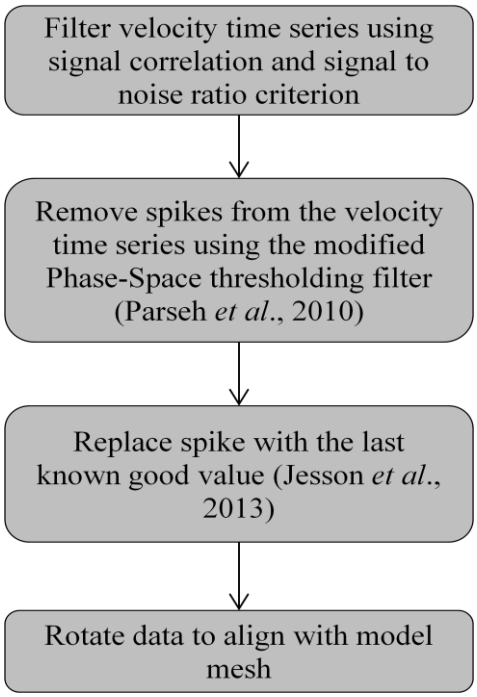

Figure 5.4.3: Flowchart used to process collected ADV data.

The ADV signals were checked for poor signal correlation (Lane *et al.*,1998), i.e. the similarity between the outgoing and return signal. Poor data can also result from a high signal to noise ratio (Wahl, 2000; Naden *et al*., 2006). Initial filtering, using correlation and signal to noise criteria, was undertaken using the software WinADV (Wahl, 2000). The signal to noise (SNR) criterion is set as recommended by the manufacturer as 0.15 (Nortek, 2000). Values where any individual beam displaying a signal correlation of less than 0.5 were removed from the data. This criterion was relaxed from the recommended value of 0.7 (Nortek, 2000). The relaxation is supported by Lhermitte and Serafin (1984), McLelland and Nicholas (2000), Wahl (2000) and Naden *et al*. (2006).

When considering turbulence, it is also important to identify and correct for aliasing. As the ADV measures velocities using the Doppler shift principle, the phase shift can only be measured within the range -180^{o} to $+180^{o}$. Any shift outside

of this range leads to a spike in the velocity time series, a phenomenon known as aliasing (Lane *et al*., 1998; Goring and Nikora, 2002; Jesson *et al*., 2013). An example velocity time series collected on the River Lambourn with spikes present is shown in Figure 5.4.4. Spikes were defined as values greater than those expected in a Gaussian distribution of the same sample size, based on the mean and standard deviation of each individual time series (Naden *et al*., 2006).

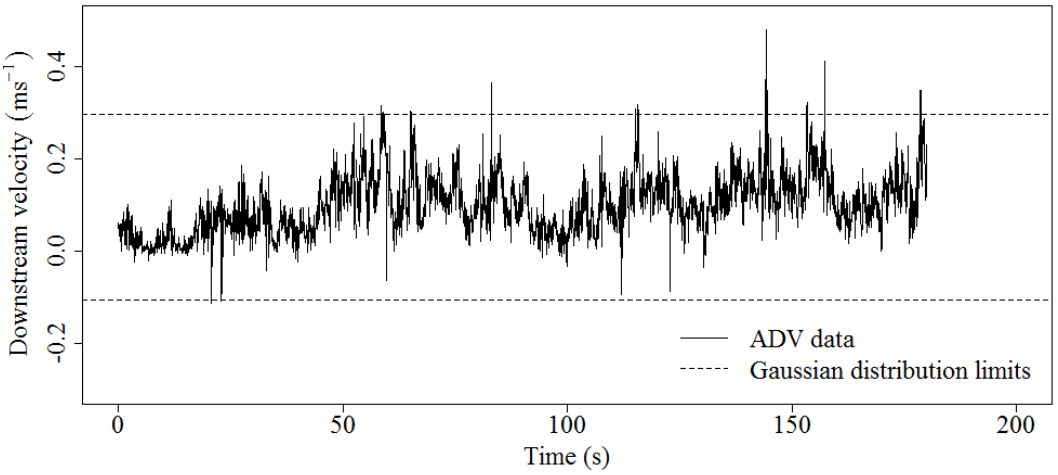

Figure 5.4.4: Example data point containing spikes collected on the River Lambourn. Data taken from the May 2011 before cut case, XS2 profile G-G at a height of 0.05m above the bed.

Spikes in the velocity time series were removed using the modified phase-space thresholding filter of Parseh *et al*. (2010). The method is based upon that of Goring and Nikora (2000), a previous *de facto* standard for the processing of ADV data (Jesson *et al*., 2013). Some studies (e.g. McLelland and Nicholas, 2000; Naden *et al*., 2006) argue that the use of phase-space filters are not necessary for datasets where few spikes are present, instead preferring a Chebyshev filter. However, there has been a shift in recent years to more advanced approaches to spike removal in ADV datasets (Jesson *et al*., 2013) necessitating the use of such filters. Where a complete time-series dataset is required (i.e. for spectral analysis), spikes removed must be replaced with an approximated value. A number of methods exist for doing

this: last good value (LGV); linear interpolation (LI); and 12-point polynomial (12PP). Tests undertaken by Jesson *et al*. (2013) on the appropriate replacement method for velocity despiking filters showed that LGV was most appropriate for the method used by Parseh *et al*. (2010), and this replacement method is used in this study. The same dataset shown in Figure 5.4.4 following spike removal is shown in Figure 5.4.5. Table 5.4.1 shows the effect of the filter on the mean downstream velocity, its standard deviation and root mean square error. The percentage of points determined as valid following the application of the despiking filter was used as a final check of the applicability of the filter.

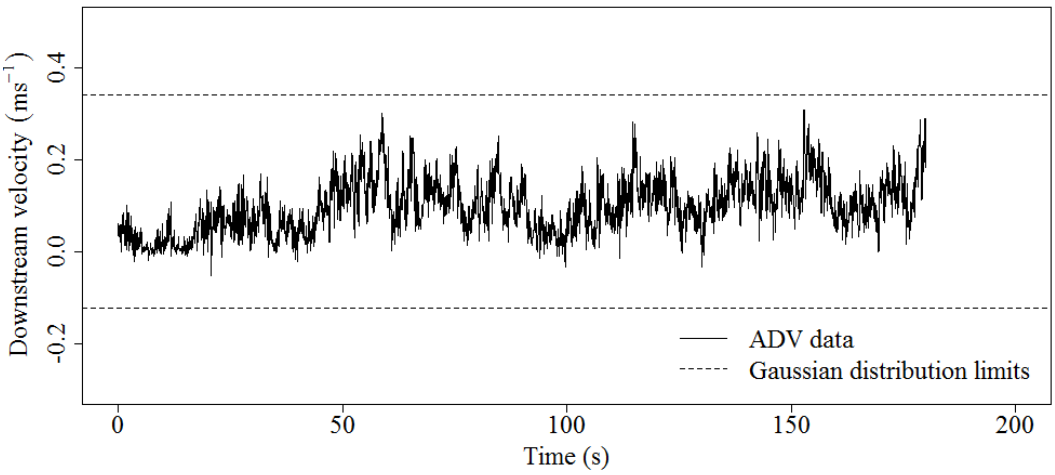

Figure 5.4.5: Filtered velocity time series data using the modified phase-space thresholding method and last-good value replacement strategy (mPST-LGV).

Table 5.4.1: Results of filter application to the measured data.

Despiking method	Mean downstream velocity (ms^{-1})	Standard deviation (ms^{-1})	RMS (ms^{-1})	Percentage valid
Raw data	0.101	0.061	0.117	100
mPST-LGV	0.100	0.058	0.114	97.56

For the filter applied, there is very little change from the raw data. This is due to the relatively low percentage of spikes in the dataset (2.44%). The method has little effect on the mean downstream velocity, standard deviation and RMS values. This is reflected in the high percentage of data marked as valid (97.6%).

Finally the data were orientated to be aligned with the cross section of interest. Such a step is crucial. Roy *et al*. (1996) found that errors in flow data can vary as much as between -13 to 7 percent per degree of rotation. To orientate the measured ADV data to the necessary reference grid, the angle between the prism bar and the cross section was determined using the relationship:

$$\tan\theta = \left|\frac{m_{1-}m_2}{1 + m_1 m_2}\right|$$

5.4.1

where m_1 and m_2 are the slopes between the prisms and cross section respectively. Rotation was undertaken to the nearest integer degree. The angle was then adjusted for the angle between the prisms and the stabilising bar (Figure 5.4.2a), set between -30^o and $+30^o$ dependent on the line of sight between the ADV and the surveying equipment. The resulting time-averaged streamwise (u) and lateral (v) velocity profile, along with the associated turbulent kinetic energy (TKE) profile, following filtering and rotation is shown in Figure 5.4.6. TKE is calculated from the turbulent velocity fluctuations by the ADV using the equation:

$$TKE = 0.5\rho\left(\overline{u'^2} + \overline{v'^2} + \overline{w'^2}\right)$$

5.4.2

where ρ is the fluid density and $\overline{u'}$, $\overline{v'}$ and $\overline{w'}$ are the mean fluctuations of velocity in the downstream, lateral and vertical directions respectively. The profile shown is taken from the May 2011 before cut dataset at XS2 profile C-C.

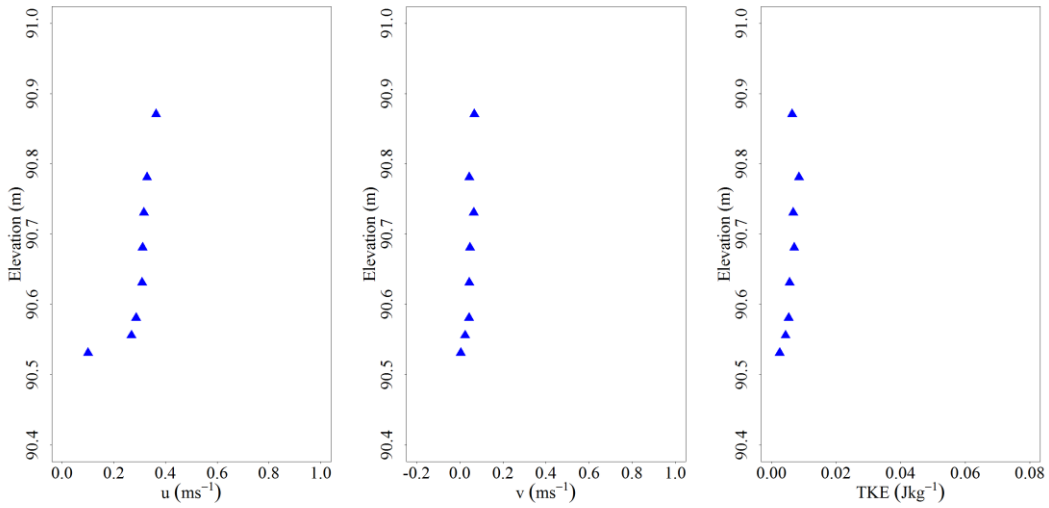

Figure 5.4.6: Example ADV streamwise velocity (u), lateral velocity (v) and TKE profile. Dataset: May 2011 before cut, XS2 G-G.

5.4.3.Electromagnetic current profiler (EMCM)

The electromagnetic current meter (EMCM) deployed in this study measures velocities in two dimensions, namely downstream and lateral flow if oriented perpendicular to the flow. The advantage of the EMCM is that measurements can be taken within macrophyte patches, something which cannot be achieved using acoustic approaches. The sensor used was hence chosen to cause minimal disturbance within the vegetation. A Valeport Model 802 2 Axis current meter was deployed in this study using a discus probe. The discus probe had a diameter of 32mm with a sampling volume of 16mm projected from the sensor face. The EMCM was mounted on a wading rod, enabling the height above the bed of the probe to be set to an accuracy of one centimetre.

Again, two sampling strategies were employed for the measurements taken using the EMCM. Measurement locations are shown in Figure 5.4.8. For the November 2010 field campaign, EMCM measurements were undertaken at a series of locations on the experimental reach. For the May 2011 field campaign, measurements were undertaken at the cross sections described in the collection of the ADV data. Profiles were collected every metre over the cross section. At each location, the water depth was recorded and the profile divided into six measurement points; adjacent to the channel bed, 0.2D, 0.4D, 0.6D, 0.8D and adjacent to the surface (BS 3680 1973). Measurements were taken over a thirty second averaging period. Once complete, velocities in the streamwise and lateral directions were recorded, along with their standard deviation. An example EMCM profile is shown in Figure 5.4.7, taken from the May 2011 after cut dataset at XS2 profile E-E.

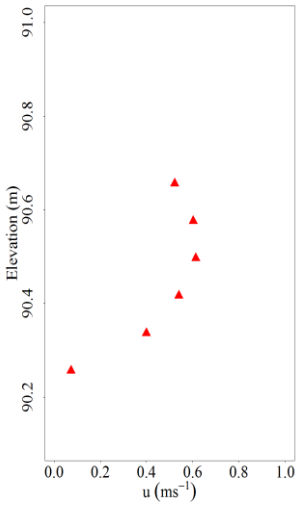

Figure 5.4.7: Example EMCM streamwise velocity (*u*) profile. Dataset: May 2011 after cut, XS2 E-E.

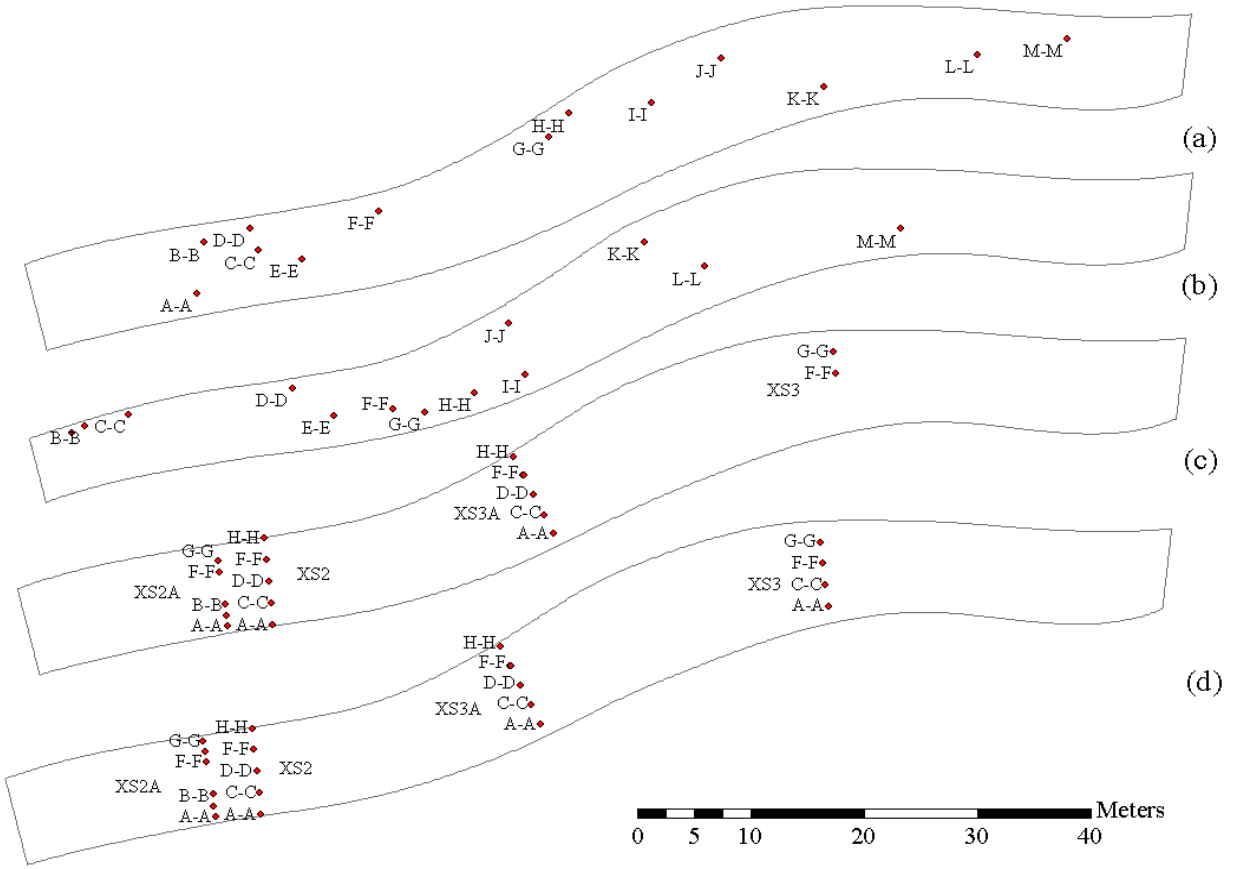

Figure 5.4.8: Location of EMCM measurements in the experimental reach for (a) November 2010 before cut; (b) November 2010 after cut; (c) May 2011 before cut and (d) May 2011 after cut.

5.4.4.Free surface measurements

To validate the free surface predicted by the model, measurements of the water surface elevation were taken along each bank of the experimental reach at regular intervals of 2-3 metres. Measurements were taken by resting the survey staff on the water surface. This could be difficult, which may have led to errors in measurement. To try and achieve accurate measurements, the staff was levelled before each measurement using a levelling bubble. Measurements were undertaken before and after each vegetation cut. Free surface measurements at each bank for all cases are shown in Figure 5.4.9.

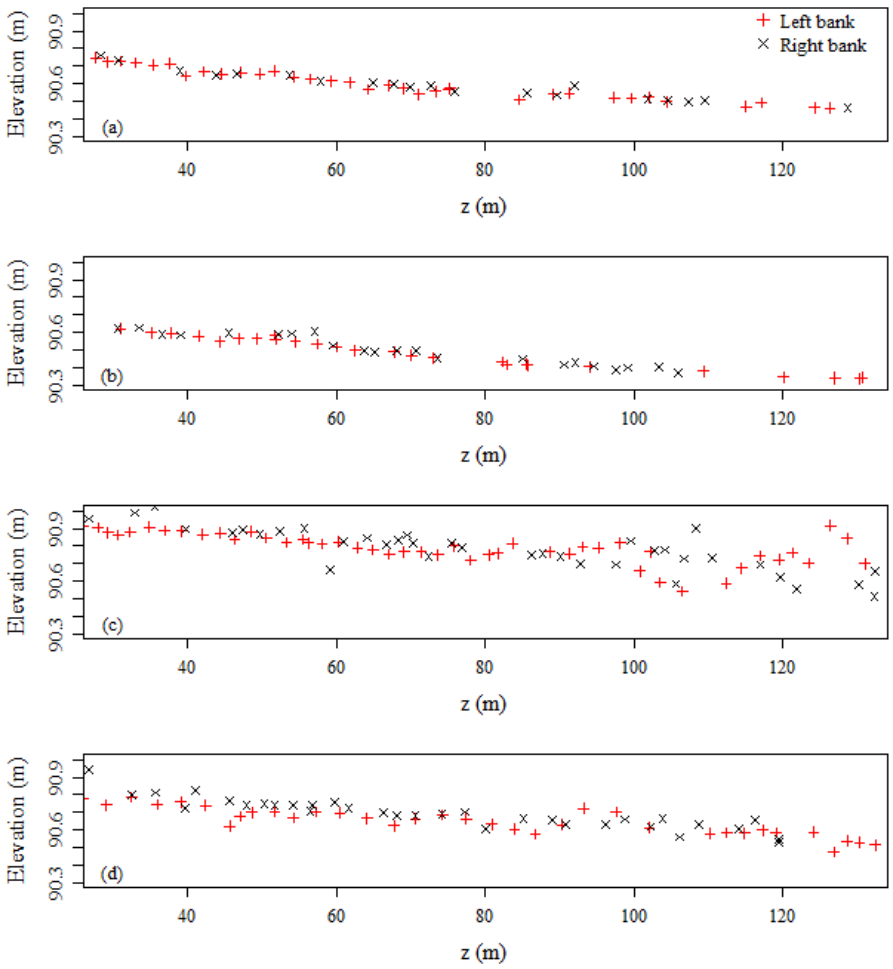

Figure 5.4.9: Reach free surface measurements at both banks for (a) November 2010 before cut; (b) November 2010 after cut; (c) May 2011 before cut; (d) May 2011 after cut.

5.5.Conclusions

The data relating to the dynamic conditions of the model, along with appropriate post processing have been described in this chapter. Two main areas have been discussed, those relating to discharge and velocity and those relating to the water surface. Flow measurements using an ADCP deployed in Section by Section are in their infancy. However, this study has shown that with careful attention to measurement protocol, measurements with a relatively low uncertainty can be produced (less than 5% in most cases). Appropriate signal filtering for ADV data was undertaken, and the data orientated to be perpendicular to the cross section of interest. Finally, reach free surface measurements, necessary to validate free surface elevations within the model, were presented.

Chapter 6. Representing vegetation within the model

In order to represent vegetation within a 3D hydraulic model, two datasets are required: (i) data relating to the three dimensional shape of vegetation patches and (ii) data to inform the parameterisation of vegetation drag within the model. The main species present at the CEH River Lambourn Observatory (Section 3.3) were surveyed. For the modelled cases, these include *Ranunculus penicillatus* subsp. *pseudofluitans* var. *pseudofluitans*, *Berula erecta*, *Callitriche obtusangula* and *Rorippa nasturtium aquaticum*. For brevity, these species are hereafter referred to as *Ranunculus*, *Berula*, *Callitriche* and *Rorippa*.

The shape of a vegetation patch in a natural river is complex, with plant shape responding to changes in flow (Sand-Jensen, 2003, Sand-Jensen, 2005, Sukhodolov, 2005, Green, 2005d, Statzner et al., 2006). Plant patches are streamlined bodies whose shape varies along their length in three dimensions. In order to represent this streamlined form within the model mesh, data relating to the 2D patch planform shape for the given flow condition were collected along with measurements of the patch underwater structure. These two datasets were later combined (Section 7.4) to form an overall patch morphology. Measurements of plant volume and surface area were undertaken to provide porosity values for the model and the area parameter of the drag term (Section 3.1.2).

6.1. Vegetation patch shape

Plant patches are defined here as a distinct area of vegetation of a single species. This may be a single plant (e.g. *Ranunculus*) or a coherent stand of individual plants (e.g. *Berula*, *Callitriche* and *Rorippa*). Within the channel, some areas contained a mixture of these species, the outlines of which were also surveyed. Such areas are

hereafter referred to as ‘Mixed’. Plant patch shape was characterized in this study through the measurement of patch planform and the patch depth coverage. The collection of these data enabled a generalised description of the patch shape in three dimensions. The planform shape of all patches in the modelled reach was collected using the integrated surveying system described in Chapter 4. To assess the coverage in the depth dimension, data were collected for a range of individual plants. The variation in the maximum vertical extent of the patch, termed the top profile, was measured using the integrated surveying system. These data were coupled with evidence from underwater photography to determine the bottom profile and the extent to which a void area exists between the patch and the channel bed. This overcame limitations of previous studies (e.g. Nikora *et al*., 2008; Rameshwaran and Naden, 2012; Luhar and Nepf, 2013) where it was assumed that coverage is uniform throughout the water depth, something which is not necessarily true.

A different morphology was observed for *Ranunculus* in November 2010 to that in May 2011. During November 2010, *Ranunculus* adopted a streamlined shape close to the channel bed. Conversely, in May 2011 the species occupied a large proportion of the flow depth. During May, patches of *Ranunculus* extended towards the water surface to enable the species to flower. During November, however, the combination of a high incident velocity along with species die back led to the patch flattening towards the channel bed. Throughout this chapter, the morphology of *Ranunculus* present in November 2010 is referred to as ‘near-bed *Ranunculus*’ and that present in May 2011 as ‘full-depth’ *Ranunculus.*

6.1.1. Plant patch planform data

The method applied in this study relating to patch planform was a manual survey of all the vegetation patches in the modelled reach using the integrated surveying system. Individual macrophyte patches in the reach were identified by finding where the plant was rooted and how it related to neighbouring stands in terms of the position in the water column. To aid this, the vegetation patches were viewed through Polaroid lenses to ensure a distinct patch was identified by removing glare from the water surface.

Once an individual stand was identified, the extent of the patch was surveyed at a spacing of approximately 0.25m, working in a clockwise direction from the root to the tip and back to the root. The patch was given a unique ID to distinguish it from other stands of the same species. Using the method described, the morphology of each individual patch could be accurately mapped for the given flow condition and growth stage, thus incorporating its reconfiguration to the actual flow conditions being simulated in the model. The total time taken to survey the experimental reach was around 8-10 hours dependent on the extent of macrophyte cover on the survey date.

In order to relate the planform coverage to the model mesh, a polygon dataset of vegetation coverage was created for each case. Using the unique ID assigned during surveying, groups of points were digitised into polygons in ArcGIS using the workflow in Figure 6.1.1.

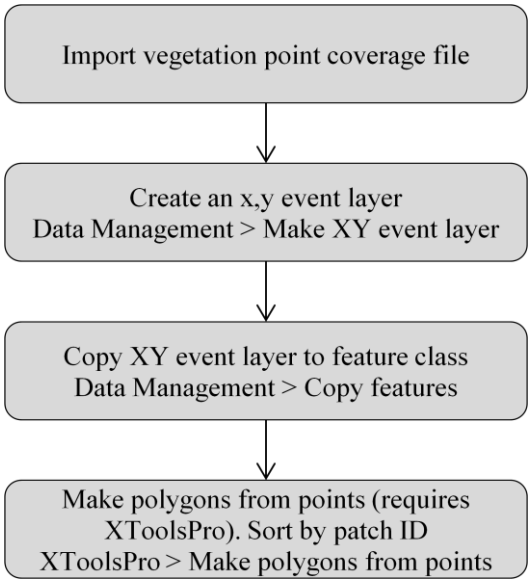

Figure 6.1.1: Workflow to produce vegetation polygons from surveyed points using ArcGIS

An example of the surveyed data points and the resulting polygon coverage generated is shown in Figure 6.1.2.

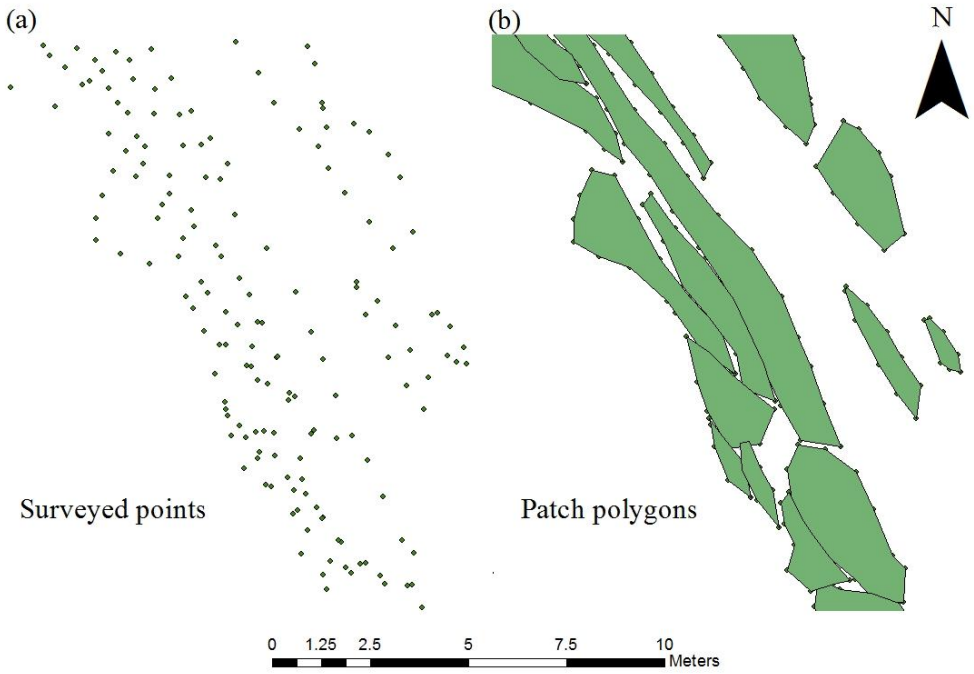

Figure 6.1.2: (a) Surveyed data points; (b) Polygon coverage generated for the surveyed data points. Data shown are taken from the May 2011 after cut case. All patches shown are of *Ranunculus.*

The workflow in Figure 6.1.1 was applied to each of the four vegetation datasets collected. The final polygon coverage dataset for the experimental reach for each of these datasets is shown in Figure 6.1.3.

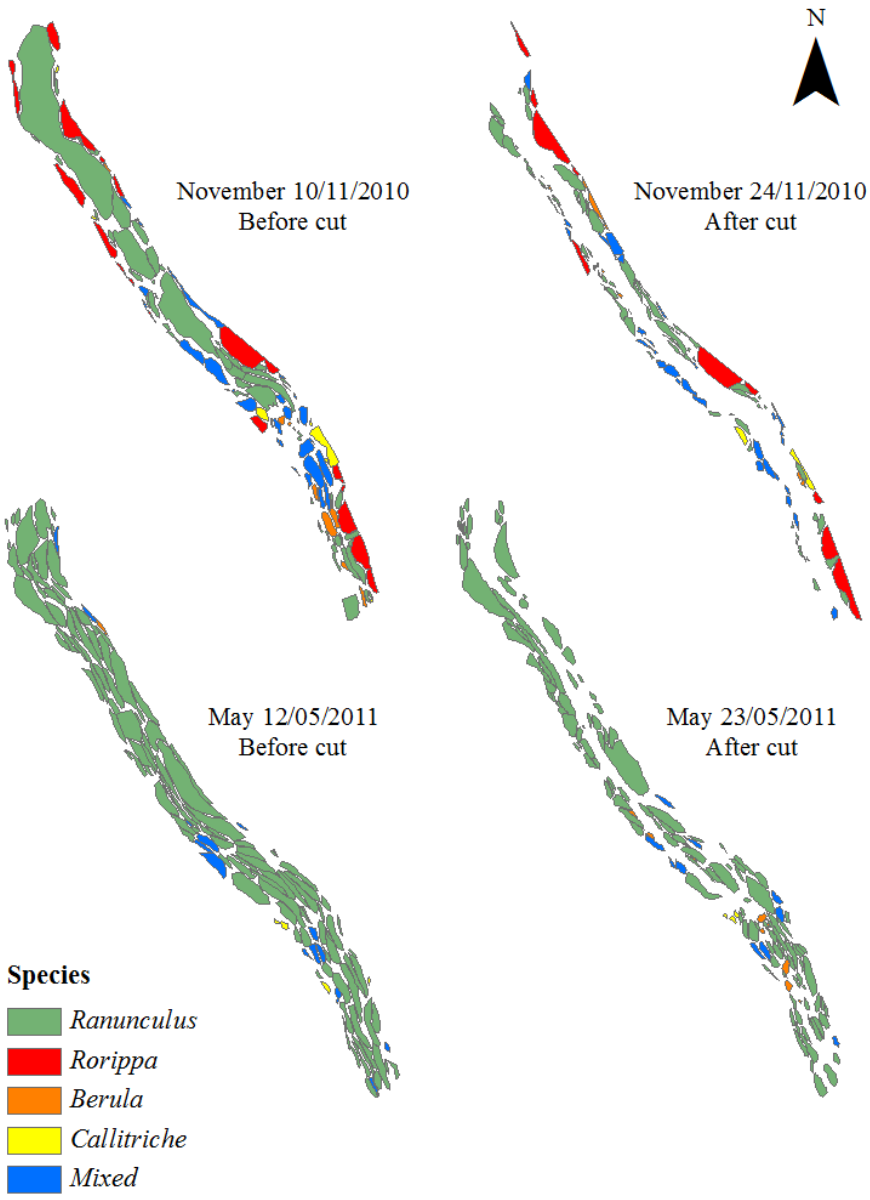

Figure 6.1.3: Polygon coverage generated in ArcGIS for each of the four surveyed datasets.

6.1.2. Plant vertical structure

In order to gain an understanding of the shape of vegetation patches in the depth dimension, shape profiles were surveyed for a sample of plants of each species. The upper surface of the plant was surveyed using the integrated surveying system. A number of profiles were collected throughout the study reach to incorporate variation in growth and changes in flow. Profiles were surveyed from the root to the tip of each patch along the centreline at a maximum spacing of 0.25m. Working from the root, the foot of the surveying staff was placed on the surface of the plant, taking care not to push the plant closer to the bed. The staff was levelled using a bubble level mounted at eye level and the measurement recorded. As in the patch survey, an alpha numeric code was used to distinguish different species.

The total number of surveyed top profiles was seven for *Berula*, four for *Callitriche*, twelve for near-bed *Ranunculus* and ten for full-depth *Ranunculus*. The number of profiles for *Callitriche* is low due to the low abundance of the species in the experimental reach, with a maximum of three patches found in any one sampling period. Top profiles for *Rorippa* were not required, as this species extends from the channel bed to above the water surface. The surveyed top profiles for each species are shown in Figure 6.1.4. Relative distance along the patch is used in order to provide a dimensionless description of patches of different length.

Figure 6.1.4 shows a clear variation in height above the bed between species, as is to be expected. Within species variation occurs in *Ranunculus* dependent on the time of year the plant is surveyed. Near-bed *Ranunculus* is prevalent during the latter stages of the growing season. The water depth is reduced and water velocity is higher, leading to a more streamlined profile closer to the channel bed. The opposite is true when *Ranunculus* is in its flowering stage, typically early in the growing

season. At this time the plant is at its most dense and buoyant, leading to a top profile which extends towards the water surface.

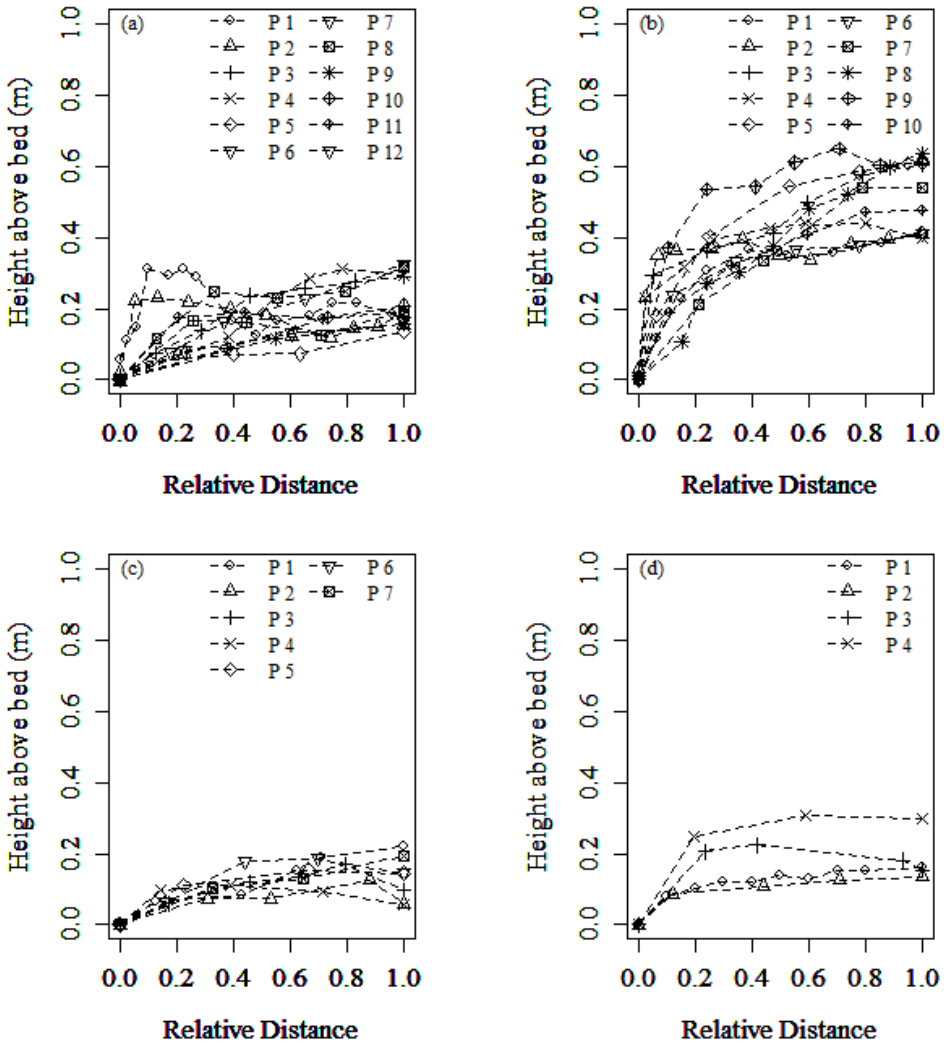

Figure 6.1.4: Surveyed top profiles for (a) near-bed *Ranunculus*; (b) full-depth *Ranunculus*; (c) *Berula*; (d) *Callitriche.*

Whilst the top profile of any vegetation patch is relatively easy to determine, any profile present between the bottom of the patch and the bed is more difficult to observe. In this study, a Splashcam Delta Vision Industrial underwater camera was used to both photograph and video the bottom profile of plant patches (Figure 6.1.5).

Figure 6.1.5: Splashcam Delta Vision Industrial underwater camera (credit: Delta Vision, July 2014).

The use of underwater photography to document aquatic vegetation is common in large rivers, estuaries and lakes (e.g. Spears *et al*., 2009). However, the use of such a method is usually applied to the monitoring of macrophyte presence and density rather than its underwater structure. In this study, the underwater camera was mounted upon a wading rod and set at a height where both the bed and the bottom profile of the plant could be seen, as shown in Figure 6.1.6.

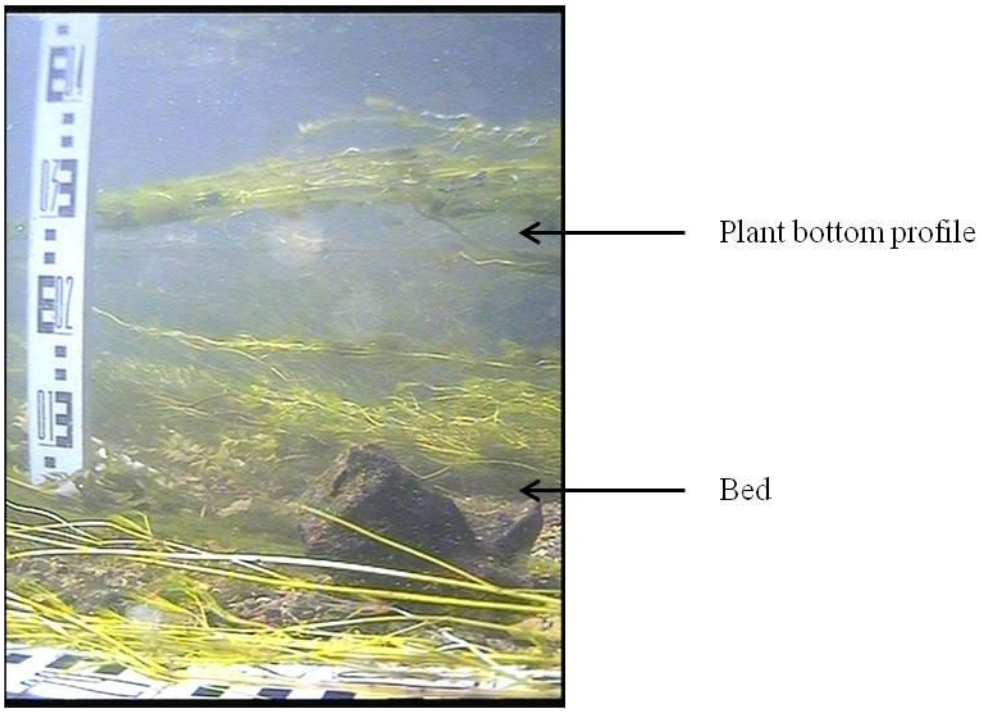

Figure 6.1.6: Example of underwater photograph taken of a patch of *Ranunculus* illustrating the presence of the bed and bottom profile.

Photographs and videos were then taken at a spacing of 0.1m for smaller patches or 0.2m for larger patches, measured by placing a survey leveling staff on the bed next to the patch. At each location, another survey leveling staff was placed at the far extent of the image next to the patch of interest to allow the recording of the height of the bottom profile above the bed. A thirty second video was then taken to allow the determination of the average height above the bed. This was particularly important near the tips of *Ranunculus* patches, where plant movement meant that the height of the tip varied greatly over the sampling period.

A total of two patches of *Berula*, one of *Callitriche*, five of near-bed *Ranunculus* and five of full-depth *Ranunculus* were photographed and videoed. More emphasis was placed on the sampling of the two *Ranunculus* cases following initial tests which showed that a bottom profile was not relevant for *Berula* and

Callitriche as these species appeared to be rooted to the bed along their entire length. The limited number of samples reflects the difficulty of locating a suitable plant patch to survey. Surveyed plant patches needed to be entirely distinct from neighbouring patches with at least a one meter gap between them. This was necessary to situate the camera far enough away from the patch being surveyed to include both the bed and the bottom profile of the plant in the picture. The result was that bottom profiles were surveyed independently of the top profiles. Although this meant that the shape of any one particular plant patch was not determined, the average of a number of top and bottom profiles can be used to generate a representative patch shape for each species. This can then be applied throughout the modeled reach.

Images from each plant patch were manually stitched together. As the spacing between photographs was minimal, there was considerable overlap between the images. However, due to a lack of control points in the images it was not possible to use commercial photographic software to perform the stitching process. Hence, stitching was performed manually by matching stems, leaves, filaments or gravel in each photograph. An example of the result of this stitching for each species is shown in Figure 6.1.7 with the bottom profile highlighted.

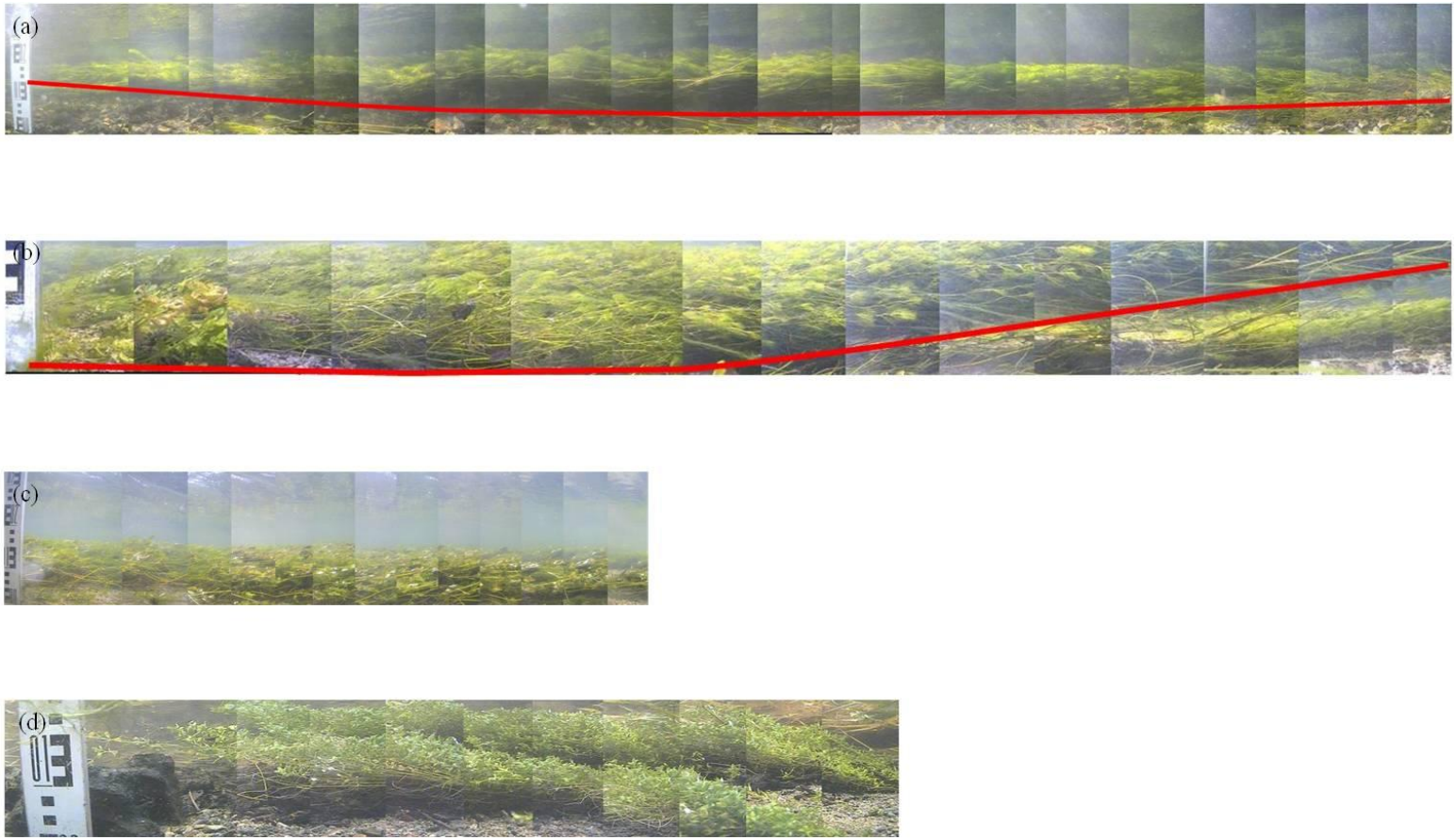

Figure 6.1.7: Example underwater photographs of (a) near-bed *Ranunculus*; (b) full-depth *Ranunculus*; (c) *Berula* and (d) *Callitriche*. For both the near-bed and full-depth *Ranunculus* the bottom profile is highlighted in red working from right-left and left-right respectively.

The survey levelling staff placed at the edge of each image was used to determine the measurement of the height of the lower boundary of the plant above the bed. The average height was estimated from the thirty second video taken at each spacing along the bed. The raw data from these observations for near-bed *Ranunculus* and full-depth *Ranunculus* are shown in Figure 6.1.8.

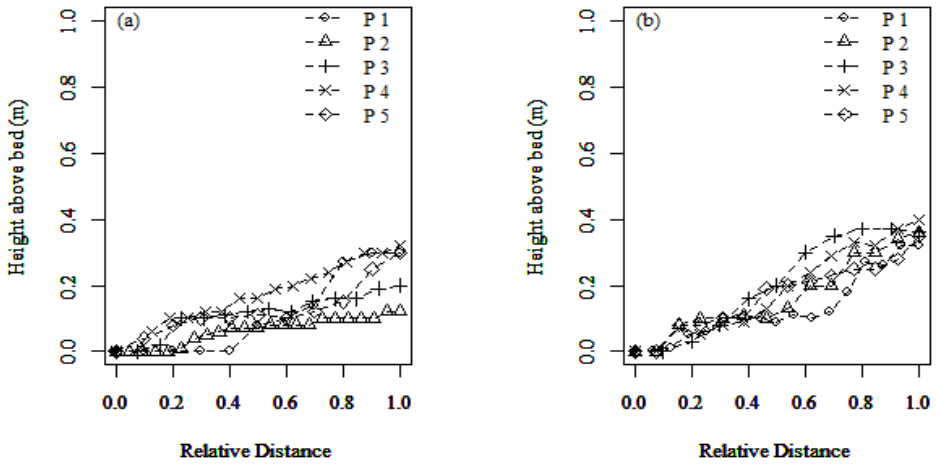

Figure 6.1.8: Observed bottom profiles for: (a) near-bed *Ranunculus*; (b) full-depth *Ranunculus*.

It is clear from Figure 6.1.8 that the lower boundary of full-depth *Ranunculus* extends, on average, to a greater height above the bed. Also, the angle of the rise is much steeper than that of the near-bed case, matching the characteristic of the top profiles in Figure 6.1.4. This suggests that, overall, the plant is more streamlined in the depth dimension during November when flow velocities are higher and water depth is reduced than when compared to its peak extent when flowering during May.

6.2. Vegetation parameters at the sub-patch scale

The previous section described the overall patch shape, incorporating its reconfiguration to the actual flow conditions as simulated in the model. This section

considers the more detailed vegetation variables needed for the model. In order to inform the DANS model equations introduced in Section 3.1, values were required relating to porosity (ϕ), i.e. the ratio of the volume of plant to the volume of water within each model cell. In addition to this, an appropriate area term is required in the drag force equation. In this study, the drag force which relates to the vegetation elements is parameterised as in the atmospheric literature (Wilson and Shaw, 1977; Raupach and Shaw, 1982; Finnigan, 1985), and so specification of the total surface area of the vegetation elements per unit volume A_{sv} was also required. In this study, both the plant volume and surface area per unit volume were determined for each species from laboratory measurements of field samples.

6.2.1. Sampling strategy

Vegetation samples were collected over three years between November 2010 and October 2013. Care was taken to collect samples from a range of locations within the model reach to ensure any spatial variation in plant structure was captured. Samples collected during 2010 and 2011 did not have measurements of surface area performed on them. The acquisition of a LICOR leaf area meter allowed measurement of leaf surface area to be performed on the samples collected during May 2013 and October 2013. The May 2013 sampling campaign consisted of five samples for each of the species types: full-depth *Ranunculus*; *Berula;* and *Callitriche.* A further ten samples were collected for the species: full-depth *Ranunculus*; *Berula;* and *Callitriche* along with samples for *Rorippa nasturtium aquaticum*, in October 2013 to detect any seasonal variation which may have occurred. Parameters for plant volume and surface area of mixed vegetation areas were taken as an average of the species present in each month.

Samples were collected as follows. The trailing edge of the plant was trimmed so a measurable straight line was produced at that point. The plant was then trimmed so that a width (w) of 0.1m on the surface could be collected. Before the plant was cut free of the main stand, the depth of water (d) which it occupied was measured and recorded. This allowed the calculation of the volume of water which the plant occupied. The sample was then cut free from the stand at a distance (l) from the initial trim line. Care was taken to collect the entire sample within the measured volume to allow the accurate assessment of the parameters of volume and surface area. Samples were stored immediately upon collection in non-permeable bags before returning to the lab. Processing of the samples was undertaken within 24 hours of collection to ensure the turgidity of the samples remained representative whilst measurements were undertaken. Processing often took place the day following collection. Due to this, samples were refrigerated overnight to prevent deterioration.

6.2.2. Vegetation porosity

The volumetric porosity of vegetation samples was determined by displacement, undertaken using a method similar to that of Grant and Nickling (1998). First, the total volume of water from which the sample was taken (V_t) was determined ($d.l.w$) using measurements taken whilst the sample was in situ in the field. An example of a sample of each species is shown in Figure 6.2.1.

Figure 6.2.1: Example of each of the main species (a) near-bed *Ranunculus*, (b) full-depth *Ranunculus*, (c) *Callitriche*, (d) *Berula*.

Secondly, the volume of each plant sample was determined. Each sample was placed in a 1000ml measuring cylinder which was subsequently filled with water at 20ºC from a second cylinder of the same volume. Once the 1000ml mark was reached in the cylinder containing the sample, the remaining volume of water in the second cylinder was noted. This was taken to represent the volume of plant material V_v. The fluid only volume V_f is given by 1- V_v. Care was taken in both cases to record the lowest point of the meniscus produced by the surface tension of water. This was repeated for all samples for each species. Subsequently, the value of porosity for each species could be determined using:

$$\phi = \frac{V_f}{V_t} \qquad 6.2.1$$

where ϕ is porosity, V_f is the fluid only volume in m^3 and V_t is the total volume of the averaging domain in m^3.

Mean porosities for each species, along with their standard deviation (σ), are shown in Table 6.2.1 for samples taken in May 2013 and October 2013. Values from this period were selected in preference to those collected prior to May 2013 due to the ability to pair these measurements with leaf surface area following the acquisition of a leaf area meter. As mentioned previously, the values for mixed vegetation are taken as an average all species present for each month.

Table 6.2.1: Mean porosities for each species ± the standard deviation σ

Species	Mean Porosity (± σ) May 2013	Mean Porosity (± σ) October 2013
Ranunculus (near-bed)	0.976 ± 0.006	0.979 ± 0.005
Ranunculus (full-depth)	0.988 ± 0.002	N/A
Berula.	0.974 ± 0.001	0.982 ± 0.003
Callitriche.	0.989 ± 0.005	0.988 ± 0.004
Rorippa.	N/A	0.986 ± 0.006
Mixed	0.980	0.983

The values of porosity between the two sampling periods are broadly similar, with only a slight change in the porosity of *Berula* of 0.008 evident. The value of porosity for *Ranunculus* is similar to that quoted by Naden *et al.* (2004) as 0.981. Porosity values for other species are unavailable in the literature, however, they are of similar magnitude to those surveyed on the River Blackwater by Rameshwaran and Naden (2012) for the species *Potomageton Natans* (0.948), *Sparganium emersum* (0.921) and *Sparganium erectum* (0.905) in May 2001.

6.2.3. Vegetation surface area

The method selected for this study to measure vegetation surface area was a desktop leaf area meter (Figure 6.2.2) because of its ability to measure leaves of less than $1cm^2$ (LI-COR, 2004), including the narrow filaments of *Ranunculus*. Each sample comprising of plant stems and leaves was spread out into individual leaves or filaments dependent on the species, and passed through the leaf area meter in small subsamples in order to gain an accurate measurement. Between subsamples the leaf area meter was dried and cleaned to avoid any carry over from subsample to subsample. The resulting measurement for the plant as a whole was recorded to the nearest square centimetre. The value recorded represents a one sided leaf area. To represent the total vegetation surface area within the model, this was doubled to represent both sides of the leaf. For *Rorippa*, only the leaves were passed through the leaf area meter due to the thickness of the main stems for this species. The surface area of the stems, assumed to be cylindrical, was determined using the calculation $2\pi rh$ (where r is the radius of the stem and h is the length of the stem) and added to the surface area of the leaves. The total plant surface area determined using the leaf area meter and the estimate of stem area was then converted to a surface area per unit volume using the known volumes of water from which the samples were taken. Values of surface area per unit volume for each species, along with their standard deviation, are shown in Table 6.2.2.

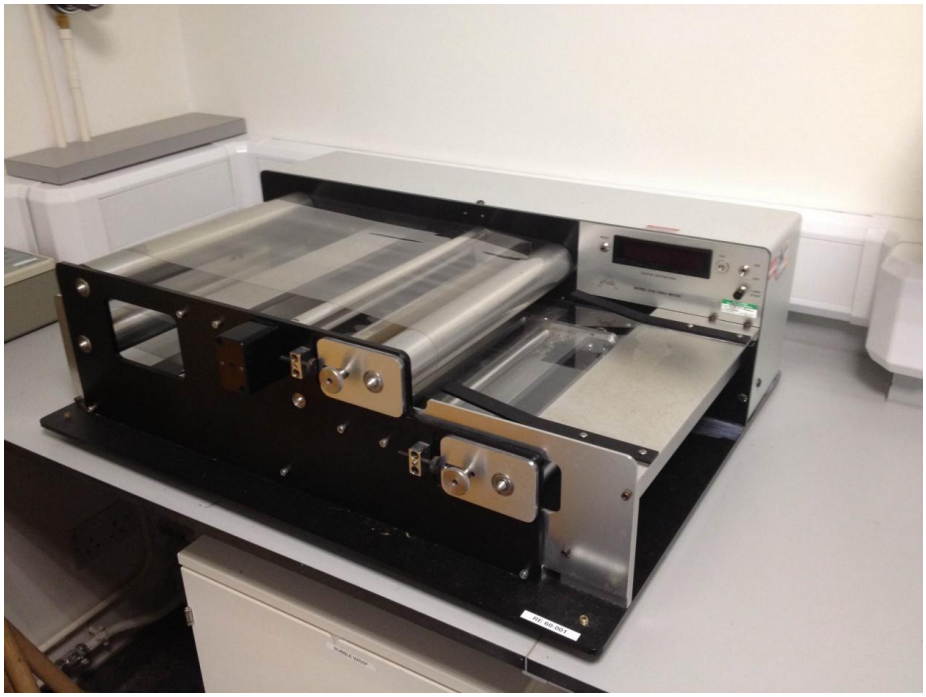

Figure 6.2.2: LI-COR leaf area meter based in the laboratory at CEH Wallingford.

Table 6.2.2: Values of mean plant surface area per unit volume by species

Species	A_{sv} (m^2m^{-3}) ± σ May 2013	A_{sv} (m^2m^{-3}) ± σ October 2013
Ranunculus (Near-bed)	39.1 ± 14.4	25.9 ± 10.7
Ranunculus (Full-depth)	28.1 ± 5.2	N/A
Berula	37.4 ± 5.5	24.3 ± 7.0
Callitriche	20.2 ± 11.0	14.2 ± 14.2
Rorippa	N/A	9.6 ± 9.6
Mixed	32.2	21.5

Values are of a similar order of magnitude to those found in Naden *et al*. (2004) for *Ranunculus* ($24.8m^2m^{-3}$) and Rameshwaran and Naden (2012) for *Potomageton Natans* ($24.4m^2m^{-3}$), *Sparganium emersum* ($77.7m^2m^{-3}$) and *Sparganium erectum* ($27.0m^2m^{-3}$). Not surprisingly, the values of plant surface area per unit volume

exhibit a high standard deviation. This variation is particularly high for the near-bed *Ranunculus*. This results from differences in the number of leaves and number of stems in the sample and the diameters of those stems. Where a sample has a higher number of stems, the leaf surface area is often markedly higher. In the case of *Ranunculus*, the stem diameter also has a role in the resulting measurement of leaf surface area per unit volume. Figure 6.2.3 highlights this where two samples of near-bed *Ranunculus* have clearly different average stem diameters resulting in a very different surface area per unit volume of $37.7 m^2 m^{-3}$ in Figure 6.2.3a and $22.0 m^2 m^{-3}$ in Figure 6.2.3b.

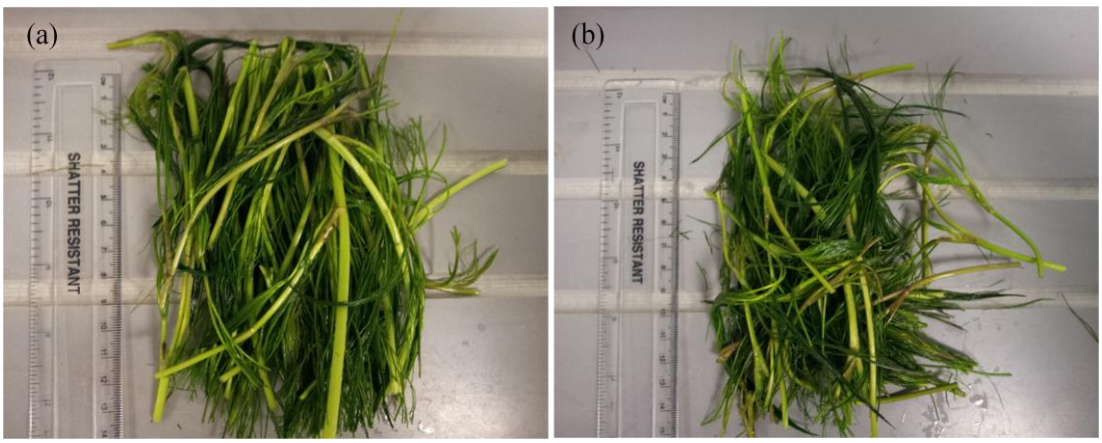

Figure 6.2.3: Photographs of samples (a) near-bed *Ranunculus* with larger stem diameter and high stem to filament ratio (b) near-bed *Ranunculus* with low stem to filament ratio and smaller stem diameter.

6.3. Conclusions

The datasets required in order to represent aquatic vegetation in a 3D CFD are the vegetation patch shape in three dimensions and information about plant volume and surface area per unit volume of water. A simple survey method was applied to gather data relating to the planform coverage of vegetation, using the integrated surveying system. A method was devised for surveying the third dimension of the vegetation

structure using an underwater camera. Limited data were collected for the top and bottom profiles for two cases of *Ranunculus*. Values of vegetation volume and surface area were measured on samples taken in the field. Parameters of porosity and surface area per unit water volume were determined using measurement by displacement and using a desktop leaf area meter respectively. These measurements represent a considerable addition to the literature where relatively few similar measurements of porosity and surface area are available. Resulting values are of similar magnitude to those found in the literature for other aquatic macrophyte species.

Chapter 7. Building the 3D river model

The model equations introduced in Section 3.1 require a domain within which they can be solved. Chapter 4 and Chapter 5 provided details of the collection and processing of data relating to the physical boundaries of the model (i.e. channel topography and water surface) necessary to construct the solution domain. In this chapter construction of the model mesh is described. Five meshes were required; one for the minimum vegetation case in February 2010, two for November 2010 (before and after the vegetation cut) and two for May 2011 (before and after the vegetation cut).

At the gravel bed, defined as the first five layers of the model mesh (Section 4.4.4) a value for the bulk drag coefficient of the gravel $C_{dg}S_{fg}$ is required. Calibration of $C_{dg}S_{fg}$ was carried out for the minimum vegetation case, defined in Section 3.5 (Section 7.2). Following this calibration, the numerical accuracy of the model, in terms of providing a mesh-independent solution, was explored using the method given by Roache (1994).

Once the bulk drag coefficient for the gravel was calibrated, the vegetation was applied to the mesh for the November 2010 (before and after the vegetation cut) and May 2011 (before and after the vegetation cut) cases. Data collected in order to represent vegetation within the model were described in Chapter 6. In this chapter, a representative patch morphology is developed for each species (near-bed *Ranunculus*, full-depth *Ranunculus*, *Berula*, *Callitriche*, *Rorippa* and for a Mixed area of vegetation) using the patch planform and vertical structure data, and measured vegetation parameters given in Sections 6.1 and 6.2, respectively. The bulk vegetation drag coefficient $C_{dv}S_{fv}$ was then calibrated.

7.1.Mesh generation

Boundary-fitted coordinates were used in the Cartesian frame to generate the model mesh, based upon the assumption that the water surface is planar in the initial simulation. In order to generate the mesh for the model, two datasets were needed: the planar water surface slope for all cases (Section 5.3) and the channel topography (Section 4.1).

7.1.1. Fixed lid generation

The fixed lid was provided by the reach free surface measurements taken from the staff gauge boards (Chapter 5 section 5.3). The staff gauge boards were deemed to provide the most reliable water level measurements due to their fixed location, determined using the integrated surveying equipment, and even spacing along the modelled reach. The fixed lid was produced by fitting a linear regression through the four staff gauge board measurements which lay within the modelled reach. Within the model, the water depth is used as the outlet boundary condition. Hence, the intercept of the linear regression was set as the height of the staff gauge board adjacent to the model outlet. The five fitted regressions, their equations and R^2 values are shown in Figure 7.1.1. The fixed lids that were produced have slopes ranging between 1/379 and 1/466 and generally show a decrease in slope following a vegetation cut.

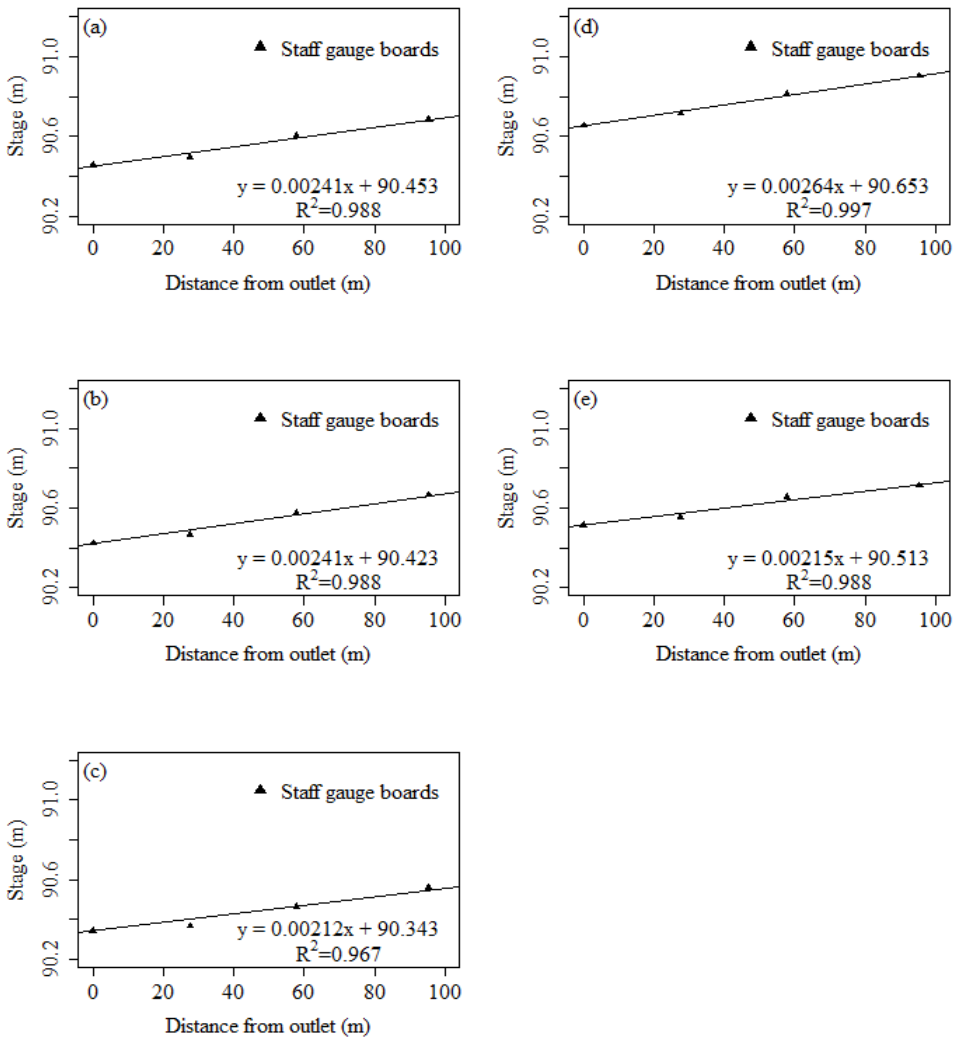

Figure 7.1.1: Regression lines fitted to staff gauge board readings for: (a) February 2010; (b) November 2010 before-cut; (c) November 2010 after-cut; (d) May 2011 before-cut; and (e) May 2011 after-cut.

7.1.2. Refinement of the topographic domain

The intersection between the fixed lid and the topography provides the model domain. However, in order to ensure model convergence, a number of refinements were required. First, close to the stone bridge at which the ADCP measurements took place there is a sharp rise in the channel bed where the overall depth changes from approximately 1m to a depth of 30cm. This leads to complex flow structures in this area. Hence, to avoid model convergence issues and problems in mesh generation,

particularly when the upstream water depth is low, the start of the modelled domain was taken 30m downstream of the upper extent of the topography dataset. The resultant modelled reach totalled 105m in length.

Non-orthogonal model cells are likely to result in model convergence issues. Hence, to produce orthogonal cells at the channel margins, vertical banks were required. To achieve this, the channel topography was cut a further 0.10m below the fixed lid. The resulting bank extents are shown in Figure 7.1.2. For the February 2010, November 2010 before-cut, and May 2011 before and after-cut cases, the mesh edge location generated is similar. The water depth at the outlet for these four cases ranges between 0.32m and 0.52m, with the lowest water level being the November 2010 before-cut case. Hence, the November 2010 before-cut case was used as the mesh upon which these four cases was based (i.e. the base model mesh). The use of a base model mesh allowed the use of a consistent model domain with only the height of the fixed lid varying the overall domain size. For the November 2010 after-cut case, the resulting channel area is greatly reduced due to the low water depth (a further 0.18m on average below the other cases) for this case. This is reflected in the resulting bank extent (Figure 7.1.2). Hence, a separate mesh was generated for the November 2010 after-cut case. The mesh extent differed from the November 2010 before cut case, with the channel becoming narrower due to the reduced water level.

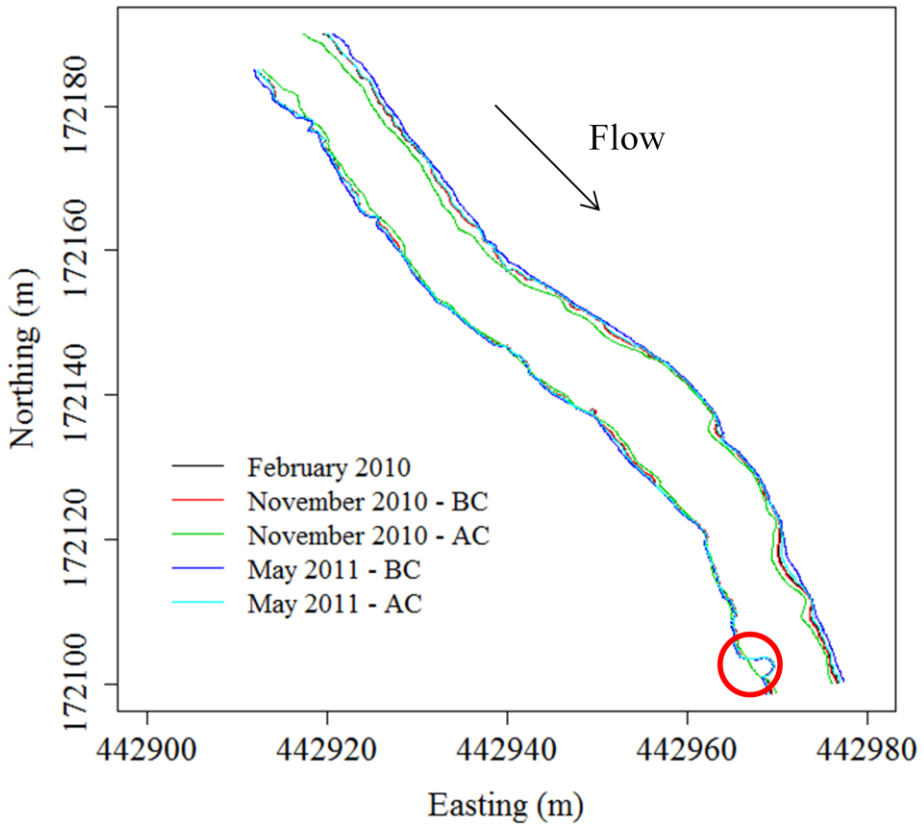

Figure 7.1.2: Mesh edges produced by intersecting water surfaces with the channel topography. Red circle highlights a constriction close to the model outlet.

Secondly, an area was identified near the model outlet (grid reference 442970, 172100) where the channel had become highly constricted (Figure 7.1.3a). This constriction had been generated in the topography in the absence of any topographic data, the collection of which had been precluded by the presence of a tree overhanging the channel. Topography was re-generated for this region by moving the bank line back to be in line with survey points before and after the constriction occurred. Topography values were then linearly interpolated in the cross stream and downstream directions. The resulting topography following removal of the constriction is shown in Figure 7.1.3b.

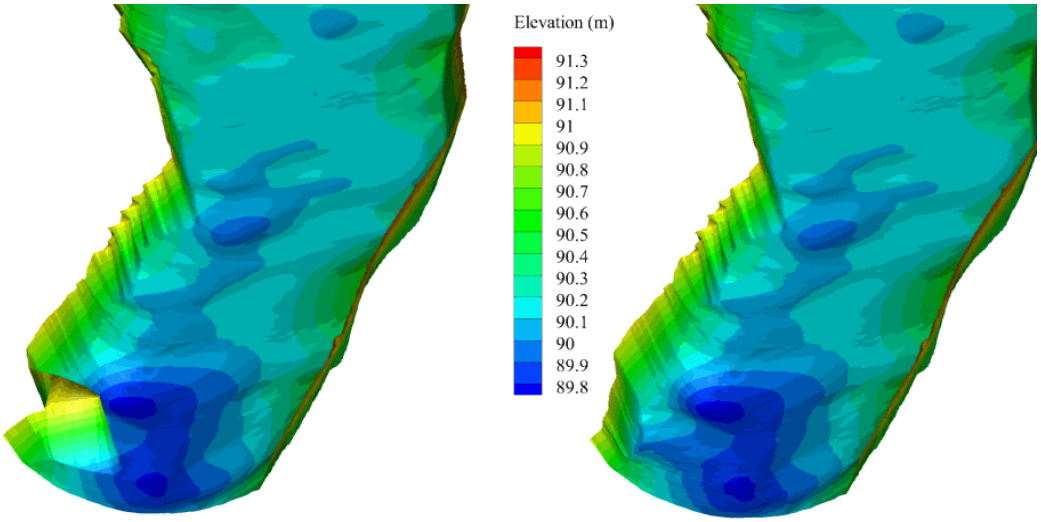

Figure 7.1.3: (a) Constriction in the channel close to the model outlet; (b) Channel topography following removal of constriction.

Following the first two steps, the surveyed data were rotated so that the downstream flow direction was the Cartesian x-axis as required by the model software. Once rotated a third step was undertaken to smooth the bank extents. This smoothing was necessary to remove the jagged bank lines which were produced as an artefact of the intersection with the water surface, rather than being representative of the banks of the River Lambourn. The smoothing was undertaken using the LOESS method with a span value of $\alpha = 0.5$. The results of the rotation and smoothing are shown in Figure 7.1.4. Downstream units are given as distance in metres from the ADCP flow survey cross section.

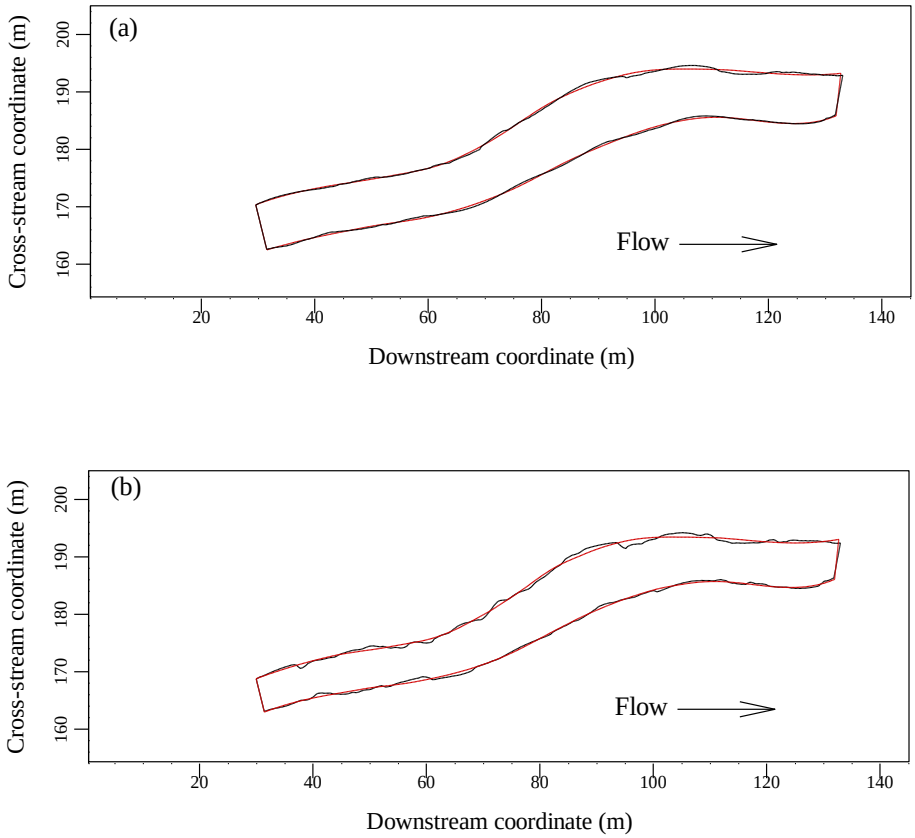

Figure 7.1.4: (a) Meshes based on November 2010 before-cut case. (b) Mesh based on November 2010 after-cut case. Black line represents mesh edge before smoothing and red after smoothing.

Figure 7.1.4 shows that although the bank edges have been smoothed, the general shape of the channel has been maintained. Following the smoothing, the location of the mesh edges was compared with the location of the free surface measurements (Figure 7.1.5). The location of the free surface measurements compares well with the mesh edges generated for the February 2010, November 2010 before-cut case and May 2011 before and after-cut cases (Mesh edge 1). For the November 2010 after-cut case (Mesh edge 2), the free surface measurements do not fall within the mesh edge at the true left bank between 35m and 65 metres. The mesh used effectively narrows the channel too much at this location. This resulted from the water depth, which was particularly shallow for this case, being made shallower by the 0.10m cut

required to form the channel banks. The overall loss of channel area due to this, however, is minimal (approximately 0.3m^2).

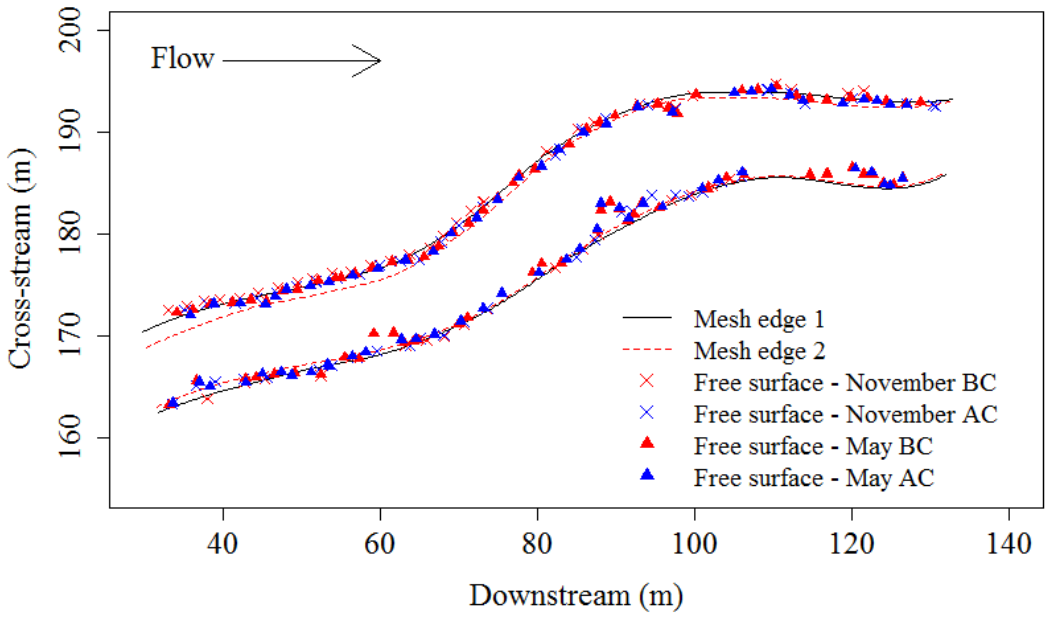

Figure 7.1.5: Generated mesh edges compared to free surface measurement locations.

7.1.3. Mesh construction

A model mesh of dimensions 468 x 60 x 20 cells in the downstream, cross-stream and vertical directions, respectively, was selected for the flow domain. The dimensions chosen were at the finest resolution possible whilst maintaining a reasonable convergence time (i.e. less than 48 hours). The first five layers of the mesh (termed the near-bed zone) were constructed using a fixed height of 0.01m (Section 4.4) in order to represent the gravel surface. Above this height, the mesh dimension was determined by the distance between the top of the near-bed zone and the planar water surface determined in Section 7.1.1. The typical average cell size

above the gravel bed is 0.22m x 0.14m x 0.02m. An example of the cross sectional and plan view mesh generated for the February 2010 case is shown in Figure 7.1.6.

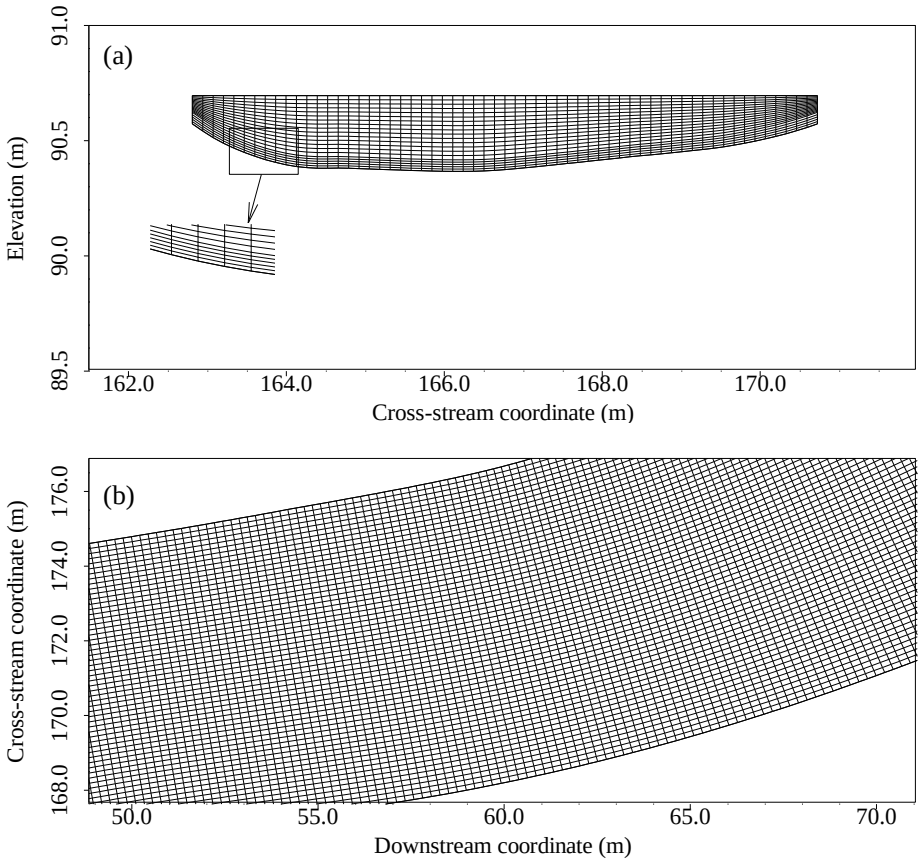

Figure 7.1.6: (a) Cross-sectional view. (b) Top plan view of modelled reach between 50 and 70m.

7.2. Calibration of the bulk gravel drag coefficient

To approximate the drag force which relates to the gravel bed (Section 3.1.2), the bulk drag coefficient $C_{dg}S_{fg}$ was calibrated for the February 2010 minimum vegetation case. The spatially-averaged gravel bed parameters processed in Section 4.4 were specified along with appropriate boundary conditions (Section 3.2.1). The inlet flow was set using data described in Section 5.2.

The steps of the calibration procedure were as follows. The initial value for $C_{dg}S_{fg}$ was estimated at 0.5. Then, the model was run to convergence and the difference between the pressure at the fixed lid and atmospheric pressure at the true left bank was calculated using equation 3.2.5. This difference was added to the height of the fixed lid to determine the model energy slope. The true left bank was selected as it was on this side that the staff gauge boards were installed. If the model energy slope was lower than that of the field energy slope, the bulk drag coefficient was increased. If the model energy slope was higher, the bulk drag coefficient was decreased. The model was then re-run and the procedure repeated until the difference between the modelled and measured energy slopes was $\leq$0.0001. Following calibration, $C_{dg}S_{fg}$ for the gravel bed on the River Lambourn was determined to be 0.45.

The free surface treatment of Rameshwaran and Naden (2004) was then applied and the mesh re-gridded accordingly (see Section 3.2.1). Re-gridding is necessary because a difference between the pressure on the fixed lid and the atmospheric pressure represents a mis-specification of the water surface height. Where the pressure is greater than atmospheric, this represents super-elevation of the water surface. Where the pressure is less than atmospheric, this represents a depression in the water surface.

The modelled free surface for the true left bank is compared to staff gauge board measurements in Figure 7.2.1. With a calibrated bulk drag coefficient of 0.45 the energy loss represented by the measured free surface gradient is captured well by the simulation.

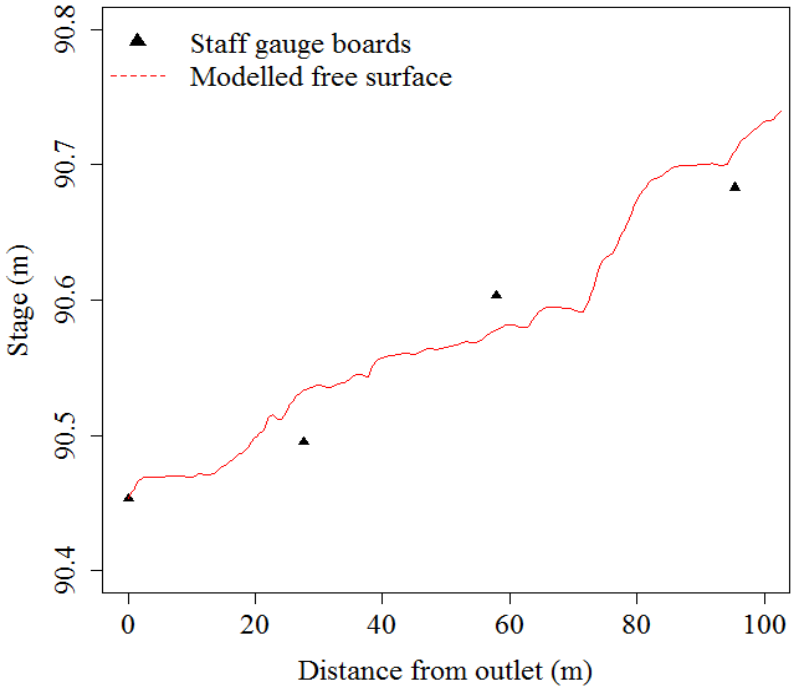

Figure 7.2.1: Comparison of modelled free surface after adjustment to staff gauge board measurements.

7.2.1. Discussion

To ensure the calibrated value of $C_{dg}S_{fg}$ was sensible, an analysis of drag values reported in the literature was undertaken. The results are shown in Table 7.2.1., and are grouped as: those calculated from laboratory results for single particles; those calculated from laboratory results for groups of particles; and those determined using modelling approaches both in the laboratory and in the field. The definition of the projected area used to calculate the drag coefficient in each case is given, as this has an effect on the value reported. Where results are given for a single particle, C_{dg} is quoted as there is no sheltering effect (S_{fg}) due to neighbouring particles. For groups of particles, the value quoted is $C_{dg}S_{fg}$.

Table 7.2.1: Values of drag coefficients for gravel reported in the literature for (a) laboratory results for single particles; (b) laboratory results for groups of particles; (c) modelling approaches both in the laboratory and in the field.

(a)

Reference	Approach	Drag parameterisation	C_{dg}
Schmeeckle (1998) Single particle.	Determined by measurement of drag and lift forces on a natural gravel particle using a laser Doppler velocimeter	$F_D = \frac{\rho}{2} C_D A U^2$ A = full projected area of the test particle.	0.9
Papanicolaou *et al*. (2002) Single particle.	Based on Wiberg and Smith (1987). For fully developed flow C_d is greater than or equal to 0.2. Used to determine the drag exerted on a sphere fully exposed to flow.	$F_d = \frac{1}{2} C_D \frac{\pi}{4} d^2 \rho U^2$ d = diameter of spherical particle	0.2

(b)

Reference	Approach	Drag parameterisation	$C_{dg}S_{fg}$
Roberson and Chen (1970) Array of particles.	Particles resting on a smooth bed in turbulent flow	$\mathrm{F_D} = \frac{1}{2} \mathrm{C_D A_p U^2}$ A_p= particle cross sectional area	0.65-0.70 (spheres) 1.1-1.2(cubes).
Brayshaw *et al*. (1983) Array of particles.	C_d determined for two hemispheres placed at various distances between each. Hemisphere of height 1.3 times the diameter of the particle.	$\mathrm{F_D} = \frac{1}{2} \mathrm{C_D A_p U^2}$ A_p= particle cross sectional area	0-0.35
Taylor *et al*. (1985) Array of particles.	Discrete element model developed for flow over rough surfaces. Model calibrated using data from Schlichting (1936).	$F_D = \rho \frac{C_D}{2} U^2 H$ H = particle height	0.6

Reference	Approach	Drag parameterisation	$C_{dg}S_{fg}$
Wiberg and Smith (1987) Array of particles.	Drag coefficient here is determined from the experimental relationship for spheres as a function of the particle Reynolds number.	$F_D = \frac{1}{2} C_D A_p U^2$ A_p= particle cross sectional area	0.5-0.15 (dependent on Reynolds number).
Apperley and Raudkivi (1989) Array of particles.	Measurements of drag on a sphere above a bed of similar spheres.	$F_D = \frac{1}{2} C_D A_p U^2$ A_p= particle cross sectional area	0.68
Thompson *et al*. (2004) Array of particles.	Drag coefficient determined using flow deceleration over a roughened flat bed in an annular flume. Gravel patches of one grain in thickness.	$\mathrm{F_D} = \mathrm{AC_D}\rho\overline{\mathrm{u}}^2$ A= area of interaction.	3x10-3
Schmeeckle *et al*. (2007) Array of particles.	Sphere, cube and natural particles respectively. Smooth bed	$F_D = \frac{\rho}{2} C_D A U^2$ A = full projected area of the test particle.	0.76, 1.36 and 0.91.

(c)

Reference	Approach	Drag parameterisation	$C_{dg}S_{fg}$
Wiberg and Smith (1991) Array of particles.	Model compared to measured stream profiles. C_d determined by relationship to particle Reynolds number for spheres.	$F_D = \frac{\rho}{2} (C_D)\langle u^2 \rangle (A_D)$ A_D = grain cross sectional area perpendicular to flow.	0.45
Nicholas (2005) Gravel bed.	Estimated by adjusting C_d until the drop in water elevation between observed and measured was equal to 1/ñg times the drop in pressure. Performed for three rivers.	$F_D = -\frac{\rho}{2D_{50}} N C_D S_f u^2$ N = number of obstacles per unit length along random bed sample S_f = shading factor accounting for reduced drag due to wake effects.	1/1.25/6.5

Reference	Approach	Drag parameterisation	$C_{dg}S_{fg}$
Carney *et al*. (2006) Gravel bed.	Model compared to stream measurements.C_d assumed to be the same as Wiberg and Smith (1991)	$F_D = \frac{\rho}{2}(C_D)\langle u^2\rangle(A_D)$	0.45
Rameshwaran *et al*. (2011) Array of particles.	Model of flow over hemispheres representing Lawless and Robert (2001) experiment.	$F_D = -\frac{\rho}{2}C_D S_f A_p \lvert\langle\overline{u}\rangle\rvert\langle\overline{u}\rangle$ A_p = average frontal projected area of roughness element.	0.27-0.85
Rameshwaran and Naden (2012) Gravel bed.	Matching modelled free surface to surveyed free surface on the River Blackwater.	$F_D = -\frac{\rho}{2}C_D S_f A_p \lvert\langle\overline{u}\rangle\rvert\langle\overline{u}\rangle$	0.69
Zeng and Li (2013) Gravel bed.	Double averaging methodology modelling of flows over gravel-beds. Results compared to flume experiments by Lawless and Robert (2001) and Nikora et al (2001)	$F_D = \frac{\rho}{2}C_D C_s b_s N\langle\overline{u}\rangle^2$ C_s= shielding factor b_s= effective projected width of the roughness element N = number of roughness elements per 1m^2	0.23-0.87

From Table 7.2.1, it is clear that the value for the drag coefficient varies depending on whether it relates to a single particle or an array of particles, the grouping or spacing of particles, the definition of the representative area used to calculate drag, and the shape of the particle being considered. When considering a single particle (e.g. Schmeeckle, 1998; Papanicolaou *et al*., 2002) the drag coefficient can be seen to vary markedly depending on the reference area used to calculate it. Schmeeckle (1998) considers only the projected area whereas Papanicolaou *et al*. (2002) consider the full surface area of the particle with an associated reduction in the drag coefficient.

In reality, gravel particles exist in groups on river beds. The spacing of the particles involves consideration of the sheltering factor S_{fg} which often results in a reduction in the value of the drag coefficient (Nowell and Church, 1979). This occurs due to the effects of wake interaction between two or more particles. Brayshaw *et al*. (1983) explored this relationship for two particles resulting in a variation of C_{dg} between 0 and 0.35 dependent on the spacing. Other studies (e.g. Roberson and Chen, 1970; Taylor *et al*., 1985; Wiberg and Smith, 1987 and Schmeeckle *et al*., 2007) report values of C_{dg} ranging from 0.15-1.36 for groups of particles. The calibrated value of $C_{dg}S_{fg}$ in this study is of the same order of magnitude as those found for gravel-bed rivers in other modelling studies (e.g. Wiberg and Smith, 1981; Nicholas, 2005, Carney *et al*., 2006; Rameshwaran and Naden, 2012) and is within the measured range for groups of particles identified above.

7.3. Grid convergence

Following the construction of the mesh and the appropriate calibration of the bulk gravel drag coefficient, the effect of the choice of mesh resolution (468 x 60 x 20) on numerical results was assessed using the Grid Convergence Index (GCI) method outlined by Roache (1994). The GCI is an index of the uncertainty associated with the solution at a particular grid resolution based on the comparison with the solution at another resolution (Lane *et al*., 2005). The method is an ASME (1993) accepted method for reporting the effects of grid refinement and hence numerical accuracy. Calculation of the Grid Convergence Index is given by:

$$\mathrm{GCI} = 3|\varepsilon|/(r^p - 1)$$

7.3.1

where ε is the estimated fractional error (i.e. the ratio of mean absolute error to the mean) for the fine grid solution and r^p is the grid refinement ratio (i.e. if the grid dimensions are halved, $r^p = 2$).

Three meshes were used to assess the effect of grid refinement: M1, M2 and M3. M3 is the simulation which was undertaken in the previous section and has the finest practical mesh. M1 and M2 represent coarser meshes, the dimensions of which are given in Table 7.3.1. Simulations using meshes M1 and M2 were run with the same value of $C_{dg}S_{fg}$ as M3.

Table 7.3.1: Summary of mesh dimensions

Mesh	Dimensions
M1	30 x 10 x 117
M2	45 x 15 x 234
M3	60 x 20 x 468

7.3.1.Results

Results for comparisons between the M1-M3 and M2-M3 meshes for the velocity components u_x, u_y and u_z and turbulent kinetic energy are shown in Figure 7.3.1. Comparisons are made based on the lower resolution mesh points with the higher resolution results linearly interpolated onto these points. Results for the M1-M3 comparison are highly scattered, with correlation values of 0.978, 0.987 and 0.919 for u_x, u_y and u_z respectively. Results for TKE are even more highly scattered with a correlation value of 0.784. The results for the M2-M3 comparison are much less scattered, with correlation values of 0.995, 0.997 and 0.959 for the velocity components u_x, u_y and u_z respectively. Results for TKE also improve with a correlation value of 0.949. The values for the slope and intercept of a linear

regression fitted for each variable also show that as the mesh is refined, the values of the slope and intercept tend towards 1 and zero respectively.

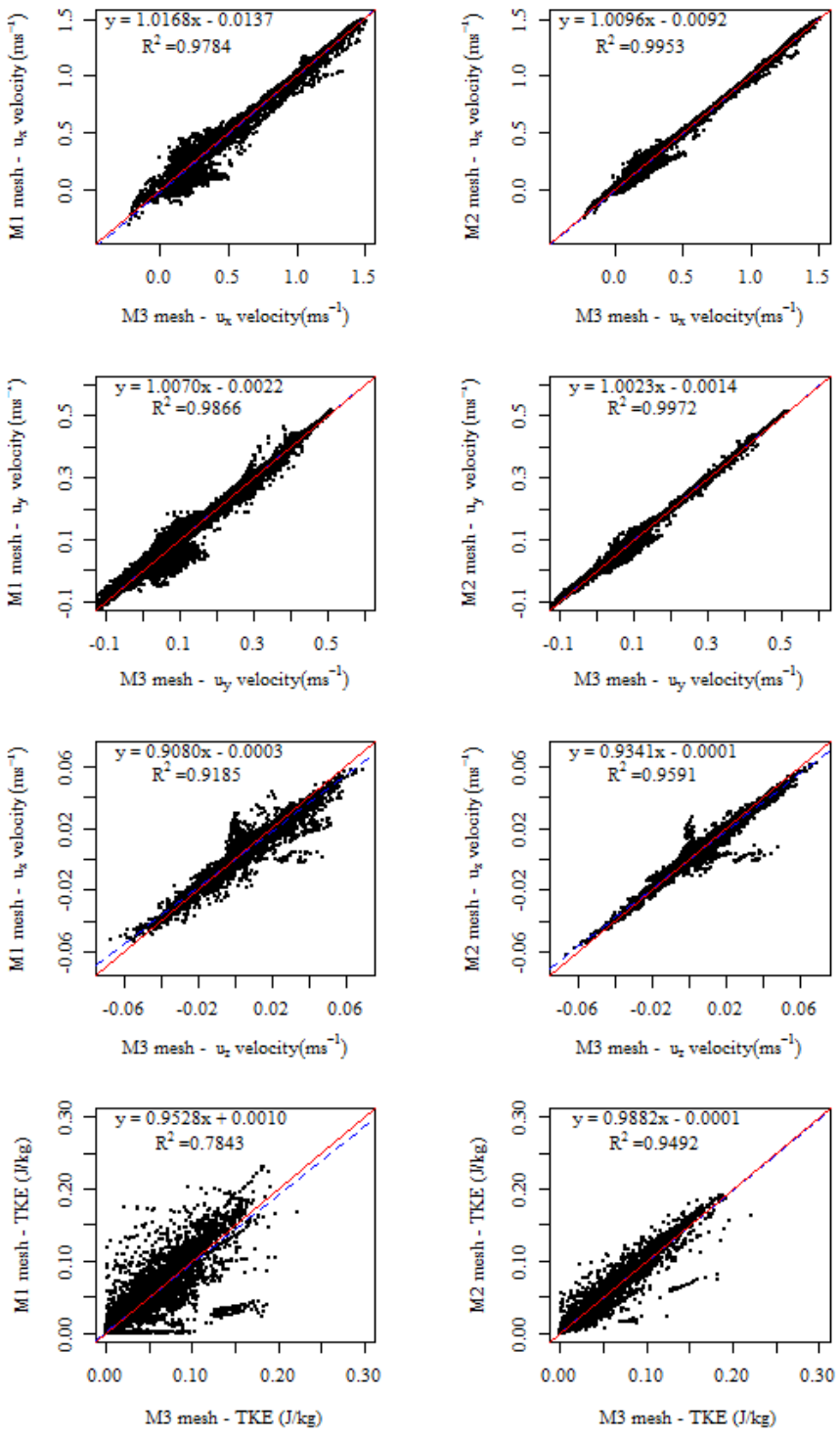

Figure 7.3.1: Comparison of the velocity components u_x, u_y and u_z and turbulent kinetic energy between meshes M1-M3 and M2-M3. A 1:1 relationship is shown in red along with the linear regression in blue.

Calculation of the Grid Convergence Index suggest that the predictions have converged towards a mesh independent solution (Table 7.3.2), with the median values of GCI for each flow variable decreasing with increasing mesh refinement.

Table 7.3.2: Median values of Grid Convergence Index

Meshes	u_x (%)	u_y (%)	u_z (%)	k (%)
M1-M3	0.89	0.80	7.32	5.32
M2-M3	0.75	0.58	6.05	4.63

7.3.2.Discussion

It was noted that, as in other studies (e.g. Ferguson *et al*., 2003; Hardy *et al*., 2003; Rameshwaran and Naden, 2004; Rameshwaran *et al*., 2013), that turbulent kinetic energy and the vertical velocity component u_z are most sensitive to mesh resolution. The high degree of scatter for TKE and u_z was an area of concern. Investigations into the regions of this error revealed that high percentage differences occurred in the first and last 10 slabs of the model where flow is not fully developed, the first profile at either bank where the water depth is low, and results within the porous bed layers. Once data from these areas are removed, the degree of scatter is much lower for all variables (Figure 7.3.2). Overall, the median values of GCI presented (Table 7.3.2) suggest that the model predictions are converging towards a grid-independent solution, with results from the M3 mesh relatively free of numerical error.

The previous sections have covered the construction of the mesh, calibrating the bulk drag coefficient for the gravel bed, and assessing the effect of grid refinement on numerical accuracy. The mesh that was developed has been shown to be numerically accurate and hence suitable for the model.

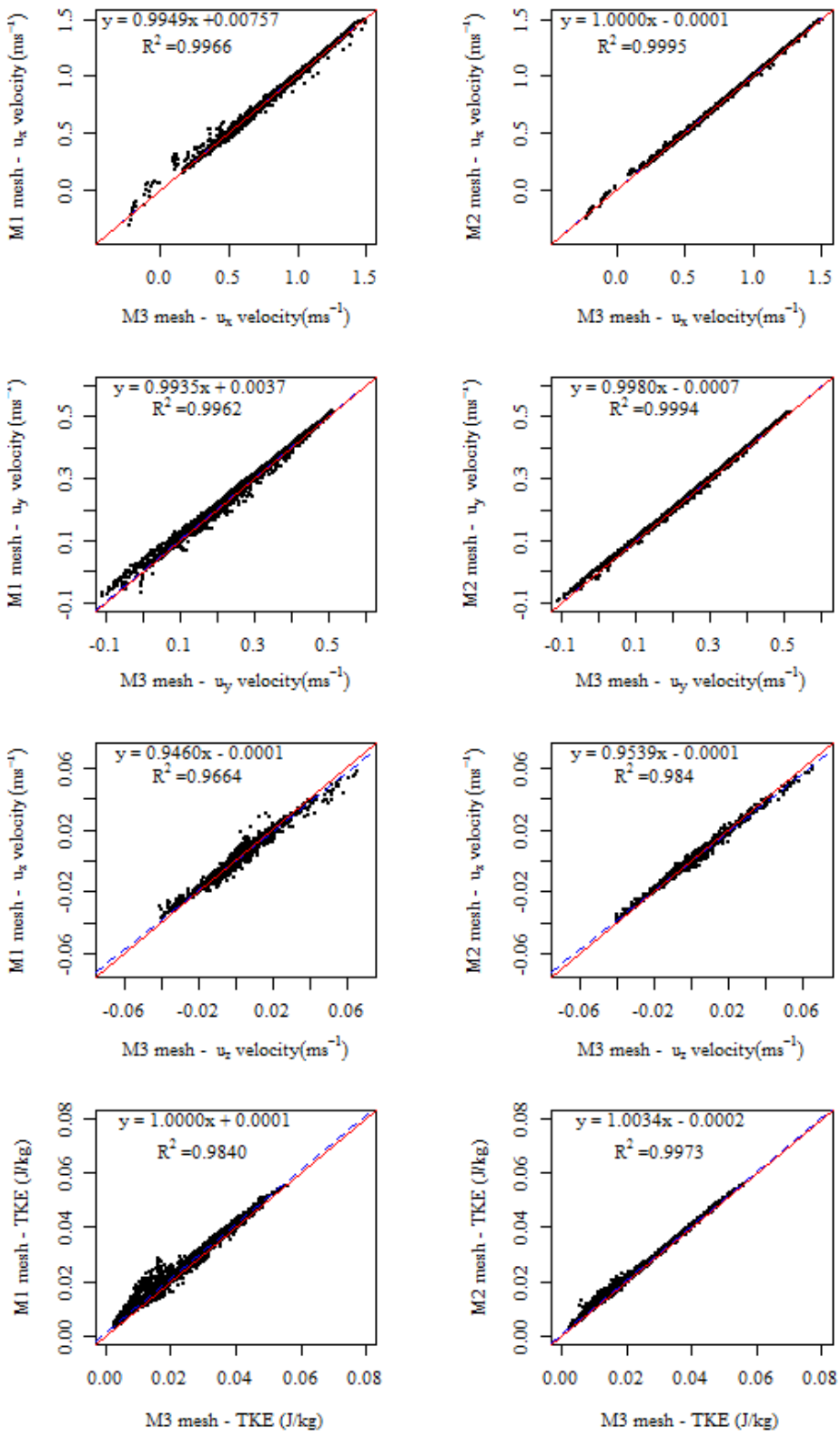

Figure 7.3.2: Comparison of (a) the velocity components u_x, u_y and u_z turbulent kinetic energy between meshes M1-M3 and M2-M3 following data screening. A 1:1 relationship is shown in red along with a linear regression shown in blue.

7.4. Determining the three-dimensional coverage of vegetation

To determine the three-dimensional coverage of aquatic vegetation, the planform patch polygons from Section 6.1.1 were overlain by the model mesh. The mesh was joined to the vegetation polygons using the Identity tool in ArcGIS. This was the first step in determining the proportion of each planform model cell that was occupied by vegetation.

The domain extent for the top layer of the model mesh, showing its relationship to the vegetation patch polygon datasets is shown in Figure 7.4.1; the highlighted stretch is shown in more detail in Figure 7.4.2. The second step was to determine which of the layers was occupied by the vegetation. In order to do this, a method to relate the plant vertical structure to the model mesh was devised by trialling a number of mathematical functions.

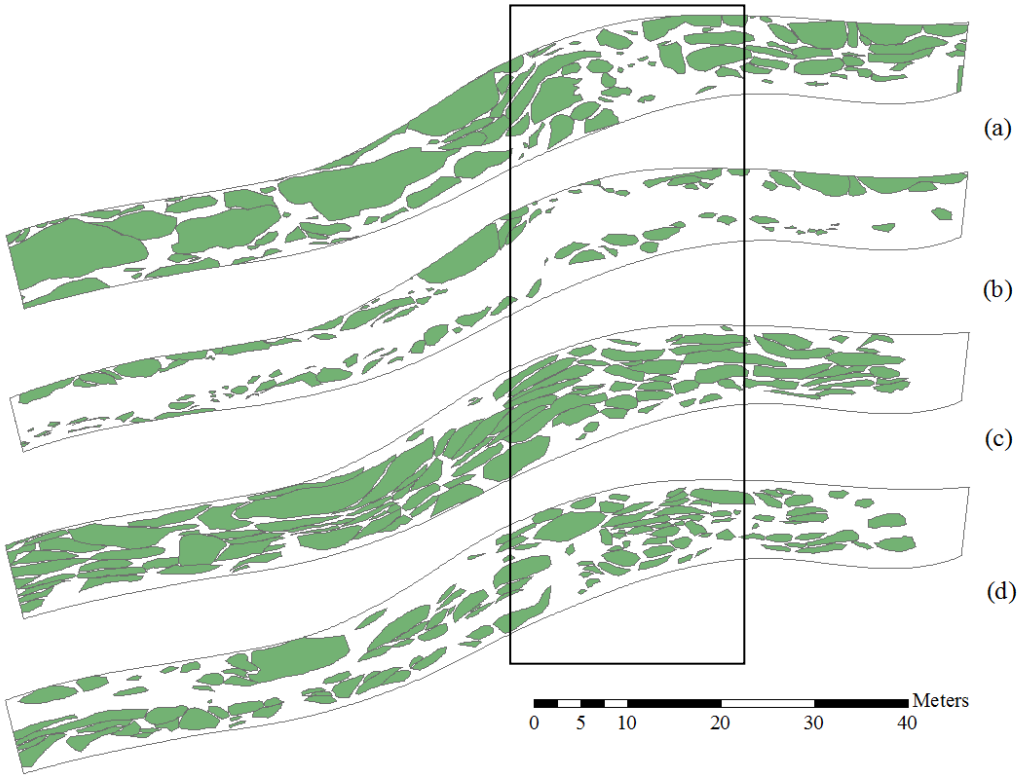

Figure 7.4.1: Vegetation patches overlain by the model mesh extent for (a) November 2010 before-cut; (b) November 2010 after-cut; (c) May 2011 before-cut; (d) May 2011 after-cut. Area highlighted is shown in detail in Figure 7.4.2.

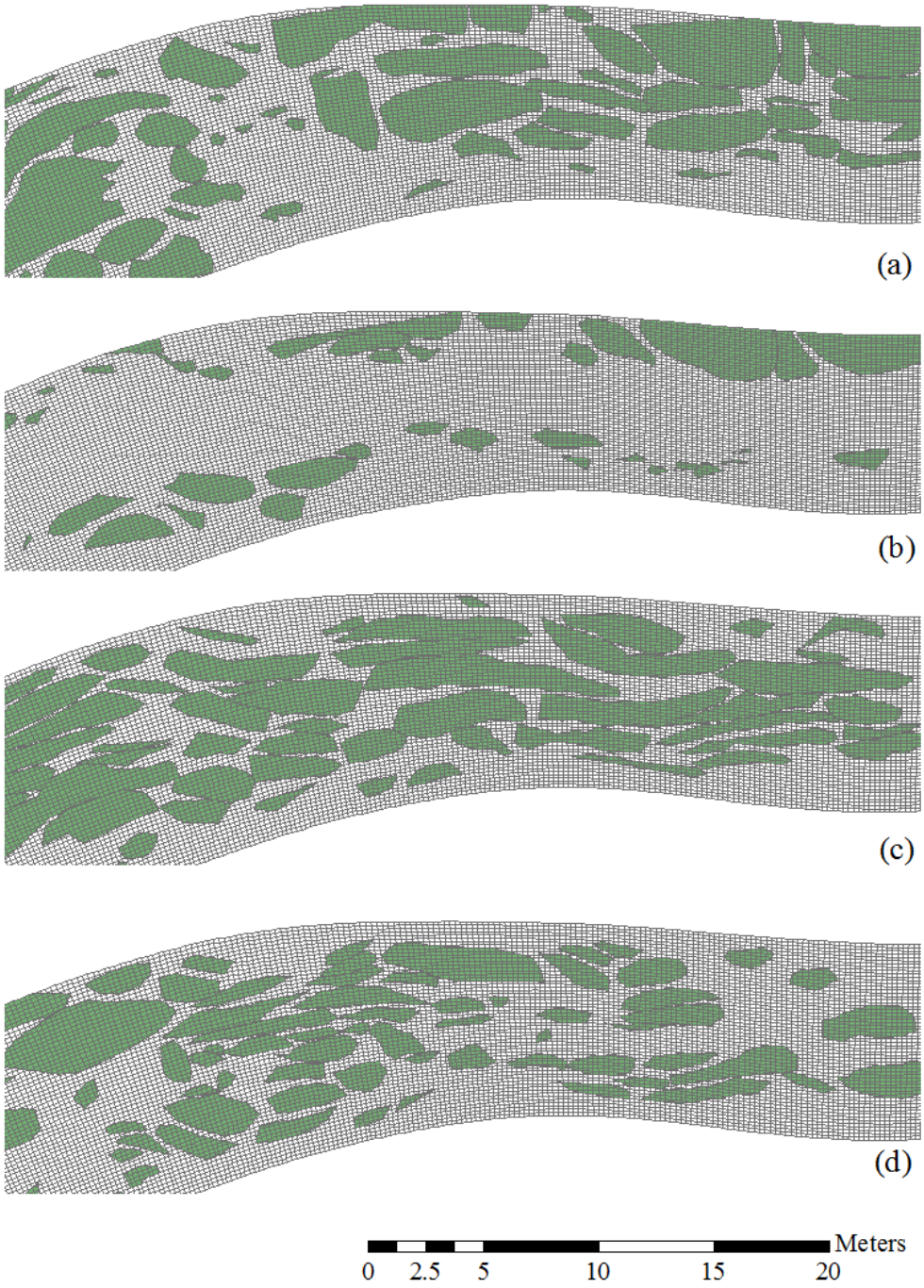

Figure 7.4.2: Vegetation patches overlain by the model mesh for (a) November 2010 before-cut; (b) November 2010 after-cut; (c) May 2011 before-cut; (d) May 2011 after-cut.

7.4.1. Vertical extent of aquatic vegetation on the River Lambourn.

When relating the vertical structure of plant patches to the model mesh, it was important to consider how each species behaves in response to flow. Each of the species present on the River Lambourn during the two study periods, *Ranunculus penicillatus* subsp. *pseudofluitans* var. *pseudofluitans*, *Berula erecta*, *Callitriche obtusangula* and *Rorippa nasturtium aquaticum*, exhibit differing morphologies. *Ranunculus* and *Callitriche* are rooted at the upstream extent of the patch only, whereas *Berula* and *Rorippa* are rooted along their length. Due to the buoyancy of *Ranunculus*, its location in the model mesh was determined using the relative height of the patch above the bed. The relative height is defined by dividing the height of the plant above the bed by the total water depth. For the lower growing *Callitriche*, high sediment retention on the River Lambourn limited its buoyancy. Hence, its vertical extent in the model was given by the absolute height above the channel bed. Absolute height was also used for *Berula* and *Rorippa* as these species are rooted along the length of the patch.

7.4.2. Representing vegetation morphology

To allow the application of species shape within the model mesh, the fit of a number of mathematical functions to surveyed data (Section 6.1.2) was trialled. For each vegetation patch, the total length along the surveyed top centreline was calculated. The relative distance along the patch at each top centreline point was then determined. This allowed consistent application of the mathematical functions between vegetation patches of different length. As discussed previously, for *Ranunculus* the relative height of the plant above the bed was used. For other

species, the absolute height above the bed was used. The following mathematical functions were trialled:

- Quadratic: $f(x) = ax^2 + bx + c$
- Cubic: $f(x) = ax^3 + bx^2 + cx + d$
- Asymptotic: $f(x) = a(1 - e^{-bx})$

where x is the relative distance along the patch in metres and a, b, c and d are coefficients. The coefficients of the quadratic, cubic and power functions were determined using a non-linear least squares approach in R, with the function fitted through the origin i.e. the plant root. For the asymptotic fit, the asymptote (a) and slope (b) were adjusted iteratively to best represent the surveyed data, determined to have been achieved when the root mean square error had been minimised.

The fitted functions for each species are shown in Figure 7.4.3. To determine goodness of fit, the root mean square error (RMSE) was calculated for each function (Table 7.4.1). The evidence in Figure 7.4.3 led to the selection of the asymptotic function to represent the top profile for all species. Although this function had marginally higher values of RMSE for the species *Berula* and *Callitriche* (Table 7.4.1) the general shape of the surveyed profiles was best represented using the asymptotic fit.

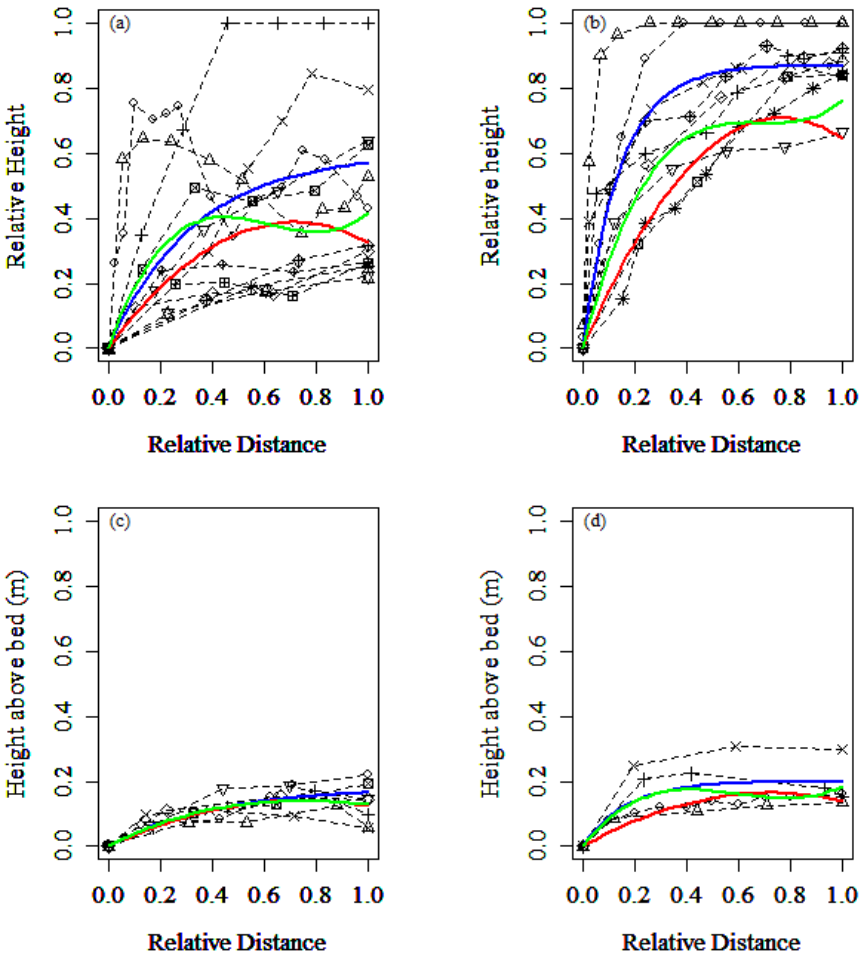

Figure 7.4.3: Asymptotic (blue), quadratic (red) and cubic (green) functions fitted to surveyed top profiles (grey) for (a) Near-bed *Ranunculus*; (b) Full-depth *Ranunculus*; (c) *Berula* and (d) *Calltriche.*

Table 7.4.1: RMSE values for the fitted top profile functions.

	Asymptotic	Quadratic	Cubic
Near-bed Ranunculus	0.243	0.270	0.244
Full-depth Ranunculus	0.265	0.300	0.271
Berula	0.042	0.037	0.036
Callitriche	0.068	0.054	0.058

The equations used to represent the top profiles, using the asymptotic form, are shown in Table 7.4.2.

Table 7.4.2: Equations used to represent the species top profiles.

Species	Function	Equation
Near-bed *Ranunculus*	Asymptotic	$0.6(1-e^{-3x})$
Full-depth *Ranunculus*	Asymptotic	$0.87(1-e^{-7x})$
Berula	Asymptotic	$0.19(1-e^{-2.5x})$
Callitriche	Asymptotic	$0.20(1-e^{-7x})$

The procedure was repeated to represent the bottom profiles of the two variants of *Ranunculus*. The fitted profiles and RMSE values are shown in Figure 7.4.4 and Table 7.4.3 respectively.

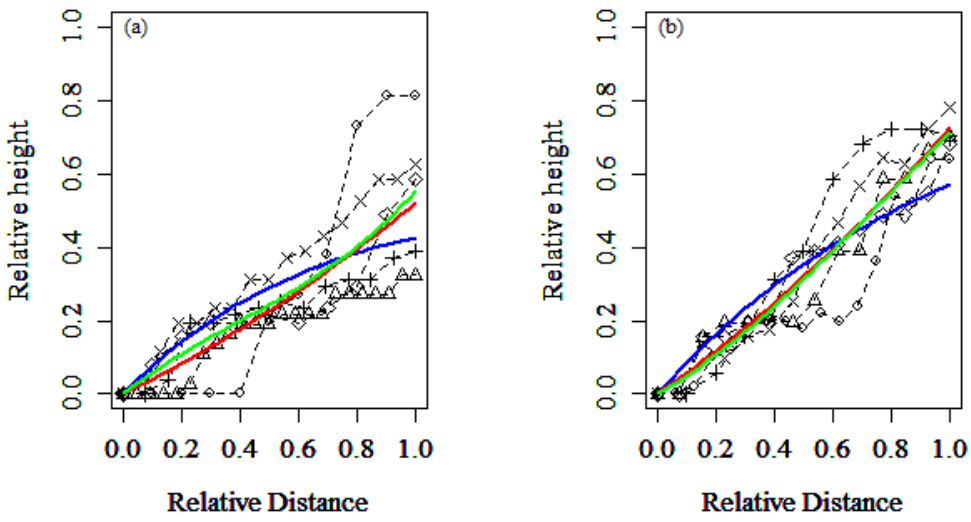

Figure 7.4.4: Asymptotic (blue), quadratic (red) and cubic (green) functions fitted to surveyed bottom profiles (grey) for (a) Near-bed *Ranunculus*; (b) Full-depth *Ranunculus*.

Table 7.4.3: RMSE values for the fitted bottom profile functions.

Species	Asymptotic	Quadratic	Cubic
Near-bed *Ranunculus*	0.119	0.106	0.107
Full-depth *Ranunculus*	0.080	0.080	0.102

For the bottom profiles, the quadratic function was selected. Although the asymptotic function had an equally low RMSE as the quadratic function for the full-depth *Ranunculus*, the form of the asymptotic function did not represent the general upward trend of the surveyed profiles. The equations used to represent the bottom profiles are shown in Table 7.4.4. The top and bottom functions combined form the representative shape of the two variants of *Ranunculus* which are used in the model (Figure 7.4.5). Overall, the full-depth *Ranunculus* (Figure 7.4.5b) occupies a greater volume in the depth dimension. This result matches well with patches observed in the field and evidence found in the literature discussed previously (Section 2.1.1).

Table 7.4.4: Equations used to represent the species bottom profiles.

Species	Function	Equation
Near-bed *Ranunculus*	Quadratic	$0.133x^2 + 0.387x$
Full-depth *Ranunculus*	Quadratic	$0.173x^2 + 0.553x$

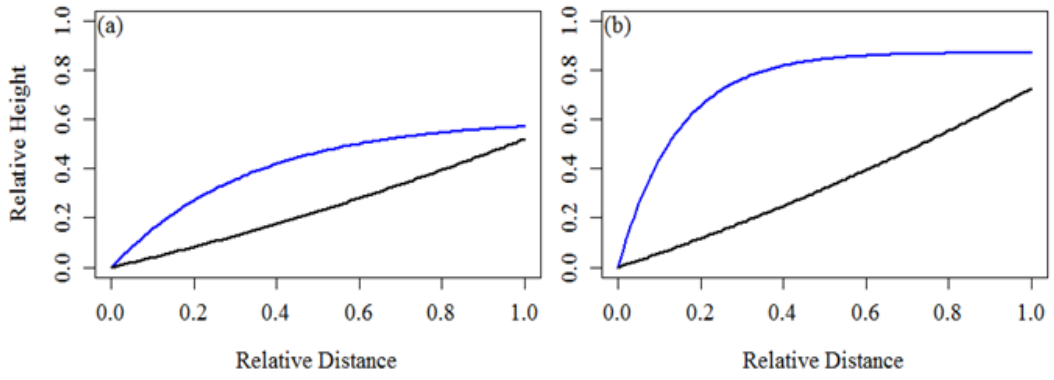

Figure 7.4.5: Top (blue) and bottom (black) profiles combined to form the overall representative shape for (a) Near-bed *Ranunculus* and (b) Full-depth *Ranunculus*.

7.5.Relating vegetation shape to the model mesh

When locating the vegetation within the model mesh we must consider how the surface and bottom profiles were surveyed. The bottom of the survey staff consisted of a circular foot of diameter 8cm which when surveying the surface profile of the vegetation sat on top of the vegetation. At the root, the foot sat on the surface of the gravel bed. For the bottom profile, the ruler placed in front of the camera to determine the height of the plant above the bed also sat on the surface of the gravel bed. For these reasons, the vegetation surveyed always relates to the grid cells above those representing the gravel bed. Accordingly, the shape profiles developed were applied to the model mesh starting at the sixth layer of the mesh, i.e. above the near-bed zone.

The location of the vegetation within the mesh was described by modifying the volume porosity of each cell (cf. Naden *et al*., 2004; Rameshwaran and Naden, 2012). For *Ranunculus* the root height was used as a reference plane above which the patch must sit to avoid the shape of the plant following undulations in the bed. For other species the function was applied as the height above the bed along the length of

the patch. The depth occupancy of the plant was determined by integrating the appropriate species shape function. This was then divided by the mesh cell area to give the number of cells in the vertical occupied by plant material. For the two types of *Ranunculus*, this was repeated for the area under the bottom curve to determine the number of cells beneath the plant which were occupied by water. The volume porosity was scaled depending on the occupancy of the cell at each location in the model mesh using:

$$\phi = 1 - (P_A * C_A * \phi)$$

7.5.1

where P_A is the planform proportion of the cell occupied, C_A is the proportion of the cell height occupied, and ϕ is the vegetation volume per unit volume. The value of ϕ refers to the values given in Table 6.2.1 and varies with species.

7.5.1. Treatment of vegetation roots

Vegetation is rooted through the gravel spaces in the near-bed zone. Within the gravel bed (layers one to five), the plant roots add material to the mesh cells which are already partially occupied by gravel. To represent this, the solid fractions of the gravel and vegetation were summed and the result subtracted from one (i.e. open water) to form the new volume porosity value for the model mesh. Figure 7.5.1 shows how this relates to each species on the River Lambourn. For the species *Berula*, *Callitriche*, *Rorippa* and mixed areas of vegetation, plants are rooted along the full length of the patch. In this circumstance the vegetation solid fraction was added to each of the first five layers of the model along the whole length of the patch, decreasing the porosity in each of these layers as a result. For *Ranunculus*, the

patch is rooted only at the upstream extremity of the patch. In this case, the vegetation solid fraction was added to the first five layers only in the first slab in which the patch is located. In Figure 7.5.1a, whilst the porosity is determined using the plant shape, it is represented in the model over the entire cell. Hence, no discontinuity exists between the volume porosity of the plant roots and the plant at this location.

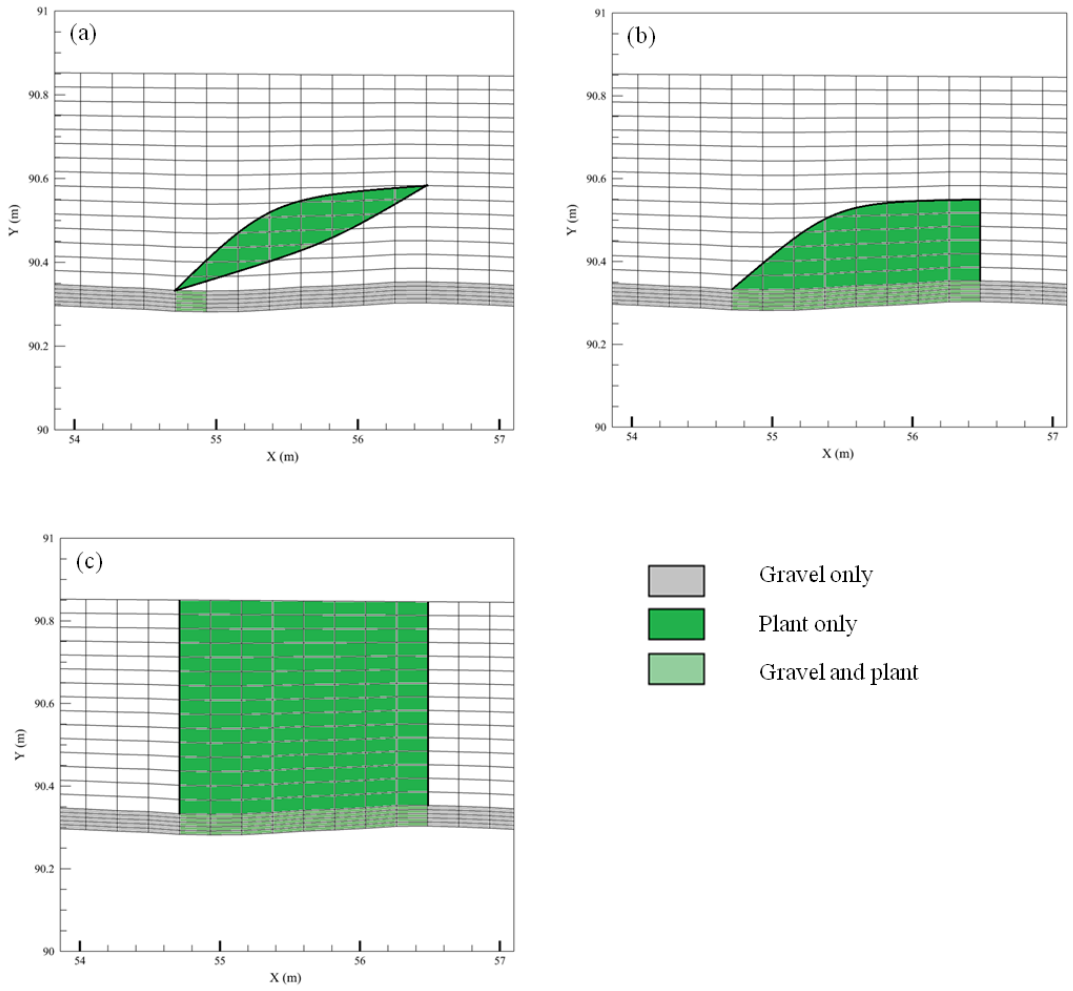

Figure 7.5.1: Schematic representation of plant patches above and within the gravel bed for: (a) *Ranunculus*; (b) *Berula* , *Callitriche* and mixed; (c) *Rorippa*.

7.5.2. Comparison to field photographs

Figure 7.5.2 to Figure 7.5.5 show the representation of the vegetation within the model mesh for four cross sections compared to photographs of the November 2010 and May 2011 cases. This highlights the difference in application for the near-bed (November) and full-depth (May) variants of *Ranunculus*. In all cases, the position of *Ranunculus* within the water column is well replicated. For the November before-cut case, the locations of cross sections XS2A and XS3A are approximated as these were not established until May 2011. Model cross sections show the patches as if facing upstream; in the photographs flow moves from right to left.

Occupancy of the plants in the depth dimension during November is lower than at other times during the year. This is reflected in the representation within the mesh, with most plants occurring within the bottom half of the flow depth. Vegetation present at the left bank for XS3A and XS3 and the right bank of XS2A is the emergent species *Rorippa* and as such occupies the full depth of the channel. Where vegetation is placed within the first five layers of the model, i.e. to represent the roots, these areas are shown in purple. This represents the fact that additional material has been added to the gravel bed, reducing its porosity.

Figure 7.5.3 shows the same cross sections for the after-cut case. Photographs of cross sections XS2A and XS3A were unavailable for this date. Clearly, a large amount of vegetation has been removed from the channel, commensurate with the evidence presented previously (Figure 6.1.3).

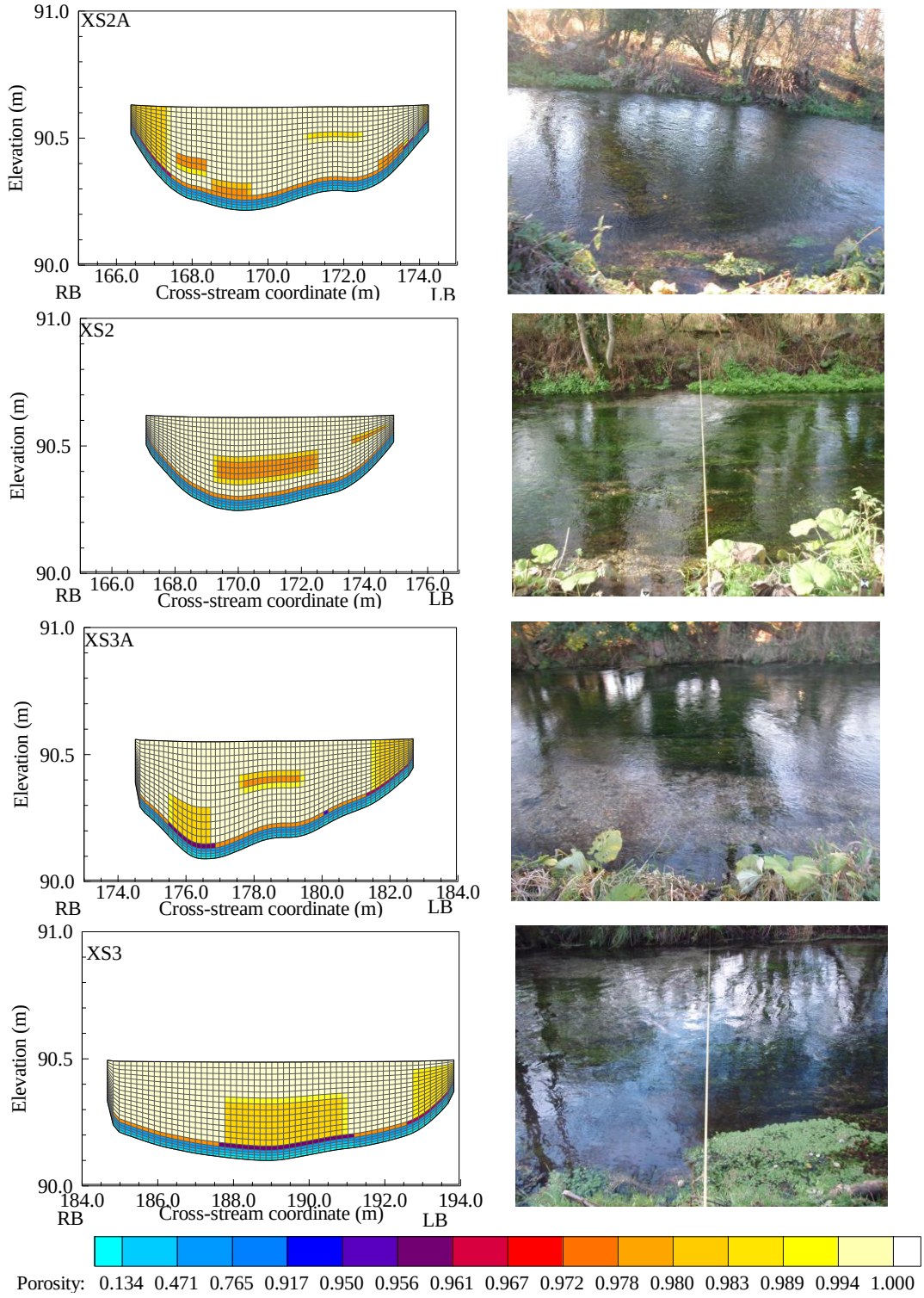

Figure 7.5.2: Comparison of vegetation represented within the model and photographs taken of the November 2010 before-cut case. Photographs are taken looking from the true left bank. In the model, LB and RB represent true left bank and true right bank respectively.

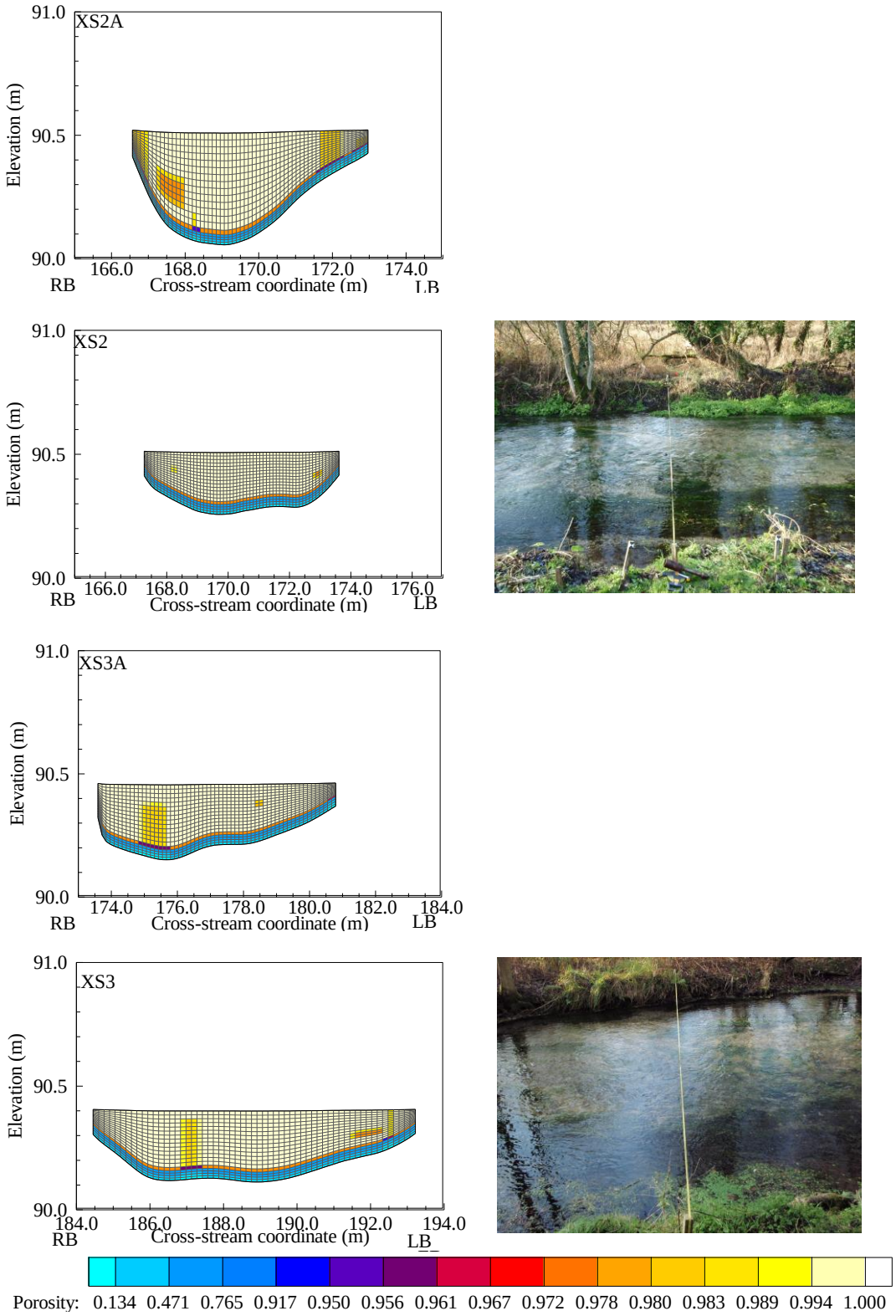

Figure 7.5.3: Comparison of vegetation represented within the model and photographs taken of the November 2010 after-cut case. Photographs are taken looking from the true left bank. In the model, LB and RB represent true left bank and true right bank respectively.

The distribution of vegetation was markedly different for the May 2011 case (Figure 7.5.4 and Figure 7.5.5). Figure 7.5.4 shows a reasonably good representation of vegetation patches within the model mesh when compared to photographs for the May 2011 before-cut case. A clear increase in vegetation occupancy is evident due to the presence of the full-depth variant of *Ranunculus*. Where patches of full-depth *Ranunculus* are present, they do not come completely to the surface in the model whereas it is apparent that this is the case in reality. This is to be expected, however, as the profile fitted to the surveyed data represents an average of some patches where the plant has come completely to the surface whereas some lay just beneath. This results, on average, in two cells in the depth dimension which are not covered by plant material towards the tip of full-depth *Ranunculus* patches. Vegetation present in the foreground of the photographs is riparian vegetation and hence is not included in the model.

The evidence in Figure 7.5.5 shows the effect of the May 2011 cut. At the cross sections photographed, large areas have been opened up to the flow; the location of which varies dependent on the location along the channel. In the upper part of the reach (XS2A, XS2) this area of open flow is in the centre of the channel. Further down the reach, the patch removal was on an *ad hoc* basis, in order to create a sinuous channel in these locations.

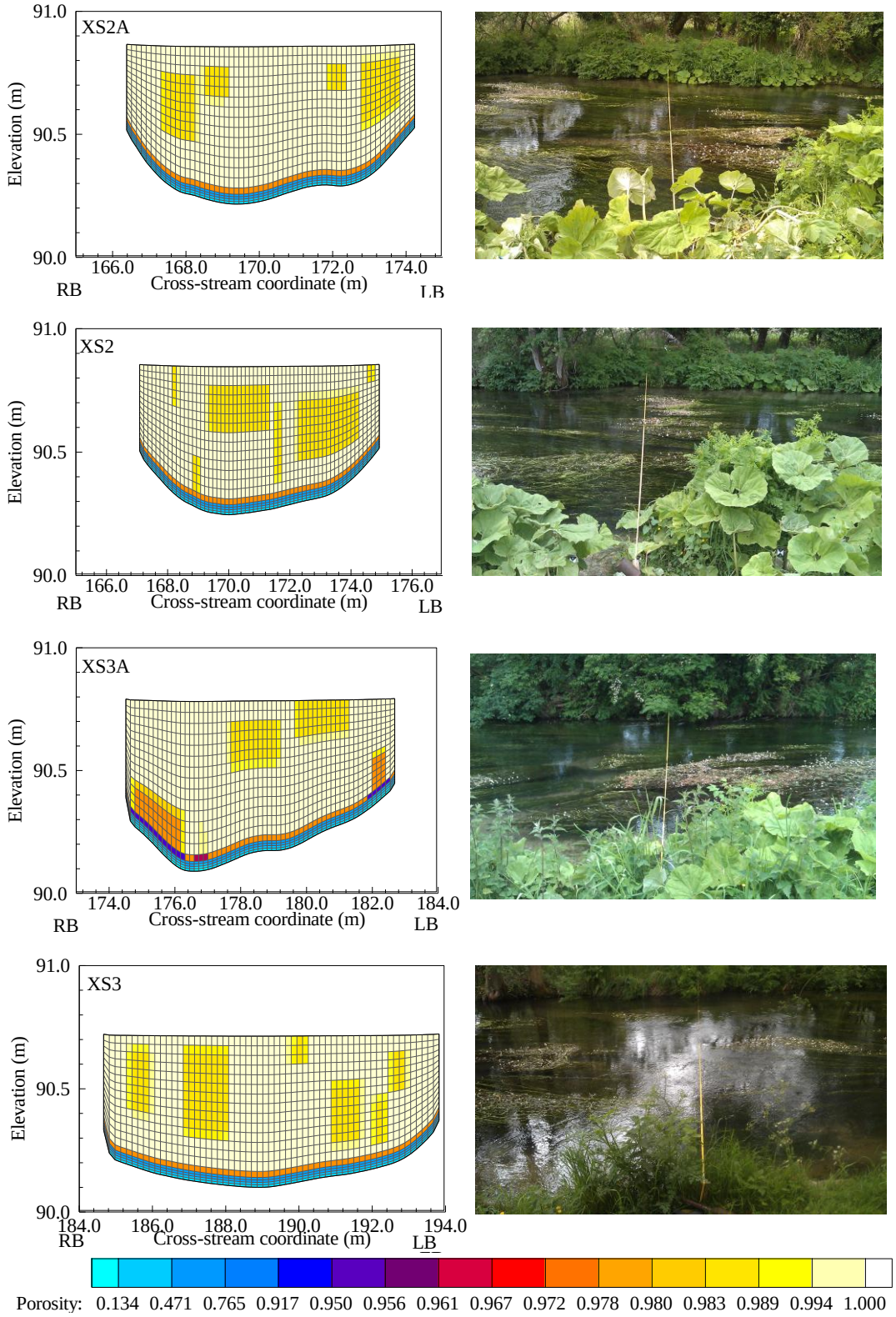

Figure 7.5.4: Comparison of vegetation represented within the model and photographs taken of the May 2011 before-cut case. Photographs are taken looking from the true left bank. In the model, LB and RB represent true left bank and true right bank respectively.

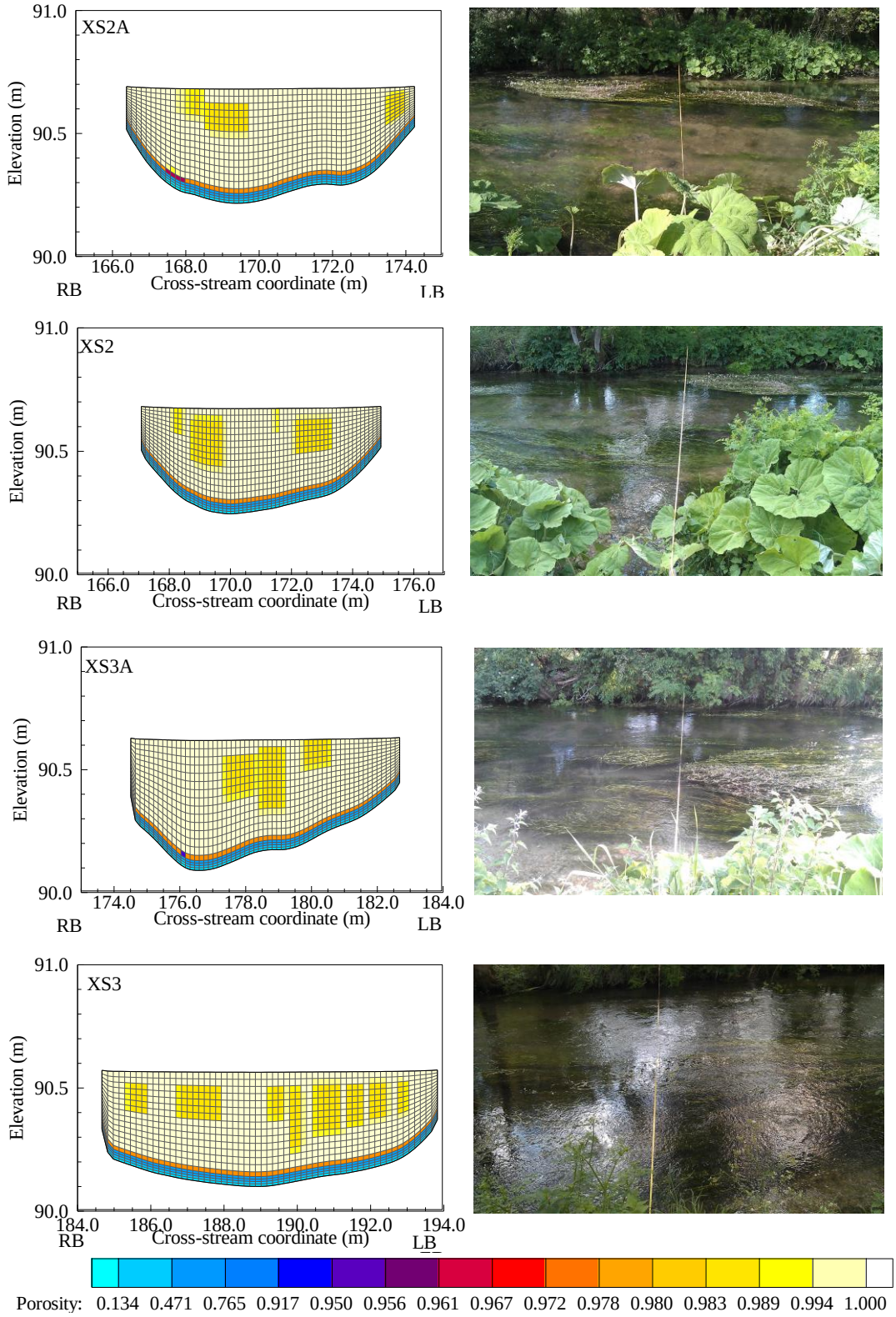

Figure 7.5.5: Comparison of vegetation represented within the model and photographs taken of the May 2011 after-cut case. Photographs are taken looking from the true left bank. In the model, LB and RB represent true left bank and true right bank respectively.

7.6.Calibration of the bulk drag coefficient for vegetation

To calibrate values of the bulk drag coefficient for vegetation $C_{dv}S_{fv}$, models of each case were constructed using the meshes described in section 7.1. The location of vegetation within each mesh was determined using the procedure in section 7.5. At the sub-grid scale, vegetation drag was parameterised as outlined in Section 3.1.2. Values for the spatially-averaged momentum absorbing area A_{sv} were specified from Table 6.2.2. Appropriate boundary conditions were applied (Section 3.2.1) with inflow conditions as in Table 5.2.3. Calibration of $C_{dv}S_{fv}$ was undertaken using the same method as that for the bulk drag coefficient for gravel, outlined in Section 7.2.1. When applying the free surface treatment (Section 3.2.1) the location of the vegetation within each model cell remained the same with only the dimensions of the mesh changed to account for discrepancies between the model free surface and atmospheric pressure. Results for the calibrated bulk drag coefficient for vegetation $C_{dv}S_{fv}$ for each case are shown in Table 7.6.1, with the final free surface following mesh adjustment shown in Figure 7.6.1. Field measurements of the water surface at each bank are also shown. Figure 7.6.1 shows that the modelled free surface, following calibration of $C_{dv}S_{fv}$ and appropriate mesh adjustment, compares well to the overall slope of the staff gauge boards.

Table 7.6.1: Calibrated values of $C_{dv}S_{fv}$.

Case	Calibrated $C_{dv}S_{fv}$
November 2010 – before-cut	0.63
November 2010 – after-cut	0.42
May 2011 – before-cut	0.68
May 2011 – after-cut	0.14

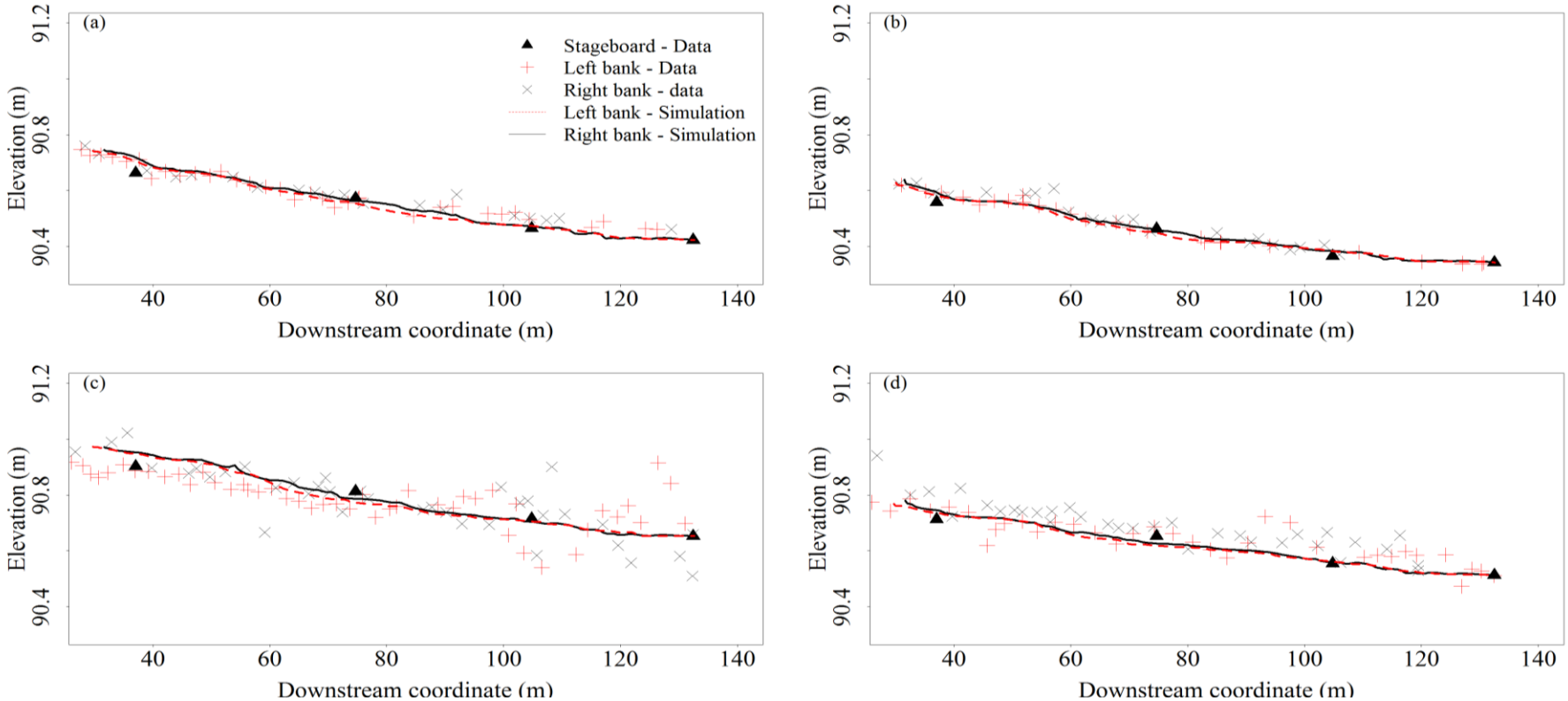

Figure 7.6.1: Simulated free surface profiles against field measurements of water surface and staff gauge boards for (a) November 2010 before cut; (b) November 2010 after cut; (c) May 2011 before cut; (d) May 2011 after cut.

Figure 7.6.1 shows that the water surface profiles along the reach are predicted reasonably well for all both cases when compared to field measurements.

7.7.Discussion

Analysis of the literature revealed that drag coefficients relating to vegetation fall into four groups: (i) measurement of drag on pseudo plants, i.e. plastic representations of 'real' plants; (ii) values obtained from either measurement or modelling of 'real' plants; (iii) flume measurement of drag on a cylinder or groups of cylinders designed to represent a plant or groups of plants; and (iv) model representation of such flume experiments. The reported drag coefficient values, the approaches to obtain these values; and the parameterisation of vegetative drag in these studies are given in Table 7.7.1.

Table 7.7.1: Values of drag coefficients relating to vegetation quoted in the literature for (a) measurements taken on artificial plants; (b) natural plants; (c) flume measurements of drag on cylinders; (d) model representation of flume experiments on cylinders.

(a)

Reference	Approach	Drag parameterisation	C_{dv}
Nepf and Vivoni (2000)	Laboratory measurements of flow with a plastic plant prototype	$F_D = \frac{1}{2} C_d \alpha \langle u^3 \rangle$	1.0-3.0
Callaghan et al (2007)	Direct measurement of exerted drag on three test objects (1) Rigid cylinder; (2) An artificial representation of the aquatic plant *Egeria densa*; (3) A bunch of *Egeria densa.* Measurements made using a submersible drag gauge.	$C_D = D(0.5\rho A U^2)^{-1}$ Where *D* is the drag force measured in Newtons and *A* is the characteristic area of the test object. Only results for *Egeria* presented in this paper.	0.7-1.4

(b)

Reference	Approach	Drag parameterisation	C_{dv}
Sand-Jensen (2003)	Assessment of drag on the species *Egeria densa, Hygrophilia corymbosa, Limnophilia aquatic, Myriophilium tuberculatum* and *Villisneria natans* in a flume.	$F_D = 0.5 C_D \rho A_c U^2$ where A_c is the characteristic area of the object.	0.01-0.1
Naden *et al* (2004)	Modelled singular patch of *Ranunculus*. Results compared to measurements taken of flow around patch in a flume.	$F_D = -\frac{\rho}{2} C_D S_f A_s \lvert\langle\overline{u}\rangle\rvert\langle\overline{u}\rangle$	0.5
Puijalon *et al* (2005)	Observed response of two species, (1) *Berula erecta* and (2) *Mentha aquatica*, to increasing hydraulic stress in a flume.	$C_D = 2D/(\rho S U^2)$ Where *D* is drag in N, *S* is the total leaf area.	(1) 0.065-0.155 (2) 0.120-0.220
Rameshwaran and Naden (2012)	Patchy vegetation in the River Blackwater. Patches assumed to occupy full depth. Modelled free surface matched to field measurements.	$F_D = -\frac{\rho}{2} C_D S_f A_s \lvert\langle\overline{u}\rangle\rvert\langle\overline{u}\rangle$ A_s = vegetation surface area per unit volume.	0.15 (C_{dv} S_{fv})

(c)

Reference	Approach	Drag parameterisation	C_{dv} S_{fv}
Nepf (1999)	Emergent vegetation represented by groups of cylinders in a flume.	$F_D = \frac{1}{2}\overline{C_D} a U^2$ Where *a* is the projected plant area per unit volume.	0.2-1.2
Ghisalberti and Nepf (2004)	Investigation into the growth of vegetated shear layers. Flume experiment.	$F_D = \frac{1}{2} C_d a U \left(\overline{2u'^2} + \overline{v'^2}\right)$ Where *a* is the characteristic vegetation area per unit volume.	0.79-1.4

Reference	Approach	Drag parameterisation	C_{dv} S_{fv}
Ghisalberti and Nepf (2006)	Flow through a submerged aquatic canopy. Canopies were both rigid and flexible. Rigid canopies comprised of wooden dowels. Flexible canopies designed to mimic eel grass (*Zostera Marina*).	$$C_D(z) = \frac{\frac{\partial \overline{u'w'}}{\partial z}\Big\|_{h<z<z_2-} - \frac{\partial \overline{u'w'}}{\partial z}(z)}{\frac{1}{2}aU^2(z)}$$	0.61-0.81
Tanino and Nepf (2008)	Cd for cylinder arrangements providing solid fraction range of between 35% and 9.1%	Related to particle Reynolds number. Values established from laboratory measurements.	0.2-0.95
Kothyari *et al* (2009)	Measurement of drag force on an array of cylinders in a flume.	$$C_D = \frac{F_x}{\frac{1}{2}\rho d h {V_c}^2}$$ where V_c is the depth averaged flow velocity, *d* is the cylinder diameter and *h* is the flow depth.	0.7-2.0
Ghisalberti (2010)	Flow through a submerged canopy of dowels in a flume.	Not quoted.	0.65
Plew (2011)	Flow through suspended canopies. Canopies represented by suspended cylinders. Measurements undertaken in a flume.	$$F_D = -\frac{1}{2}\rho C_D(z) a \langle U(z) \rangle^2$$ Where *a* is the unit volume of the canopy. Values quoted are averaged over the canopy height.	0.6-1.35
Chen *et al*. (2013)	1) Cd estimated to be close to that of an isolated cylinder for solid volume fraction of 1.2% and 2.6%.	Estimated using empirical relation for isolated cylinder (White, 1991) as $$C_D = 1 + 10{Re_d}^{-2/3}$$	1.2 (C_{dv})

(d)

Reference	Approach	Drag parameterisation	C_{dv} S_{fv}
Shimizu and Tsujimoto (1994)	Modelled flow through rigid cylinders	$F_D = \frac{1}{2}\rho\lambda C_d U\sqrt{U^2+V^2}$ Where λ is vegetation density defined as projected area to flow per unit volume of water.	1.0
Fischer-Antze *et al*. (2001)	Modelled laboratory experiments of Tsujimoto et al (1991), Lopez and Garcia (1997) and Pasche (1984).	$F_D = \rho\frac{{U_i}^2}{2}C_D\lambda$ Where λ is vegetation density defined as projected area to flow per unit volume of water.	1.0 (approximated)
Lopez and Garcia (2001)	Modelled flow through rigid submerged cylinders	$F_D = \frac{1}{2}C_d a\langle {u_i}^2\rangle$ Where *a* is a measure of the ratio of the differential frontal areas of the obstacles.	1.13
Erduran and Kutija (2003)	Quasi 3D modelling of submerged vegetation (cylinders)	$F_D = m\frac{h_r C_d u_x\sqrt{{u_x}^2+{u_y}^2}d}{2\Delta z}$ Where *m* is the density of vegetation, *d* is the diameter of vegetation and h_r is the effective height of vegetation.	1.1

Table 7.7.1 shows that there is a wide range in the parameterisation of the characteristic area of vegetation. This and the different types of vegetation or its approximation precludes direct comparison of the drag coefficients calibrated in this study with any particular study from the literature. However, the most appropriate study for comparison is that of Rameshwaran and Naden (2012) which has the same

form for parameterisation of drag used in this study. A key difference in Rameshwaran and Naden (2012), however, is the consideration of vegetation shape and the reduction of the drag coefficient of a patch based on its aspect ratio. The values of the after cut cases in this study compare well with their quoted value of 0.15, although before cut cases have a significantly higher value.

In general, the literature shows that the proximity of vegetation patches to each other has an important effect on the overall value of the drag coefficient. When considering vegetation as cylinders, C_{dv} has been shown to be influenced by the presence and relative location of adjacent cylinders. Where cylinders are in the wake of an upstream cylinder, the velocity they are exposed to is reduced, leading to a corresponding reduction in drag (Petryk, 1969; Zdradkovich and Pridden, 1977; Schindler *et al*., 2003; Blevins, 2003; Tanino and Nepf, 2008; Zong and Nepf, 2011).

The implication of this in understanding the values in Table 7.6.1 is that, following a vegetation cut, patches become more distributed which may lead to a reduction in drag where patches are in close proximity. Values in Table 7.6.1 show that the bulk drag coefficient $C_{dv}S_{fv}$ is higher before a vegetation cut and lower following a cut. For the November 2010 after-cut case, it is likely that the value of $C_{dv}S_{fv}$ is higher than the equivalent May 2011 case due to the nature of the cut (Figure 7.4.1b). This is because the vegetation removed was along the channel centreline. As a result, resistance due to vegetation following the cut, was only at the channel margins, an area where flow velocities would be lower due to emergent vegetation (*Rorippa*) which increases resistance to flow. The value of $C_{dv}S_{fv}$ is, therefore, higher in order to match the measured energy slope in the field. As the May 2011 cut was more patchy in nature, vegetative resistance is throughout the reach and a lower value of $C_{dv}S_{fv}$ is needed to match the energy losses.

A possible reason for the overall difference in values between the before and after cut cases is the role that the reconfiguration of plants plays in determining vegetative drag. The planform streamlining of vegetation patches, before and after cutting, was accounted for within the model when surveying the patches. In the depth dimension, however, the profiles surveyed related to the after cut case only with the same depth profile applied to all plant patches. Following vegetation cuts, plants experience changes in the local velocity field. Where flow velocity increases following a cut, plants bend towards the bed. Hence, in the before cut cases, the depth occupancy of vegetation may have been under-represented, necessitating an increased value of $C_{dv}S_{fv}$ to match the field energy slope.

7.7.1. Potential sources of error

The representation of vegetation in the model comprises three key datasets: (i) the planform shape of vegetation; (ii) the depth coverage of a vegetation patch; (iii) the sub-grid scale vegetation parameters relating to plant volume and total surface area per unit volume. These datasets introduce potential sources of error and may affect the calibrated values of $C_{dv}S_{fv}$.

The planform shape of vegetation was surveyed directly in the field for each case. Although it was difficult, in some circumstances, to determine where one patch began and another ended, overall the confidence in this dataset was high. As such, little variation in $C_{dv}S_{fv}$ should be expected as a result of errors in this dataset. The representation of the dominant vegetation type *Ranunculus* is related to the relative height, so the occupancy in the depth dimension should be consistent between the before and after-cut cases. Indeed, when considering the comparison between the representation in the model mesh and photographs from the field (Figure 7.5.2-Figure 7.5.5) this appears to be the case. However, as the profiles relating to the

depth dimension were always measured after the vegetation cut by necessity (i.e. sufficient space between patches to undertake the underwater photography), the representation of the underwater structure of the patch may not be entirely representative of that in the field before the cut. Also, as the number of profiles used to represent this morphology was limited, discrepancies may occur where the volume of vegetation is over or under represented. Where vegetation volume is over represented, we would expect the value for $C_{dv}S_{fv}$ to decrease with the opposite true for under representation.

For the November and May cases, this should partly have been accounted for by the definition of two variants of *Ranunculus*, with the most appropriate variant being used for a specific time of year i.e. near-bed or full-depth as termed in this study. Variation in other species was also accounted for by surveying their morphology at the relevant time of year. Vegetation structure also changes throughout the growing season particularly with reference to leaf structure, stem density, and leaf and stem area. Such variation was accounted for in the model through the sampling of vegetation patches in order to undertake measurements of vegetation porosity and surface area (Section 6.2). For all species, there is an overall tendency for the surface area to decrease between May and October with a corresponding increase in porosity for most species (Table 6.2.1, Table 6.2.2). Values for surface area and porosity within the model were taken as an average of all samples. The standard deviation of porosity values for all species was relatively low (0.003-0.006). Values for vegetation surface area, however, exhibited a high standard deviation for all species, between $5.2 m^2 m^{-3}$ and $14.2 m^2 m^{-3}$. Also, the act of cutting the vegetation may leave behind the thicker stems and/or more dense parts of

the plant patch. Such variations in the data could lead to variation in the calibrated value of $C_{dv}S_{fv}$.

7.8. Conclusions

A three-dimensional model of the River Lambourn was constructed for five cases of differing vegetation cover: a minimum vegetation case necessary to calibrate the bulk drag coefficient for the gravel bed, and a further four cases with substantial vegetation cover for two different growth stages, pre and post cutting. The bulk drag coefficient $C_{dg}S_{fg}$ for gravel was calibrated and the value of $C_{dg}S_{fg}$ = 0.45 obtained was within the range of those found in the literature. Tests undertaken to determine the effect of grid resolution on model results (Roache, 1994) suggested that the mesh produced was converging towards a grid-independent solution and was relatively free of numerical error.

In conjunction with data relating to the top and bottom profiles of vegetation patches, representative patch shapes were developed by fitting mathematical functions to surveyed data. By integrating the area under these functions, the shape for each species could be transferred to the model mesh. This allowed an explicit representation of vegetation volume within the 3D CFD model. When compared to field photographs, the method appears to represent the location of vegetation within the model mesh fairly accurately. This was combined with data representing the sub-grid scale description of aquatic vegetation (namely its volume and surface area per unit volume) to form an overall method of representing aquatic vegetation within three dimensional hydraulic models. However, when simulations were run to calibrate the value of the bulk drag coefficient for vegetation $C_{dv}S_{fv}$, differences were observed between before and after-cut cases. Differences in values were also found

between the November after-cut and May after-cut cases, potentially as a result of the pattern of cut employed.

The possible causes for these discrepancies, with specific reference to the datasets collected and methods used in this study, were discussed with a number of possible sources of error identified. These were namely the depth dimension of the vegetation and the vegetation surface area and porosity.

Chapter 8. Results from the river model with vegetation

This chapter presents the results from the river model with vegetation. Firstly, the results of the model at the reach scale are presented, with a discussion of how the distribution of velocities, turbulent kinetic energy and vegetation volume changes following vegetation cuts. Secondly, a detailed assessment of model results is undertaken for the May 2011 case. Modelled results at four cross sections before and after the vegetation cut are compared to EMCM and ADV measurements, as described in Section 5.4. From this, inference is made to the overall performance of the model in terms of predictions of streamwise velocity and turbulent kinetic energy. Finally, the impact on flow at the plant scale is analysed. A single patch of *Ranunculus* was selected, and modelled flow along a streamwise transect through the patch assessed at regular intervals for streamwise velocity, turbulent kinetic energy and Reynolds stress.

8.1. Model results at the reach scale

The reach scale model results of streamwise velocity and turbulent kinetic energy are presented before (Figures 8.1.1 to 8.13) and after vegetation cuts (Figures 8.1.4 to 8.1.6) for three planform layers: the layer just above the gravel bed; the layer at approximately half the water depth; and the layer at the water surface. Values for the mean streamwise velocity, turbulent kinetic energy and percentage volume occupied by vegetation for each layer are given in Tables 8.1.1 and 8.1.2 for the before cut and after cut cases, respectively.

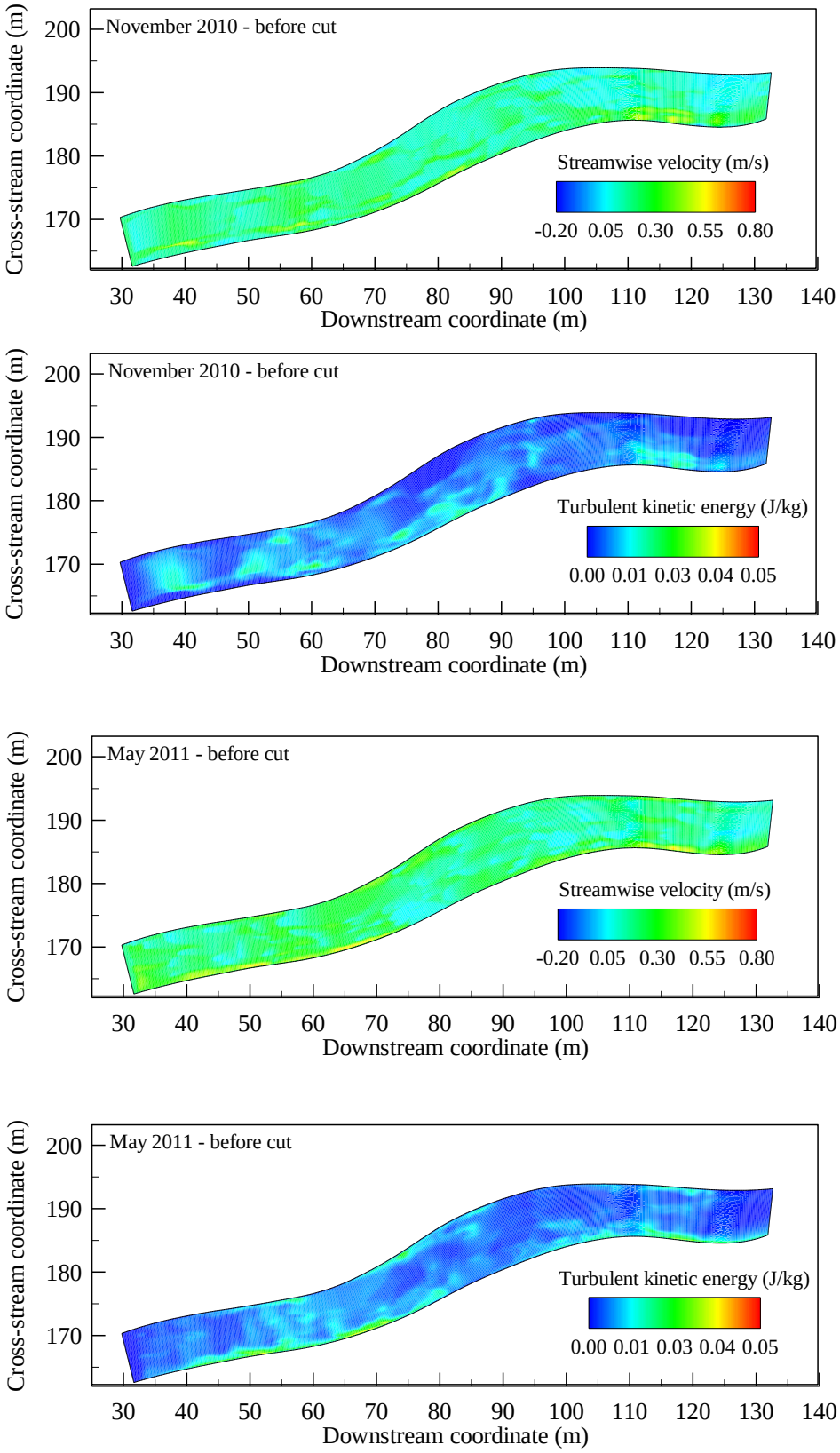

Figure 8.1.1: Planform results for streamwise velocity and turbulent kinetic energy adjacent to the gravel bed before vegetation cuts.

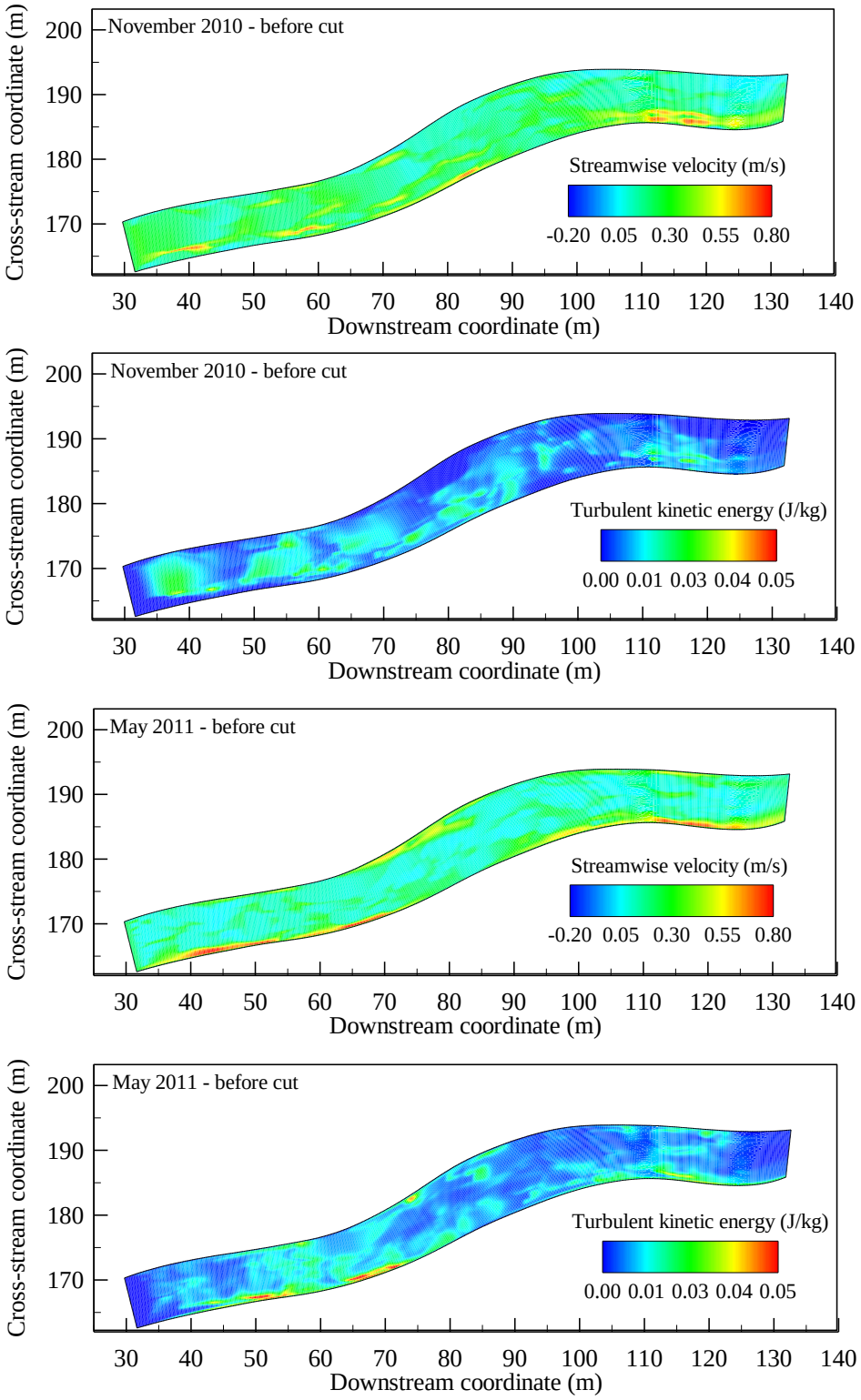

Figure 8.1.2: Planform results for streamwise velocity and turbulent kinetic energy at approximately half the water depth before vegetation cuts.

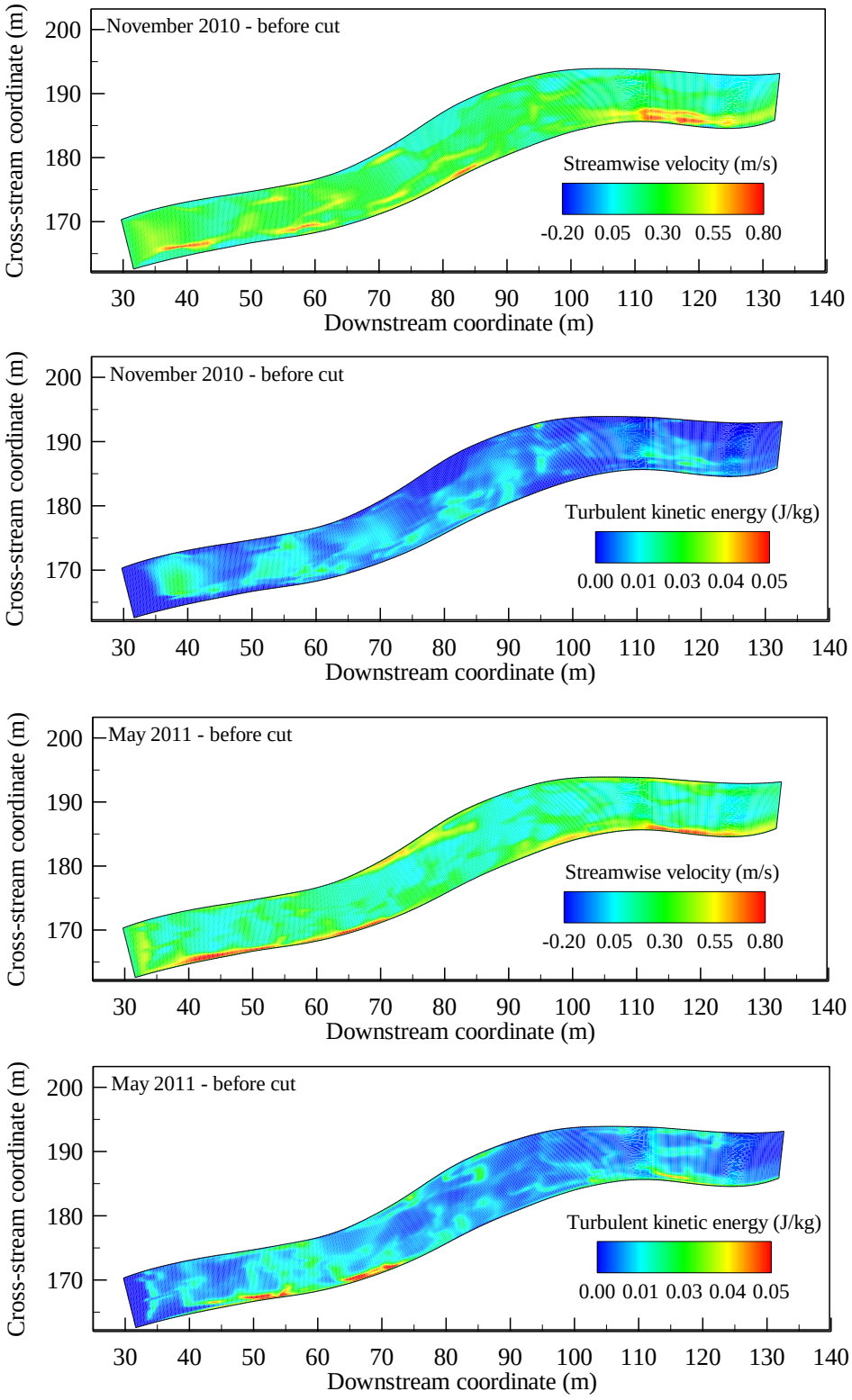

Figure 8.1.3: Planform results for streamwise velocity and turbulent kinetic energy at the water surface before vegetation cuts.

Table 8.1.1: Values of mean streamwise velocity, turbulent kinetic energy and vegetation occupancy by layer for before vegetation cut cases. Average mean streamwise velocity and turbulent kinetic energy are weighted by cell volume.

Case	Water level (m)	Layer	Mean streamwise velocity (ms^{-1})	Mean turbulent kinetic energy (Jkg^{-1})	Percentage volume occupied by vegetation (%)
November 2010 – before cut $Q = 0.557\ m^3s^{-1}$	90.81	Adjacent to bed	0.16	0.0060	26.15
		Half water depth	0.22	0.0077	33.49
		Water surface	0.27	0.0068	8.08
May 2011 – before cut $Q = 0.841\ m^3s^{-1}$	90.98	Adjacent to bed	0.19	0.0062	9.28
		Half water depth	0.16	0.0090	47.07
		Water surface	0.20	0.0093	0.00

Results for the before-cut cases show that, adjacent to the gravel bed (Figure 8.1.1), the magnitude of flow velocities ($0.16ms^{-1}$) and turbulent kinetic energy (TKE) ($0.006\ Jkg^{-1}$) are low throughout the reach. This is due to the overall density of vegetation (see Figure 7.4.1) before the vegetation cut with ~26% and ~9% of the layer volume occupied by vegetation for the November and May cases, respectively. The lower volume occupancy in May results from the morphology of *Ranunculus*, where the patch bottom profile rises more steeply from the channel bed than in November (see Figure 7.4.5). *Rorippa* (~18% of total vegetation coverage) is the second most abundant species during November, increasing the vegetation volume throughout the water column, compared to May.

Moving into the middle layer, flow velocities in November increase to an average of 0.22ms^{-1} due to acceleration around plant patches and increased height above the channel bed, with the volume occupied by vegetation increasing to an average of ~33%. Areas of shear where water accelerates around vegetation patches can be identified by increases in TKE (from 0.0060 to 0.0077 Jkg^{-1}) resulting from the large velocity gradients which occur due to low flow within plant patches with faster flow around the plant.

In May, velocities in the middle layer decrease when compared to the layer adjacent to the bed, to an average of 0.16ms^{-1}. This occurs due to the greatly increased volume occupancy of vegetation from ~9% to ~47%. The differing volume of vegetation between the November and May cases can be attributed to the depth occupancy of near-bed *Ranunculus* (November) and full-depth *Ranunculus* (May) as defined in Chapter 7.4 (see Figure 7.4.5). Moving to the top layer, both the November and May cases have increased flow velocity, mean 0.27ms^{-1} and 0.20ms^{-1} respectively, where the volume of vegetation is lower (~9% and 0%). The ~9% occupancy in November relates to *Rorippa* as this species extends to the water surface.

For the November before-cut case, the overall effect of the vegetation created a patchy distribution of flow velocities and TKE due to the acceleration of flow around vegetation patches (e.g. Figure 8.1.2). The high density of vegetation for the May 2011 before-cut case, particularly at half the channel depth, pushes the water towards the channel margins, and this is reflected by the high flow velocities observed in these areas in all layers. The narrow space between the vegetation patches and the channel margin leads to high velocity gradients in these areas, shown

by the high magnitude of TKE particularly between 50 and 70m where the cross sectional coverage of vegetation is at its highest (~40 %).

Results for the cases following the vegetation cuts are shown in Table 8.1.2 and Figures 8.1.4 to 8.1.6. Maps showing where vegetation has been removed, for reference, can be found in Chapter 7 (Figure 7.4.5).

Table 8.1.2: Values of mean streamwise velocity, turbulent kinetic energy and volumetric occupation of vegetation by layer for after vegetation cut cases. Percentage changes compared to the equivalent value before the cut are shown in parentheses. Average mean streamwise velocity and turbulent kinetic energy are weighted by cell volume.

Case	Water level (m)	Layer	Mean streamwise velocity (ms^{-1})	Mean turbulent kinetic energy (Jkg^{-1})	Percentage volume occupied by vegetation (%)
November 2010 – after cut $Q = 0.603\ m^3s^{-1}$ (+8%)	90.68 (-17%)	Adjacent to bed	0.26	0.0090	13.75
		Half water depth	0.38	0.0066	15.09
		Water surface	0.43	0.0053	5.66
May 2011 – after cut $Q = 0.906\ m^3s^{-1}$ (+7%)	90.81 (-18%)	Adjacent to bed	0.24	0.0058	7.49
		Half water depth	0.30	0.0061	32.08
		Water surface	0.33	0.0063	0.00

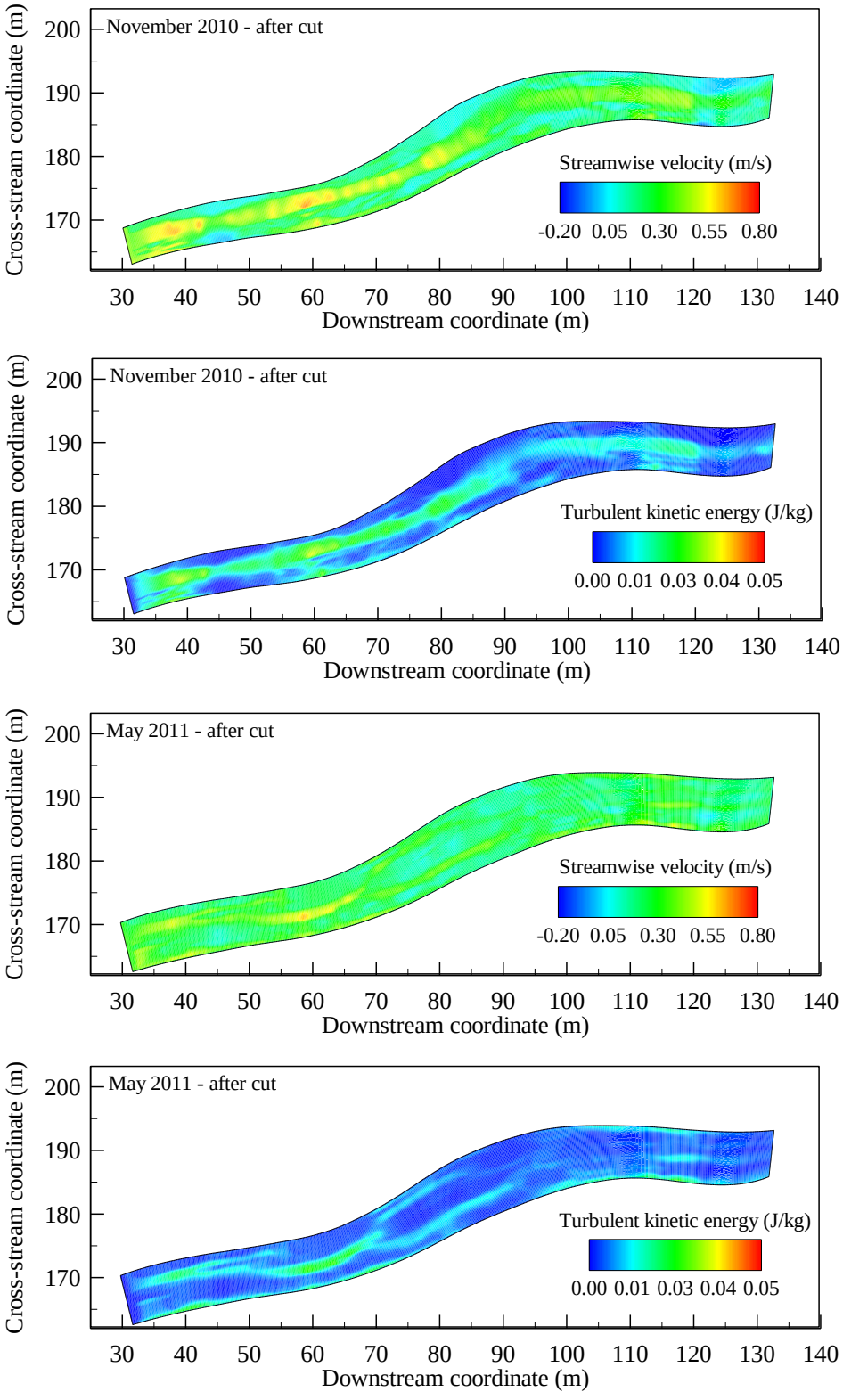

Figure 8.1.4: Planform results for streamwise velocity and turbulent kinetic energy adjacent to the gravel bed after vegetation cuts.

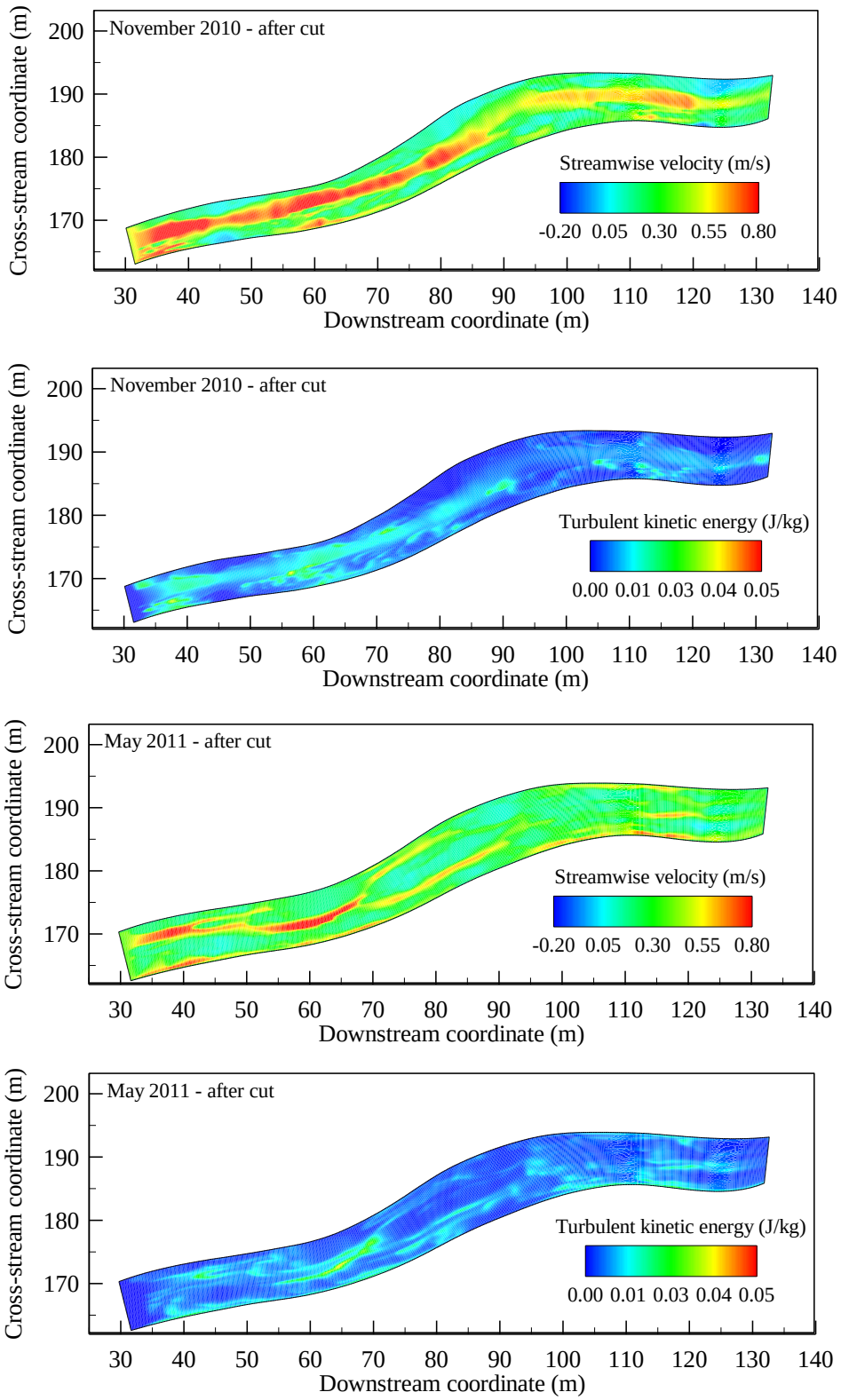

Figure 8.1.5: Planform results for streamwise velocity and turbulent kinetic energy at approximately half the water depth after vegetation cuts.

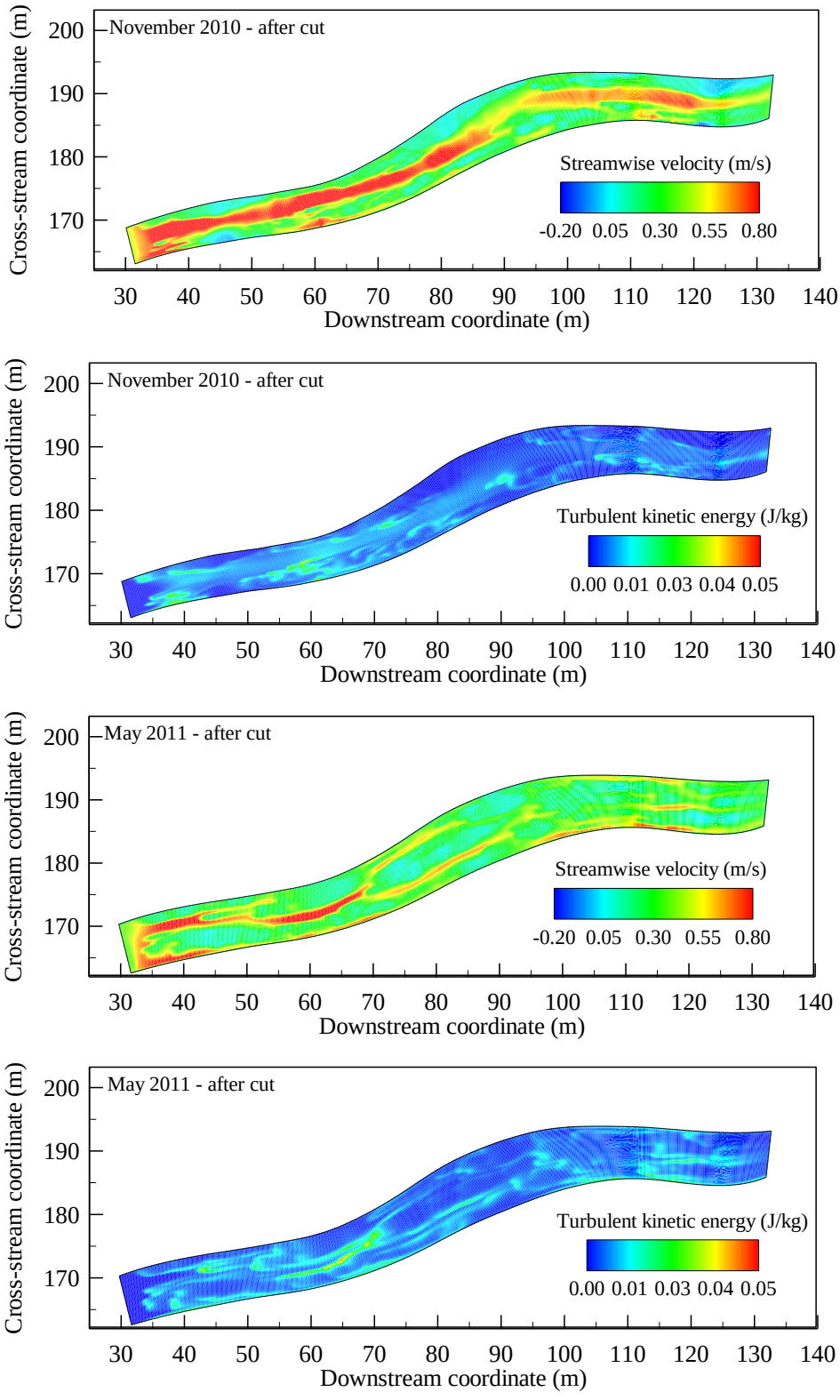

Figure 8.1.6: Planform results for streamwise velocity and turbulent kinetic energy at the water surface after vegetation cuts.

To consider the effect of the vegetation cuts, three variables must be taken into account; (i) discharge, (ii) water depth and (iii) the volume of vegetation. Discharges between the before and after cut cases remained broadly the same for both the November and May cases, with a maximum change of 8% measured using the ADCP. Hence, if discharge is discounted, a relationship must exist between the change in water depth and change in volumetric occupation of vegetation. Following the November and May cuts respectively, reductions in water depth of ~17% and ~18% were observed. This reduces the cross sectional area. In addition to this, there is a drop in volume occupancy of aquatic vegetation, which falls in the layers analysed from a maximum of ~47% before a vegetation cut to ~32% following a cut. Both the reduction in water level and in vegetation volume results in an increase in velocity for the near constant discharge.

Overall, with regards to flow distribution, two different effects can be seen. For the November 2010 case where the cut was mainly down the channel centreline (see Figure 7.4.1), flow velocities along this centreline increased from an average of 0.18 ms^{-1} to 0.51ms^{-1} an increase of ~265%. As a result of the cut, TKE increases in magnitude along the channel centreline at the bed from 0.0002 Jkg^{-1} to 0.0004 Jkg^{-1}, an increase of 100%. Flow velocity in the channel margins close to the left bank increases from 0.16ms^{-1} to 0.19ms^{-1}. At the right bank, velocity also increases marginally from 0.25ms^{-1} to 0.26ms^{-1}. At the boundary between the faster velocity in the centre of the channel and the lower velocity at the margins, TKE is high (approximately 0.08Jkg^{-1}). This is due to areas of high shear due to the interaction of faster flow velocities with the boundary of marginal vegetation patches , for example *Rorippa* which extends to the water surface.

The more patchy nature of the May 2011 cut reveals different results, particularly in the lower part of the modelled reach. Within vegetation patches flow velocities remain low, however the impact of removing vegetation in clear cut channels can be seen throughout the water depth with flow velocities increasing by between 26 and 86%. This is reflected in the results for TKE which show areas of high velocity gradients, where shear zones exist between low flow within patches and faster flow outside. The impact of removing vegetation in this manner is shown in detail by comparing the before and after-cut results for streamwise velocity and TKE at the water surface between 60m and 110m (Figure 8.1.7).

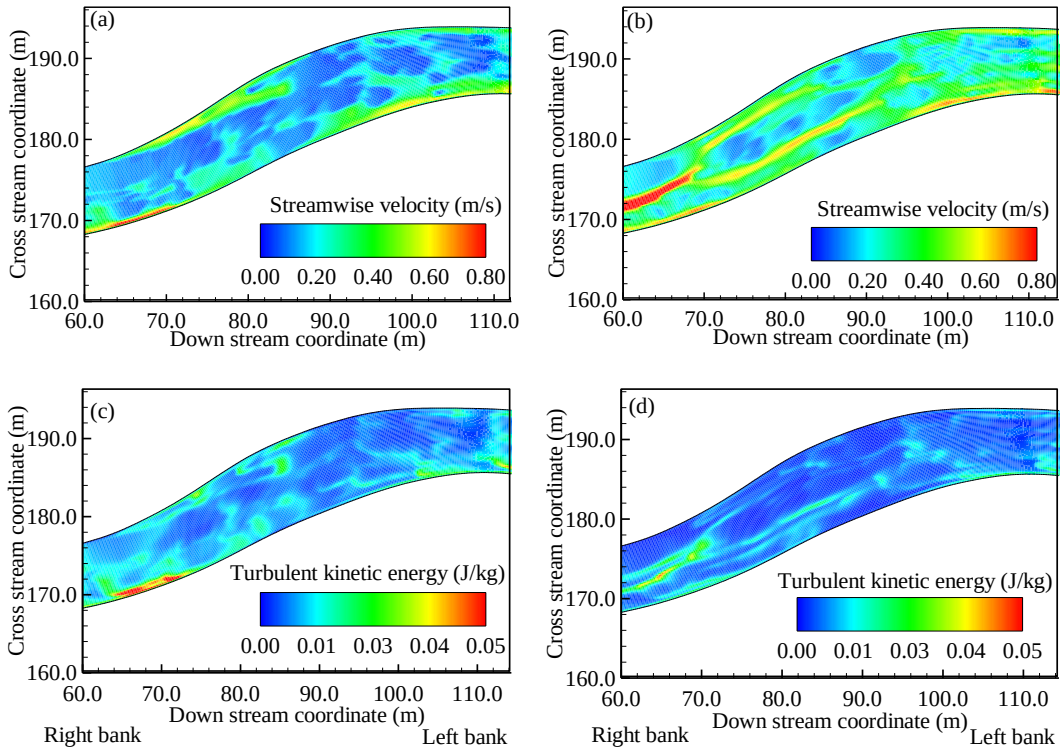

Figure 8.1.7: Planform results at the water surface for (a) Streamwise velocity May 2011 before cut; (b) Streamwise velocity May 2011 after-cut; (c) Turbulent kinetic energy May 2011 before cut; (d) Turbulent kinetic energy May 2011 after-cut.

In the region shown in Figure 8.1.7, before the vegetation cut, flow is predominantly diverted to the channel margins, with correspondingly high values of

TKE in these regions. The distribution of flow velocities is very patchy following the cut. Flow can be seen to be high at the channel centreline before deflecting around a patch of vegetation left behind during the cut (see Figure 7.2.1). The deflection is highlighted when analysing TKE, the magnitude of which is particularly high at the point of deflection at the patch root (70m downstream, 174m cross-stream). The high velocity gradients at the patch margins generate shear zones, producing high turbulent kinetic energy, areas of which are clearly evident in Figure 8.1.7d following the cut.

8.1.1.Discussion

Overall, results show how the spatial patterns of in-channel macrophytes vary following management in the form of cutting. The model captures the expected pattern of low velocities within plant patches with flow accelerating around patch margins. A key difference between flow modification in November 2010 and May 2011 can be seen. During November 2010 before the vegetation cut takes place, flow is distributed evenly over the reach planform. However, in May 2011 before the vegetation cut, flow is predominantly diverted towards the channel margins. The overall impact of this flow diversion was to create areas of slow flow through the centre of the channel. A similar trend was observed by Cotton *et al*. (2006) on a reach of the River Frome near Pallington, Dorset. They found that discrete patches of *Ranunculus* could not be discerned during May and July due to its high density, leading to a diversion of flow towards the channel margins.

The overall impact of the two vegetation cuts on the River Lambourn can also be summarised in terms of (i) percentage of vegetation removed; (ii) change in water depth; (iii) change in channel roughness and (iv) change in conveyance capacity (Table 8.1.3). Overall channel roughness is expressed using Manning's *n*.

Although it has been argued that this is not appropriate for representing the flow resistance due to vegetation (e.g. Gioia and Bombardelli, 2002), its values are included for comparison with existing studies.

Conveyance capacity was calculated for the bankfull level at XS2. The bankfull level was defined as that measured in July 2008. Using this level, the cross sectional area (A) and hydraulic radius (R) were calculated and the channel slope *S* determined using the staff gauge boards. To determine conveyance capacity for the November 2010 and May 2011 cases, Equation 8.1.1 was used, specifying the hydraulic radius and cross sectional area as measured in July 2008. Manning's *n* was set as the value calculated for the November 2010 and May 2011 cases in Table 8.1.3.

$$Q = \frac{1}{n} A R^{2/3} \sqrt{S}$$

8.1.1

Table 8.1.3: Change in percentage vegetation cover, flow depth, reach mean streamwise velocity, Manning's *n* values and conveyance capacity following vegetation cuts.

Case	Vegetation coverage by planform area (%)	Water level (m)	Manning's *n*	Conveyance capacity (m^3s^{-1})
November 2010 – before cut	61.15	90.81	0.14	2.06
November 2010 – after-cut	23.27 (-61%)	90.68 (-17%)	0.07 (-50%)	3.99 (+94%)
May 2011 – before cut	51.53	90.98	0.17	1.60
May 2011 – after-cut	33.61 (-35%)	90.81 (-18 %)	0.09 (-47%)	3.04 (+90%)

The vegetation cuts removed ~61% and ~35% of total vegetation planform area for the November 2010 and May 2011 cuts respectively, with a corresponding drop in water level of 0.13m and 0.17m. The drop in water level resulted largely from the removal of vegetation as changes in discharge were small (~8% and ~12%). The removal of vegetation led to a corresponding decrease in overall roughness, represented by Manning's *n*, of ~50% and ~47%. An increase in calculated values of conveyance capacity following vegetation cuts was ~94% and ~90% for November and May respectively, with a marginally larger increase in conveyance capacity occurring for the November 2010 cut due to the percentage of vegetation removed. Monitoring of previous cuts undertaken on the CEH River Lambourn Observatory between 2008 and 2010 by Old *et al*. (2014) showed comparable increases in conveyance capacity of between 89 and 141%.

8.2.Assessment of model results

In reality, there is local variation in the micro-topography of the gravel bed and in the structure of vegetation at both the patch and sub-grid scale. As it was not practically possible to survey all of this local variation, parameters relating to gravel (Section 4.4) and vegetation (Section 6.2) were specified as a mean value of spatially distributed samples taken within the modelled reach. With regards to patch morphology, the depth dimension was represented using an idealised shape fitted to a limited number of field measurements. The approximation of bank height (Section 4.2.5), necessary to generate topography for the model, may also have some bearing on the model predictions. Hence, the results from the model represent those of a simplified representation of the complex field case. The overall performance of the

model was assessed for a series of four cross-sections both in terms of the ability of the model to predict expected changes in flow velocity and turbulent kinetic energy following vegetation removal and in relation to field measurements.

The effects of vegetation removal over a cross section are shown for the May 2011 cut at cross-sections XS2A, XS2, XS3A and XS3 (Figure 8.2.1) for streamwise velocity (Figure 8.2.2) and turbulent kinetic energy (Figure 8.2.3). Before the vegetation cut (left column of Figure 8.2.2 and Figure 8.2.3) flow can be seen to be predominantly down the channel margins, with low flow velocities within the vegetated zone. Following the vegetation cut, the distribution is markedly different with zones of high velocity distributed across the cross sections. The reduction in velocity at the channel margins is evident for XS2A and XS2, with three clear channels now present in these cross sections. Referring to Figure 8.2.1, it can be seen that these channels of higher velocity correspond to where vegetation was removed, particularly along the channel centreline. The presence of these clear channels is also reflected in the TKE results (Figure 8.2.3) with high values of TKE occurring where flow accelerates between vegetation patches. At XS3, two channels of higher velocity following the cut can be identified at 176.5m and 181.5m across the channel, again reflecting where vegetation was removed (Figure 8.2.1). At XS3 very little vegetation was removed, hence, only small changes in velocity and TKE can be seen.

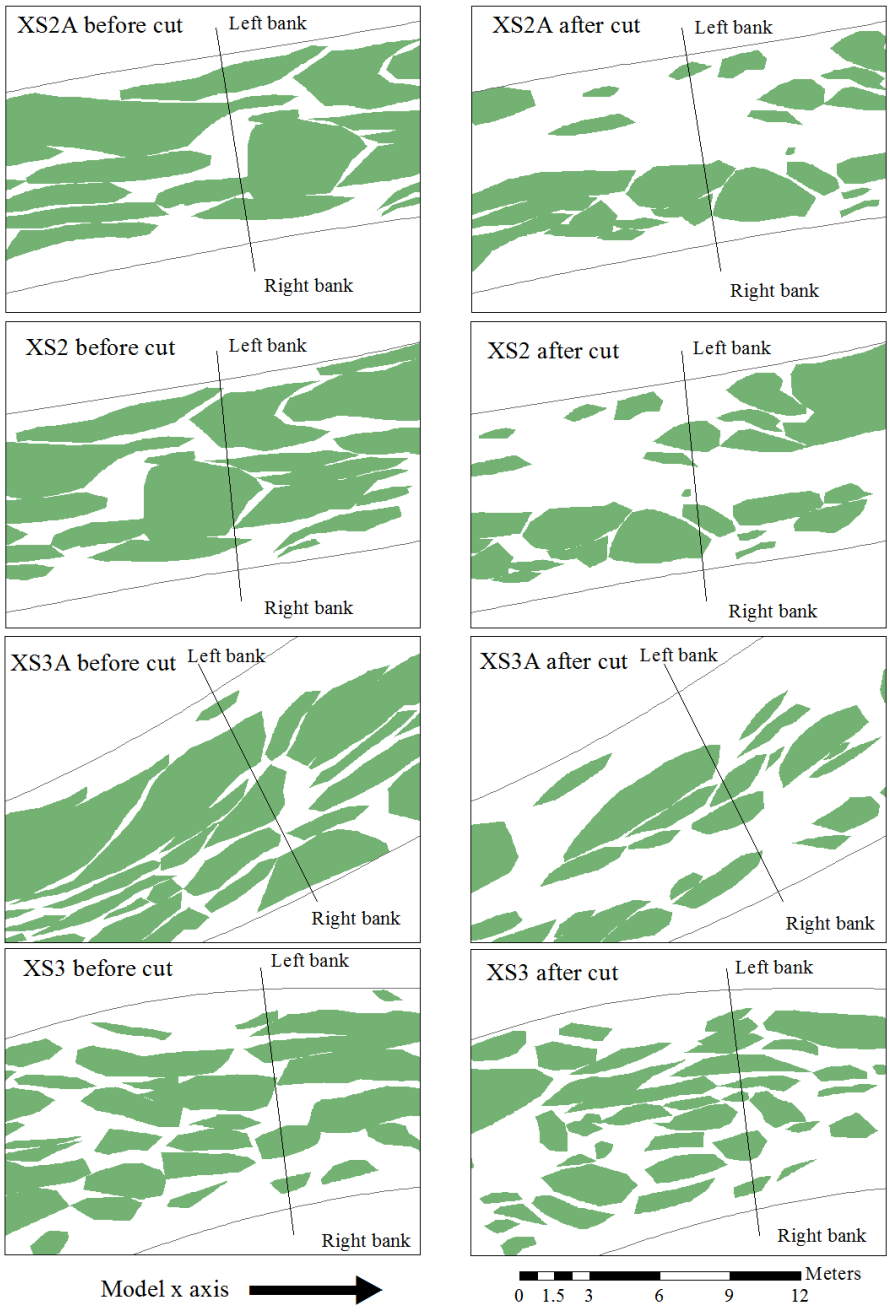

Figure 8.2.1: Change in vegetation patch coverage following the May 2011 cut at XS2A, XS2, XS3A and XS3.

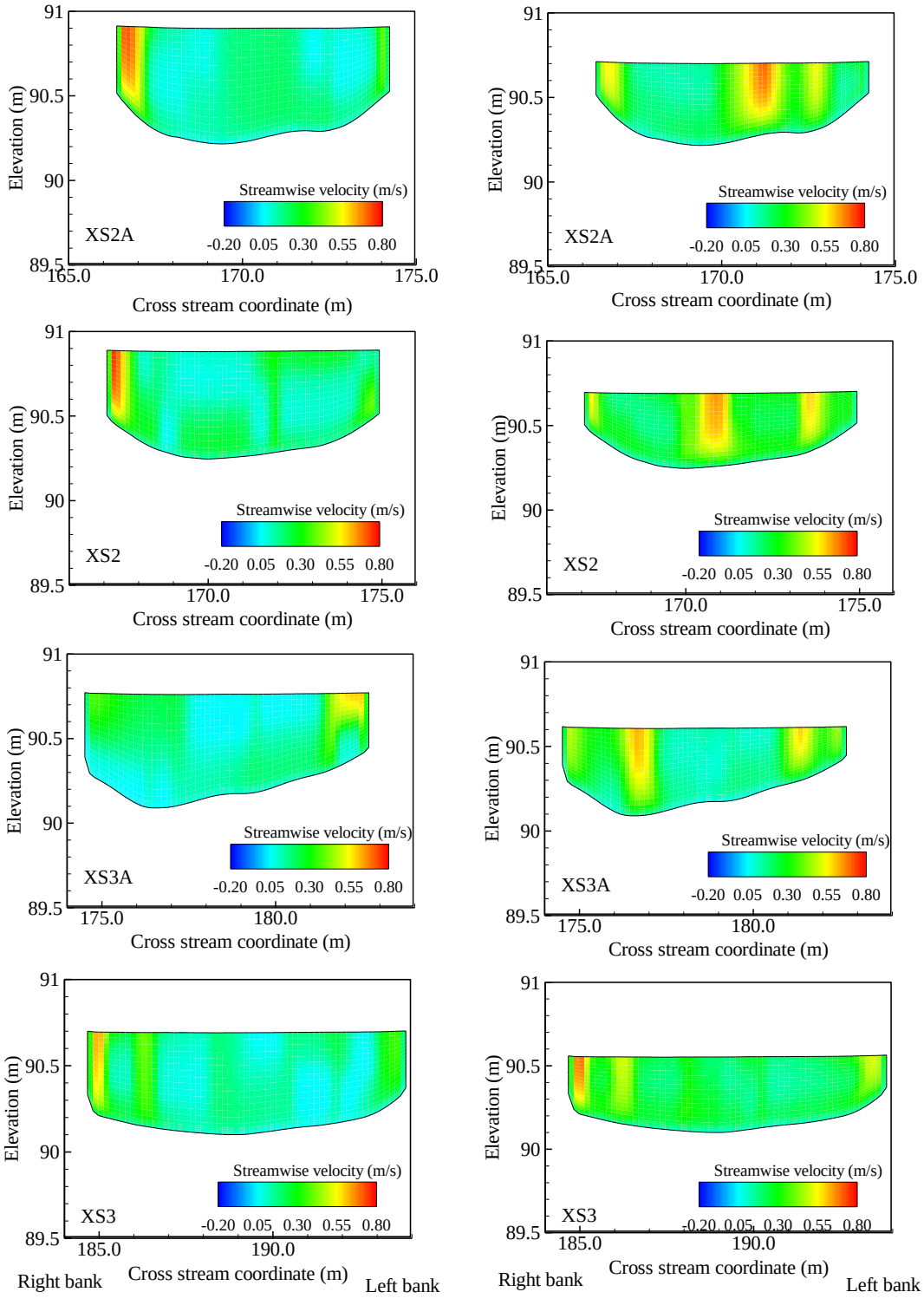

Figure 8.2.2: Cross sectional streamwise velocity before and after May 2011 vegetation cut.

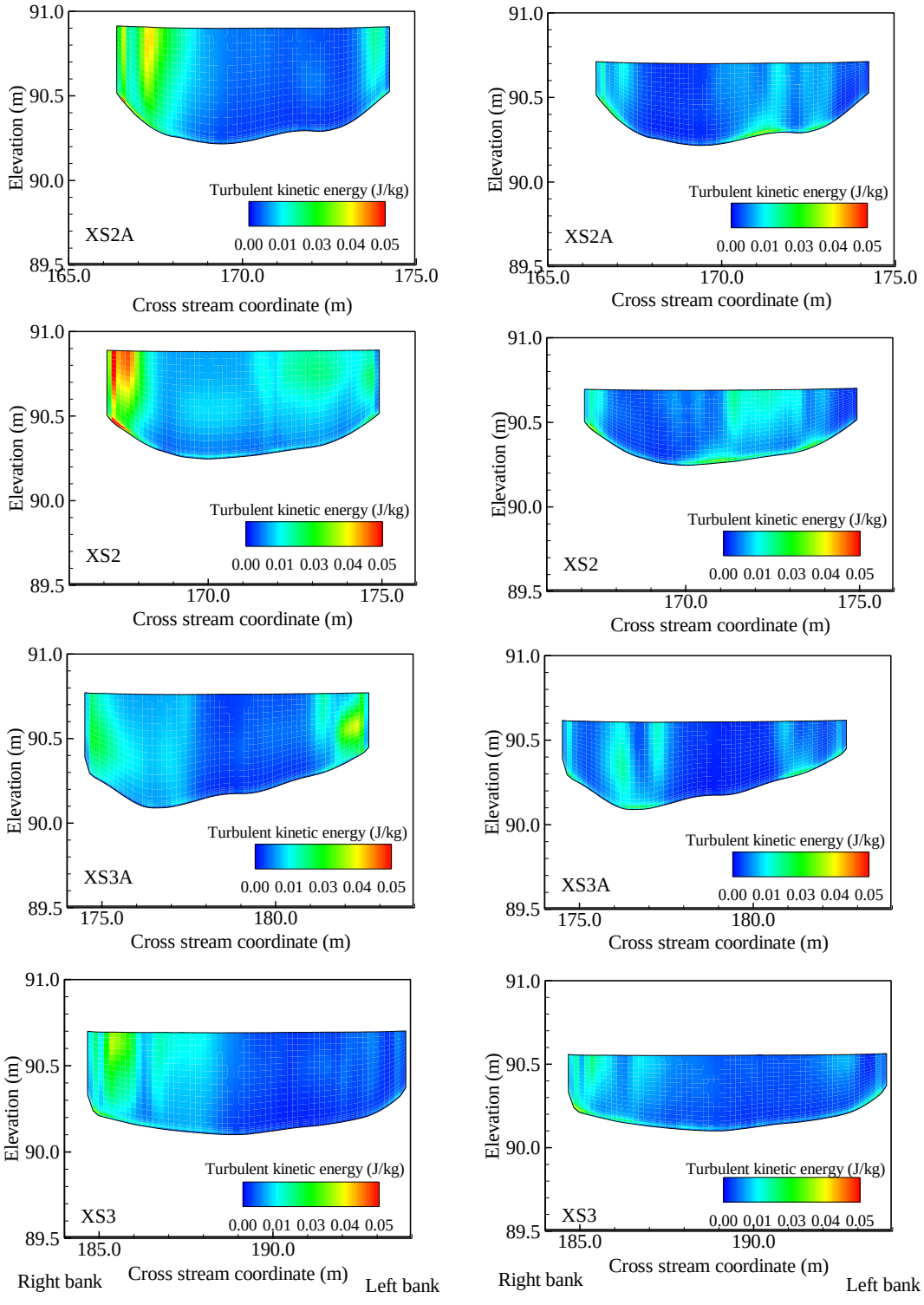

Figure 8.2.3: Cross sectional turbulent kinetic energy before and after May 2011 vegetation cut.

The results presented, along with those in section 8.1, show the ability of the model to reflect the impact of vegetation removal on the spatial patterns of velocity and turbulent kinetic energy. A quantitative assessment of model results was performed by comparing model predictions of streamwise velocity and turbulent kinetic energy at the four cross sections to field measurements for the May 2011 before and after-cut cases. In order to directly compare model results to the measurements taken in the field, it was necessary to resolve the Cartesian *x* (u_x) and *y* (u_y) velocities in order to obtain velocity predictions perpendicular to the cross section of interest. To achieve this, the cross section angle (θ) was determined and the streamwise (u) and lateral (v) components of velocity determined using the equation:

$$u = u_x \sin\theta + u_y \cos\theta$$

$$v = u_x \sin\theta - u_y \cos\theta$$

8.2.1

EMCM measurements were aligned perpendicular to the cross section in the field. ADV measurements were rotated in order to align the streamwise and lateral components of velocity to the model cross section, as described in S 5.4.2. A 3x3 grid (Figure 8.2.4) surrounding the velocity measurement is used to provide an estimate of the range of model results in the vicinity.

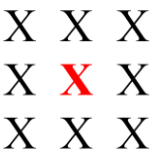

Figure 8.2.4: Representation of model results. Location of flow measurement shown in red, with surrounding points used to determine the range of neighbouring model cells.

This is necessary as EMCM and ADV are point measurements at a small scale (e.g. $3.46x^{10-7}m^3$ for the ADV), whilst model results are an average flow within the model cell scale ($0.0006m^3$). Considering Figure 8.2.5, if a flow measurement was taken at a point outside a vegetation patch (represented by the black cross), the model cell within which the flow measurement falls may be partly occupied by vegetation. The velocity reported by the model is an average of the entire cell. Hence, model results in nearby cells A, B, C, E or H may be more representative of that measured in the field, as these cells do not contain vegetation. Consequently, the measured profile may match one of the extremes of the range given rather than lying in the centre of the range.

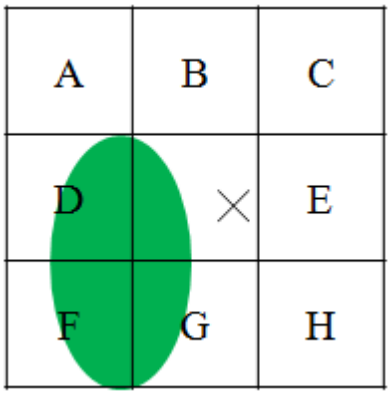

Figure 8.2.5: Illustration of the issue of point measurement versus grid cell average. Black cross represents the point at which a velocity measurement was taken in the field. Vegetation patch shown in green.

Results are presented on a cross-section basis, moving downstream in the order XS2A, XS2, XS3A and XS3, with paired before and after-cut data to show differences in flow following vegetation cuts. Measurements relating to TKE are presented separately in order to show their relation to local vegetation patch structure.

8.2.1. Streamwise velocity results

Figure 8.2.6 and Figure 8.2.7 show results for XS2A before and after the vegetation cut respectively. The reduction in water surface elevation after the cut is reflected in both the field and model results. Overall the model reasonably predicts differences in velocity within (profile C-C) and outside (profile D-D) vegetation patches for the before cut case (Figure 8.2.6). Model performance at the channel margins however is poor, as evidenced in profile A-A. Here the model over-predicts velocity which suggests that resistance in the near bank area in the model is not sufficient. This could be due to the lack of riparian vegetation in the model, under-representation of bank roughness, or a result of the bank angle prediction undertaken (Section 4.2.4) and mesh simplification (Section 7.1.2).

Predictions for the after-cut case (Figure 8.2.7) are more varied, particularly when compared to the EMCM data. Again, model performance is poor in the near bank area. However, the model captures the increase in flow velocity where vegetation has been removed at profiles F-F and G-G. At profile E-E, the depth averaged flow velocity has increased substantially from 0.18 ms^{-1} to 0.55 ms^{-1} when compared to the equivalent location in Figure 8.2.6. Although there is no change in vegetation at this profile, the water depth has decreased leading to a marked increase in velocity for the near-similar discharge.

Figure 8.2.8 and Figure 8.2.9 show the results for XS2 before and after the vegetation cut respectively. Again the model performs reasonably well with regards to differentiating between low and high velocities within and outside vegetation patches. Velocity is often slightly over predicted, however the general form of the velocity profiles match reasonably well with those measured in the field. An exception to this is profile F-F in Figure 8.2.9. Here, high velocity underneath the plant is predicted by the model, with lower velocities in the centre of the profile. The field measurements, however, imply that vegetation volume occupancy is highest close to the bed, with decreasing volume occupancy towards the water surface. This suggests that, for this profile, the vegetation shape applied in the depth dimension was not appropriate. Predictions at the channel margins fall within the range of the results from the model, represented by the error bars, both before and after the vegetation cut.

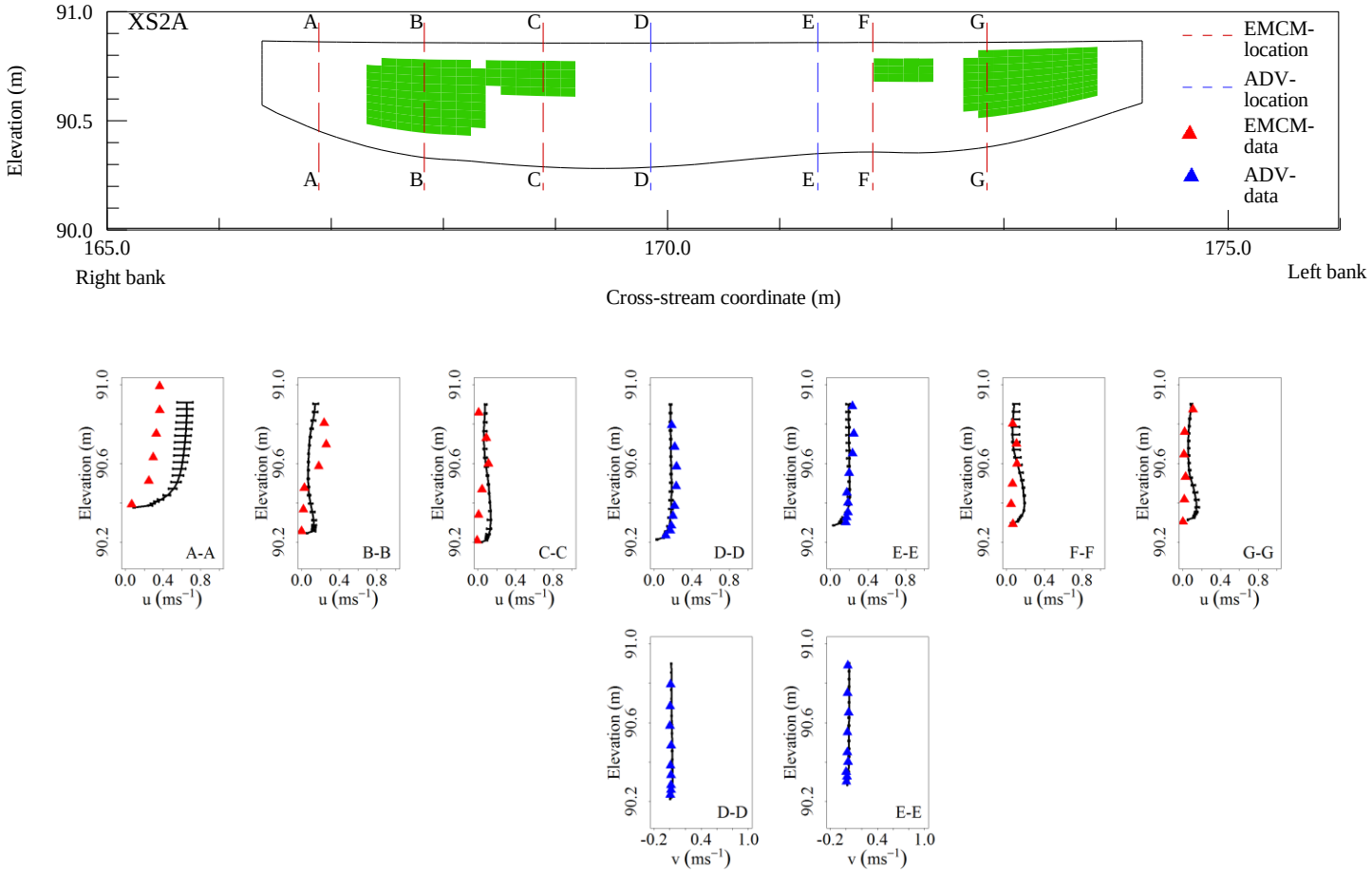

Figure 8.2.6: Comparison of model streamwise velocity against field measurements for XS2A May 2011 before cut case.

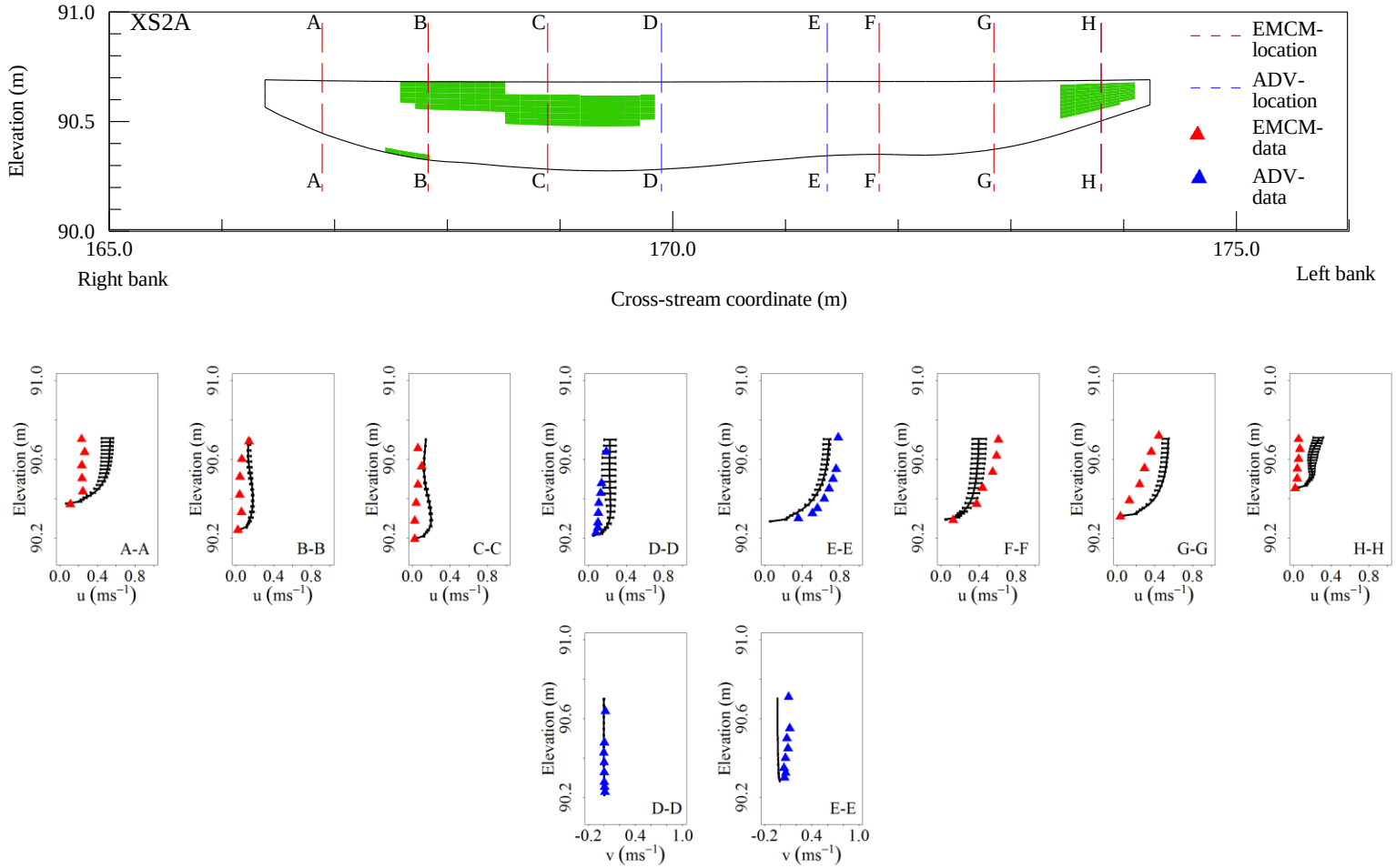

Figure 8.2.7: Comparison of model streamwise velocity against field measurements for XS2A May 2011 after-cut case.

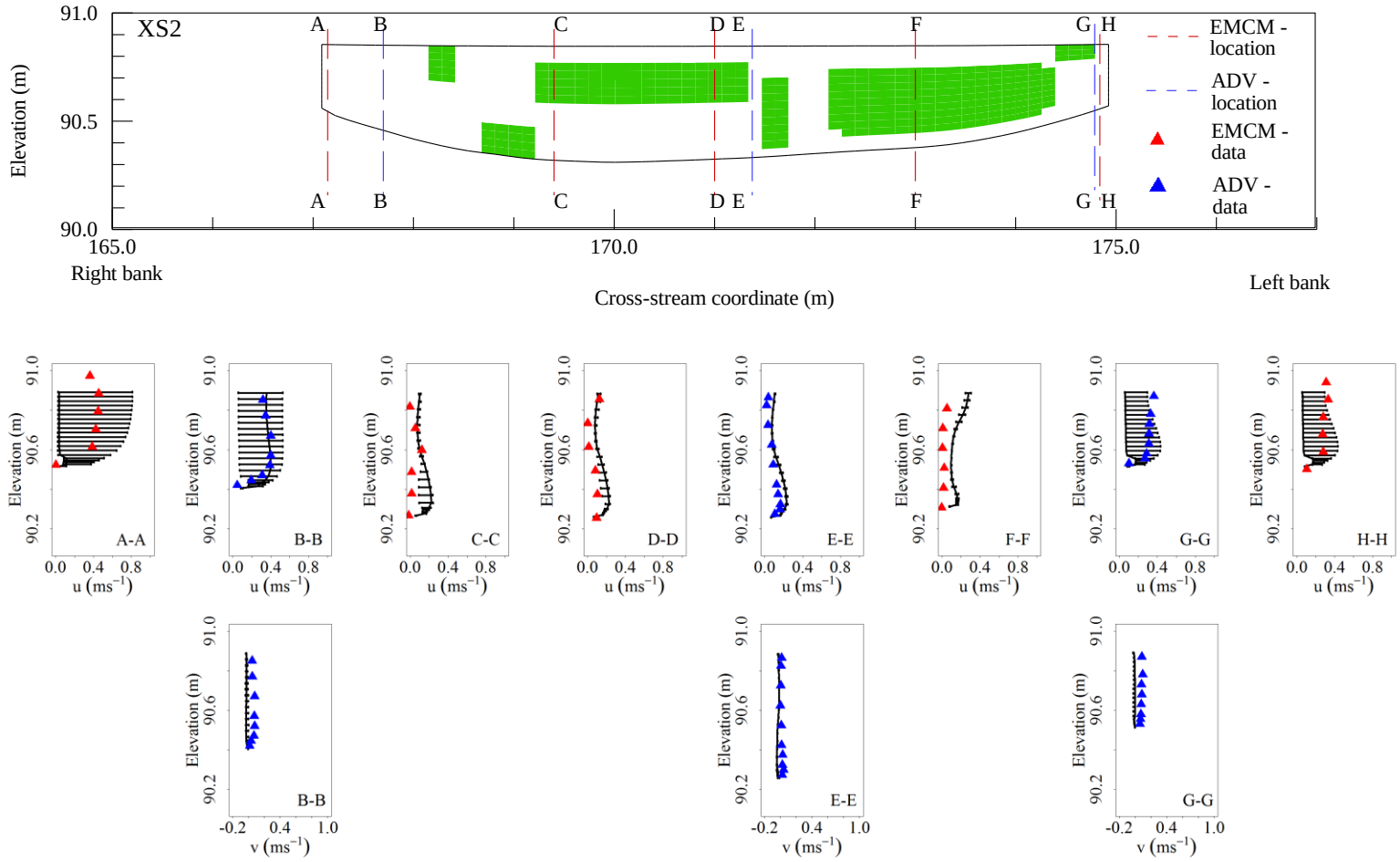

Figure 8.2.8: Comparison of model streamwise velocity against field measurements for XS2 May 2011 before cut case.

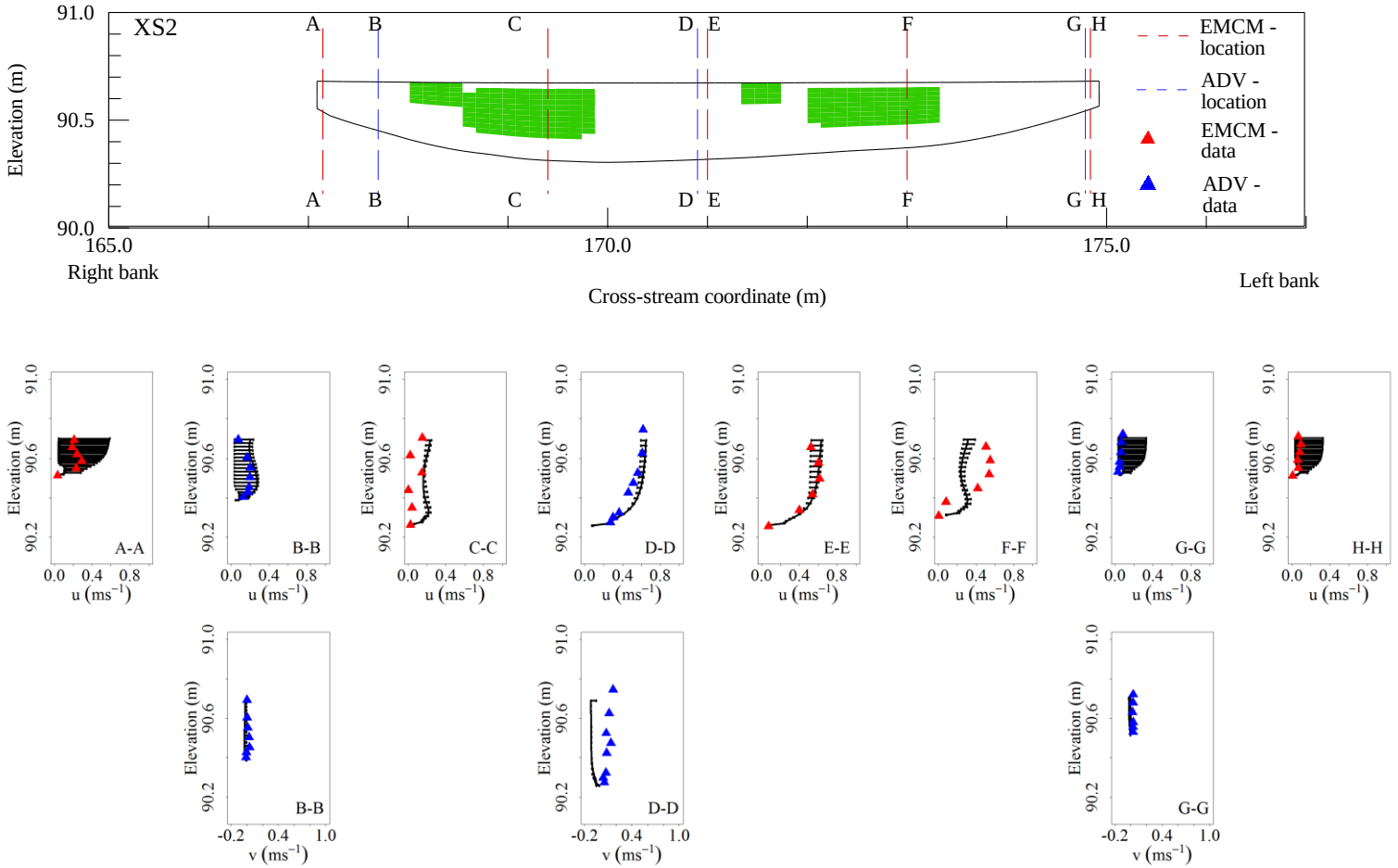

Figure 8.2.9: Comparison of model streamwise velocity against field measurements for XS2 May 2011 after-cut case.

Moving towards the downstream extent of the modelled reach, results for XS3A are shown in Figure 8.2.10 and Figure 8.2.11. XS3A is the widest cross section in the modelled reach. At profiles C-C, D-D and H-H, the final point of each EMCM measurement are outside the water level in the model by approximately 0.05m. This implies that, at these locations, either the water depth in the model is not correct or the foot of the wading rod upon which the EMCM is mounted is sat on a gravel particle protruding from the channel bed. Over the cross section as a whole, field measurements imply that the vegetation location in the depth dimension is incorrect within the model. For example, profile A-A in the before cut case is predicted well in the region close to the channel bed. However, field measurements of velocity suggest that vegetation volume occupancy increases towards the water surface shown by flow retardation in this region. This is not captured within the model. A possible reason for this is estimation of the vegetation depth occupancy based upon an idealised shape applied to all plant patches of the same species. Flow retardation in profile A-A may also be attributed to riparian vegetation trailing in the water. In other locations, e.g. profile F-F in the after-cut case, it is one of the extremes of the range of model results, represented by the error bar, which matches the measurement (as explained in Figure 8.2.5). Here, the presence of vegetation was captured by the minimum modelled velocity profile.

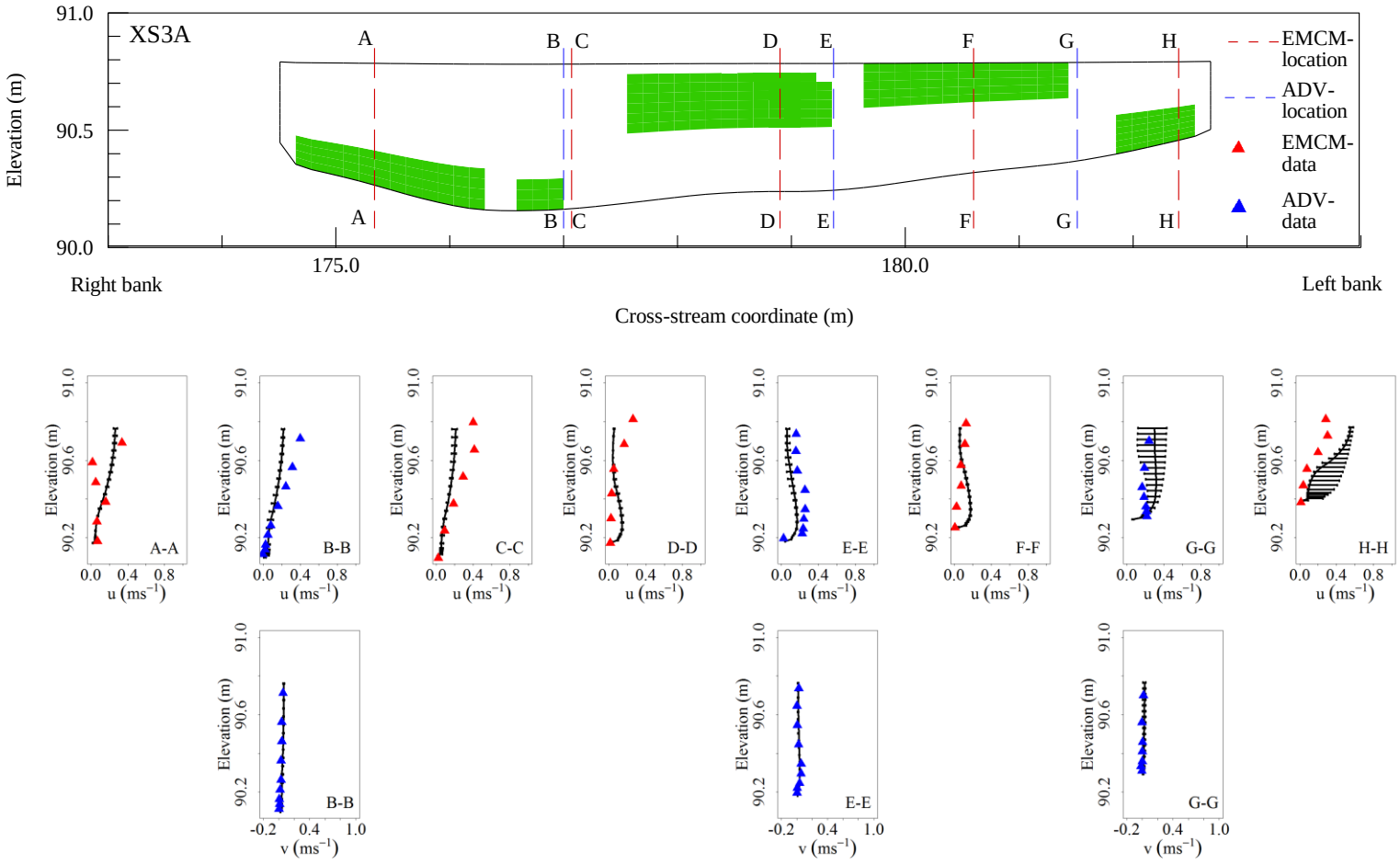

Figure 8.2.10: Comparison of model streamwise velocity against field measurements for XS3A May 2011 before cut case.

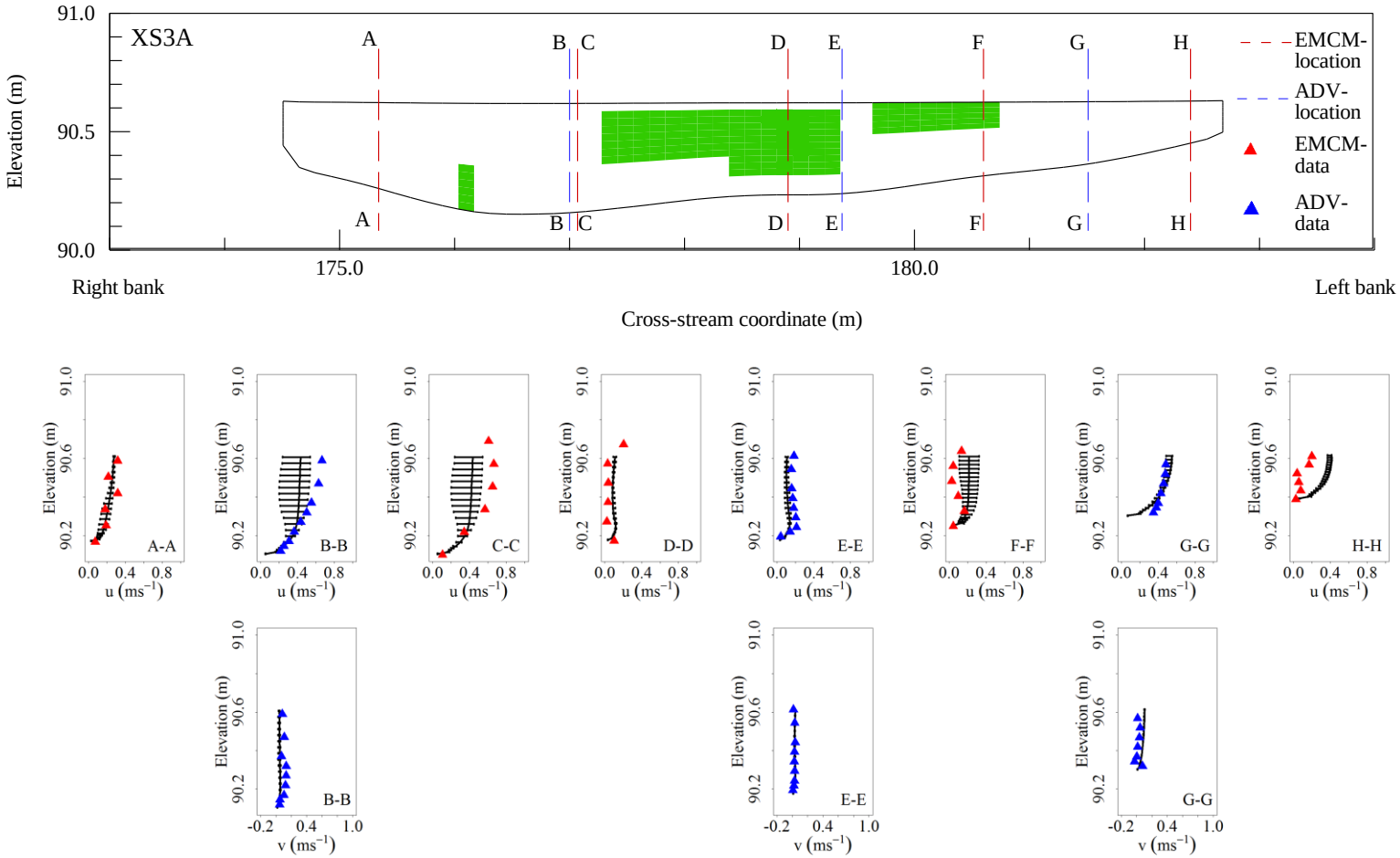

Figure 8.2.11: Comparison of model streamwise velocity against field measurements for XS3A May 2011 after-cut case.

Figure 8.2.12 and Figure 8.2.13 show the results relating to XS3. Measurements for this cross section for the before cut case are limited, and as such before and after-cut comparisons for the whole cross section are not possible. There is a good match between the limited field measurements and model results in the before-cut case, with only slight discrepancies in velocity magnitude evident. For the after-cut case, the model performs well for two out of the seven velocity profiles measured (A-A, B-B). Field measurements for profiles C-C, D-D, F-F and G-G suggest that vegetation is present which is not captured by the model. At profiles C-C and D-D, field measurements imply that there is a vegetation patch which is present from the bed up to approximately half the water depth which is not captured by the model. Model results for profile E-E match field measurements up until approximately half the water depth. Above this, field measurements imply there is no vegetation. This is not captured by the model, however the low velocities exhibited may result from the close proximity of a vegetation patch upstream (Figure 8.2.1).

Overall, results from XS3, where patches are small, high in number and in close proximity to one another (Figure 8.2.1), indicate that there is an increased likelihood that patch shape is not accurately represented within the model. This may result from patches being missed when surveying due to the high number. An alternative explanation is that if a patch is cut in half in the downstream plane, its actual depth occupancy would change. However, as the patch depth occupancy is based upon relative length, the height following the cut would still extend almost to the water surface at the tip of the plant (see Figure 7.4.5).

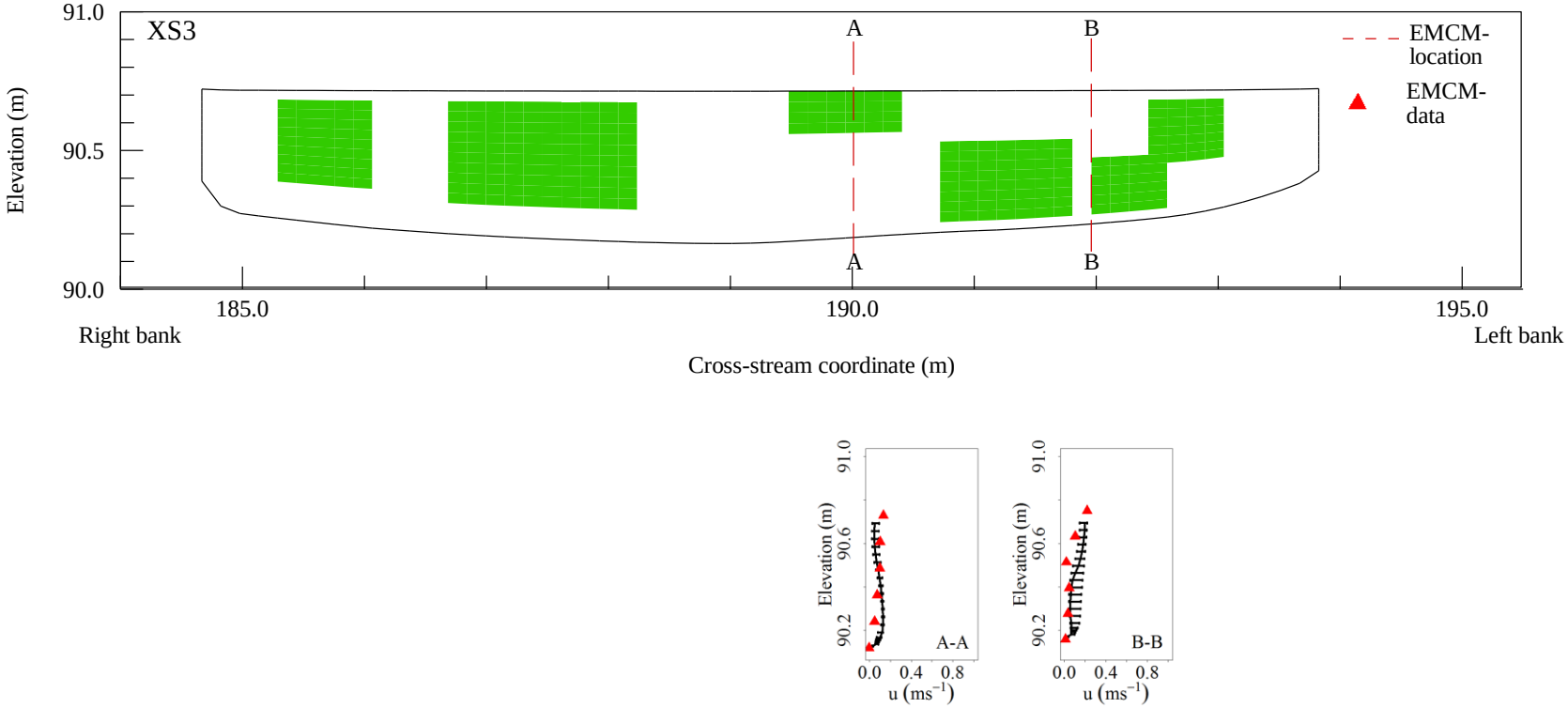

Figure 8.2.12: Comparison of model streamwise velocity against field measurements for XS3 May 2011 before cut case.

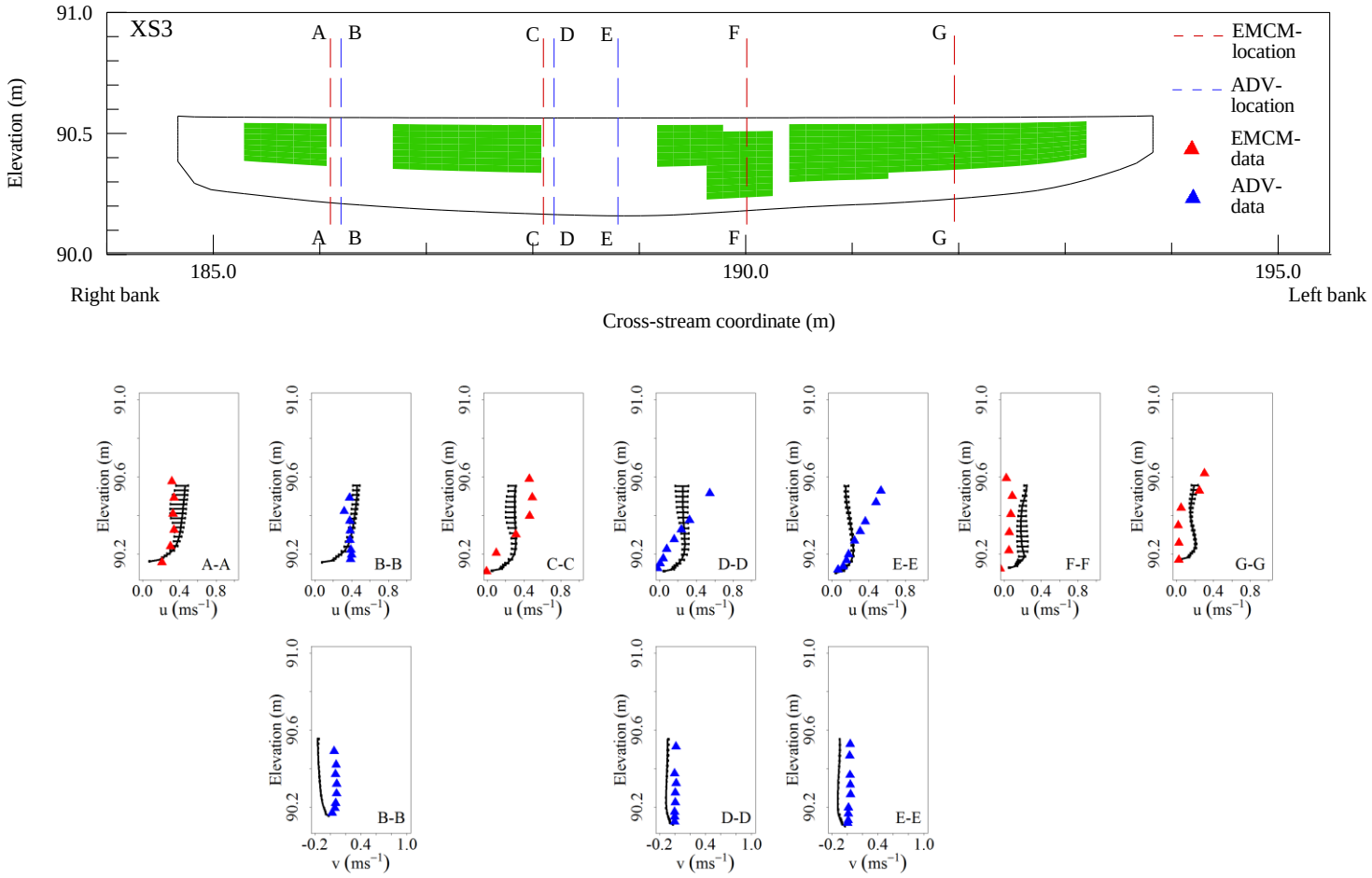

Figure 8.2.13: Comparison of model streamwise velocity against field measurements for XS3 May 2011 after-cut case.

8.2.2. Turbulent kinetic energy (TKE) results

The results of the comparison of TKE measurements undertaken using the ADV in the field against those predicted in the model for XS2A before and after the vegetation cut are shown in Figure 8.2.14 and Figure 8.2.15 respectively. The local patch morphology is also included to aid discussion of results. For XS2A in the before and after-cut cases, the prediction of TKE in the model results is reasonably accurate when compared to field measurements.

Moving downstream to XS2, in the before cut case (Figure 8.2.16), modelled results for profiles E-E and G-G for TKE show reasonable agreement. For profile B-B however, this is not the case. When analysing the gradients in the downstream velocity both in the model and field, the largest gradients are found in the near-bed area, and indeed this is reflected in the modelled TKE profile. However, the model greatly over predicts the TKE in comparison to that measured in the field. A suggested explanation for this is the close proximity of the measured profile to a vegetation patch immediately upstream. High TKE within the water column is attributable to its generation in shear zones around plant patches. In the field measurements, any TKE thus generated has been dissipated before reaching the measurement location. However, in the model this is not the case and may suggest that turbulent kinetic energy is not dissipated rapidly enough. This could possibly be corrected for by specifying additional turbulence terms in the model equations which would alter the behaviour of the production and dissipation of turbulent kinetic energy, or by using an alternative turbulence model. For the after cut case (Figure 8.2.17), the magnitude of TKE for all profiles compares well to field measurements.

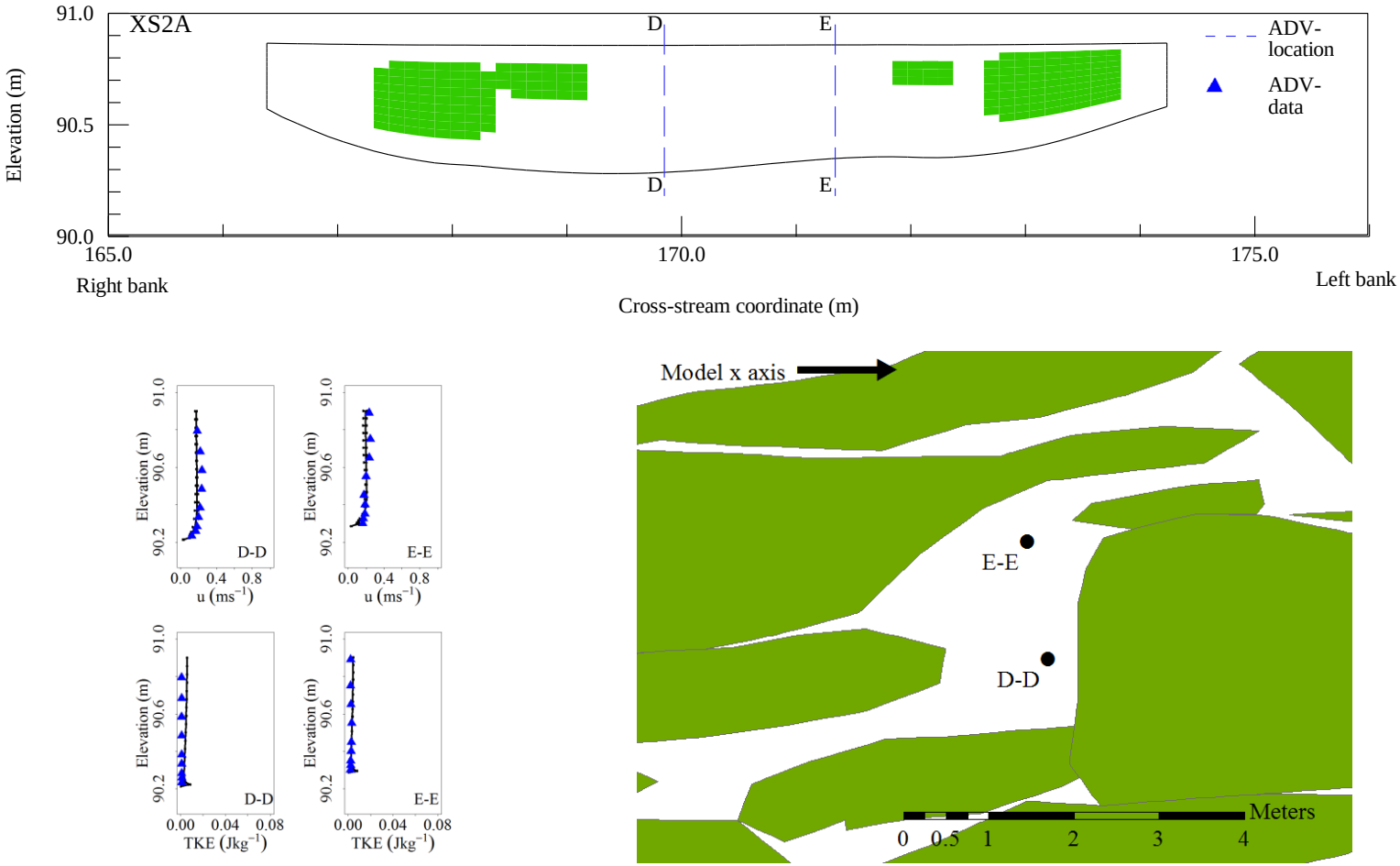

Figure 8.2.14: Comparison of model turbulent kinetic energy against field measurements for XS2A May 2011 before cut case

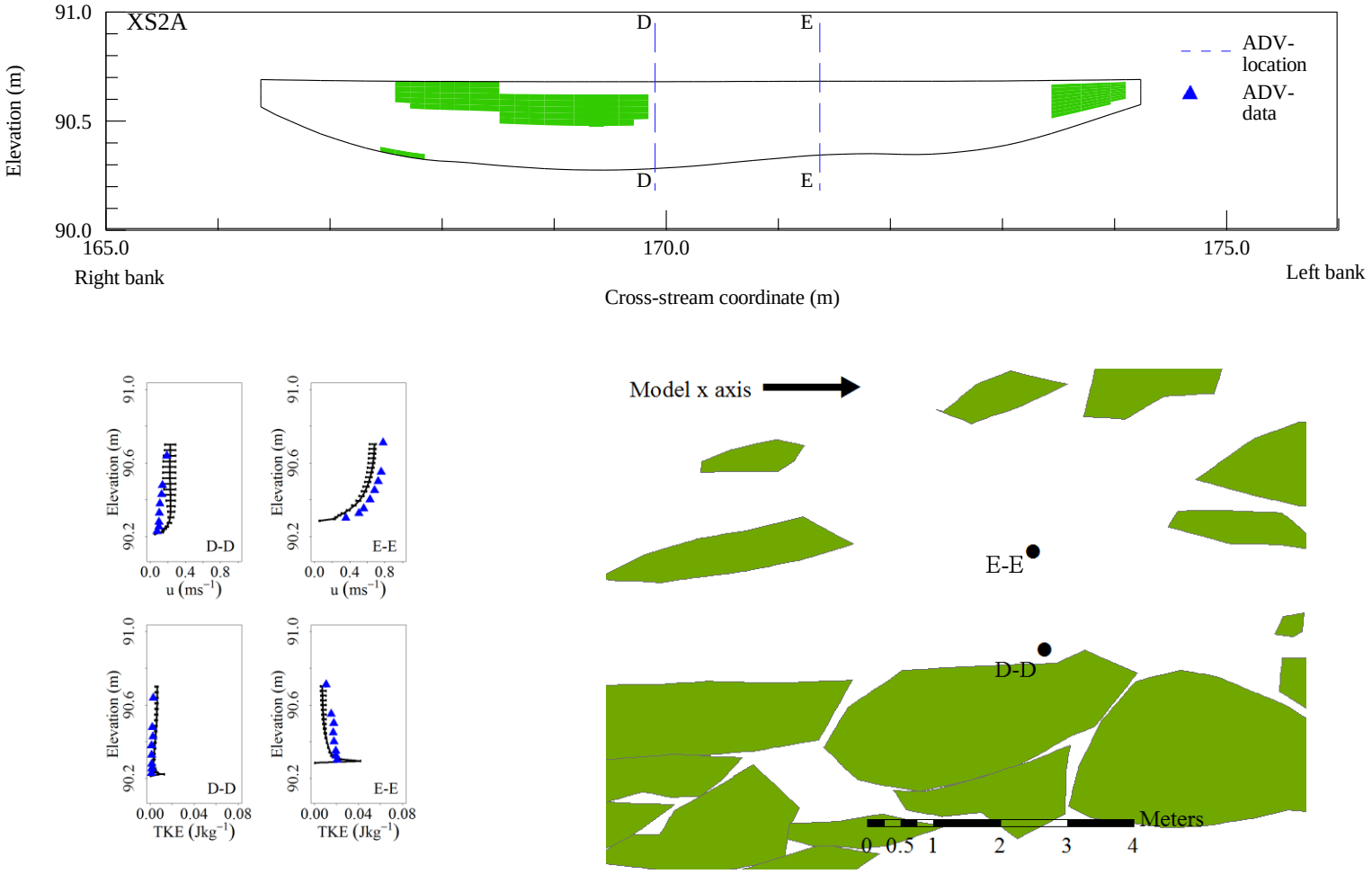

Figure 8.2.15: Comparison of model turbulent kinetic energy against field measurements for XS2A May 2011 after-cut case.

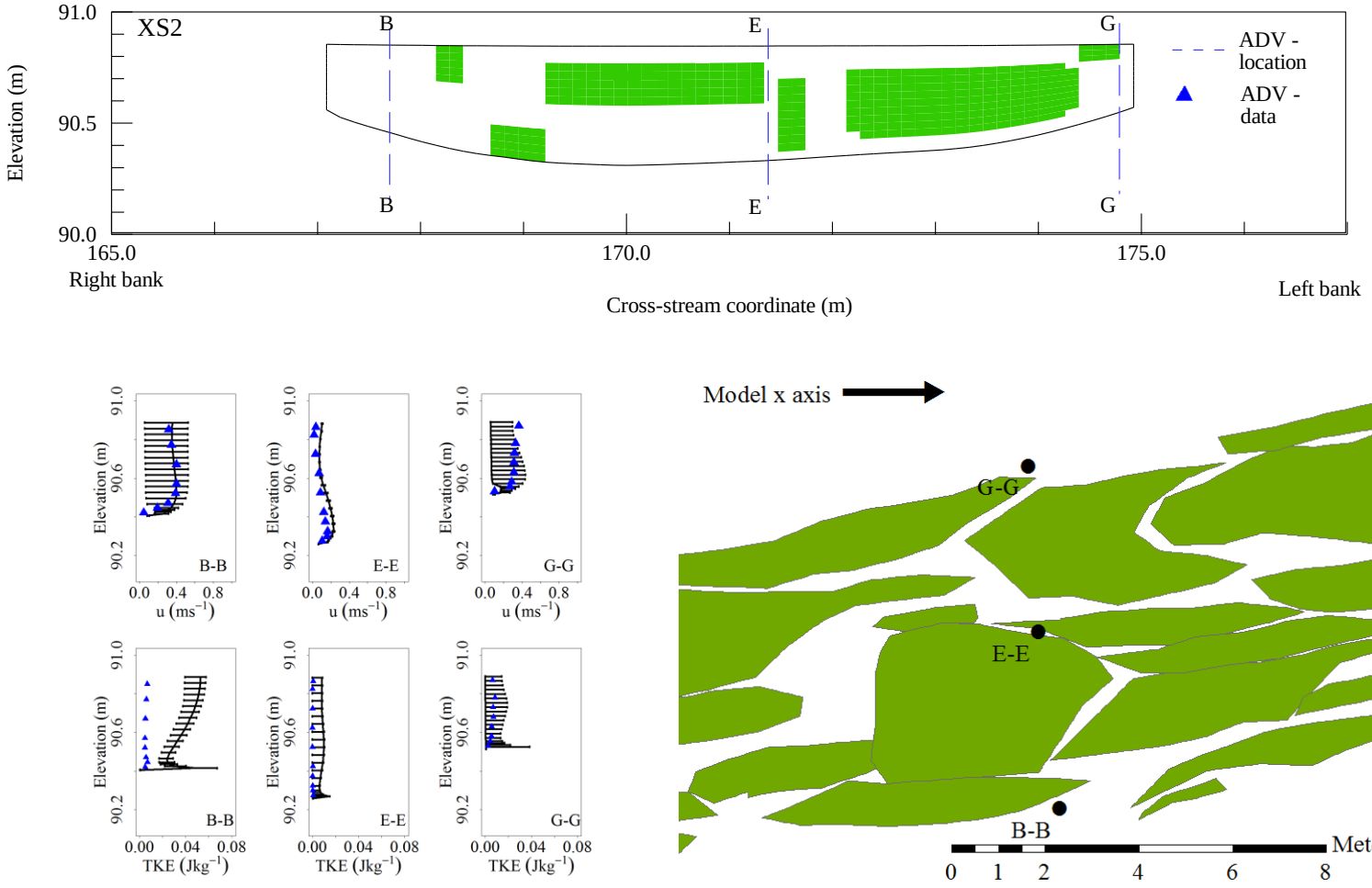

Figure 8.2.16: Comparison of model turbulent kinetic energy against field measurements for XS2 May 2011 before cut case.

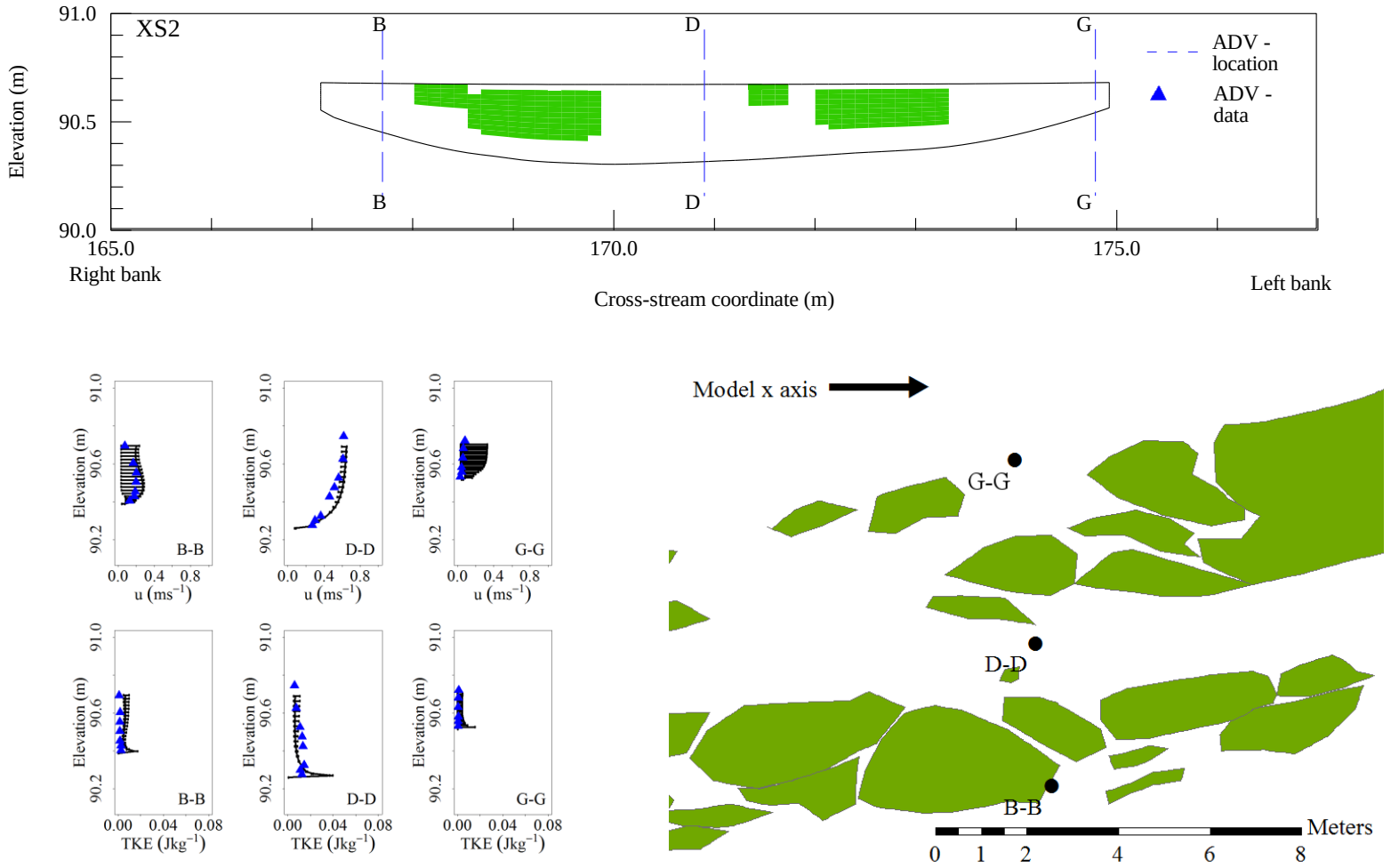

Figure 8.2.17: Comparison of model turbulent kinetic energy against field measurements for XS2 May 2011 after-cut case.

Moving downstream to XS3A for the before cut case (Figure 8.2.18), the modelled TKE profiles match well to those measured in the field for profiles B-B and E-E. Results for profile G-G are not as good, with TKE over-predicted by the model when compared to the field measurements. Here, field measurements imply that turbulent kinetic energy is low higher up in the water column. In the model, a possible reason for the additional turbulent kinetic energy exhibited is the close proximity of a patch of vegetation, around which shear zones are present. Hence, the footprint of the patch immediately adjacent to G-G may have been surveyed incorrectly. For the after-cut case (Figure 8.2.19) a good level of agreement between field measurements and model results is displayed for all profiles.

For XS3, ADV measurements were not undertaken for the before cut case. Results for the after-cut case are not good (Figure 8.2.20). If the general form of a velocity profile is logarithmic, the peak turbulent kinetic energy occurs close to the bed with an exponential decrease towards the water surface. Values of TKE at profiles D-D and E-E in the near bed region are generally well predicted by the model. However, field measurements for these profiles show high levels of turbulent kinetic energy higher up in the water column, possibly attributable to its generation in shear zones around the patch immediately upstream. This additional turbulent kinetic energy is not captured by the model.

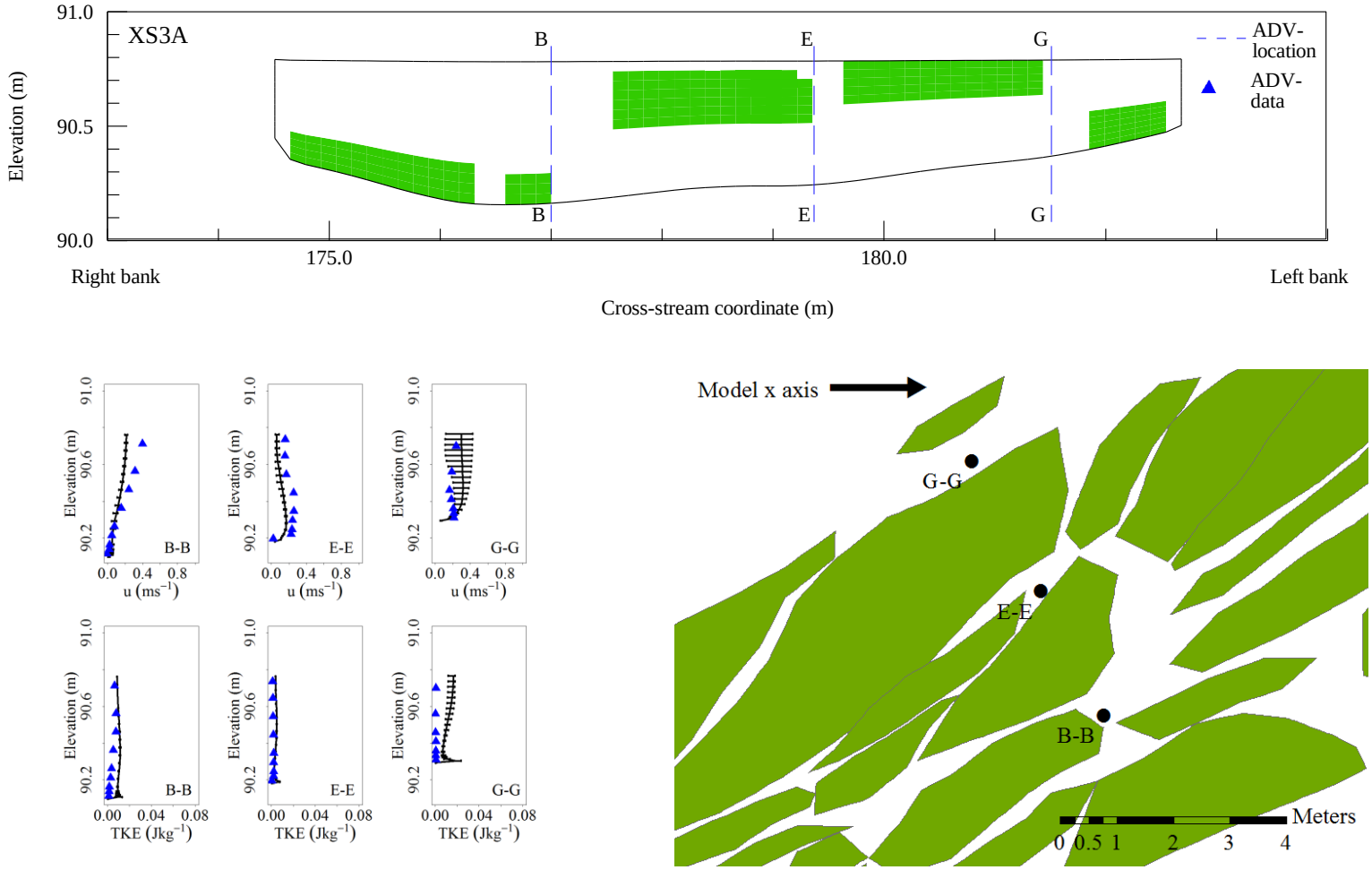

Figure 8.2.18: Comparison of model turbulent kinetic energy against field measurements for XS3A May 2011 before cut case.

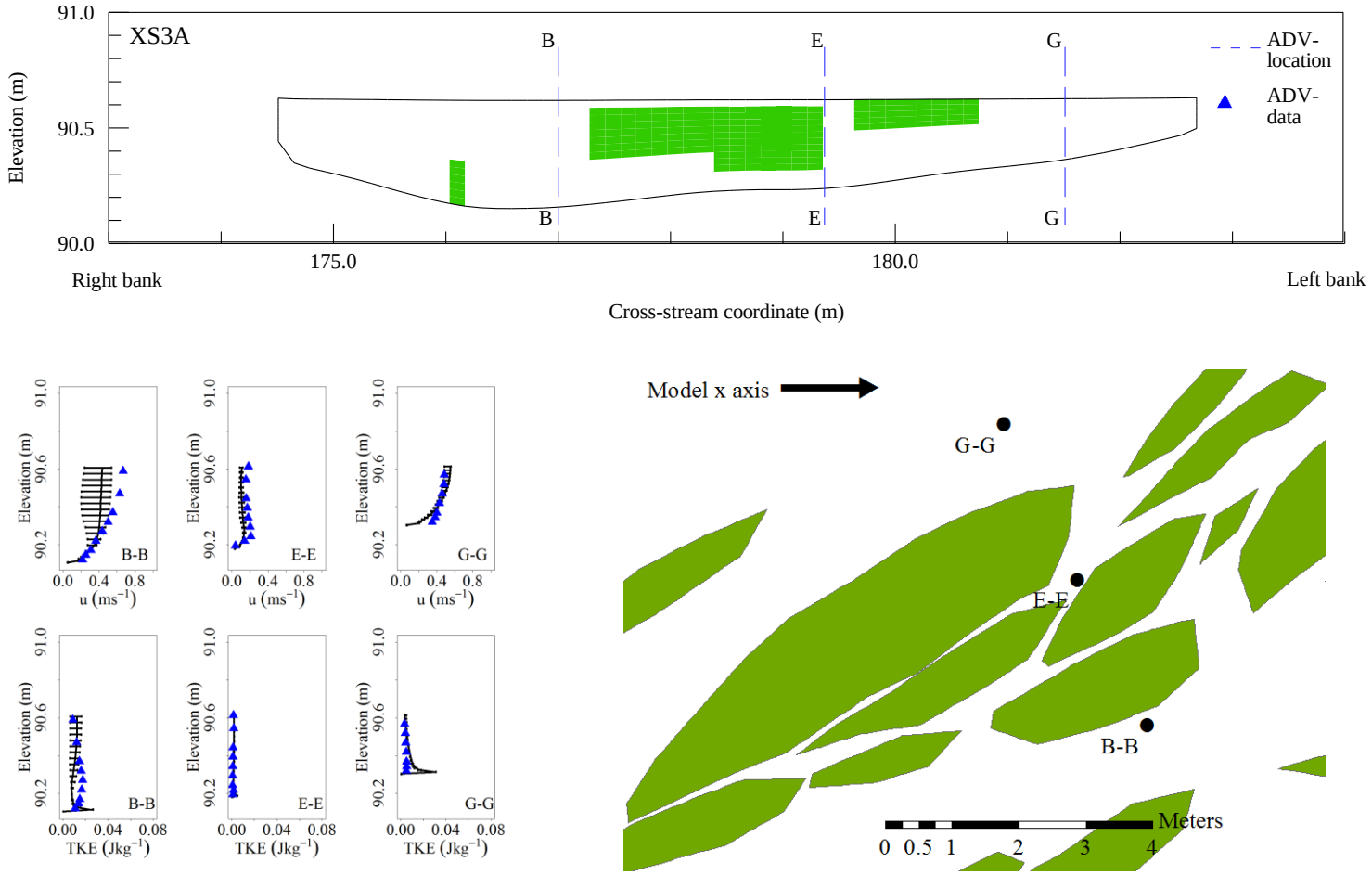

Figure 8.2.19: Comparison of model turbulent kinetic energy against field measurements for XS3A May 2011 after-cut case.

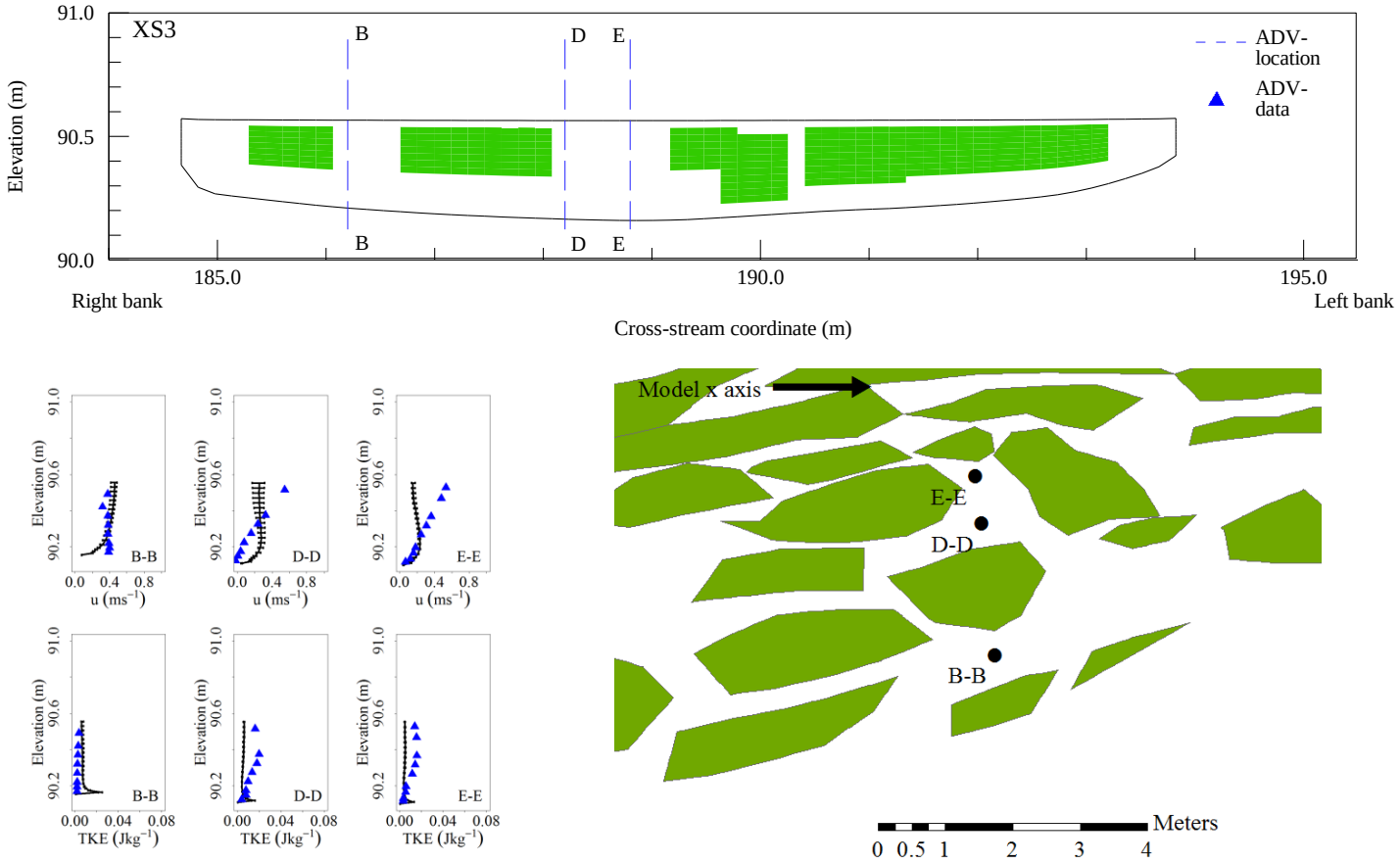

Figure 8.2.20: Comparison of model turbulent kinetic energy against field measurements for XS3 May 2011 after-cut case.

8.2.3. Overall assessment of model performance

In light of the assumptions, necessary to construct the model, outlined at the beginning of this section, the model performs reasonably well. The results presented for the May case show that the model captures (i) the spatial variation in flow within and outside vegetation patches; (ii) some of the variation in the velocity profile due to vegetation location; and (iii) local increases in velocity where vegetation has been removed during a cut. In general, the model performs poorly in the channel margins where velocity is often over predicted. This may result from additional resistance not accounted for at the channel margins as the result of spatial averaging of gravel roughness parameters, incorrect specification of the bank angle, simplification of the model mesh, or under-representation of vegetation in this region. In November 2010, EMCM measurements were also undertaken but at a number of points rather than over a cross section. There were also some ADV measurements collected but these were few due to equipment malfunction. Results for the November 2010 before and after-cut cases displayed a similar level of agreement between field measurements and model results, and can be found in the Appendix.

The removal of vegetation in the May 2011 cut allowed high flow velocities to be redistributed from being predominantly at the right bank to a number of channels through the vegetation, created by the cut. The nature of the May 2011 cut was captured well by the model (Figure 8.2.2 and Figure 8.2.3) with the impact of vegetation removal varying along the reach. In the upper extent of the reach (XS2A and XS2), a series of wide channels of vegetation were removed, In the lower reach (XS3A and XS3) vegetation was more selectively removed and this resulted in a heterogeneous distribution of velocities and hence turbulent kinetic energy following the cut. The effect of vegetation removal over a cross section observed in the results

compares well to that reported in the literature for measurements undertaken over entire channel cross sections (e.g. Marshall and Westlake, 1990; Watts and Watts, 1990; Sukhodolova, 2004; Naden *et al*., 2006; Old *et al*., 2014). These changes, coupled with the drop in water level, are likely to have important consequences for fish and invertebrate populations, given that most species have specific physical habitat requirements, defined by hydraulic variables such as velocity and turbulent kinetic energy.

With regards to the detailed assessment of modelled results, the incorporation of vegetation shape within the model appears to have been reasonably successful, with many profiles in the model comparing well to field measurements. Results shown have demonstrated that the shape of a velocity profile is entirely dependent on the location of a plant in the vertical profile. With relatively little data relating to the shape of a specific patch in the depth dimension, reasonable replication of the measured flow velocity profile can be generated within the model.

However, it is also clear that the use of an average profile limits accuracy in some areas, particularly where patches are small and high in number (XS3A and XS3). Results relating to turbulent kinetic energy are mostly well reproduced within the model. In some areas, the model has not dissipated the turbulent kinetic energy produced rapidly enough, reflected by a higher TKE in the model results compared to the field data. It is suggested that this may result from the need to include additional terms within the $\langle k-\varepsilon \rangle$ turbulence model, however further work is required to confirm this. Overall, the fit of modelled results to measured data is comparable to that observed for other studies (e.g. Naden *et al*., 2004; Rameshwaran and Naden, 2012).

8.3.Detailed assessment at the plant scale

This work has taken initial steps to represent the actual underwater shape of plant patches in the model based on measurements taken in the field, and described using a combination of mathematical functions. It is important to assess how this assumed shape affects the modelled flow at the plant scale. A single patch of *Ranunculus* was chosen for analysis from the May 2011 after-cut case. The criteria for patch selection were set *a priori* to be (i) a patch of at least 5m in length, (ii) a separation of at least 1m from any patch upstream and (iii) a separation of at least 1m from any patch downstream. The May 2011 after-cut case was chosen as patches of *Ranunculus* were at their most distinct from neighbouring patches. The selected patch is shown in Figure 8.3.1. The patch met the selected criteria, with a downstream length of 6.8m and an upstream and downstream separation distance from neighbouring patches of 1.5m and 2.0m, respectively.

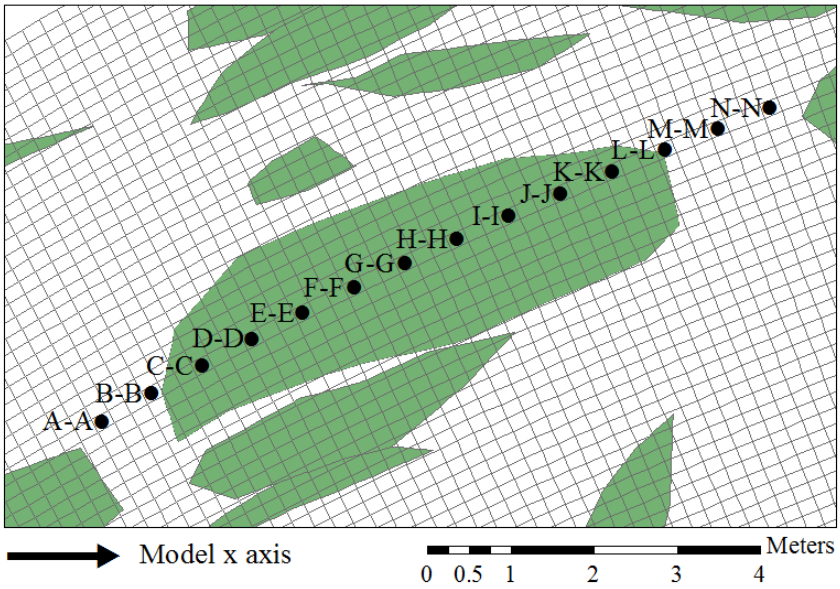

Figure 8.3.1: Patch of *Ranunculus* used to analyse flow at the patch scale.

Vertical profiles of modelled streamwise velocity, turbulent kinetic energy, and Reynolds stress were extracted before, through and after the patch at downstream intervals of approximately 0.7m. Reynolds stress (τ_R) values were resolved to the streamwise direction from the Cartesian stresses calculated in Phoenics using:

$$\tau_R = \rho\left(\tau_{zx}\cos\theta + \tau_{xy}\sin\theta\right)$$

8.3.1

where ρ is the fluid density in kgm^{-3}, τ_{zx} is the Cartesian Reynolds stress in the *x* direction on the plane perpendicular to the *z* direction in Nm^{-2}, τ_{xy} is the Cartesian Reynolds stress in the *y* direction on the plane perpendicular to the *x* direction and θ is the angle between the *x* direction and the line joining two profiles, e.g. A-A and B-B (Figure 8.3.2):

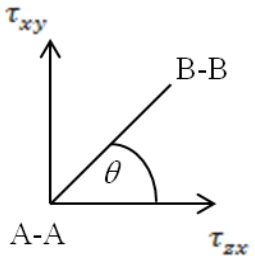

Figure 8.3.2: Definition of the angle θ to resolve the Cartesian Reynolds stresses.

A total of 14 profiles A-A to N-N are presented in Figure 8.3.3. An equivalent contour plot for each variable is shown in Figure 8.3.4 along with a superimposition of the shape of the *Ranunculus* patch as applied in the model.

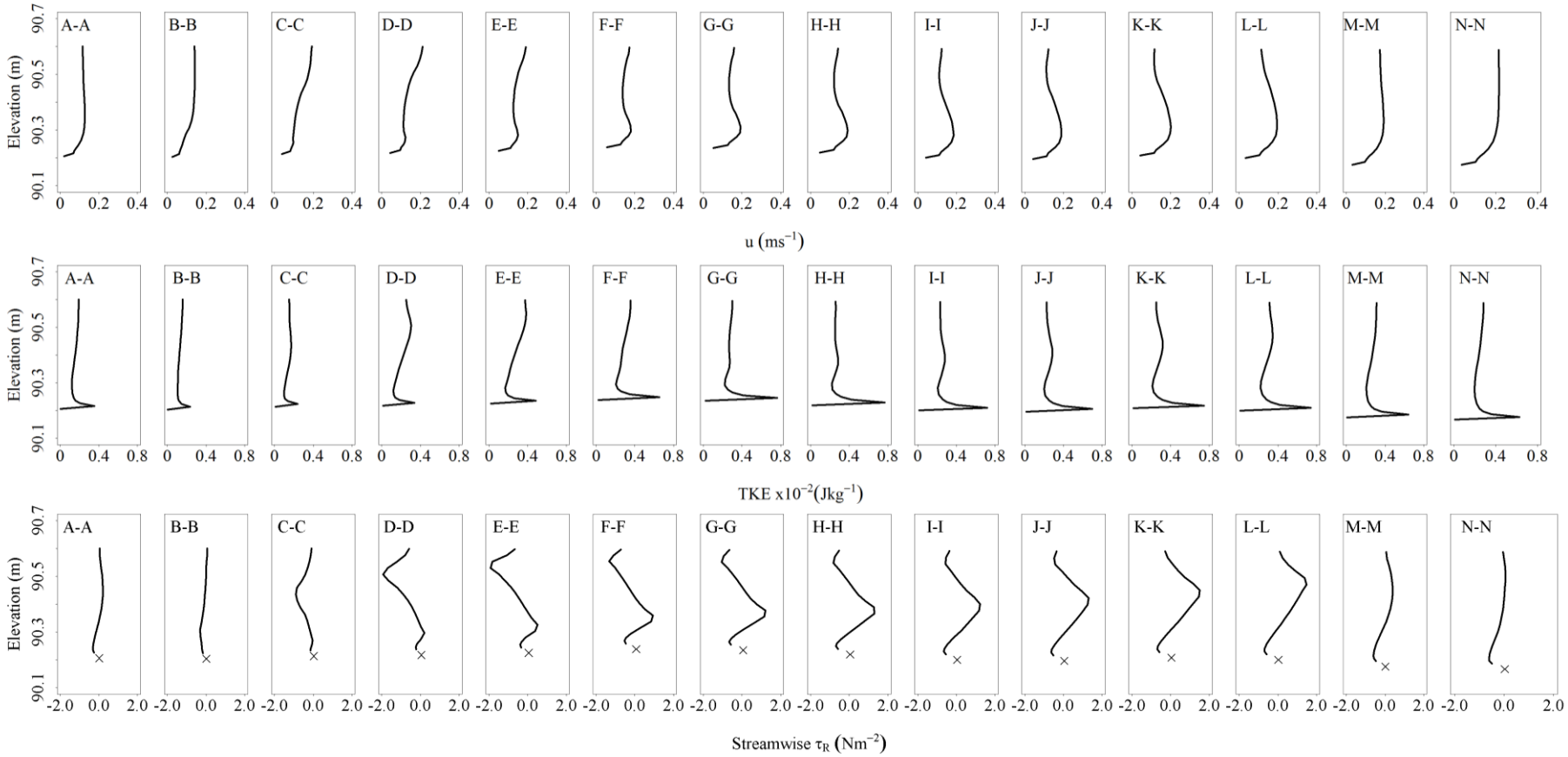

Figure 8.3.3: Profiles for streamwise velocity, turbulent kinetic energy and streamwise Reynolds stress for flow through a single patch of *Ranunculus*. Bed shear stress is shown using a black cross.

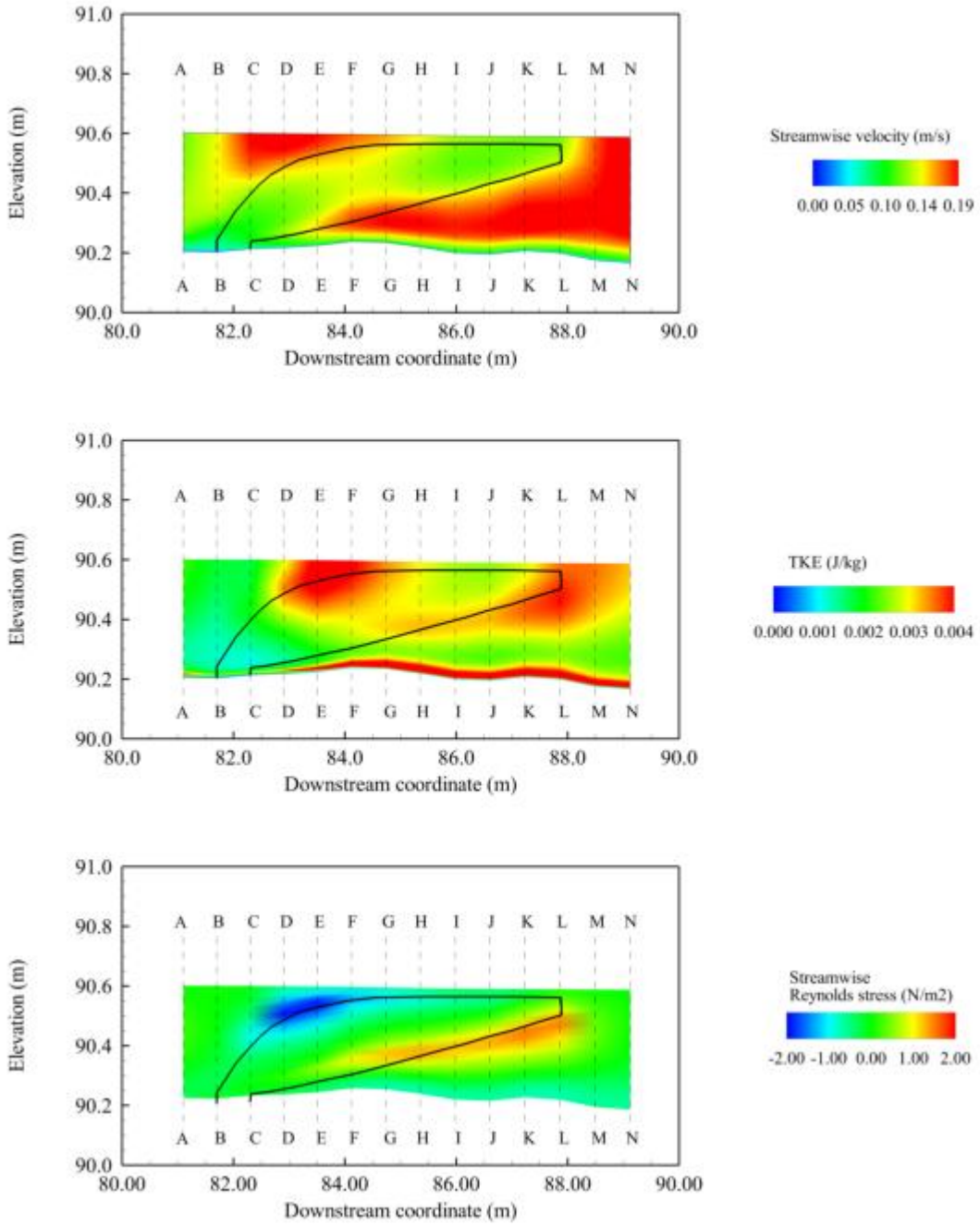

Figure 8.3.4: Flow through a single patch of *Ranunculus.*

Upstream of the plant patch at profile A-A, flow takes the expected form of a logarithmic velocity profile unaffected by vegetation with correspondingly low Reynolds stress values due to low velocity gradients. The root of the patch occurs between profiles B-B and C-C, and a corresponding reduction in flow in the near-bed

region can be observed, coupled with a reduction in peak TKE. From profile C-C to M-M, significant changes in the form of the velocity profile, TKE profile and Reynolds stress profiles can be seen. As flow encounters the vegetation canopy, it initially accelerates over the top of the vegetation canopy (C-C to F-F). The acceleration leads to an increase in shear, reflected in the high magnitude of Reynolds stress in this region. This results in high TKE both outside and within the upper part of the plant. From G-G onwards, a reduction in near-surface velocity is evident as the plant approaches the water surface and diverts the majority of flow around it.

Below the canopy, between B-B and E-E, flow velocity remains low due to the volume occupancy of vegetation. As the height of the canopy above the bed increases between F-F and L-L, flow converges underneath the patch and accelerates. This acceleration in flow velocity generates steep velocity gradients in two locations: (i) beneath the vegetation canopy and (ii) adjacent to the gravel bed. These steep velocity gradients result in shearing of the flow in these regions, and this is reflected by the high magnitude of Reynolds stress values. These shear zones also drive the production of turbulent kinetic energy in this region. Moving out of the vegetation canopy from profile L-L onwards the velocity gradients occurring above and below the canopy become smaller and the velocity profile reverts to a logarithmic profile. TKE remains high in this zone downstream of the plant.

The planform results for the same patch at approximately half the water depth are shown in Figure 8.3.5. The patch outline highlighted in red represents the planform projected shape of the patch. As Figure 8.3.5 represents a slice taken through the patch, the actual extent of the vegetation in this layer is smaller than the outline shown in red. Flow retardation within the patch can be seen with zones of

increased TKE occurring at the patch margins due to high velocity gradients. The presence of shear zones generating the turbulent kinetic energy is identified by the streamwise Reynolds stress results. The magnitude of Reynolds stress is negative and high near to the upstream extent of the patch where flow deceleration occurs. The opposite is true where Reynolds stress values are positive and high at the patch tip where flow acceleration from within the patch occurs. Beyond the patch tip, the value of Reynolds stress becomes close to zero.

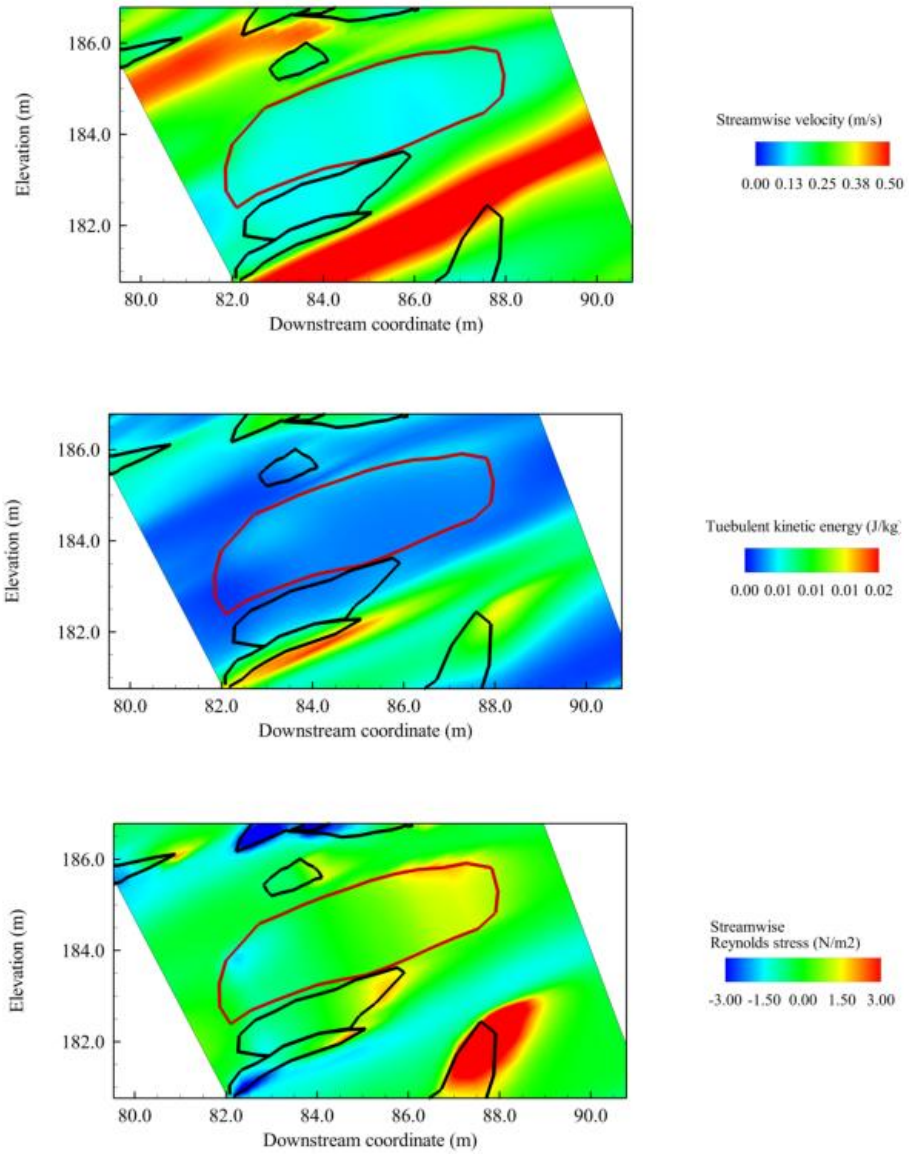

Figure 8.3.5: Planform results at half the water depth for streamwise velocity, turbulent kinetic energy and streamwise Reynolds stress. Patch of interest is highlighted in red, with other neighbouring patches shown in black.

8.3.1. Discussion

The results shown in this section imply that flow through a vegetation patch, which has variable morphology along its length, is complex. Accelerations of flow above and below vegetation patches observed in this study have been noted in the literature for *Ranunculus* (Green, 2005a; Wharton *et al*., 2006). However, as data relating to turbulence within and around natural plants in real rivers is scarce, the modelled results of flow velocity, turbulent kinetic energy, and Reynolds stresses, and how these vary when moving through a patch of *Ranunculus* represents a significant addition to the literature.

Two areas of steep gradients in flow velocity were observed for the patch of *Ranunculus*, with correspondingly high values of TKE and Reynolds stress. The high negative value of Reynolds stress above the patch identifies shearing due to flow acceleration in this area. Similar results have been observed above vegetation patches by Ghisalberti and Nepf (2006) and Nepf and Ghisalberti (2009). The development of these shear zones drives the production of turbulent kinetic energy which contributes to the overall resistance due to aquatic vegetation at the reach scale.

8.4.Conclusions

This chapter has addressed three areas (i) the overall impact of vegetation management; (ii) a quantitative analysis of model results over four cross sections for the May 2011 case and (iii) a detailed assessment of flow modification at the patch scale.

The impact of vegetation on flow in natural rivers has been clearly demonstrated in this study. When vegetation occupies a large proportion of the

channel area, flow has been shown to be diverted towards the channel margins. The pattern of flow distribution varies markedly following a vegetation cut, dependent on the type of cut employed. The spatial distribution of flow over both the planform and cross section changes greatly, with areas of high turbulent kinetic energy due to the development of shear zones in areas of steep velocity gradients becoming more evident following a cut. The impact of vegetation cuts at the reach scale was explored by examining changes in flow velocity, turbulent kinetic energy and vegetation volume for three layers of the model. Large changes were found for each variable following a cut. Overall, at the reach scale, changes in resistance, flow depth, flow velocity, and conveyance capacity have shown that vegetation cuts cause large changes in overall resistance with important implications for flow depth and velocity. This in turn may impact on ecological processes within the channel.

Model performance was assessed over four cross sections by comparing model results against measurements undertaken in the field for the May 2011 case. The results presented show that the model performs reasonably well and captures the spatial variation in flow within and outside vegetation patches. The model also captures local increases in velocity where vegetation was removed during a cut. The incorporation of vegetation shape, although based upon limited data, has shown reasonable replication of measured velocity profiles, with variation in the velocity profile evident when vegetation is present. However, this simplification limits accuracy in some areas of the model where field measurements suggest that vegetation has been represented incorrectly. Results relating to turbulent kinetic energy are mostly well reproduced within the model. However, energy dissipation is an area of concern, something which could be addressed using additional terms within the $\langle k - \varepsilon \rangle$ turbulence model. In general, it is those areas where small

intricate patterns of vegetation are present which are the most difficult to model, both due to the complexity of flow velocities in these areas and the difficulty of surveying a high number of small patches.

The flow around and through a single vegetation patch has been shown to be highly complex as a result of local flow acceleration and retardation. These local changes in flow occur solely in relation to the shape of vegetation patches in both the planform and depth profiles. This has important implications for the representation of flow resistance due to vegetation in both hydraulic models and flood conveyance estimation methods.

Overall, the representation of vegetation in models of natural river channels is in its infancy. Previous approaches (Naden *et al*., 2004; Rameshwaran and Naden, 2012) provided the basis for this research, particularly with reference to the parameterisation of drag. In this study, measurements were undertaken pertaining to the actual underwater shape of a variety of plant species *in situ*. The use of this explicit plant shape proved effective and provided interesting and testable results relating to the development of shear zones around individual natural plants.

Chapter 9. Sensitivity analysis and model simplification

The construction of the model of the River Lambourn necessitated the compilation and use of a number of datasets, specifically input flow, stage, gravel roughness, vegetation parameters and vegetation patch shape. In most cases, the mean value of each parameter was specified. The model was then calibrated by adjusting the values of the bulk drag coefficient for the gravel ($C_{dg}S_{fg}$) and the bulk drag coefficient for the vegetation ($C_{dv}S_{fv}$). With regards to the DANS equations, further assumptions were made as described in Chapter 3 (Section 3.1). These can be summarized as: (i) a spatially-averaged $\langle k - \varepsilon \rangle$ turbulence closure model with standard coefficients was used; (ii) spatial correlation between the local time porosity and time-averaged flow parameters was neglected; (iii) form-induced stresses were not included; and (iv) additional terms for the sub-grid production and dissipation of turbulent kinetic energy due to blockage by the gravel and vegetation were ignored. Any errors in the data used, the application of mean parameter values, and implications of the model assumptions will thus be included in the calibrated parameters.

A full scale sensitivity analysis is not the purpose of this study. However, in order to inform future work regarding the modelling of natural channels with aquatic vegetation, the effect of variation in each of the collected datasets listed above was explored. In order to achieve this, the sensitivity of the bulk drag coefficients for gravel and vegetation to variations in model inputs was analysed for the following scenarios:

(i) Sensitivity of the bulk drag coefficient for gravel to gravel-bed structure, flow, and stage. Assessed using the February 2010 minimum vegetation case.

(ii) The propagation of error in calibration of the bulk drag coefficient for gravel to the calibration of the bulk drag coefficient for vegetation. Assessed for the May 2011 before-cut case due to the high confidence in results for this case (see Chapter 8.2).

(iii) Sensitivity of the calibration of the bulk drag coefficient for vegetation to vegetation structure and plant parameters. Assessed for all four vegetated cases.

Finally, model simplification was undertaken for the November 2010 case. Here it was assumed that practitioners could undertake an estimate of channel occupation by vegetation purely based upon an estimate of its planform area coverage and a simplified model using weighted average parameters and a schematised cut pattern was run.

9.1. Sensitivity of the bulk drag coefficient for gravel

When calibrating the value of the bulk drag coefficient for gravel (Section 7.2), it was assumed that the mean values of gravel projected area and porosity from fifteen independently sampled measurements of gravel microtopography were appropriate. With regards to stage data, necessary to provide the fixed lid for the model, measurements were recorded to the nearest centimetre. Hence, the actual water level specified may be up to a centimetre higher or lower than recorded. Finally, the discharge specified was the mean value measured by the ADCP for three crossings of the channel (Section 5.2.3). The maximum and minimum values of discharge recorded give an indication of potential error in discharge.

To assess the effect of each these parameters on the calibration of the bulk drag coefficient for gravel, the sensitivity assessment framework in Figure 9.1.1 was employed. The centre column (Model 1) represents the assumptions made during the calibration in Chapter 7. Models 2-7 assess the impact of variations in: (i) gravel roughness; (ii) water depth; and (iii) discharge. The maximum and minimum value of each dataset was used to construct an appropriate model and calibrate a value for the bulk drag coefficient for gravel using the procedure outlined previously in Chapter 7. Results are shown in Table 9.1.1.

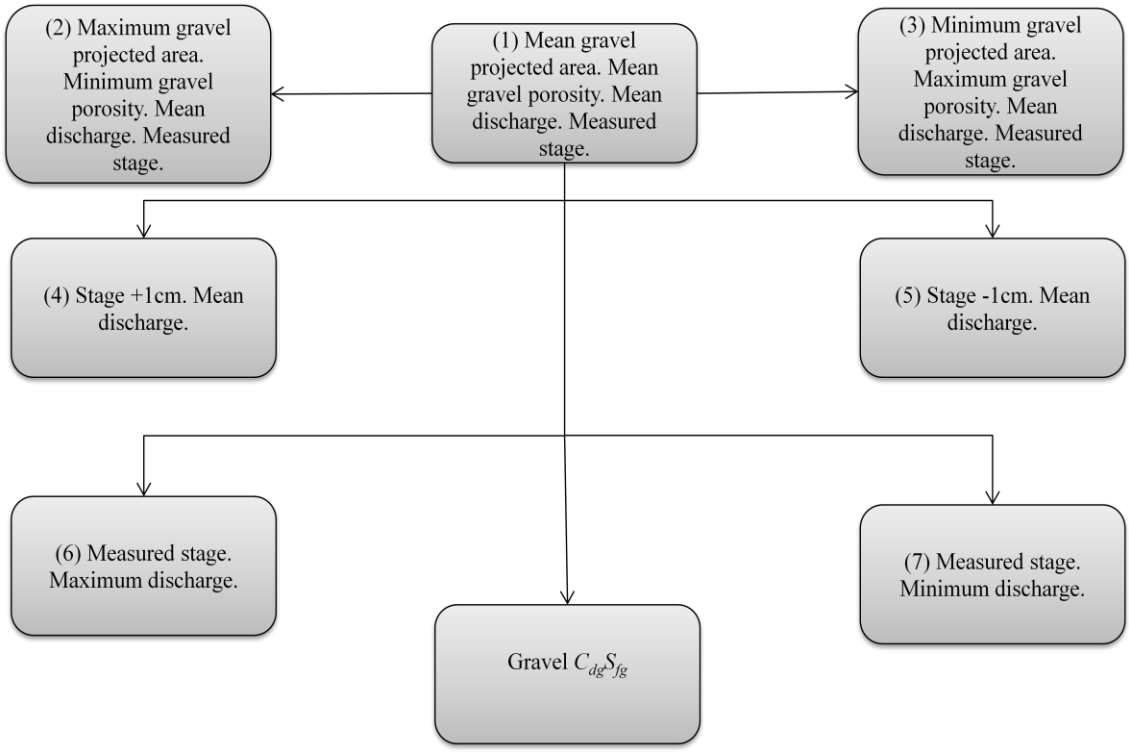

Figure 9.1.1: Sensitivity assessment framework for the calibration of $C_{dg}S_{fg.}$

Table 9.1.1: Calibrated values of bulk drag coefficient for gravel. Percentage variation in input data and difference to original bulk drag coefficient also shown.

Model		Calibrated $C_{dg}S_{fg}$	% Variation in data	% Difference to original $C_{dg}S_{fg}$
1.	Bulk drag coefficient for gravel as calibrated in Chapter 7.	0.45	-	-
2.	Increased gravel roughness. 1.Projected area. 2. Porosity.	0.40	1. +30.3 2. +27.8	-11.1
3.	Decreased gravel roughness. 1.Projected area. 2. Porosity.	0.79	1. -30.2 2. -18.5	+75.5
4.	Increased water level.	0.52	+0.2	+15.6
5.	Decreased water level.	0.38	-0.2	-15.6
6.	Increased discharge.	0.34	+7.5	-24.4
7.	Decreased discharge.	0.50	-4.2	+11.1

Measures of gravel projected area and porosity were determined from an average of fifteen samples on a layer by layer basis (see Section 4.4.1). However, there was a large variation in the roughness value exhibited by each sample (Figure 4.4.6). The extremes of roughness from all fifteen samples were identified (i.e. the roughest and smoothest) by summing the streamwise projected area of the roughness elements over all five layers in each sample. From this, it was found that Sample 15 was the 'roughest' and Sample 9 was the 'smoothest'. A similar analysis for the porosity was consistent with this in that Sample 15 had the highest total solid fraction, while Sample 9 had the lowest total solid fraction. The difference by layer in streamwise projected area (A_{px}) and porosity for Sample 15, Sample 9 and the mean value of all fifteen samples is shown in Figure 9.1.2.

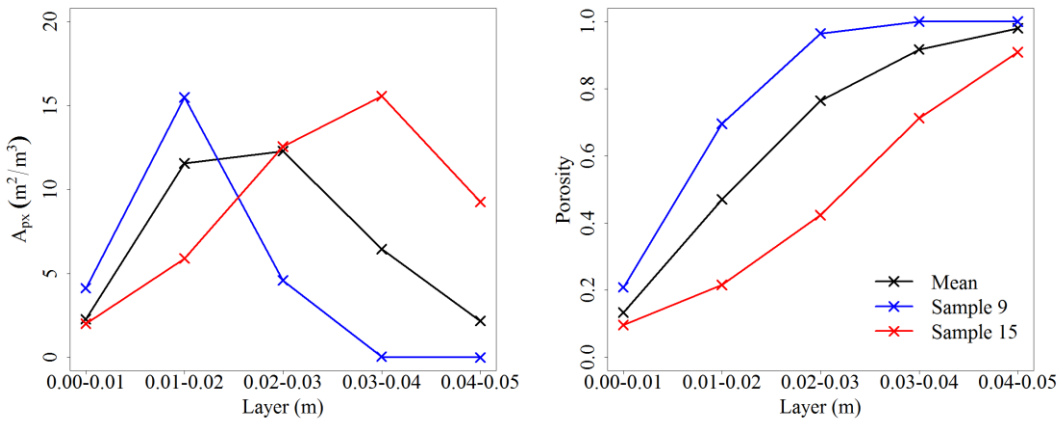

Figure 9.1.2: Variation in gravel streamwise projected area and porosity for the smoothest (Sample 9) and roughest (Sample 15) collected on the River Lambourn.

Using the values from Sample 15 and Sample 9, the models referred to as Model 2 and Model 3 in Figure 9.1.1 were constructed and the bulk drag coefficient for gravel calibrated. Where roughness due to gravel was highest (Model 2), a reduction in the bulk drag coefficient for gravel from 0.45 to 0.40 (-11%) was observed. Where the roughness was lowest (Model 3) an increase in the bulk drag coefficient for gravel to 0.79 (+75%) was necessary to match the energy slope of the staff gauge boards.

The difference in overall roughness of Samples 15 and 9, determined by summing the streamwise projected area of the roughness elements over all five layers, was of a similar magnitude (both ~±30% of the mean) with porosity varying between -18% to +30%. However, the corresponding change in bulk drag coefficient for gravel is much larger where the roughness is at its lowest. Figure 9.1.2 suggests that this results from the changes in streamwise projected area. In Sample 15, the roughness, represented by the projected area, is high throughout all five bed layers. This is reflected in the lower value of the bulk drag coefficient for gravel for Sample 15. The projected area in Sample 9 is zero in the top two bed layers. This is quite

different from the original mean value and results in a large increase in the bulk drag coefficient for gravel to compensate for the lack of blockage and drag in these two layers. The large changes in the bulk drag coefficient with bed roughness parameters shows the importance of the bed microtopography measurements for the minimum-vegetation case.

Staff gauge board readings (Section 5.3) were taken to an accuracy of ±0.01m and used to set the fixed lid of the model. To assess the effect this had, the fixed lid was increased by a height of 0.01m to construct Model 4, and lowered by 0.01m to construct Model 5. Calibrated values of the bulk drag coefficient for gravel for Models 4 and 5 were 0.52 and 0.38 respectively. Although the difference between the initial fixed lid used in Model 1 and that used in these models was low (<1%), the calibration of the bulk drag coefficient for gravel revealed a percentage change of ±16%. This suggests that the correct specification of the water depth is highly important.

The variation in input flow was defined for February 2010 using the maximum (Model 6) and minimum (Model 7) discharges measured using the ADCP. Data on this date were collected using WinRiverII (Section 5.2.3) and discharge values used for each model are shown in Table 9.1.2.

Table 9.1.2: Mean, maximum and minimum values of discharge used to calibrate the bulk drag coefficient for gravel.

Model	Q (m^3s^{-1})
1	2.191
6	2.368
7	2.103

Calibrated values of the bulk drag coefficient for gravel for Models 6 and 7 were 0.34 and 0.50, respectively. The variation in discharge when compared to the mean was low (<10%) in both cases. However, this led to a maximum variation in the bulk drag coefficient for gravel of -24% in Model 6. Again, this suggests the correct specification of input flow is important for accurate calibration of the bulk drag coefficient for gravel.

Overall, the error in the input data with regards to flow and water depth was low, <10% in all cases. However, this can result in a deviation of -24 to +11% from the calibrated value of the bulk drag coefficient for gravel using mean values. The analysis undertaken revealed that the calibration of the bulk drag coefficient for gravel was highly sensitive to the correct specification of the projected area and porosity of the gravel (Model 2 and Model 3). This was particularly evident when using the minimum roughness in the model (Model 3). The sensitivity to gravel roughness may also suggest that a distributed roughness through the reach may be appropriate if rougher and smoother areas of the channel can be identified.

9.2. Propagation of error in the bulk drag coefficient for gravel

To observe the effect of the propagation of the variation in values of the bulk drag coefficient for gravel on the drag coefficient for vegetation, the sensitivity assessment framework in Figure 9.1.1 was applied to the May 2011 before-cut case. This case was selected due to the high confidence in model results as shown in Chapter 8. For each model, the mean value of vegetation surface area and porosity (Tables 6.2.1 and 6.2.2) along with the mean vegetation shapes (Section 7.5) were

applied. Calibrated values of the bulk drag coefficient for vegetation are shown in Table 9.2.1.

Table 9.2.1: Calibrated values of the bulk drag coefficient for vegetation

Model		Calibrated $C_{dg}S_{fg}$	Calibrated $C_{dv}S_{fv}$	% Difference to original $C_{dv}S_{fv}$
1.	Mean case.	0.45	0.68	-
2.	Increased gravel roughness.	0.40	0.69	+1.4
3.	Decreased gravel roughness.	0.79	0.71	+4.4
4.	Increased water level.	0.52	0.72	+5.8
5.	Decreased water level.	0.38	0.65	-4.4
6.	Increased discharge.	0.34	0.67	-1.5
7.	Decreased discharge.	0.50	0.75	+10.3

The previous section showed that variation in the specified gravel roughness parameters can result in a difference of up to +75% (Model 3) in the calibrated bulk drag coefficient for gravel. However, when this variation is propagated through to the vegetation model (Models 2 and 3), the resulting value of the bulk drag coefficient for vegetation remains almost equal to that calibrated using the mean value of the bulk drag coefficient for gravel. This means that, provided calibration of the bulk drag coefficient for gravel is undertaken and used consistently, it is not a critical parameter for the vegetated cases.

When variations in water level and discharge are considered, it is not only the effect of the bulk drag coefficient for gravel which will affect the calibrated value of the bulk drag coefficient for vegetation. Models 4 and 5 increased and decreased the water level respectively and the height of *Ranunculus* patches was adjusted accordingly using the relative depth. The height of other species patches remained the same using their absolute height above the bed. Only small changes in the bulk drag coefficient for vegetation occurred. Where the input discharge was changed (Models 6 and 7), there is a corresponding change in the input streamwise velocity. When considering the relationship velocity has with drag (Equation 9.2.1), if the streamwise velocity $\bar{u}_i$ increases or decreases, there must be a corresponding change in the value of the bulk drag coefficient for vegetation $C_{dv}S_{fv}$ where the vegetation surface area A_{sv} remains constant.

$$F_{vi} = -\frac{1}{2}\rho C_{dv} S_{fv} A_{sv} |\langle \bar{u}_i \rangle| \langle \bar{u}_i \rangle$$

9.2.1

This is indeed the case. Where input discharge increases in Model 6, the value of the bulk drag coefficient for vegetation falls, with the opposite true where discharge is decreased in Model 7. Although the percentage change for Model 7 appears large (+10.3%), the change is actually quite small compared to the magnitude of changes observed when considering the bulk drag coefficient for gravel in Section 9.1. Overall, when compared to the bulk drag coefficient for gravel, the bulk drag coefficient for vegetation is far less sensitive to changes in gravel roughness, stage

and discharge as these have already been accounted for in the changes in the bulk drag coefficient for gravel.

9.3. Sensitivity to vegetation structure and plant parameters

The representation of vegetation within the model is subject to variation in: (i) vegetation planform; (ii) vegetation surface area and porosity; and (iii) vegetation underwater shape. Confidence in the accuracy of the planform dataset was high as the survey was undertaken manually. The vegetation planform patch dataset was a depiction of reality throughout the reach and it was difficult to see how to alter the planform distribution of plant patches in order to yield useful information about its effect on the value of the bulk drag coefficient for vegetation. Hence, a sensitivity analysis for this dataset was not undertaken.

The framework used to assess the sensitivity to the vegetation parameters of porosity and surface area per unit volume, along with changes in vegetation patch underwater shape, is shown in Figure 9.3.1.

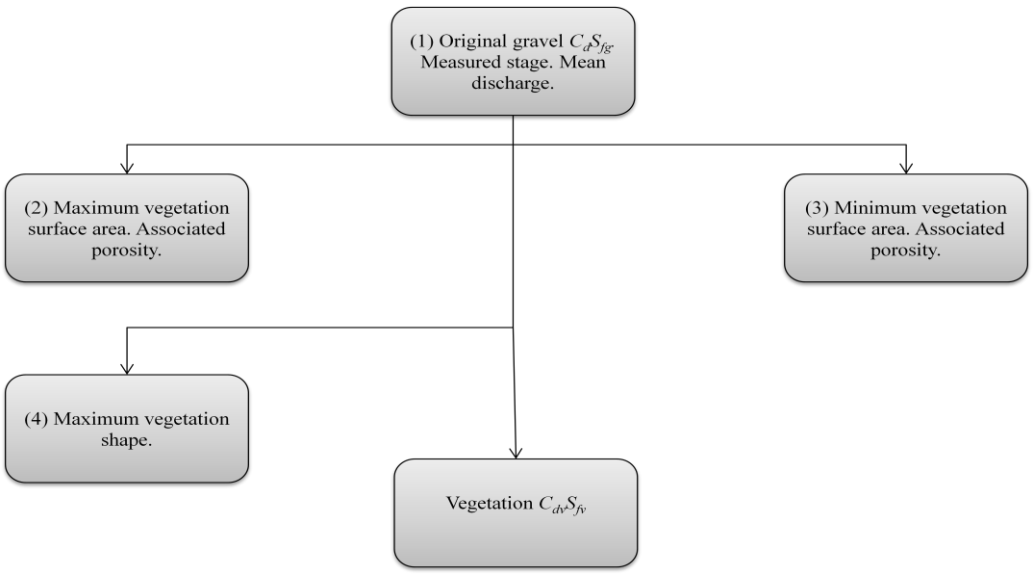

Figure 9.3.1: Sensitivity assessment framework for the calibration of the bulk drag coefficient for vegetation.

The maximum and minimum surface area by species was determined from the measurements analysed in Section 6.2. Values are shown in Table 9.3.1 and Table 9.3.2 for May and October measurements, respectively. As in Chapter 6, the calculation of surface area and porosity for Mixed vegetation is taken as an average of measurements taken for all other species. Overall, the range of values for surface area are high, while the variation in porosity is very small (less than 1%).

Table 9.3.1: Vegetation surface area and porosity for measurements collected in May 2013.

Species	Mean A_{sv} (m^2m^{-3}) / Porosity	Maximum A_{sv} (m^2m^{-3}) / Porosity	Minimum A_{sv} (m^2m^{-3}) / Porosity
Ranunculus (Near-bed)	39.1 / 0.976	60.4 / 0.975	22.0 / 0.984
Ranunculus (Full-depth)	28.1 / 0.989	34.3 / 0.988	20.0 / 0.975
Berula	37.4 / 0.974	47.9 / 0.976	22.6 / 0.975
Callitriche	20.2 / 0.988	25.4 / 0.991	11.7 / 0.990
Rorippa	N/A	N/A	N/A
Mixed	31.2 / 0.982	42.0 / 0.982	19.1 / 0.981

Table 9.3.2: Vegetation surface area and porosity for measurements collected in October 2013.

Species	Mean A_{sv} (m^2m^{-3}) / Porosity	Maximum A_{sv} (m^2m^{-3}) / Porosity	Minimum A_{sv} (m^2m^{-3}) / Porosity
Ranunculus (Near-bed)	25.9 / 0.978	45.5 / 0.974	13.8 / 0.991
Ranunculus (Full-depth)	N/A	N/A	N/A
Berula	24.3 / 0.982	31.8 / 0.986	9.4 / 0.993
Callitriche	14.2 / 0.988	19.9 / 0.984	17.2 / 0.978
Rorippa	9.6 / 0.986	15.8 / 0.979	3.7 / 0.992
Mixed	18.5 / 0.984	28.2 / 0.981	11.0 / 0.989

Data collected relating to the underwater shape of vegetation was limited, with functions fitted as an average of all surveyed profiles. To assess the effect of any misrepresentation of underwater shape, the maximum underwater coverage for each species was determined. This was achieved by taking the profile with the greatest height above the bed for *Berula* and *Callitriche*. For *Ranunculus*, the top profile with the greatest relative height and the bottom profile with the lowest relative height were combined to form a patch shape representative of the greatest coverage in the depth dimension.

Due to the nature of the data collection relating to *Ranunculus*, the generation of a minimum depth coverage was not possible as the top profile with the lowest height above the bed crossed over the bottom profile with the greatest height above the bed. Furthermore, as *Ranunculus* is the dominant species in each model, the application of a minimum shape to just *Berula* and *Callitriche* would not have yielded a noticeable change. Hence, sensitivity assessment relating to a minimum shape was not performed. The maximum shapes for *Berula*, *Callitriche*, near-bed *Ranunculus* and full-depth *Ranunculus* compared to those implemented previously are shown in Figure 9.3.2.

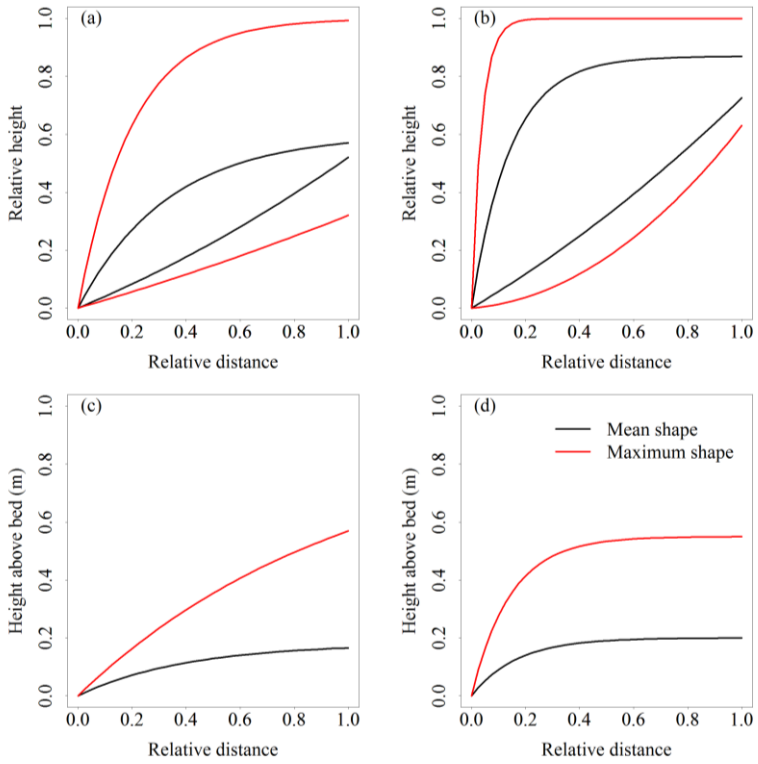

Figure 9.3.2: Comparison of maximum patch shape to mean patch shape for (a) near-bed *Ranunculus*; (b) full depth *Ranunculus*; (c) *Berula* and (d) *Callitriche*.

The calibrated values of the bulk drag coefficient for vegetation are shown in Table 9.3.3. Overall, the calibrated values for all four vegetated cases exhibit a wide range compared to the mean calibrated value, of between -74.6% and +90.5%. Models 2 and 3 assessed the effect of increasing and decreasing vegetation surface area and associated porosity, respectively, with input discharge remaining the same as in Model 1. In order to maintain the same drag force (as defined in Equation 9.2.1) where vegetation surface area increases, there must be a corresponding fall in the value of the bulk drag coefficient for vegetation with the opposite true where vegetation surface area decreases. This is indeed the case. Increases in vegetation surface area between ~22% and ~62% led to a reduction in the bulk drag coefficient of between ~14% and ~41%. Where vegetation surface area was decreased (between ~29% and 55%), an increase in the bulk drag coefficient for vegetation by between ~47% and ~91% was found. The percentage variation in the data for Model 4, where

the maximum vegetation shape was specified, is approximately double (between 60% and 112%) that of Models 2 and 3 in most cases. However, this does not produce much change in the calibrated value of the bulk drag coefficient (between 50 and 81%) for vegetation compared to the mean between all four vegetated cases. This suggests that the change in resistance resulting from changes in vegetation parameters or volume occupancy is complex and non-linear, the effect of which will be explored in the following section.

Table 9.3.3: Calibrated values of the bulk drag coefficient for vegetation for the sensitivity assessment framework in Figure 9.3.1

Case	Model		Calibrated C_dS_{fv}	% Variation in data	% Difference to original C_dS_{fv}
November 2010 – before-cut	1.	Mean case.	0.63	-	-
	2.	Increased surface area.	0.40	+62.1	-36.5
	3.	Decreased surface area.	1.20	-55.4	+90.5
	4.	Increased patch volume.	0.16	+111.8	-74.6
November 2010 – after-cut.	1.	Mean case.	0.42	-	-
	2.	Increased surface area.	0.25	+62.1	-40.5
	3.	Decreased surface area.	0.73	-55.4	+73.8
	4.	Increased patch volume.	0.08	+69.3	-81.0
May 2011 – before-cut	1.	Mean case.	0.68	-	-
	2.	Increased surface area.	0.56	+21.6	-17.6
	3.	Decreased surface area.	1.00	-29.8	+47.1
	4.	Increased patch volume.	0.25	+59.8	-63.2
May 2011 – after-cut	1.	Mean case.	0.14	-	-
	2.	Increased surface area.	0.12	+21.6	-14.3
	3.	Decreased surface area.	0.21	-29.8	+50.0
	4.	Increased patch volume.	0.07	+59.6	-50.0

Overall, the magnitude of the changes in the bulk drag coefficient for vegetation are much greater than those observed for gravel roughness parameters, flow depth, and discharge observed in Section 9.2. Hence, it can be concluded that the specification of accurate values relating to vegetation structure and plant parameters at both the patch and sub-grid scales is of crucial importance when characterising resistance due to aquatic vegetation in hydraulic models.

9.4.Model simplification

To assess the role of the spatial distribution of vegetation patches in the model, the November 2010 before and after-cut models were simplified. The overall aim was to explore the effect of removing the complex structure of vegetation patches in both the planform and the third dimension. To achieve this, the coverage of vegetation was estimated based upon its planform area. The rationale behind this was that a practical estimate of channel occupation by vegetation may easily be based upon its planform area coverage compared to the more detailed survey methods employed in this study. For the before-cut case, vegetation was assumed to occupy the entire volume of the channel. The volume porosity of each cell was modified to reflect this using an average value for all species in Table 6.2.1, weighted by the planform coverage of each species. The same treatment was applied to the vegetation surface area (Table 6.2.2).

For the after-cut case, the effect of the cut was schematised by assuming that the vegetation coverage at each bank was continuous, with the cut following the channel centreline. In a similar manner to the before-cut case, it was assumed that vegetation occupied the entire channel depth. The average number of cells occupied by vegetation patches at each bank was then determined. To achieve this, the extent

of the vegetation patches at each bank was digitised, and the number of mesh cells bounded by the vegetation extent line counted at five metre intervals (Figure 9.4.1). An average number of cells was then taken at each bank, determined to be 15 cells at the true left bank and 22 cells at the true right bank. Hence, the volume porosities were then modified for the first 22 cells and last 15 cells for each cross-section of the model mesh.

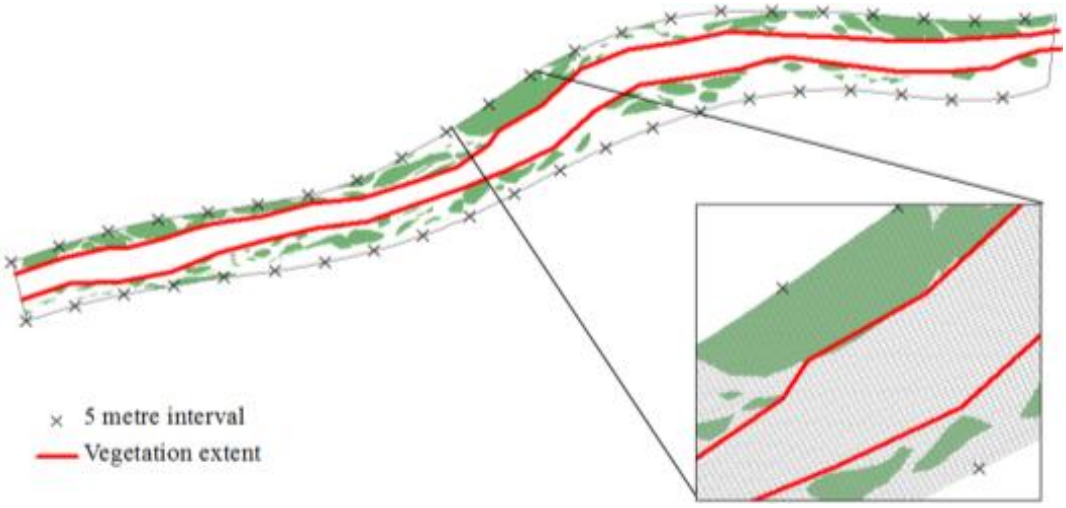

Figure 9.4.1: Determination of vegetation extent following the November 2010 vegetation cut.

The values used to calculate the weighted average of volume porosity and surface area used for each case are shown in Table 9.4.1, with the results of the calculation shown in

Table 9.4.2. For the after-cut case, the values were determined separately for the strip of vegetation at the right and left banks.

Table 9.4.1: Values of porosity, surface area and planform surface area of vegetation used to determine weighted averages of porosity and surface area for the simplified models.

Species	Porosity (ϕ)	A_{sv} (m^2m^{-3})	Before-cut planform area (m^2)	After-cut planform area at left bank (m^2)	After-cut planform area at right bank (m^2)
Ranunculus	0.978	25.9	491.9	72.7	24.8
Berula	0.982	24.4	19.6	1.2	1.3
Callitriche	0.987	14.2	18.7	4.7	3.7
Mixed	0.982	18.5	89.2	12.9	31.6
Rorripa	0.986	9.6	130.4	64.4	5.2
No vegetation	1.000	0.0	194.6	45.9	224.5

Table 9.4.2: Weighted mean values of porosity and surface area implemented in the simplified November 2010 models.

Case	Weighted mean porosity (ϕ)	Weighted mean surface area A_{sv}
November 2010 – before-cut applied to all cells	0.985	17.3
November 2010 – after-cut applied to near right bank cells.	0.982	4.6
November 2010 – after-cut applied to near leftbank cells.	0.996	14.2

Simulations were undertaken in order to calibrate the value of the bulk drag coefficient for vegetation in the same manner as described in Section 7.7 (Table 9.4.3). When compared to the calibrated values of the bulk drag coefficient for the fully specified vegetation, the calibrated values for the simplified cases are significantly lower. The bulk drag coefficient for vegetation for the before-cut case fell by ~91% from 0.63 to 0.056 whilst that for the after-cut case fell by ~71% from

0.42 to 0.12. To explore the reasons for the much lower values of the bulk drag coefficient compared to those calibrated in Chapter 7.7, the implementation of drag due to vegetation in the model was considered.

$$F_{vi} = -\frac{1}{2}\rho C_{dv} S_{fv} A_{sv} |\langle \bar{u}_i \rangle| \langle \bar{u}_i \rangle$$

9.4.1

where ρ is the fluid density, $C_{dv}S_{fv}$ is the bulk drag coefficient for vegetation, A_{sv} is the vegetation surface area per unit volume, $|\langle \bar{u}_i \rangle| \langle \bar{u}_i \rangle$ is and the square of velocity referred to hereafter as u^2. The drag force per unit volume in the model, the calibrated bulk drag coefficient for vegetation, average value of vegetation surface area per unit volume A_{sv}, and average value of $A_{sv}u^2$ are shown in Table 9.4.3.

Table 9.4.3: Values for the bulk drag coefficient for vegetation, drag force and its components.

Case	$C_d S_f$	F_d (Nm^{-3})	A_{sv} (m^{2}m^{-3})	$A_{sv}u^2$ (ms^{-2})
November 2010 – before-cut	0.63	24.79	4.66	0.079
November 2010 – before-cut simplified	0.056	23.34	17.3	0.835
November 2010 – after-cut	0.42	11.81	2.21	0.056
November 2010 – after-cut simplified	0.12	13.16	4.26	0.220

Table 9.4.3 shows that when both the before and after-cut models are simplified, the drag force per unit volume due to vegetation remains broadly the same, as necessitated by the calibration procedure. However, the bulk drag coefficients for vegetation fall by factors of 11 and 4, respectively. To account for these falls, the changes in the surface area of vegetation and the product of $A_{sv}u^2$ were considered. The surface area per unit volume of vegetation increases by a factor of 4 and 2 for the before and after-cut simplifications, respectively. However, when considering the product of $A_s u^2$, the reason for the fall in drag coefficient becomes apparent with increases of a factor of 11 and 4 for the before and after-cut cases. This demonstrates that there is a non-linear effect of plants on velocity which is potentially related to the complex three dimensional structure of vegetation, modifying flow at a local scale. The reach-mean values of surface area per unit volume A_{sv} and $A_{sv}u^2$ indicate their role in the observed changes in bulk drag coefficient for vegetation. To illustrate the detail of these changes, velocity profiles at five points over a cross section were extracted for each of the models given in Table 9.4.3.

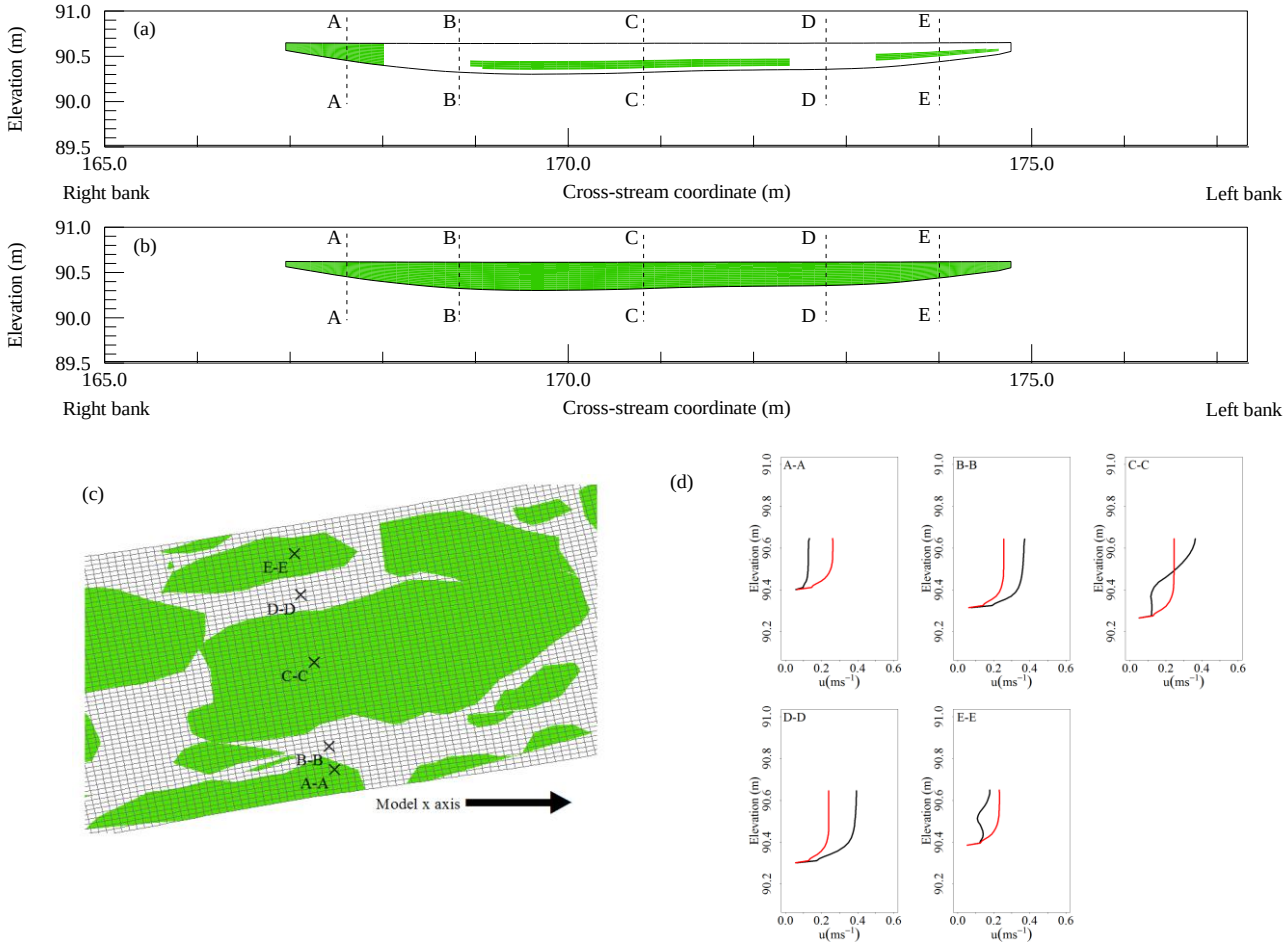

Figure 9.4.2: Comparison of modelled results for (a) original distribution of vegetation and (b) simplified model for the November 2010 before-cut case. Location of profiles shown in (c). Model results shown in (d) for the original model (in black) and simplified model (in red).

For the November before-cut case, Figure 9.4.2 shows that, over a cross section, the velocity profiles in the simplified case conform towards a logarithmic velocity profile with flow evenly distributed over the cross section. This results from the uniform distribution of vegetation throughout the water column for each profile. Where vegetation was present in the original model (e.g. profiles A-A, C-C and E-E) the velocity is greater in the simplified model. However, outside vegetation patches flow velocity is higher in the original model (profiles B-B and D-D), and a large reduction in velocity occurs in the simplified model. At profile C-C where the occupation by vegetation varied throughout the depth in the original model, the variation in velocity with depth is lost in the simplified version.

For the simplified November 2010 after-cut model (Figure 9.4.3), within the strip of vegetation at the true right bank, where vegetation was previously present (profile A-A) flow is faster in the simplified model. Conversely, at profile B-B where vegetation was absent, flow velocity is marginally slower in the simplified model than in the original. At the true left bank, where vegetation was absent within the original model (profile D-D), flow is slower in the simplified model, with the opposite true where vegetation was present at profile E-E. Velocity is similar in both the original and simplified models at both profiles B-B and C-C. This therefore suggests that it is the partially vegetated zones at either bank which necessitate the change in drag coefficient (Table 9.4.3).

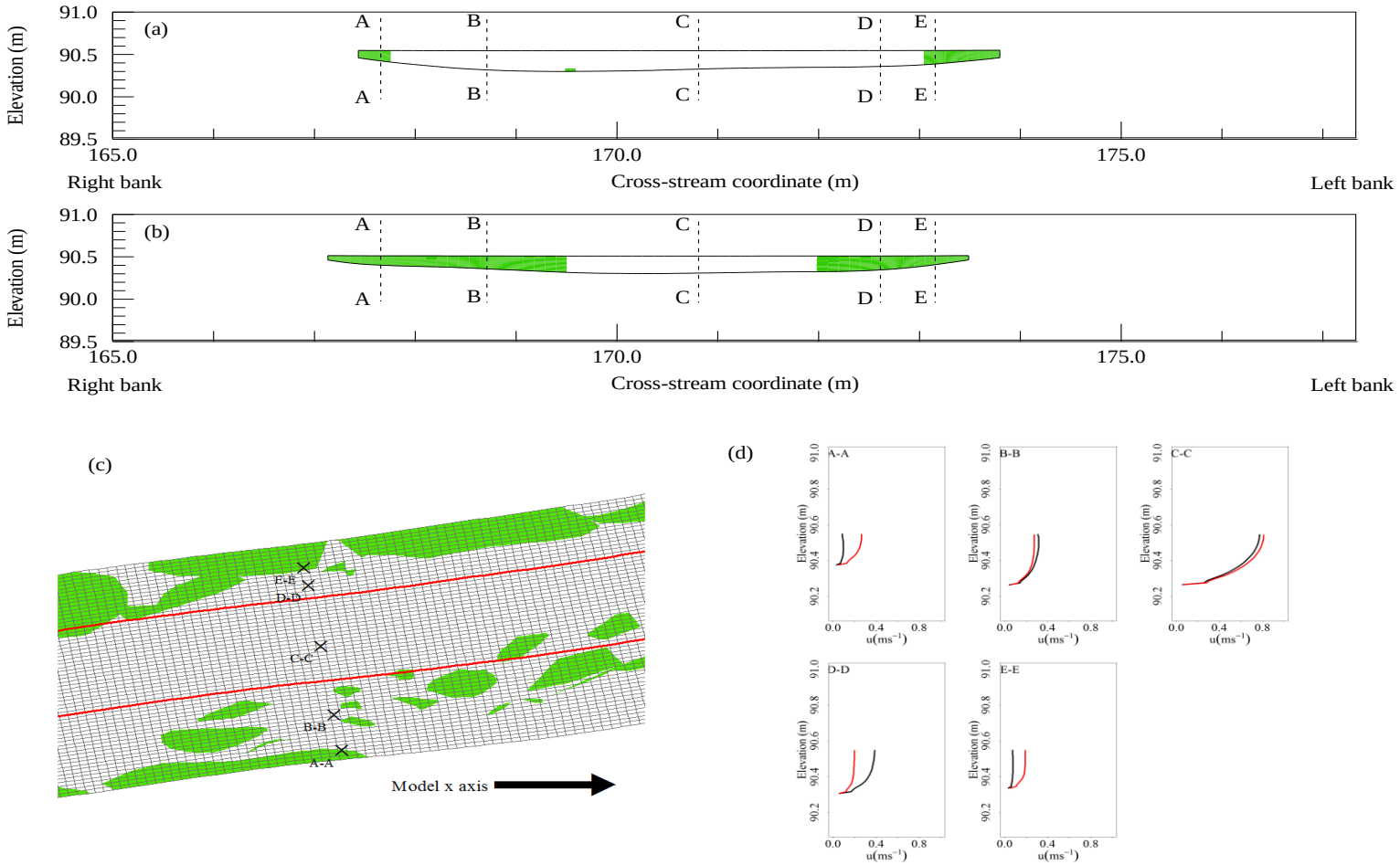

Figure 9.4.3: Comparison of modelled results for (a) original distribution of vegetation and (b) simplified model for the November 2010 after-cut case. Location of profiles shown in (c) with the vegetation extent highlighted in red. Model results shown in (d) for the original model (in black) and simplified model (in red).

9.4.1. Effects of model simplification on flow distribution

The effects of simplifying the representation of vegetation within the model were further explored by analysing the predictions of streamwise velocity and turbulent kinetic energy to those presented in Chapter 8. For the before-cut case (Figure 9.4.4), areas of local high and low velocity resulting from vegetation patches are lost with the only changes in flow velocity resulting from changes in water depth. For the after-cut case (Figure 9.4.5), although the broad reach scale velocity distribution is well replicated when schematising the cut, i.e. the area of high velocity is still predominantly along the channel centreline, key information has been lost relating to flow processes at the patch scale. For example, in the middle layer in the original model there was an area of higher velocity occurring between two vegetation patches between 55 and 65m downstream which is not captured when simplifying the modelling approach.

Another key effect is the loss of changing velocity distribution with water depth. In Figure 9.4.5, the regions of low and high velocity do not vary with increasing height above the channel bed. Results from the original model, however, demonstrated that there is a clear change in velocity distribution with increasing height above the bed due to the differing morphologies of species represented within the model. Similar differences can be observed when analysing the distribution of turbulent kinetic energy (Figures 9.4.6 and 9.4.7).

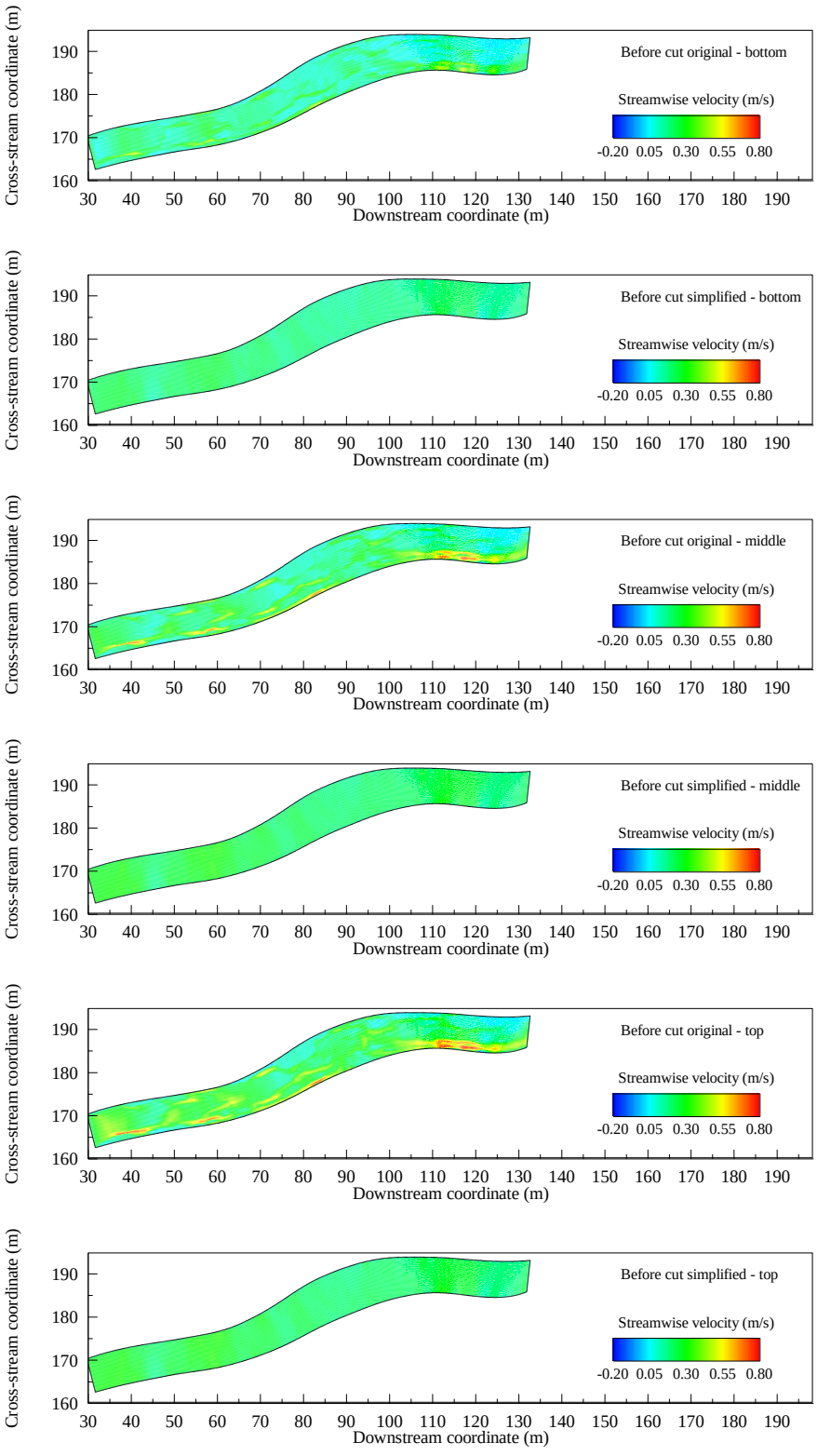

Figure 9.4.4: Planform results for streamwise velocity at the layer adjacent to the gravel bed, approximately half the water depth and at the water surface for the November 2010 before-cut cases.

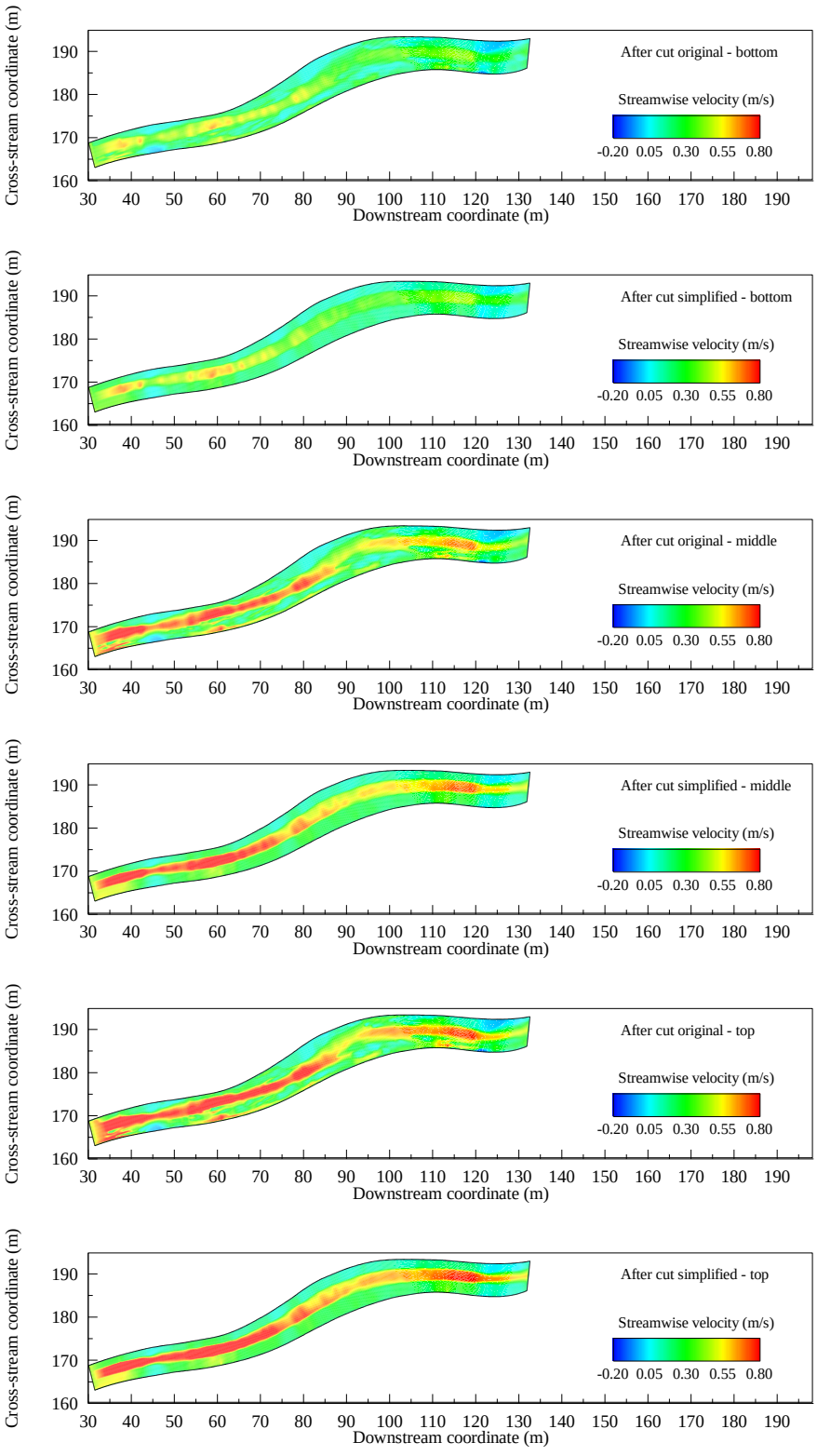

Figure 9.4.5: Planform results for streamwise velocity at the layer adjacent to the gravel bed, approximately half the water depth and at the water surface for the November 2010 after-cut cases.

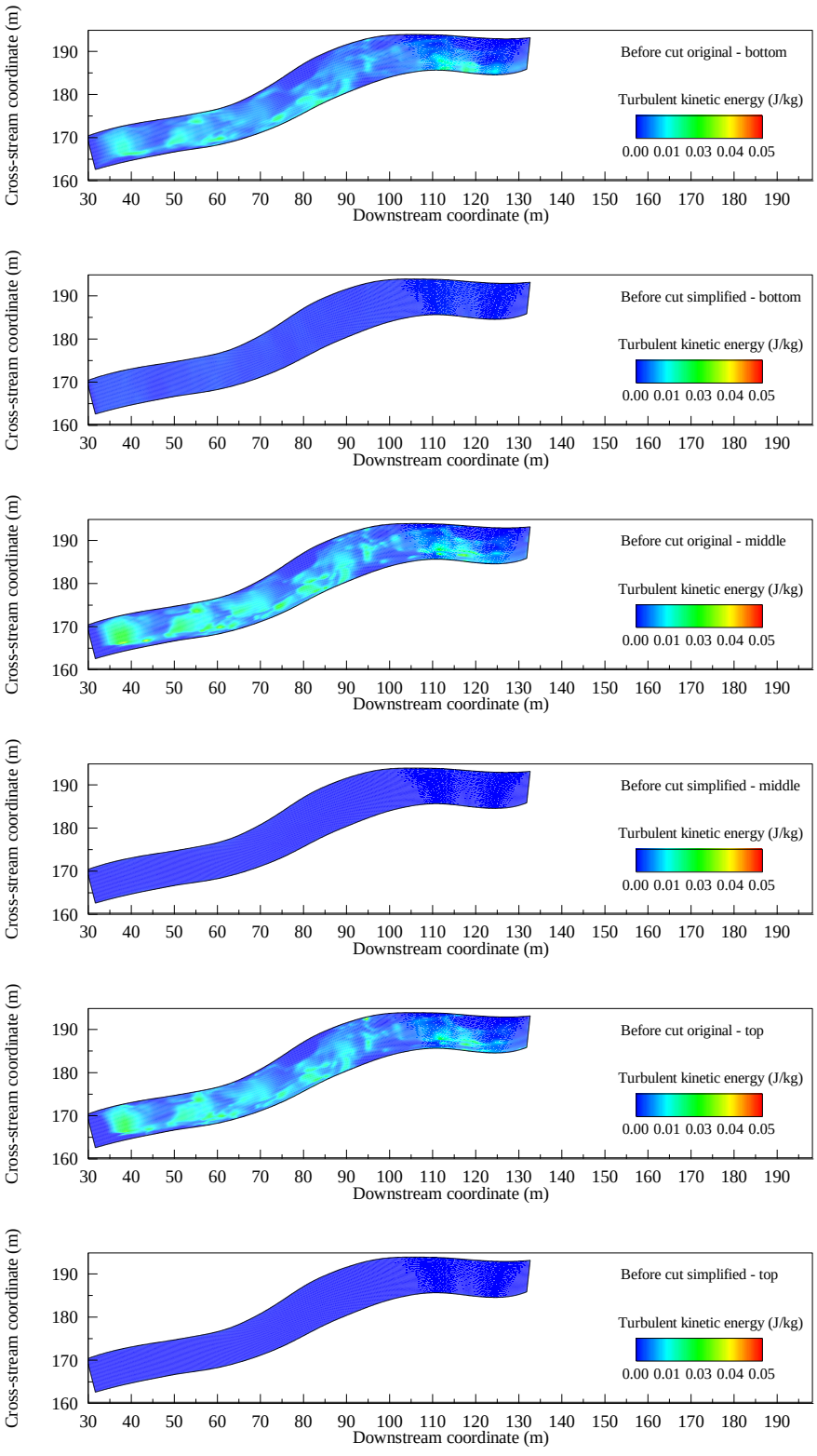

Figure 9.4.6: Planform results for TKE at the layer adjacent to the gravel bed, approximately half the water depth, and at the water surface for the November 2010 cut before-cut cases.

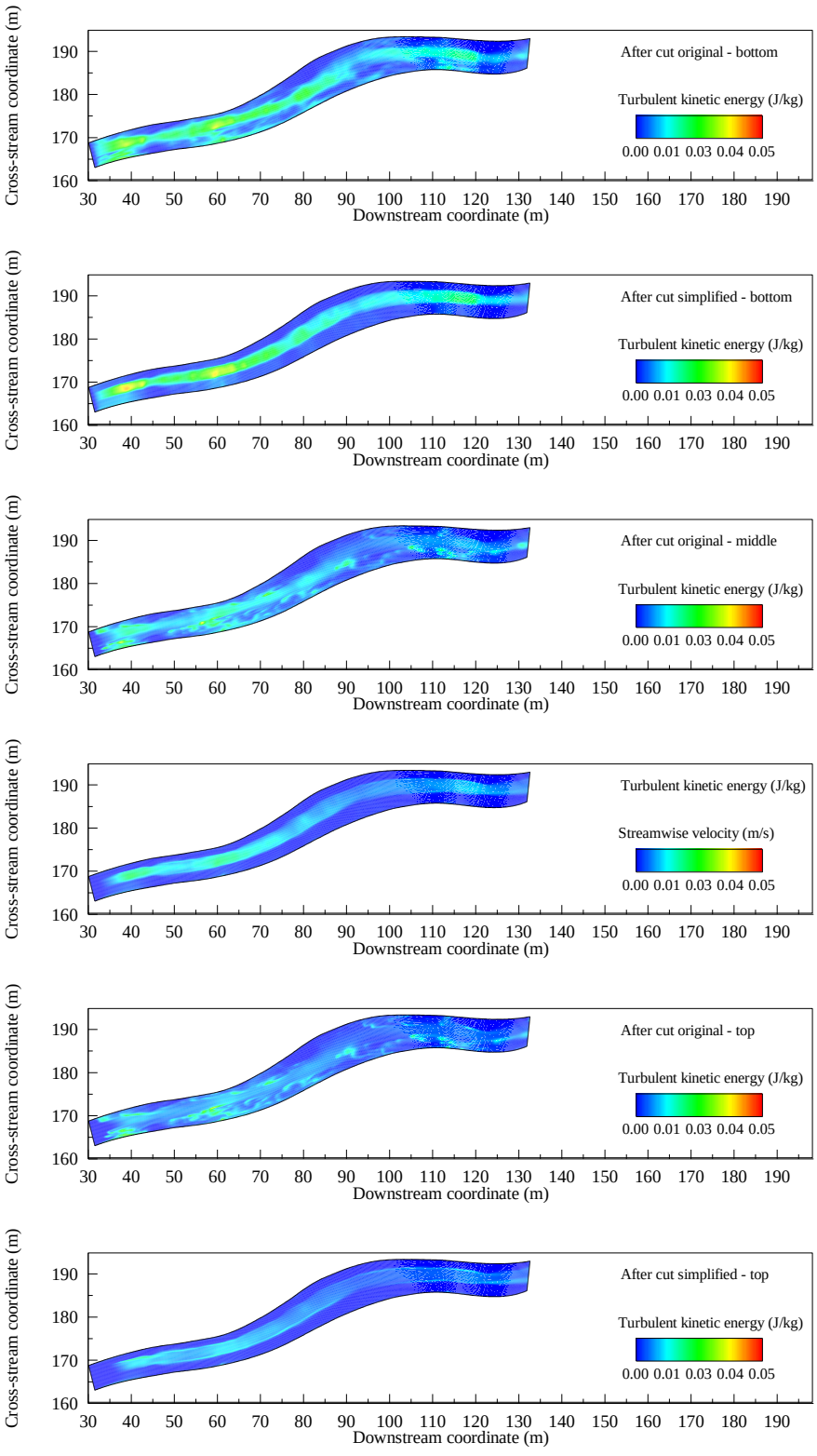

Figure 9.4.7: Planform results for turbulent kinetic energy at the layer adjacent to the gravel bed, approximately half the water depth, and at the water surface for the November 2010 cut after-cut cases.

The mosaic nature of the distribution of turbulent kinetic energy (TKE) exhibited in the original model as a result of high local velocity gradients is lost when representing the vegetation using a simplified uniform distribution in both the before-cut and after-cut cases. For the after-cut case in particular (Figure 9.4.7), results from the original model show a mosaic distribution of turbulent kinetic energy throughout the water depth due to local velocity gradients around vegetation patches. When simplifying the model, this variation is lost. Hence, the morphology of species can be demonstrated to play a key role in determining the location of high levels of turbulent kinetic energy in the water column.

The aim of simplifying the model was to explore the effect of removing the complex structure of vegetation patches, as measured in the field and previously modelled in Chapter 8. Simplifying the model demonstrated that the general spatial distribution of velocities and turbulent kinetic energy are maintained. However, local variations in flow velocity and turbulent kinetic energy due to variations in patch morphology and distribution are lost. The loss of this spatial distribution has implications for the calibrated value of the bulk drag coefficient for vegetation which becomes much smaller both before and after the vegetation cut. The method has shown that although the model can still replicate the reach scale energy loss due to aquatic vegetation through parameter calibration, the velocity profiles which are produced in no way replicate those as observed in both field measurements and modelled results presented in Chapter 8. It, therefore, demonstrates the importance of representing vegetation patches in terms of both their spatial distribution and morphology.

9.5.Conclusions

This chapter has considered the variation in the calibrated values of the bulk drag coefficient for gravel and vegetation. Consideration was given to the effects of variations in gravel bed structure, water depth, and discharge on the calibration of the bulk drag coefficient for gravel. Findings showed that the model was most sensitive to the correct specification of gravel roughness parameters. For example, where gravel roughness was at its lowest the bulk drag coefficient for gravel was approximately 75% higher than the mean value calibrated in Chapter 7. Changes in the water depth were shown to result in a change in the value of the bulk drag coefficient for gravel of ~15%. When discharge was increased by ~7% a fall in the bulk drag coefficient of ~24% was found. A decrease in discharge of ~4% resulted in an increase in the bulk drag coefficient for gravel of ~11%. All values were found to lie within the range identified from the literature (Table 7.3.1).

When using this range of values for the bulk drag coefficient for gravel in the May 2011 before-cut vegetated case, the change in values had little effect on the calibrated bulk drag coefficient for vegetation. A maximum change of +10.3% in the value of the bulk drag coefficient of vegetation was related to a decrease in discharge in combination with a decrease in the gravel drag coefficient. This suggests that energy losses at the gravel bed become less important when studying a vegetated river. Indeed, assessment of the effects of variation in vegetation surface area and porosity and vegetation underwater profiles revealed large changes in the calibrated value of the bulk drag coefficient for vegetation. Where the surface area of vegetation at the sub-grid scale was decreased, the increase in bulk drag coefficient was as high as 91%. When vegetation surface area was increased, the bulk drag coefficient for vegetation decreased by up to 41%. Increases in vegetation patch

volume occupancy resulted in a maximum reduction in the bulk drag coefficient for vegetation of 70%. Hence, the results suggest that the collection of data relating to these variables should be rigorous to avoid potential errors in the calibration of drag due to aquatic vegetation in hydraulic models.

Finally, the potential for model simplification was explored. Results showed that a method where only information relating to an estimate of planform coverage of vegetation and basic information regarding the plant porosity and surface area can result in a model where the reach scale velocity distribution and energy losses are maintained. However, large changes were observed in the calibrated values of the bulk drag coefficient due to vegetation. This was demonstrated to occur due to a non-linear relationship between the increased surface area of vegetation within the model and velocity. The simplified model demonstrated the crucial requirement for information relating to the distribution of vegetation patches, and their underwater structure, when representing them in hydraulic models if meaningful results relating to velocity and turbulent kinetic energy distributions in three dimensions are required. This becomes particularly important, if the goal of modelling river channels with aquatic vegetation is to understand the spatial volumetric distribution of in-stream habitats.

Chapter 10. Conclusions and recommendations for further research

The vegetation characteristics of a chalk stream have marked impacts on flow. This study has addressed a key gap in understanding the effects that the spatial distribution, morphology, and management of aquatic vegetation have on flow hydraulics. To achieve this, a three-dimensional hydraulic model of a reach of a typical chalk stream, the River Lambourn, Berkshire, UK was developed. The model was applied to five cases of differing vegetation cover: a minimum vegetation case necessary to calibrate the bulk drag coefficient for the gravel bed; and a further four cases with substantial vegetation cover for two different growth stages, pre and post cutting. The specific research questions, presented in Section 2.5, i.e:

- RQ1 – How can the representation of aquatic vegetation within three-dimensional hydraulic models be improved?
- RQ2 – What is the sensitivity of a three-dimensional hydraulic model containing aquatic vegetation to model inputs and parameter values?
- RQ3 – What is the impact of vegetation management on hydraulics?

have been addressed as follows.

10.1. Representation of aquatic vegetation in three-dimensional hydraulic models (RQ1)

Aquatic vegetation is three-dimensional, hence, a modelling methodology which could accommodate the complex structure of vegetation patches was needed. Due to the multi-scale property of flows in a natural river with a gravel-bed boundary and complex vegetation structure the double-averaged Navier-Stokes (DANS) equations

were used to address the important issue of spatial averaging. To incorporate vegetation within the three-dimensional hydraulic model of the River Lambourn, both the blockage and drag force due to vegetation were parameterised using measurements of: (i) patch planform morphology and spatial distribution; (ii) measurements of the underwater shape of vegetation patches; and (iii) measurements of plant volume and surface area. Measurements of plant patch planform shape (Section 6.1.1) incorporated the patchy distribution of vegetation throughout the reach, whilst also accounting for the reconfiguration of aquatic vegetation in response to flow at two different times of year. Importantly, the underwater shape of plant patches was also represented within the model, determined by surveying plant surface profiles and using underwater photography (Section 6.1.2). This accounted for variation in plant morphology for two different stages of the growing season. Finally, measurements of plant volume and surface area were taken for the range of species present (Section 6.2). Such measurements represent a considerable addition to the literature where relatively few similar measurements for aquatic macrophytes are available.

Calibration of the bulk drag coefficient for vegetation (Section 7.6) showed that values were higher before vegetation cuts, 0.63 and 0.68 for May and November, respectively, than after the cuts, 0.42 and 0.14, respectively. This occurs as, following a vegetation cut, patches become more distributed leading to a reduction in drag where patches are in close proximity. Although the spatial distribution of plant patches was explicitly included within the model (Section 7.4), the plant underwater shape, porosity, and surface area were provided by the mean sample values for each season. Although only using mean values for these parameters, a quantitative assessment of model results (Section 8.2) showed that the

model performed reasonably well in so far as the spatial variation in flow within and outside vegetation patches was captured and reasonable replication of measured velocity profiles within vegetated areas when incorporating vegetation underwater shape was found. Overall, areas where the model performed less well were those where patches were numerous but small in size. To improve on the agreement between model and field results, information would be required relating to the porosity, surface area and underwater shape of each vegetation patch, something which is not feasible due both to survey time constraints and because not all patches are discrete.

Following model calibration, an assessment of the impact of vegetation on flow hydraulics was undertaken at both the reach and patch scales. At the reach scale (Section 8.1), the distribution of vegetation patches leads to a mosaic of high and low velocities. Within patches, velocity is low, hence, faster flow outside patches leads to the development of shear zones. These shear zones drive the production of turbulent kinetic energy within the channel. Also, the volumetric occupation of vegetation impacts on flow velocities. For example, where vegetation volume occupancy is high in a given model layer flow velocities are up to 20% lower than in a model layer which does not contain vegetation, for the same discharge.

At the patch scale, the three-dimensional shape of vegetation was demonstrated to be important in capturing the location of velocity maxima and minima for any given velocity profile (Section 8.3). In addition, the three-dimensional shape had important implications with respect to the location of velocity gradients above and below vegetation patches which result in shear zones, driving the production of turbulent kinetic energy. The local changes in velocity which drive these shear zones are solely related to the shape of vegetation patches in the

planform and depth profile. Hence, the incorporation of both the distribution of vegetation patches and their underwater shape are crucial in understanding their effects on flow hydraulics.

10.2. Sensitivity to errors in model inputs and parameter values (RQ2)

Errors in model inputs and parameter values were accounted for in the calibration of the bulk drag coefficients for gravel and vegetation. To identify potential issues arising from these errors, and also to identify the datasets that are most important and hence need to be measured accurately, a sensitivity analysis was undertaken (Chapter 9). This focused on variation in the calibrated values for the bulk drag coefficients for gravel ($C_{dg}S_{fg}$) and vegetation ($C_{dv}S_{fv}$) when varying model inputs and parameters. These included: (i) gravel roughness (Section 4.4); (ii) input flow (Section 5.2); (iii) water depth (Section 5.3); (iv) vegetation underwater shape (Section 6.1); and (v) vegetation parameters (Section 6.2). In most cases, the mean of each dataset was used for the initial calibration of the model. Hence, to observe the sensitivity of the model, the maximum and minimum value of each dataset was used and changes in the bulk drag coefficients for gravel and vegetation observed.

Findings showed that, when the channel was devoid of aquatic vegetation, the bulk drag coefficient for gravel was most sensitive to changes in gravel roughness parameters. A 75% increase in the value of the bulk drag coefficient for gravel was necessary to compensate for a 30% reduction in gravel projected area and 19% reduction in gravel porosity. However, when this change in bulk drag coefficient for gravel was fed through to a model with vegetation, with all other parameters remaining the same, very little change was observed in the calibrated value of the bulk drag coefficient for vegetation (an increase of just 4%). Thus,

propagation of errors in specifying gravel roughness does not impact on the vegetation drag showing that this is the dominant force in vegetated rivers.

Variations in parameters of vegetation surface area and porosity and changes in vegetation volume occupancy were found to have a much greater impact on the calibrated value of the bulk drag coefficient for vegetation. Where vegetation surface area was increased by between 22% and 62%, a reduction in the bulk drag coefficient for vegetation was found of between 14% and 41%. Decreases in surface area (between 29% and 55%) had the greatest effect, increasing the bulk drag coefficient by between 47% and 91%. When specifying the largest patch volume, changes in vegetation volume were high, between 59% and 111% compared to the mean. This change was approximately double that found when specifying the maximum surface area of vegetation. However, a similar magnitude of change was found in the bulk drag coefficient for vegetation for both cases. This demonstrated that the change in resistance due to changes in vegetation parameters, i.e. porosity and surface area, or patch volume is complex and non-linear. Hence, if accurate representations of aquatic vegetation within three-dimensional hydraulic models are to be achieved, these parameters must be well specified. In general, the sensitivity of both the bulk drag coefficients for gravel and vegetation highlights the need for rigorous data collection when using a three-dimensional hydraulic model.

The importance of specifying plant patch shape and distribution was examined by simplifying the November 2010 models (Section 9.4). To achieve this, vegetation was represented in the model using a simple estimate of its planform coverage. Although the energy losses within the model due to vegetation could be replicated, there was a large reduction in the calibrated value of the bulk drag coefficient for vegetation from 0.63 to 0.056 in the before-cut case and 0.42 to 0.12

in the after-cut case. The drag force per unit volume within the model was shown to remain almost constant, with changes in the bulk drag coefficient for vegetation attributed to a non-linear relationship between the increased surface area of vegetation within the model and velocity.

When analysing the hydraulics, the velocity profiles produced using a simplified method did not replicate those observed in the modelled results for the equivalent case where vegetation shape and distribution were fully specified, as compared to field measurements in Section 8.2. At the reach scale, using a simplified approach resulted in the loss of local variation in velocity and turbulent kinetic energy. These local variations arise from the complex three-dimensional structure and patchiness of aquatic vegetation. The model simplification therefore demonstrated the importance of their inclusion if the model were to be used for habitat suitability considerations, for example the volumetric distribution of in-stream habitats, rather than just flood defence purposes.

10.3. Impact of aquatic vegetation management on river flow hydraulics (RQ3)

Vegetation management has a large impact on the hydraulics of a chalk stream. Two vegetation cuts were monitored in this study, one in November 2010 and a further cut in May 2011 (Section 8.1). The aim of the cut performed in November 2010 was to flush out excess silt from the reach in order to leave clean gravel for the fish spawning season the following spring, whilst at the same leaving a sufficient amount of riparian vegetation as refugia habitat for fish during potentially high winter flows. This was achieved by removing vegetation along the channel centreline. During the

cut, around 61% of the existing vegetation by planform area was removed. This resulted in a drop in water level of 17%, with a corresponding decrease in overall roughness of 50% estimated using Manning's *n*. Overall, the volume occupancy of vegetation fell from a maximum of 33% before the cut to 15% following the cut. Both the reduction in water depth and vegetation volume resulted in an increase in velocity when discharge remained almost constant. Conveyance capacity increased by 94% following the cut.

In May 2011, the aim of the cut was to increase the diversity of in-channel habitat and was timed to coincide with the flowering of *Ranunculus*. The vegetation was removed in clear cut channels in the upper part of the study reach and on a patch-wise basis in the lower part, with approximately 35% of existing vegetation removed. The water depth dropped by 18% and overall resistance, estimated using Manning's *n*, dropped from 0.17 to 0.09, a change of -47%. Again, the maximum volume occupancy of vegetation fell by a large amount, from a maximum of 47% to 32% following the cut. This, in conjunction with the reduced water depth, led to an overall increase in flow velocity and increase of 90% in conveyance capacity. Clearly, therefore, vegetation management represents an effective short term solution for decreasing water levels and increasing flow conveyance.

In general, before vegetation cuts, particularly at times of high growth, flow was seen to be diverted towards the channel margins due to the high volume occupancy of vegetation. Cutting the vegetation changed this distribution markedly, and the extent of the change was shown to be dependent on the type of cut employed. In November for example, as the vegetation was cut along the channel centreline, flow velocities increased here following a cut from a depth average of $0.18ms^{-1}$ to $0.51ms^{-1}$, an increase of 265%. At the boundary between the clear-cut

channel and vegetation patches closer to the channel margins, steep velocity gradients were created due to the low flow velocities within marginal vegetation patches (e.g. *Rorippa*). In May, however, as the cut was more selective in nature, the flow was distributed more evenly both across the width and downstream to produce a mosaic pattern of high and low velocities. As a result, in both cases, areas of high shear resulting in the production of turbulent kinetic energy became more evident following a cut.

To summarise, as research into the effects of vegetation management on flow hydraulics is scarce, this study contributes to the literature in this area. The models that have been developed provide tools in which scenarios of different amounts and types of cut could be implemented, with a view to estimating both their impact on conveyance capacity and the distribution of velocities which may be of value in habitat models. Using the models, guidance on the timing and frequency of vegetation cuts could be developed with an overall aim of developing a sensitive management regime for aquatic vegetation.

10.4. Recommendations for further research

This study has progressed our understanding of the spatial pattern of river flow velocities which occur in natural vegetated rivers at the reach and patch scale, before and after management. The spatial configuration of vegetation patches has been shown to be key in this study. Hence, to gain a broader understanding of its effects, there is a need for studies to focus on a range of patch configurations and different stream types. This may elucidate important plant-flow interactions that occur due to changes in the distribution of vegetation patches, for example through management. Once these plant-flow interactions are understood in detail, tools may be developed

to improve estimates of both flow conveyance and habitat suitability in vegetated rivers. To aid this there is a need to undertake measurements of plant morphology, surface area and plant volume at different stages during the growing season for a broad range of aquatic vegetation morphotypes and species.

With regards to the model equations, a number of assumptions were made in this study. Due to the lack of evidence to the contrary, the closure coefficients for the spatially-averaged $\langle k-\varepsilon \rangle$ turbulence model were assumed to take the same values as in the standard $k-\varepsilon$ turbulence model. Momentum fluxes due to potential spatial correlation between the local time porosity and time-averaged flow parameters were neglected. Form-induced stresses were also ignored, as equations for them are not currently available in the literature. Although these are often neglected due to the perception that they are much smaller than the Reynolds stresses, their inclusion may elucidate important processes occurring at the vegetation element surfaces.

At the sub-grid scale, additional terms for the production and dissipation of turbulent kinetic energy were ignored as again there is currently no agreed method for their representation. Results in this study showed that the model was potentially inefficient at dissipating the turbulent kinetic energy produced at the boundary between low flow within patches and faster flow outside. The introduction of additional terms in the model equations may help address this.

With regards to spatial-averaging of model parameters, the sensitivity to gravel roughness suggests that a distributed roughness throughout the reach may be appropriate if rougher and smoother areas could be identified. Finally, the movement of vegetation within the fluid domain in this study was assumed to be negligible when compared to the size of the model mesh. However, a progressive waving motion, termed monami, is often observed for aquatic plants which some researchers

argue is a mechanism by which plants reduce the drag exerted upon them. Hence, the inclusion of this motion within three-dimensional hydraulic models may reveal changes in the bulk drag coefficient of vegetation patches.

In the longer term, a broader range of studies on the manipulation of aquatic vegetation are needed to develop a sensitive and sustainable method of vegetation management. This study has demonstrated that the use of three-dimensional hydraulic models employing the double-averaged Navier-Stokes equations is a method by which this can be investigated. However, the resolution of issues relating to assumptions made when employing the model should be seen as a key step in facilitating such research. There is a particular need for studies which assess the impact of a range of cutting patterns which result in guidance for optimal timing, extent, and patterns of cutting. Such information may lead to the identification of a management strategy which works with nature, to balance improvements in conveyance capacity against the need to maintain healthy in-stream habitats.

References

Aberle, J. (2006). Spatially averaged near-bed flow field over rough armor layers. Proc. Int. Conf. on Fluvial Hydraulics River Flow 2006, 6-8 September 2006, Lisbon, Portugal. Edited by R.M.L. Ferreira, E.C.T.L. Alves, J.G.A.B. Leal, A.H. Cardoso, Taylor & Francis, Vol. 1, pp. 153-162.

Aberle, J. (2007). Measurements of armour layer roughness geometry function and porosity. *Acta Geophysica*, 55(1), 23-32.

Aberle, J. & Koll, K. (2004). Double-averaged flow field over static armor layers. Proc. Int. Conf. on Fluvial Hydraulics RiverFlow 2004, 23-25 June 2004, Naples, Italy. Edited by M. Greco, A. Carravetta, and R. Della Morte, Vol. 1, pp. 225-233.

Abril, J.B. & Knight, D.W (2004). Stage-discharge prediction for rivers in flood applying a depth-averaged model. *Journal of Hydraulic Research*, 42, 616-629.

Adams, B., Peach, D.W. & Bloomfield, J.P. (2003). *The LOCAR hydrogeological infrastructure for the Pang/Lambourn catchment*. IR/03/180. BGS: Keyworth.

Aldiss, D.T. & Royse, K.R. (2002). *The geology of the Pang-Lambourn catchment, Berkshire*. British Geological Survey Commissioned Report, CR/20/289N, BGS, Keyworth, UK.

Allen, D.J., Darling, W.G., Gooddy, Daren, C., Lapworth, D.J., Newell, A.J., Williams, A.T., Allen, D. & Abesser, C. (2010). Interaction between groundwater, the hyporheic zone and a Chalk stream: a case study from the River Lambourn, UK. *Hydrogeology Journal*, 18, 1125-1141.

Apperley, L. W. & Raudkivi, A. J. (1989), The entrainment of sediments by the turbulent flow of water, *Hydrobiologia*, 176, 39– 49.

ASME (1993). Journal of Fluids Engineering editorial policy statement on the control of numerical accuracy. *ASME Journal of Fluids Engineering*, 115, 399.

Baattrup-Pedersen, A. & Riis, T. (1999). Macrophyte diversity and composition in relation to substratum characteristics in regulated and unregulated Danish streams. *Freshwater Biology*, 42, 375-385.

Baattrup-Pedersen, A. & Riis, T. (2004). Impacts of different weed cutting practices on macrophyte species diversity and composition in a Danish stream. *River Research and Applications*, 20, 103-114.

Baattrup-Pedersen, A., Larsen, S.E. & Riis, T. (2002). Long-term effects of stream management on plant communities in two Danish lowland streams. *Hydrobiologia*, 481, 33-45.

Baattrup-Pedersen, A., Larsen, S.E. & Riis, T. (2006). Composition and richness of macrophyte communities in small Danish streams – influence of environmental factors and weed-cutting. *Hydrobiologia*, 495, 171-179.

Bache, D. H., & MacAskill, I. A. (1984). *Vegetation in civil and landscape engineering*. Granada: New York.

Baker, S. (2010). *Conveyance estimation in a U.K. chalk stream with varying macrophyte abundance.* MSc. University of East Anglia, Norwich.

Bakry, M.F., Gates, T.K. & Khattab, A.F. (1992). Field-measured hydraulic resistance characteristics in vegetation-infested canals. *Journal of Irrigation and Drainage Engineering ASCE*, 118(2), 256-274.

Bal, K.D., Bouma, T.J., Buis, J., Struyf, E., Schoelynck, J., Backx, H. & Meire, P. (2011). Trade-off between drag reduction and light interception of macrophytes: comparing five aquatic plants with contrasting morphology. *Functional Ecology*, 25, 1197-1205.

Bell, V.A., Kay, A.L., Jones, R.G., Moore, R.J. & Reynard, N.S. (2009). Use of soil data in a grid-based hydrological model to estimate spatial variation in changing flood risk across the UK. *Journal of Hydrology*, 337, 335-350.

Belvins, R.D. (2003). *Applied Fluid Dynamics Handbook*. Krieger, USA.

Beven, K. (2001). Calibration, validation and equifinality in hydrological modelling: a continuing discussion. In: M.G. Anderson & P.D. Bates, *Perspectives in Hydrological Science*, Chichester: Wiley.

Brasington, J., Rumsby, B.T. & McVey, R.A. (2000). Monitoring and modelling morphological change in a braided gravel-bed river using high resolution GPS-based survey. Earth Surface Processes and Landforms 25, 973– 990.

Brasington, J., Langham, J. & Rumsby, B. (2003). Methodological sensitivity of morphometric estimates of coarse fluvial sediment transport. *Geomorphology*, 53, 299-316.

Brayshaw, A.C., Frostick, L.E. & Reid, I. (1983). The hydrodynamics of particle clusters and sediment entrainment in coarse alluvial channels. *Sedimentology*, 30, 137-143.

Brookes, A. & Shields, F.D. (1996). Perspectives on river channel restoration. In Brookes, A. & Shields, F.D. (eds). *River channel restoration: guiding principles for sustainable projects*. Chichester: John Wiley and Sons. 1-19.

Buffin-Bélanger, T. & Roy, A.G. (2005). 1 min in the life of a river: selecting the optimal record length for the measurement of turbulence in fluvial boundary layers. *Geomorphology*, 68, 77-94.

Callaghan, F.M., Cooper, G.G., Nikora, V.I., Lamouroux, N., Statzner, B., Sagnes, P., Radford, J., Malet, E. & Biggs, B. (2007). A submersible device for measuring drag forces on aquatic plants and other organisms. *New Zealand Journal of Marine and Freshwater Research*, 41(1), 119-127.

Carney, S.K., Bledsoe, B.P. & Gessler, D. (2006). Representing the bed roughness of coarse-grained streams in computational fluid dynamics. *Earth Surface Processes and Landforms*, 31, 736-749.

Carollo, F.G., Ferro, V. & Termini, D. (2002). Flow velocity measurements in vegetated channels. *Journal of Hydraulic Engineering*, 128, 664-673.

Carollo, F.G., Ferro, V. & Termini, D. (2005). Flow resistance law in channels with submerged flexible vegetation. *Journal of Hydraulic Engineering*, 131(7), 554-564.

Carter, G.S. & Shankar, U. (1997) Creating rectangular bathymetry grids for environmental numerical modelling of gravel-bed rivers. *Applied Mathematical Modelling*, 21, 699-708.

Chandler, J. & Ashmore, P. (2002). Monitoring river-channel change using terrestrial oblique digital imagery and automated digital photogrammetry. *Annals of the Association of American Geographers*, 92(4), 631-644.

Chen, Z., Ortiz, A., Zong, L. & Nepf, H. (2012). The wake structure behind a porous obstruction and its implication for deposition near a finite patch of emergent vegetation. *Water Resources Research*, 48, W09517.

Chen, Z., Jiang, C. & Nepf, H. (2013). Flow adjustment at the leading edge of a submerged aquatic canopy. *Water Resources Research*, 49(9), 5537-5551.

Chow, V. T. (1959). *Open-channel hydraulics*. McGraw-Hill, New York.

Clarke, S.J. & Wharton, G. (2001). Sediment nutrient characteristics and aquatic macrophytes in lowland English rivers. *Science of the Total Environment*, 266, 103-112.

Cleveland, W.S. (1979). Robust locally weighted regression and smoothing scatterplots. *Journal of the Amercan Statistical Association*, 74(368), 829-836.

Clifford, N.J., Robert, A. & Richards, K.S. (1992). Estimation of flow resistance in gravel-bedded rivers: a physical explanation of the multiplier of roughness length. *Earth Surface Processes and Landforms*, 17, 111‑126.

Concentration Heat & Momentum (2013). PHOENICS Build 7601. April 2013.

Cotton, J.A., Wharton, G., Bass, J.A.B., Heppell, C.M. & Wotton, R.S. (2006). The effects of seasonal changes to in-stream vegetation cover on patterns of flow and accumulation sediment. *Geomorphology*, 77, 320-334.

Cui, J. & Neary, V.S. (2002). Large eddy simulation (LES) of fully developed flow through vegetation. *International Conference on Hydroinformatics*, Cardiff, UK, 1-5 July 2002.

Cui, J. & Neary, V.S. (2008). LES study of turbulent flows with submerged vegetation. *Journal of Hydraulic Research*, 46(3), 307-316.

Dawson, F.H. (1976). The annual production of the aquatic macrophyte *Ranunculus penicillatus* var. *Calcareous* (R.W. Butcher) C.D.K. Cook. *Aquatic Botany*, 2, 51-73.

Dawson, F.H. (1978). The seasonal effects of aquatic plant growth on the flow of water in a stream. EWRS 5th Symposium on aquatic weeds. EWRS: Amsterdam.

Dawson, F.H. & Robinson, W.N. (1984). Submerged macrophytes and the hydraulic roughness of a lowland chalk stream. *Verhandlungen Internationale Vereinigung Limnologie*, 22, 2-15.

Dawson, F.H., Clinton, E.M.F. & Ladle, M. (1991). Invertebrates on cut weed removed during weed-cutting operations along an English river, the River Frome, Dorset. *Aquaculture and Fisheries Management*, 22, 113-121.

Defra (2005). *Making space for water: taking forward a new government strategy for flood and coastal erosion risk management in England*. Defra: PB10516.

de Langre, E. (2008). Effects of wind on plants. *Annual Reviews of Fluid Dynamics*, 32, 141-162.

de Lemos, M.J.S. (2006). *Turbulence in Porous Media: Modelling and Applications*, Elsevier Ltd: Oxford.

Dinehart, R.L. & Burau, J.R. (2005). Averaged indicators of secondary flow in repeated acoustic Doppler current profiler crossings of bends. *Water Resources Research*, 41, W09405.

Environment Agency (2003). River Habitat Survey in Britain and Ireland. Field survey guidance manual: 2003 version. [online]. Available at: https://publications.environment-agency.gov.uk/skeleton/publications/ViewPublication.aspx?id=f3bea0d0-0bd5-4438-8abf-0b58718ca027. [accessed 21/05/2013]

Erduran, K.S. & Kutija, V. (2003). Quasi-three dimensional numerical model for flow through flexible, rigid, submerged and non-submerged vegetation. *Journal of Hydroinformatics*, 5, 189-202.

Ervine, D.A., Babaeyan-Koopaei, K. & Sellin, R.H.J. (2000). Two-dimensional solution for straight and meandering overbank flow. *Journal of Hydraulic Engineering*, 126, 653-669.

Fagherazzi, S., Gabet E.J. & Furbish, D.J. (2004). The effect of bidirectional flow on tidal channel planforms. *Earth Surface Processes and Landforms*, 29, 295–309.

Fathi-Moghadam, M. & Kouwen, N. (1997). Non-rigid, nonsubmerged vegetative roughness on floodplains. *Journal of Hydraulic Engineering*, 123(1), 51-57.

Fathi-Moghadam, M., Kashefipour, M., Ebrahimi, N. & Emamgholizadeh, S. (20110. Physical and numerical modelling of submerged vegetation roughness in rivers and flood plains. *Journal of Hydraulic Engineering*, 16, 858-864.

Finnigan, J.J (1985). Turbulent transport in flexible plant canopies. In: B.A. Hutchinson & B.B. Hicks (eds), *The Forest-Atmosphere Interaction*, 443-480, Utrecht, Reidel. 443-480.

Fischer-Antze, T., Stoesser, T., Bates, P. & Olsen, N.R.B. (2001). 3D numerical modelling of open-channel flow with submerged vegetation. *Journal of Hydraulic Research*, 39(3), 303-310.

Fisher, K.R. & Reeve, C.E. (1994). Impact of aquatic vegetation cutting. In: W.R. White, J. Watts. (eds). *2nd international conference on river flood hydraulics*. York: England. Chichester: John Wiley & Sons. 439-447.

Fisher, K.R. & Dawson, F.H. (2003). *Reducing uncertainty in river flood conveyance – roughness review*. London: DEFRA.

Folkard, A.M. (2011). Vegetated flows in their environmental context: a review. *Engineering and Computational Mechanics*, 164, 3-24.

Foresight Future Flooding (2004). *Executive Summary*. Office of Science and Technology.

Franklin, P. (2007). *Dynamic analysis and modelling of hydroecology in two chalk streams*. PhD. University of Reading: UK.

Franklin, P., Dunbar, M. & Whitehead, P. (2008). Flow controls on lowland river macrophytes: A review. *Science of the Total Environment*, 400, 369-378.

Frostick, L., McLelland, S. & Mercer, T. Ecological experiments. In L.E. Frostick, S.J. McLelland & T.G. Mercer (eds). *Users guide to physical modelling and experimentation. Experience of the HYDRALAB Network*. CRC Press/Balkema: Leiden. 127-170.

Gacia, E., Granata, T.C. & Duarte, C.M. (1999). An approach to measurement of partial flux and sediment retention within seagrass (Posidonia oceanic) meadows. *Aquatic Botany*, 65, 255-268.

Galland, J.C., Goutal, N. & Herveout, J-M. (1996). TELEMAC – a new numerical-model for solving shallow-water equations. *Advances in Water Resources*, 14(3), 138-148.

Ghisalberti, M. (2010). The three-dimensionality of obstructed shear flows. *Environmental Fluid Mechanics*, 10(3), 329-343.

Ghisalberti, M. & Nepf, H. (2002). Mixing layers and coherent structures in vegetated aquatic flow. *Journal of Geophysical Research*, 107(C2), 1-11.

Ghisalberti, M. & Nepf, H. (2004). The limited growth of vegetated shear-layers. *Water Resources Research*, 40, W07502.

Ghisalberti, M. & Nepf, H. (2005). Mass transfer in vegetated shear flows. *Environmental Fluid Mechanics*, 5(6), 527-551.

Ghisalberti, M. & Nepf, H. (2006). The structure of the shear layer over rigid and flexible canopies. *Environmental Fluid Mechanics*, 5(6), 527-551.

Ghisalberti, M. & Nepf, H. (2006). Shallow flows over a permeable medium: the hydrodynamics of submerged aquatic canopies. *Transport in Porous Media*, 78, 385-402.

Gioia, G. & Bombardelli, F.A. (2002). Scaling and similarity in rough channel flows. *Physical Review Letters*, 88(1), 014501.

Goff, J.A. & Nordfjord, S. (2004). Interpolation of fluvial morphology using channel-oriented coordinate transformation: a case study from the New Jersey shelf. *Mathematical Geolog*, 36, 643–658.

Gooddy, D.C., Darling, W.G., Shand, P. & Peach, D.W. (2006). Characterising groundwater movement and residence time in a lowland chalk catchment in Southern England. *EGU General Assembly*, EGU06-A-03091.

Gordon, R. L. (1996). *Acoustic Doppler current profiler principles of operation: a practical primer, second edition for Broadband ADCPs*, RD Instruments, San Diego: California.

Goring, D.G., Nikora, V.I. (2002). Despiking acoustic Doppler velocimeter data. *Journal of Hydraulic Engineering* 128, 117–126.

Graeme, D. & Dunkerley, D. L. (1993). Hydraulic resistance by the river red gum, Eucalyptus camaldulensis, in ephemeral desert streams. *Australian Geographical Studies*, 31**,** 141-154.

Grant, P.F. & Nickling, W.G. (2008). Direct field measurement of wind drag on vegetation for application to windbreak design and modelling. *Land Degradation and Development*, 9. 57-66.

Grapes, T.R., Bradley, C. & Petts, G.E. (2005). Dynamics of river-aquifer interaction along a Chalk stream: the River Lambourn, UK. *Hydrological Processes*, 19, 2035-2053.

Green, J.C. (2005a). Modelling flow resistance in vegetated streams: review and development of new theory. *Hydrological Processes*, 19, 1245-1259.

Green, J.C. (2005b). Further comment on drag and reconfiguration of macrophytes. *Freshwater Biology*, 50(12), 2162-2166.

Green, J. C. (2005c) Comparison of blockage factors in modelling the resistance of channels containing submerged macrophytes. *River Research and Applications*, 21**,** 671-686.

Green, J.C. (2005d). Velocity and turbulence around lotic macrophytes. *Hydrological Processes*, 19(6), 1245-1259.

Green , J.C. (2006). Effect of macrophyte spatial variability on channel resistance. *Advances in Water Resources*, 29, 426-438.

Griffiths, J., Binley, A., Crook, N., Nutter, J., Young, A. & Fletcher, S. (2006). Streamflow generation in the Pang and Lambourn catchments, Berkshire, UK. *Journal of Hydrology*, 330, 71-83.

Groisman, P.Y., Knight, R.W., Karl, T.R., Easterling, D.R., Sun, B. & Lawrimore, J. (2004). Contemporary changes of the hydrological cycle over the contiguous United States: trends. *Journal of Hydrometeorology*, 5, 64-85.

Gunawan, B., Sterling, M. & Knight, D.W. (2010). Using an acoustic Doppler current profiler in a small channel. *Water and Environment Journal*, 24, 147-158.

Gurnell, A. (2014). Plants as river system engineers. *Earth Surface Processes and Landforms*, 39(1), 4-25.

Gurnell, A. & Midgley, P. (1994). Aquatic weed growth and flow resistance: influence on the relationship between discharge and stage pver a 25 year river gauging station record. *Hydrological Processes*, 8, 63-73.

Gurnell, A.M., van Oosterhout, M.P., de Vlieger, B. & Goodson, J.M. (2006). Reach-scale impacts of aquatic plant growth on physical habitat, *River Research and Applications*, 22, 667-680.

Gurnell, A.M., O'Hare, J.M., O'Hare, M.T., Dunbar, M.J. & Scarlett, P.M. (2010). An exploration of associations between assemblages of aquatic plant morphotypes and channel geomorphological properties within British rivers. *Geomorphology*,116, 135-144.

Ham, S. F., Cooling, D. A., Hiley, P. D., McLeish, P. R., Scorgie, H. R. A. and Berrie, A. D. (1982a). Growth and recession of aquatic macrophytes on a shaded section of the River Lambourn, England, from 1971 to 1980. *Freshwater Biology* **12**: 1-15.

Hamming, R. (1983). Digital filters: Prentice Hall, Englewood Cliffs: NJ.

Hardy, R.J., Lane, S.N., Lawless, M.R., Best, J.L., Elliott, L. & Ingham, D.B. (2005). Development and testing of a numerical code for treatment of complex river channel topography in three-dimensional CFD models with structured grids. *Journal of Hydraulic Research*, 43(5), 468-480.

Hardy , E.J., Lane, S.N., Ferguson, R.I. & Parsons, D.R. (2007). Emergence of coherent flow structure over a gravel surface: A numerical experiment. *Water Resources Research*, 43, W03422.

Haslam, S.M. (1978). *River plants: the macrophytic vegetation of water courses*. Cambridge: Cambridge University Press.

Hatton-Ellis, T.W., Grieve, N. & Newman, J. (2003). *Ecology of water courses characterised by Ranunculion fluitantis and Callitrichio-Batrachion vegetation*. Conversing Natura 2000 rivers ecology series, vol 11. Peterborough: English Nature.

Hearne, J.W. & Armitage, P.D. (1993). Implications of the annual macrophyte growth cycle on habitat in rivers. *Regulated Rivers: Research and Management*, 8, 313-322.

Heritage, G.L, Milan, D.J., Large, A.R.G. & Fuller, I.C (2009). Influence of survey strategy and interpolation model on DEM quality. *Geomorphology*, 112, 334-344.

Heritage, G.L. & Milan, D.J. (2009). Terrestrial Laser Scanning of grain roughness in a gravel-bed river. *Geomorphology*, 113, 4-11.

Hervouet, J-M. (2007). *Hydrodynamics of free surface flows. Modelling with the finite element method*. Chichester: Wiley

Hervouet, J-M. & van Haren L. (1996). Recent advances in numerical methods for fluid flow. In: M.G. Anderson, D.E. Walling & P.D. Bates (eds), *Floodplain Processes*, Chichester: Wiley. 183-214.

Hilldale, R.C. & Raff, D. (2008). Assessing the ability of airborne LiDAR to map river bathymetry. *Earth Surface Processes and Landforms*, 33(5), 773-783.

Hodge, R., Brasington, J. & Richards, K. (2009). Analysing laser-scanned digital terrain models of gravel bed surfaces: linking morphology to sediment transport processes and hydraulics. *Sedimentology*, 56, 2024-2043.

Horrit, M. S. (2005) Parameterisation, validation and uncertainty analysis of CFD models of fluvial and floods hydraulics in the natural environment. In Bates, P., Lane, S.N. & Ferguson, R.I. (Eds.) *Computational Fluid Dynamics: Applications in Environmental Hydraulics.* Chichester, Wiley. 193-213.

Huai, WX., Han, J., Zeng, Y.H., An, X. & Qian, Z.D. (2009). Velocity distribution of flow with submerged flexible vegetations based on mixing length approach. *Applied Mathematics and Mechanics*, 30(3), 343-351.

Hui, E. & Hu, X. (2010). A study of drag coefficient related with vegetation based on the flume experiment. *Journal of Hydrodynamics*, 22(3), 329-337.

Huntington, T.G. (2006). Evidence for intensification of the global water cycle: review and synthesis. *Journal of Hydrology*, 319, 83-95.

Ingham, D.B. & Ma, L. (2005). Fundamental equations for CFD in river flow simulations. In *Computational Fluid Dynamics: Applications in Environmental Hydraulics*, Bates, P.D., Lane, S.N. & Ferguson, R.I (eds). John Wiley and Sons: Chichester; 19–49.

Intermap Technologies. NEXTMap Britain: Digital terrain mapping of the UK, [Internet]. NERC Earth Observation Data Centre, 2007, June 2013. Available from http://badc.nerc.ac.uk/view/neodc.nerc.ac.uk__ATOM__dataent_1165838344211836

IPCC (2007). *Climate change 2007. Impacts, adaptation and vulnerability*. *Contribution of Working Group II to the fourth assessment report of the Intergovernmental Panel on Climate Change*. Cambridge University Press: New York.

Isaaks, E.H. and Srivastava, R.H. (1989) *An Introduction to Applied Geostatistics*. Oxford: Oxford University Press.

James, C.S., Birkhead, A.L., Jordanova, A.A. & O'Sullivan, J.J. (2004). Flow resistance of emergent vegetation. *Journal of Hydraulic Research*, 42(4), 390-398.

Järvelä, J. (2002). Flow resistance of flexible and stiff vegetation: a flume study with natural plants. *Journal of Hydrology*, 269, 44-54.

Jesson, M., Sterling, M. & Bridgeman, J. (2013). Despiking velocity time-series – Optimisation through the combination of spike detection and replacement methods.

Johnston, K., Ver Hoef, J.M., Krivoruchko, K. & Lucas, N. (2001) *Using ArcGIS Geostatistical Analyst*. GIS by ESRI.

Keylock, C.J., Hardy, R.J., Parsons, D.R., Ferguson, R.I., Lane, S.N. & Richards, K.S. (2005). The theoretical foundations and potential for large-eddy simulation (LES) in fluvial geomorphic and sedimentological research. *Earth-Science Reviews*, 71, 271-304.

Kim, D. & Muste, M. (2012). Multi-dimensional representation of river hydrodynamics using ADCP data processing software. *Environmental Modelling & Software*, 38, 158-166.

Kinzel, P.J., Wright, C.W., Nelson, J.M., & Burman, A.R. (2008). Evaluation of an experimental LIDAR for surveying a shallow, braided, sand-bedded river. *Journal of Hydraulic Engineering*, 133, 838-842.

Kourgialas, N, N. & Karatzas, G.P. Flood management and a GIS modelling method to assess flood-hazard areas – a case study. *Hydrological Sciences Journal*, 56(2), 212-225.

Kothyari, U.C., Hayashi, K. & Hashimoto, H.H. (2009). Drag coefficient of unsubmerged rigid vegetation stems in open channel flows. *Journal of Hydraulic Research*, 47(6), 691-699.

Kouwen, N. (1992). Modern approach to design of grassed channels. *Journal of Irrigation and Drainage Engineering ASCE*, 118(5), 733-743.

Lamber, M.F & Sellin, R.H.J. (1996). Discharge prediction in straight compound channels using the mixing length concept. *Journal of Hydraulic Research*, 3493), 381-394.

Lane, S.N. & Ferguson, R.I. (2005). Modelling reach-scale alluvial flows. In *Computational Fluid Dynamics: Applications in Environmental Hydraulics*, Bates, P.D., Lane, S.N. & Ferguson, R.I (eds). John Wiley and Sons: Chichester; 217-270.

Lane, S., Chandler, J. & Richards, K. (1994). Developments in monitoring and modelling small-scale river bed topography. *Earth Surface Processes and Landforms*, 19(4), 349-368.

Lane, S.N., Biron, P.M., Bradbrook, K.F., Butler, J.B., Chandler, J.H., Crowell, M.D., McLelland, S.J., Richards, K.S. & Roy, A.G. (1998). Three-dimensional measurement of river channel flow processes using acoustic Doppler velocimetry. *Earth Surface Processes and Landforms*, 23, 1247-1267.

Lane, S.N., Hardy, R.J., Elliott, L. & Ingham, D.B. (2002). High-resolution numerical modelling of three-dimensional flows over complex river bed topography. *Hydrological Processes*, 16(11): 2261-2272

Lane, S. N. and Hardy, R. J. and Ingham, D. B. & Elliott, L. (2004). Numerical modeling of flow processes over gravelly-surfaces using structured grids and a numerical porosity treatment. *Water Resources Research*., 40 . W01302.

Lane, S.N., Hardy, S.J., Ferguson, R.I. & Parsons, D.R. (2005). A framework for model verification and validation of CFD schemes in natural open channel flows. In *Computational Fluid Dynamics: Applications in Environmental Hydraulics*, Bates, P.D., Lane, S.N. & Ferguson, R.I (eds). John Wiley and Sons: Chichester; 169-192.

Launder, B.E. & Spalding, D.B. (1974). The numerical computation of turbulent flows. Computer Methods in Applied Mechanics and Engineering 3: 269‑289

Lawless, M. & Robert, A. (2001). Three dimensional structure around small-scale bedforms in a simulated gravel bed environment. *Earth Surface Processes and Landforms*, 26, 507-522.

Leclerc, M., Capra, H., Valentin, S., Bouderault, A. & Cote, Y. (1996). *Ecohydraulics 2000: Proceedings of the Second IAHR International Conference on Habitat Hydraulics*. Quebec, IAHR.

Le Coz, J., Gilles, P., Magali, J. & Andre, P. (2007). Mean vertical velocity profiles from ADCP river discharge measurement datasets. *Proceedings 32nd Congress of International Association of Hydraulic Engineering and Research*, Venice, Italy.

Legleiter, C.J. & Kyriakidis, P.C. (2007). Forward and Inverse Transformations between Cartesian and Channel-fitted Coordinate Systems for Meandering Rivers. *Mathematical Geology*, 38(8), 927-958.

Legleiter, C.J. & Kyriakidis, P.C. (2008) Spatial prediction of river channel topography by kriging. *Earth Surface Processes and Landforms* 33, 841-867.

Legleiter, C.J. (2012). Remote measurement of river morphology viafusion of LiDAR topography and spectrally based bathymetry. *Earth Surface Processes and Landforms*, 37, 499-518.

Lhermitte, R. & Serafin, R. (1984). Pulse-to-pulse Doppler sonar signal processing techniques. *Journal of Atmospheric and Oceanic* Technology, 4, 293–308.

Li, Y., Ofosu Anim, D., Wang, Y., Tang, C., Du, W., Yu, z. & Acharya, K. (2014). An open-channel flume study of flow characteristics through a combined layer of submerged and emerged flexible vegetation. *Ecohydrology*, 7, 633-647.

Liffen, T., Gurnell, A.M., O'Hare, M.T., Pollen-Bankhead, N. & Simon, A. (2013). Biomechanical properties of the emergent aquatic macrophyte *Sparganium erectum:* Implications for fine sediment retention in low energy rivers. *Ecological Engineering*, 37(11), 1925-1931.

Liu, X., Zhang, Z., Peterson, J. & Chandra, S. (2007). The effect of LiDAR data density on DEM accuracy. In: *MODSIM07: International Congress on Modelling and Simulation: Land, Water and Environmental Management: Integrated Systems for Sustainability,* 10-13 Dec 2007, Christchurch, New Zealand.

Liu, D., Diplas, P., Fairbanks, J.D. & Hodges, C.C. (2008). An experimental study of flow through rigid vegetation. *Journal of Geophysical Research*, 113, 1-16.

Lohrmann, A., Cabrera, R., & Kraus, N.C. (1995). Acoustic-Doppler velocimeter (ADV) for laboratory use. In *Proceedings of Conference on Fundamentals and Advancements in Hydraulic Measurements and Experimentation*. American Society of Civil Engineers: 351–365.

López, F. & García, M.H. (2001). Mean flow and turbulence structure of open-channel flow through non-emergent vegetation. *Journal of Hydraulic Engineering*, 127, 392–402.

Luhar, M. & Nepf, H. (2013). From the blade scale to the reach scale: a characterisation of aquatic vegetative drag. *Advances in Water Resources*, 51, 305-316.

Luis, S.J. & McLaughlin, D. (1992). A stochastic approach to model validation. *Advances in Water Resources*, 15, 15-32.

Maddock, I., Harby, A., Kemp, P. & Wood, P. (2013). Ecohydraulics: an introduction. In: I. Maddock, A. Harby, P. Kemp & P. Wood (eds), *Ecohydraulics: an integrated approach*, Chichester: Wiley. 1-6.S

Madsen, J.D., Chamber, P.A., James, W.F., Koch, E.W. & Westlake, D.F. (2001). The interaction between water movement, sediment dynamics and submersed macrophytes. *Hydrobiologia*, 444, 71-84.

Mainstone, C. (1999). Chalk rivers: nature, conservation and management. WRc. Medmenham.

Mainstone, C.P. & Parr, W. (2002). Phosphorous in rivers – ecology and management. *Science of the Total Environment*, 282-283, 25-47.

Mandlburger, G., Hauer, C., Höfle, B., Habersack, H. & Pfeifer, N. (2009). Optimisation of LiDAR derived terrain models for river flow modelling. *Hydology and Earth System Sciences*, 13, 1453-1466.

Marion, A., Tait, S.J. & McEwan, I.K. (2003). Analysis of small-scale gravel bed topography during amoring. *Water Resources Research*, 39(12), 1334.

Marshall, E.J.P. & Westlake, D.F. (1990). Water velocities around plants in chalk streams. *Folia, Geobotanica and Phytotaxonomica*, 25, 279-289.

McGahey, C., Samuels, P.G. & Knight, D.W. (2006). A practical approach to estimating the flow capacity of rivers – Application and analysis. In: R.M.L. Ferreira, C.T.L Fernandes, G.A.B. Leal & A.H. Cardoso (eds), *River Flow 2006*, Lisbon, Portugal.

McGahey, C., Samuels, P.G., Knight, D.W. & O'Hare, M.T. (2008). Estimating river flow capacity in practice. *Journal of Flood Risk Management*, 1, 23-33.

McGahey, C., Knight, D.W. & Samuels, P.G. (2009). Advice, methods and tools for estimating channel roughness. *Proceedings of the Institution of Civil Engineers – Water Managment*, 162(6), 353-362.

McLelland, S.J. & Nicholas, A.P. (2000). A new method for evaluating errors in high-frequency ADV measurements. *Hydrological Processes*, 14, 351-366.

McMillan, H.K & Brasington J. 2007. Reduced complexity strategies for modelling urban floodplain inundation. *Geomorphology*, 90, 226‑243.

Meadows, T.I. (2010). *The impacts of spatial resolution on the interpolation of river bathymetry data via kriging*. MSc. University of Nottingham: UK.

Merwade, V.M, Maidment, D.R. & Hodges, B.R. (2005). Geospatial representation of river channels. *Journal of Hydrologic Engineering*, 10, 243–251.

Milan, D.J., Heritage, G.L., Large, A.R.G. & Charlton, M.E. (2001). Stage-dependent variability in shear stress distribution through a riffle-pool sequences. *Catena* 44, 85–109.

Milan, D.J., Hetherington, D. & Heritage, G.L. (2007). Application of a 3D laser scanner in the assessment of erosion and deposition volumes and channel change in a proglacial river. *Earth Surface Processes and Landforms*, 32, 1657–1674.

Miler, O., Albayrak, I., Nikora, V. & O'Hare, M.T. (2012). Biomechanical properties of aquatic plants and their effects on plant-flow interactions in streams and rivers. *Aquatic Sciences*, 74(1), 31-44.

Mueller, D.S., & Wagner, C.R. (2009). Measuring discharge with acoustic Doppler current profilers from a moving boat: U.S. Geological Survey Techniques and Methods 3A-22, 72 p. U.S. Geological Survey [online] Available http://pubs.water.usgs.gov/tm3a22. [accessed 21/05/2013]

Mulligan, M. & Wainwright, J. (2004). Modelling and model building. In: J. Wainwright & M. Mulligan (eds), *Environmental Modelling: Finding Simplicity in Complexity*, Chichester: Wiley. 7-73.

Mullinger, N.J., Binley, A.M., Pates, J.M. & Crook, N.P. (2007). Radon in chalk streams: spatial and temporal variation of groundwater sources in the Pang and Lambourn catchments, UK. *Journal of Hydrology*, 339(3-4), 172-182.

Muste, M., Yu, K. & Spasojevic, M. (2004a) Practical aspects of ADCP data use for quantification of mean river flow characteristics; Part I: Moving-vessel measurements. *Flow Measurement and Instrumentation*, 15(1), 1-16.

Muste, M., Yu, K. & Spasojevic, M. (2004b). Practical aspects of ADCP data use for quantification of mean river flow characteristics; Part I: moving-vessel measurements. *Flow Measurement and Instrumentation*, 15, pp.1-16.

Naden, P.S., Rameshwaran, P. & Vienot, P. (2004). Modelling the influence of instream macrophytes on velocity and turbulence. In: *Proceedings IAHR 5th international symposium on ecohydraulics*, September 2004, Madrid.

Naden, P.S., Rameshwaran, P., Mountford, O. & Robertson, C. (2006). The influence of macrophytic growth, typical of eutrophic conditions, on river flow velocities and turbulence production. *Hydrological Processes*, 20, 3915-3938.

Naot, D., Nezu, I. & Nakagawa, H. (1996). Hydrodynamic behaviour of partly vegetated open channels. *Journal of Hydraulic Engineering*, 122, 625‑633.

National River Flow Archive (2012). Flow statistics – 39019 – Lambourn at Shaw. [online] available at http://www.ceh.ac.uk/data/nrfa/data/station.html?39019. Accessed 20th June 2012.

Neary, V.S., Constantinescu, S.G., Bennett, S.J. & Diplas, P. (2012). Effects of vegetation on turbulence, sediment transport and stream morphology. *Journal of Hydraulic Engineering*, 138(9), 765-776.

Nepf, H. (1999). Drag, turbulence and diffusivity in flow through emergent vegetation. *Water Resources Research*, 35(2), 479-489.

Nepf, H. & Vivoni, E.R. (2000). Flow structure in depth-limited, vegetated flow. *Journal of Geophysical Research*, 105(C12), 28547-28557.

Nepf, H, & Ghisalberti, M. (2008). Flow and transport in channels with submerged vegetation, *Acta Geophysica*, 56 (3):753-777

Neumier, U. (2005). Quantification of vertical density variations of salt-marsh vegetation. *Estuarine, Coastal and Shelf Science*, 63, 489-496.

Nicholas, A.P. (2001). Computational Fluid Dynamics Modelling of Boundary Roughness in Gravel-bed Rivers: An Investigation of the Effects of RandomVariability in Bed Elevation. *Earth Surface Processes and Landforms*, 26, 345–362.

Nicholas, A.P. (2003) Investigations of spatially distributed braided river flows using a two-dimensional hydraulic model. *Earth Surface Processes and Landforms*, 28, 655-674.

Nicholas, A.P. (2005). Roughness parameterization in CFD modelling of gravel-bed rivers. In *Computational Fluid Dynamics: Applications in Environmental Hydraulics*, Bates, P.D., Lane, S.N. & Ferguson, R.I (eds). John Wiley and Sons: Chichester; 329–355.

Nicholas, A.P. & Sambrook Smith, G.H. (1999). Numerical Simulation of Three-dimensional Flow Hydraulics in a Braided Channel. *Hydrological Processes*, 13, 913–929.

Nikora, V. (2009). Hydrodynamics of aquatic ecosystems: an interface between ecology, biomechanics and environmental fluid mechanics. *River Research and Applications*, 26(4), 367-384.

Nikora, V.I., Goring D.G. & Biggs B.J.F. (1998). On gravel-bed roughness characterisation, *Water Resources Research*, 34(3), 517-527.

Nikora, V.I., Goring, D.G., McEwan, I., & Griffiths, G. (2001). Spatially-averaged open-channel flow over a rough bed. *Journal of Hydraulic Engineering*, 127(2), 123-133.

Nikora, V.I., McEwan, I., McLean, S., Coleman, S., Pokrajac, D. & Walters, D. (2007a). Double-averaging concept for rough-bed open-channel and overland flows: theoretical background. *Journal of Hydraulic Engineering*, 133, 873-883.

Nikora, V.I., McEwan, I., McLean, S., Coleman, S., Pokrajac, D. & Walters, D. (2007b). Double-averaging concept for rough-bed open-channel and overland flows: theoretical background. *Journal of Hydraulic Engineering*, 133, 884-895.

Nikora, V., Larned, S., Nikora, N., Debnath, K., Cooper, G. & Reid, M. (2008). Hydraulic resistance due due to aquatic vegetation in small streams: a field study. *Journal of Hydraulic Engineering*, 134(9), 1326-1332.

Nikora, V., Ballio, F., Coleman, S. & Pokrajac, D. (2013). Spatially averaged flows over mobile rough beds: definitions, averaging theorems and conservation equations. *Journal of Hydraulic Engineering*, 139(8), 803-811.

Nortek 2000. *Nortek 10 MHz Velocimeter Operations Manual*. Sandvika: Norway.

Nowell , A.R.M. & Church, M. (1979). Turbulent flow in a depth-limited boundary layer. *Jounral of Geophysical Research*, 84(C8), 4816-4824.

O'Hare, M.T., Hutchinson, K.A. & Clarke, R.T. (2007). The drag and reconfiguration experienced by five macrophytes from a lowland river. *Aquatic Botany*, 86, 253-259.

O'Hare, M.T., Clarke, R.T., Bowes, M.J., Cailes, C., Henville, P., Bissett, N., McGahey, C. & Neal, M. (2010). Eutrophication impacts on a river macrophyte. *Aquatic Botany*, 92(3), 173-178.

O'Hare, M.T., McGahey, C., Bisset, N., Cailes, C., Henville, P. & Scarlett, P. (2010b). Variability in roughness measurements for vegetated rivers near base flow, in England and Scotland, *Journal of Hydrology*, 385, 361-370.

Old, G.H., Naden, P.S., Rameshwaran, P., Acreman, M.C., Baker, S., Edwards, F.K., Sorensen, J.P.R, Mountford, O., Gooddy, D.C., Stratford, C.J., Scarlett, P.M., Newman, J.R. & Neal, M. (2014). Instream and riparian implications of weed cutting in a chalk river. *Ecological Engineering*, 71, 290-300.

Oliver, M.A. & Webster, R. (1990). Kriging: a method of interpolation for geographical information systems. *International Journal of Geographical Information Systems*, 4, 313-332.

OS MasterMap Topography Layer [GML geospatial data], Coverage: Ayr, Updated Jan 2009, Ordnance Survey, GB. Using: EDINA Digimap Ordnance Survey Service, <http://edina.ac.uk/digimap>, Downloaded: January 2011

Palmer, T.N. & Räisänen, J. (2002). Quantifying the risk of extreme seasonal precipitation events in a changing climate. *Nature*, 415, 512-514.

Papanicolaou, A.N., Diplas, P., Evaggelopoulos, N. & Fotopoulos, S. (2002). Stochastic incipient motion criterion for spheres under various bed packing conditions. *Journal of Hydraulic Engineering*, 128, 369-380.

Parseh, M., Sotirpoulos, F. & Porté-Agel, F. (2010). Estimation of power spectra of acoustic-Doppler data contaminated with intermittent spikes. *Journal of Hydraulic Engineering*, 368, 368-378.

Parsons, D.R., Jackson, R., Czuba, J., Oberg, K., Mueller, D., Rhoads, B., Best, J., Johnson, K., Engel, F. & Riley, J. (2013). Velocity Mapping Toolbox (VMT): a processing and visualization suite for moving-vessel ADCP measurements. *Earth Surface Processes and Landforms.*

Pasche, E. & Rouvé, G. (1985). Overbank flow with vegetatively roughened flood plains. *Journal of Hydraulic Engineering*, 111, 1262-1278.

Pedras, M.H.J. & de Lemos, M.J.S. (2001). Macroscopic turbulence modelling for incompressible flow through undeformable porous media. *International Journal of Heat and Mass Transfer*, 44, 1081–1093.

Pepper, A.T. & Rickard, C.E. (2009). Fluvial design guide. [online] available at http://evidence.environment-agency.gov.uk/FCERM/en/FluvialDesignGuide.aspx. Accessed 28th August 2014.

Petryk, S. (1960). *Drag on cylinders in open channel flow*. Dissertation, Colorado State University, USA.

Pitt, M. (2008). *Learning lessons from the 2007 floods – full report.* [online] available at http://webarchive.nationalarchives.gov.uk/20100807034701/http:/archive.cabinetoffice.gov.uk/pittreview/thepittreview/final_report.html. Accessed September 2014.

Plew, D.R. (2011). Depth-averaged drag coefficient for modelling flow through suspended canopies. *Journal of Hydraulic Engineering*, 137(2), 234-247.

Puilajon, S., Bornette, G. & Sagnes, P. (2005). Adaptations to increasing hydraulic stress: morphology, hydrodynamics and fitness of two higher plant species. *Journal of Experimental Botany*, 412, 777-786.

Puilajon, S. & Bornette, G. (2013). Multi-scale macrophyte responses to hydrodynamic stress and disturbances: adaptive strategies and biodiversity patterns. In: I. Maddock, A. Harby, P. Kemp & P. Wood (eds), *Ecohydraulics: an integrated approach*, Chichester: Wiley. 261-273.

Py, C., de Langre, E. & Moulia, B. (2006). A frequency lock-in mechanism in the interaction between wind and crop canopies. *Journal of Fluid Mechanics*, 568, 425-449.

Rameshwaran, P. & Naden, P.S. (2004b). Three-dimensional modelling of free surface variation in a meandering channel. *Journal of Hydraulic Research*, 42(6), 603-615.

Rameshwaran, P. & Shiono, K. (2007). Quasi two-dimensional model for straight overbank flows through emergent vegetation on floodplains. *Journal of Hydraulic Research*, 45(3), 302-315.

Rameshwaran, P., Naden, P.S. & Lawless, M. (2011). Flow modelling in gravel-bed rivers: rethinking the bottom boundary condition. *Earth Surface Processes and Landforms*, 36, 1350-1366.

Rameshwaran, P. & Naden, P.S. (2012). Modelling the influence of macrophyte patches on river flow. In *Proc. Int. Conf. on Fluvial Hydraulics River Flow 2012*, 5-7 September 2012, San José, Costa Rica.

Rameshwaran, P., Sutcliffe, A.G., Naden, P.S. & Wharton, G. (2014). Modelling river flow responses to weed management. In *Proc. Int. Conf. on Fluvial Hydraulics River Flow 2014*, 2-6 September 2014, Lausanne, Switzerland.

Raupach, M.R. & Shaw, R.H. (1982). Averaging procedures for flow within vegetation canopies. *Boundary-Layer Meteorology*, 22, 79–90.

RD Instruments (2009). StreamPro ADCP Operation Manual.

Reed, P.M., Ellsworth, T.R. & Minsker, B.S. (2004) Spatial interpolation methods for nonstationary plume data. *Ground Water* 42: 190-202.

Rhee, D.S., Woo, H., Kwon, B.A. & Ahn, H.K. (2008). Hydraulic resistance of some selected vegetation in open channel flows. *River Research and Applications*, 24, 673-687.

Rickard, C.E., Day, R. & Purseglove, J. *River Weirs- Good Practice Guide*. Environment Agency Publication W5B-023/HQP. [online] available at https://www.gov.uk/government/uploads/system/uploads/attachment_data/file/290655/sw5b-023-hqp-e-e.pdf. Accessed May 2014.

Riis, T. & Biggs, B.J.F. (2003). Hydrologic and hydraulic control of macrophyte establishment and performance in streams. *Limnology and Oceanographic Methods*, 48, 1488-1497.

Roache, P.J. (1994). Perspective: a method for uniform reporting of grid refinement studies. *Journal of Fluids Engineering*, 116, 405-413.

Roberson, J.A. & Chen, C.K. (1970). Flow in conduits with low roughness concentration. *Journal of the Hydraulics Division ASCE*, 36(HY4), 941-957.

Rodi, W. (1993). *Turbulence models and their application in hydraulics.* A.A Balkema. Rotterdam.

Roy, A.G., Biron, P. & De Serres, B. (1996). On the necessity of applying a rotation to instantaneous velocity measurements in river flows. *Earth Surface Processes and Landforms*, 21, 817–827.

Rumsby, B.T., Brasington, J., Langham, J.A., McLelland, S.J., Middleton, R. & Rollinson, G. (2008). Monitoring and modelling particle and reach-scale morphological change in gravel-bed rivers: Applications and challenges. *Geomorphology*, 93, 40-54.

Samuels, P.G., Bramley, M.E. & Evans, E.P. (2002). Reducing uncertinaty in conveyance estimation. In *Proc. Int. Conf. on Fluvial Hydraulics River Flow 2002*, 4-6 September 2002, Louvain-la-Neuve, Belgium.

Sand-Jensen, K. (1998). Influence of submerged macrophytes on sediment composition and near-bed flow in lowland streams. *Freshwater Biology*, 39, 663-679.

Sand-Jensen, K. (2003) Drag and reconfiguration of freshwater macrophytes. *Freshwater Biology*, 48**,** 271-283.

Sand-Jensen, K. (2005) Aquatic plants are open flexible structures - a reply to Sukhodolov. *Freshwater Biology*, 50**,** 196-198.

Sand-Jensen, J. (2008). Drag forces on common plant species in temperate streams: consequences of morphology, velocity and biomass. *Hydrobiologia*, 610(1), 307-319.

Sand-Jensen, K. & Mebus, J.R. (1996). Fine-scale patterns of water velocity within macrophyte patches in streams. *Oikos*, 76,169-180.

Sand-Jensen, K. & Pedersen, O. (1999). Velocity gradients and turbulence around macrophyte stands in streams. *Freshwater Biology*, 42, 315-328.

Schäppi, B., Perona, P., Schneider, P. and Burlando, P. (2010) Integrating river cross section measurements with digital terrain models for improve flow modelling applications. *Computers and Geosciences*, doi:10.1016/j.cageo.2009.12.004.

Schindler, R.J., Lane, S.N., Keylock, C.J. & Naden, P.S. (2003). Characterisation of stem wake dynamics using PIV imagery. In *Proceedings of the International Shallow Flows Symposium*, June, Delft; 275-284.

Schmeeckle, M.W. (1998). The mechanics of bedload sediment transport. PhD. University of Colorado: CO, USA.

Schmeeckle, M.W., Nelson, J.M. & Shreve, R.L. (2007). Forces on stationary particles in near-bed turbulent flows. *Journal of Geophysical Research*, 112, F02003.

Schoelynck, J., De Groote, T., Bal, K., Vandenbruwaene, W., Meire, P. & temmerman, S. (2012). Self-organised patchiness and scale-dependent bio-geomorphic feedbacks in aquatic river vegetation. *Ecography*, 24, 760-768.

Sellin, R.H.J. & van Beesten, D.P. (2004). Conveyance of a managed two-stage river channel. *Proceedings Institution of Civil Engineers Water Managment*, 157, 21-33.

Shimizu, Y. & Tsujimoto, T. (1994). Numerical analysis of turbulent open-channel flow over a vegetation layer using a *k-e* turbulence model. *Journal of Hydroscience and Hydraulic Engineering*, 11(2), 57-67.

Shiono, K. & Knight, D.W. (1988). Two dimensional analytical solution for a compound channel. In: Y. Iwasa and N. Tamai (eds). *Proceedings of 3rd International Symposium on Refined Flow Modelling and Turbulence Measurements*. Tokyo. Japan. 591-599.

Shiono, K. & Knight, D.W. (1990). Mathematical models of flow in two or multi stage straight channels. In: W.R. White, ed. *Proceedings of International Conference on River Flood Hydraulics, Paper G1*. Chichester: Wiley and Sons.

Shiono, K. & Knight, D.W. (1991). Turbulent open-channel flows with variable depth across the section. *Journal of Fluid Mechanics*, 222, 617-646.

Simpson, M.R. (2001). *Discharge Measurements Using a Broad-Band Acoustic Doppler Current Profiler*. Sacramento: USGS.

Simpson, M.R. & Oltmann, R.N. (1993). *Discharge measurement using an acoustic Doppler current profiler*. USGS.

Siniscalchi, F., Nikora, V. (2012). Flow-plant interactions in open-channel flows: A comparative analysis of five freshwater plant species. *Water Resources Research*, 48, W05503,

Smart, G.M., Duncan M.J. & Walsh, J. (2002). Relatively Rough Flow Resistance Equations. *Journal of Hydraulic Engineering*, 128(6), 568–578.

Smith, M., Vericat, D. & Gibbins, C. (2012). Through-water terrestrial laser scanning of gravel beds at the patch scale. *Earth Surface Processes and Landforms*, 37, 411-421.

Spalding, D.B. (1980). Mathematical modelling of fluid mechanics, heat-transfer and chemical reaction processes. *A lecture course*, HTS/80/1, Imperial College London.

Spears, B.M., Gunn, I.D.M., Winfield, I.J., Dudley, B., Murphy, K. & May, L. (2009). An evaluation of methods for sampling macrophyte maximum colonisation depth in Loch Leven, Scotland. *Aquatic Botany*, 91(2), 75-81.

Statzner, B., Lamouroux, N., Nikora, V. & Sagnes, P. (2006) The debate about drag and reconfiguration of freshwater macrophytes: comparing results obtained by three recently discussed approaches. *Freshwater Biology*, 51, 2173-2183.

Stone, H.L. (1968). Iterative solution of implicit approximations of multi-dimensional partial differential equations. *SIAM Journal on Numerical Analysis*, 5, 530-558.

Stone, B. & Shen, H.T. (2002). Hydraulic resistance of flow in channels with cylindrical roughness. *Journal of Hydraulic Engineering*, 128, 500-506.

Sukhodolov, A. (2005) Comment on drag and reconfiguration of macrophytes. *Freshwater Biology*, 50**,** 194-195.

Sukhodolov A,N., Thiele, M. & Bungartz, H. (1998). Turbulence structure in a river reach with sand bed. *Water Resources Research*, 34, 1317–1334.

Sun , X., Shiono, K., Rameshwaran., P., & Chandler, J. (2010). Modelling vegetation effects in irregular meandering river. *Journal of Hydraulic Research*, 48(6), 775-783.

Swales, S. (1982). Impacts of weed-cutting on fisheries: an experimental study in a small lowland river. *Fisheries Managment*, 13(4)**,** 125-137.

Szupiany, R. N., Amsler, M.L., Best, J.L. and Parsons, D.R. (2007). A comparison of fixed- and moving-vessel measurements with an acoustic Doppler profiler (ADP) in a large river, *Journal of Hydraulic Engineering*, 133(12), 1299–1310.

Tanino, Y. & Nepf, H. (2008). Laboratory investigation on mean drag in a random array of rigid, emergent cylinders. *Journal of Hydraulic Engineering*, 134(1), 4-41.

Taylor, R.P., Coleman, H.W. & Ho, B.K. (1985). Prediction of a turbulent rough-wall skin friction using a discrete element approach. *Journal of Fluids Engineering*, 107, 251-257.

Thompson, C.E.L., Amos, C.L., Lecouturier, M. And Jones, T.E.R. (2004). Flow deceleration as a method of determining drag coefficient over roughened flat beds. *Journal of Geophysical Research*, 109, C03001.

Tsujimoto, T., Shimizu, Y., Kitamura, T. & Okada, T. (1992). Turbulent open-channel flow over bed covered by rigid vegetation. *Journal of Hydroscience and Hydraulic Engineering*, 10(2), 13-26.

UK Meteorological Office. MIDAS Land Surface Stations data (1853-current), [Internet].NCAS British Atmospheric Data Centre, 2006, *2014*. Available from http://badc.nerc.ac.uk/view/badc.nerc.ac.uk__ATOM__dataent_ukmo-midas

UK Biodiversity Action Plan (1994). The UK Biodiversity Action Plan 1992-2012. *Joint Nature Conservation Committee*.

van Prooijen, B.C., Battjes, J.A. & Uijttewaal, W.S.J. (2005). Momentum exchange in straight uniform compound channel flow. *Journal of Hydraulic Engineering*, 131, 175-183.

Vereecken, H., Baatens, J., Viaene, P., Mostaert, G. & Meire, P. (2006). Ecological management of aquatic plants: effects in lowland streams. *Hydrobiologia*, 570, 205-210.

Voulgaris, G. & Trowbridge J.H. (1998). Evaluation of the acoustic Doppler velocimeter (ADV) for turbulence measurements. *Journal of Atmospheric and Oceanic Technology* 15, 272–289.

Wade, P.M. (1994). Managment of macrophytic vegetation. In P. Calow, G.E. Petts (eds). *The rivers handbook, vol 2*. Oxford: Blackwell Scientific. 363-385.

Wahl T, L. (2000). Analyzing ADV data using WinADV. In *Joint Conference on Water Resources Engineering and Water Resources Planning and Management, July–August 2000, Minneapolis, USA*. American Society of Civil Engineers.

Wark, J.B., Samuels, P.G. & Ervine, D.A. (1990). A practical method of estimating velocity and discharge in compound channels. In: W.R White (ed). *Proceedings of the International Conference on River Flood Hydraulics*, Wiley, 163-172.

Watson, D. (1987). Hydraulic effects of aquatic weed in UK rivers. *Regulated Rivers Research and Management*, 1(3), 211-228.

Watts, J.F. & Watts, G.D. (1990). Seasonal change in aquatic vegetation and its effect on river flow. In: J.B. Thorne (ed), *Vegetation and Erosion*, Chichester: Wiley. 257-267.

Webster, R. & Oliver, M.A. (2001) *Geostatistics for Environmental Scientists.* Chichester: Wiley.

Wharton, G., Cotton, J.A., Wootton, R.S., Bass, J.A.B., Heppell, C.M., Trimmer, M., Sanders, I.A. & Warren, L.A. (2006). Macrophytes and suspension feeding invertebrates modify flows and fine sediments in the Frome and Piddle catchments, Dorset, UK. *Journal of Hydrology*, 330, 171-184.

Wheeldon J. (2003). The River Avon cSAC Conservation Strategy. English Nature, Peterborough.

White, B. & Nepf, H. (2007). Shear instability and coherent structures in shallow flow adjacent to a porous layer. *Journal of Fluid Mechanics*, 593, 1-32.

Wiberg, P.L. & Smith, J.D. (1991). Velocity distribution and bed roughness in high gradient streams. *Water Resources Research*, 27, 825–838.

Wilby, R.L., Beven, K.J. & Reynard, N.S. (2008). Climate change and fluvial flood risk in the UK: more of the same? *Hydrological Processes*, 22, 2511-2523.

Wilson, C.A.M.E. (2007). Flow resistance models for flexible submerged vegetation. *Journal of Hydrology*, 3342, 213-222.

Wilson, C.A.M.E. & Horritt, M.S. (2002). Measuring the flow resistance of submerged grass. *Hydrological Processes*, 16(13), 2589-2598.

Wilson, C.A.M.E., Stoesserm T., Bates, P. & Bateman-Pinzen, A. (2003). Open channel flow through different forms of submerged flexible vegetation. *Journal of Hydraulic Engineering*, 129(11), 847-853.

Wilson J.T., Morlock S.E., & Baker N.T. (1997). *Bathymetric Surveys of Morse and Geist Reservoirs in Central Indiana made with Acoustic Doppler Current Profiler and Global Positioning System Technology*. Water-Resource Investigations Report 97-4099, U.S. Geological Survey. [online] Available at http://in.water.usgs.gov/bathymetry.web/ [accessed 21/05/13]

Wilson, N.R. & Shaw, R.H. (1977). A higher order closure model for canopy flow. *Journal of Applied Meteorology*, 16, 1197‑1205.

Wormleaton, P.R. (1996). Floodplain secondary circulation as a mechanism for flow and shear stress redistribution in straight compound channels. In: P.J. Ashworth, S.J. Bennett, J.L. Best & McLelland, S.J. (eds). *Coherent flow structures in compound channels*. Chichester: John Wiley and Sons. 581-608.

Wright, J. F., Hiley, P. D., Stephanie F, H. A. M. & Berrie, A. D. (1981) Comparison of three mapping procedures developed for river macrophytes. *Freshwater Biology,* 11**,** 369-379.

Wright, J.F., Cameron, A.C., Hiley, P.D., & Berrie, A.D. (1982). Seasonal changes in biomass of macrophytes on shaded and unshaded sections of the River Lambourn, England. *Freshwater Biology*, 12, 271-283.

Wu, F.C., Shen, H.W. & Chou, Y.J. (1999). Variation of roughness coefficients for unsubmerged and submerged vegetation. *Journal of Hydraulic Engineering*, 125(9), 934-942.

Zeng, C. & Li, C.W. (2013). Modeling flows over gravel beds by a drag force method and a modified S-A turbulence closure. *Advances in Water Resources*, 46, 84-95.

Zong, L. & Nepf, H. (2011). Vortex development behind a finite porous obstruction in a channel. *Journal of Fluid Mechanics*, 691, 368-391.

Zdravkovich, M.M. & Pridden, D.L. (1977). Interference between two circular cylinders; series of unexpected discontinuities. *Journal of Industrial Aerodynamics*, 2, 255-270.

Appendix

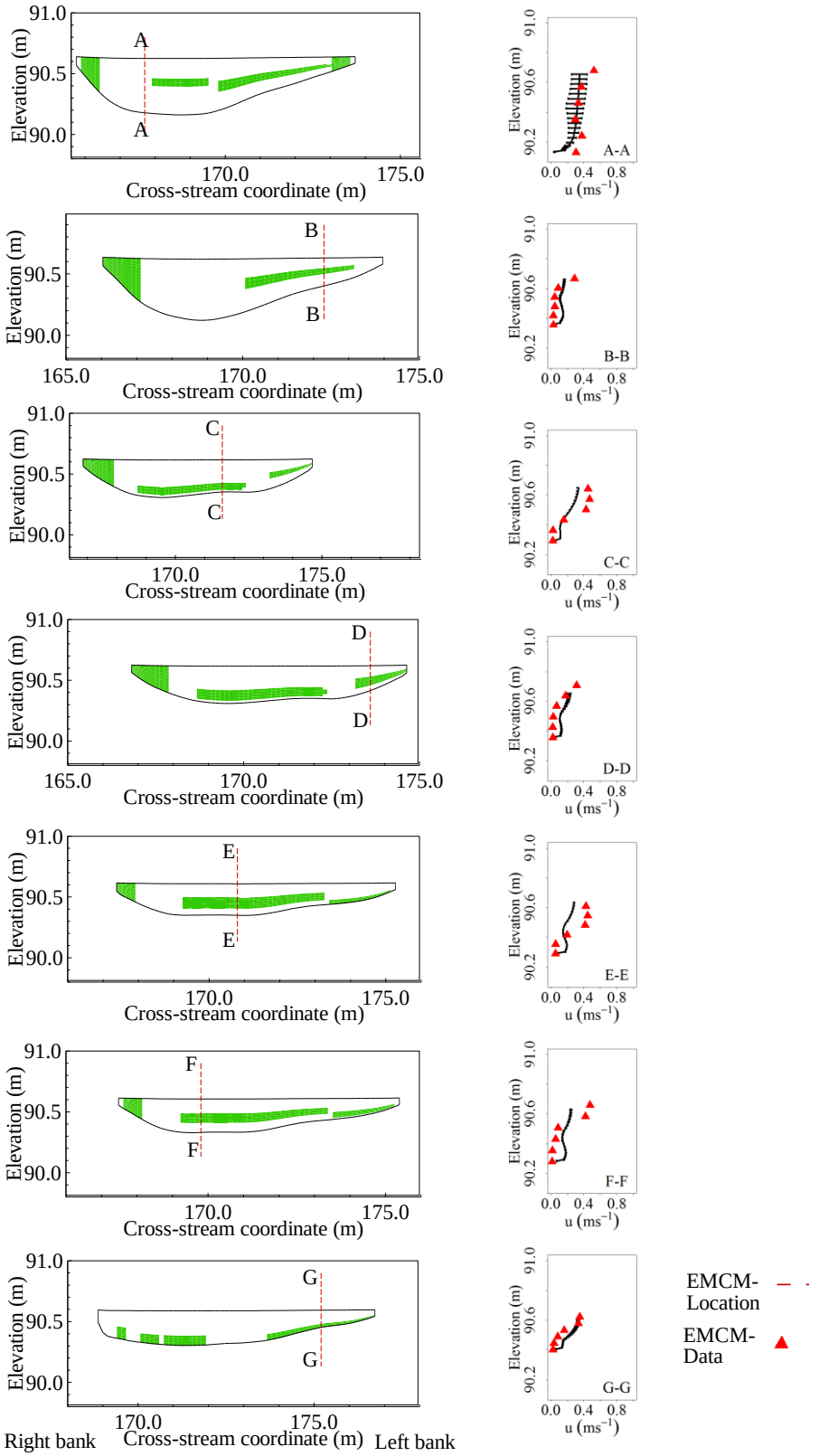

Figure 1: Comparison of model streamwise velocity for November 2010 before cut to field measurements. Profiles A-A to G-G.

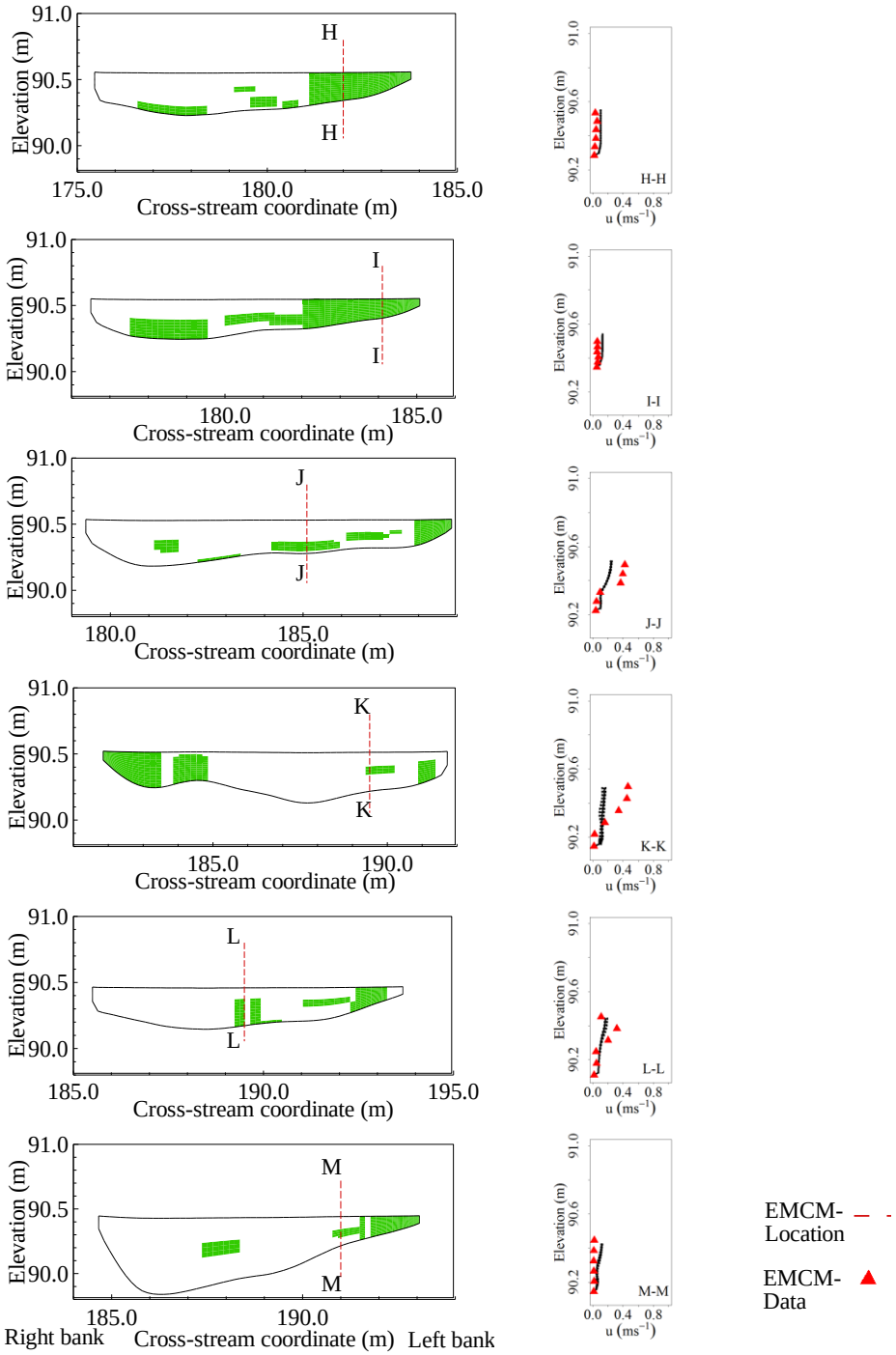

Figure 2: Comparison of model streamwise velocity for November 2010 before cut to field measurements. Profiles H-H to M-M.

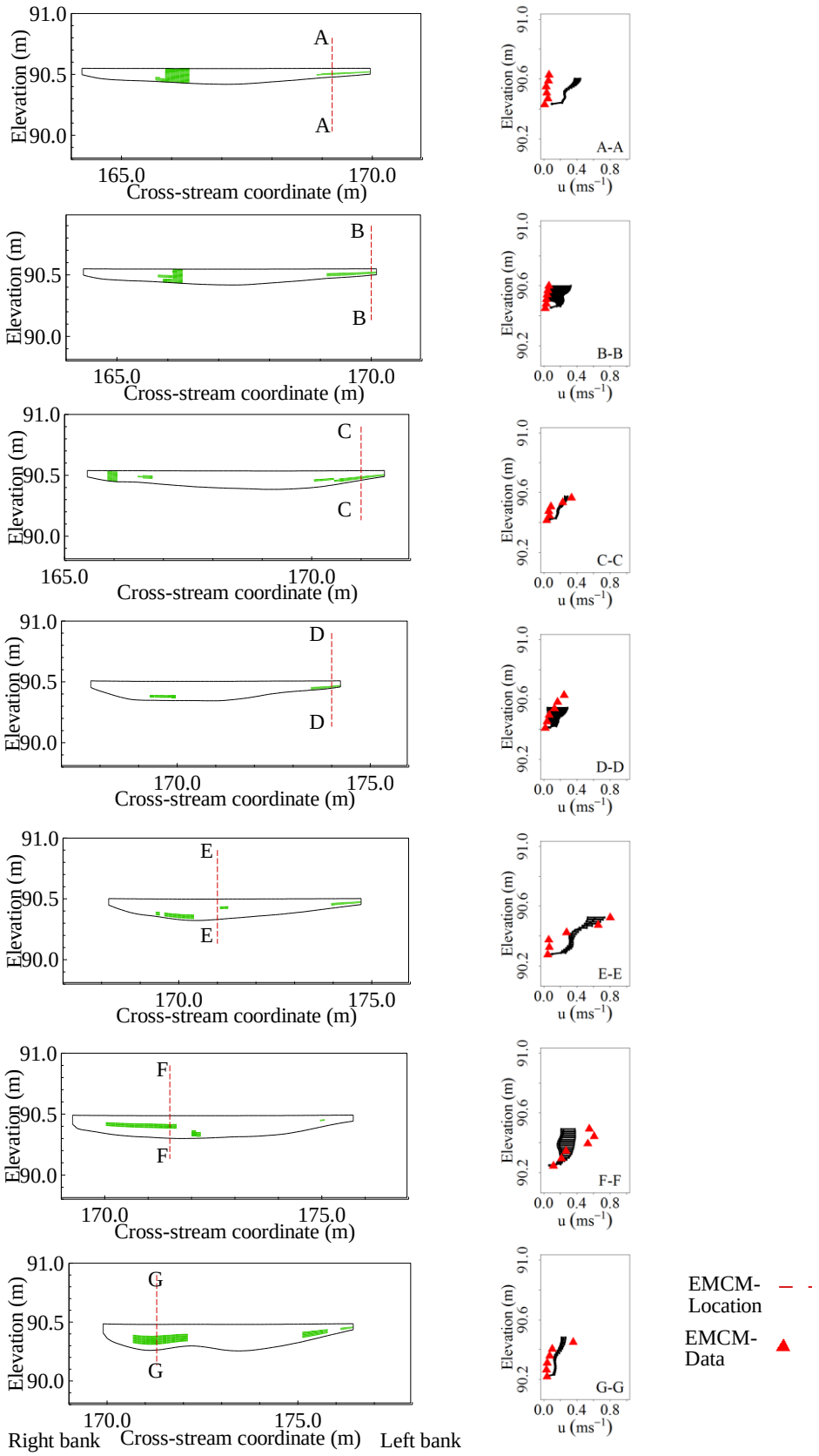

Figure 3: Comparison of model streamwise velocity for November 2010 after cut to field measurements. Profiles A-A to G-G.

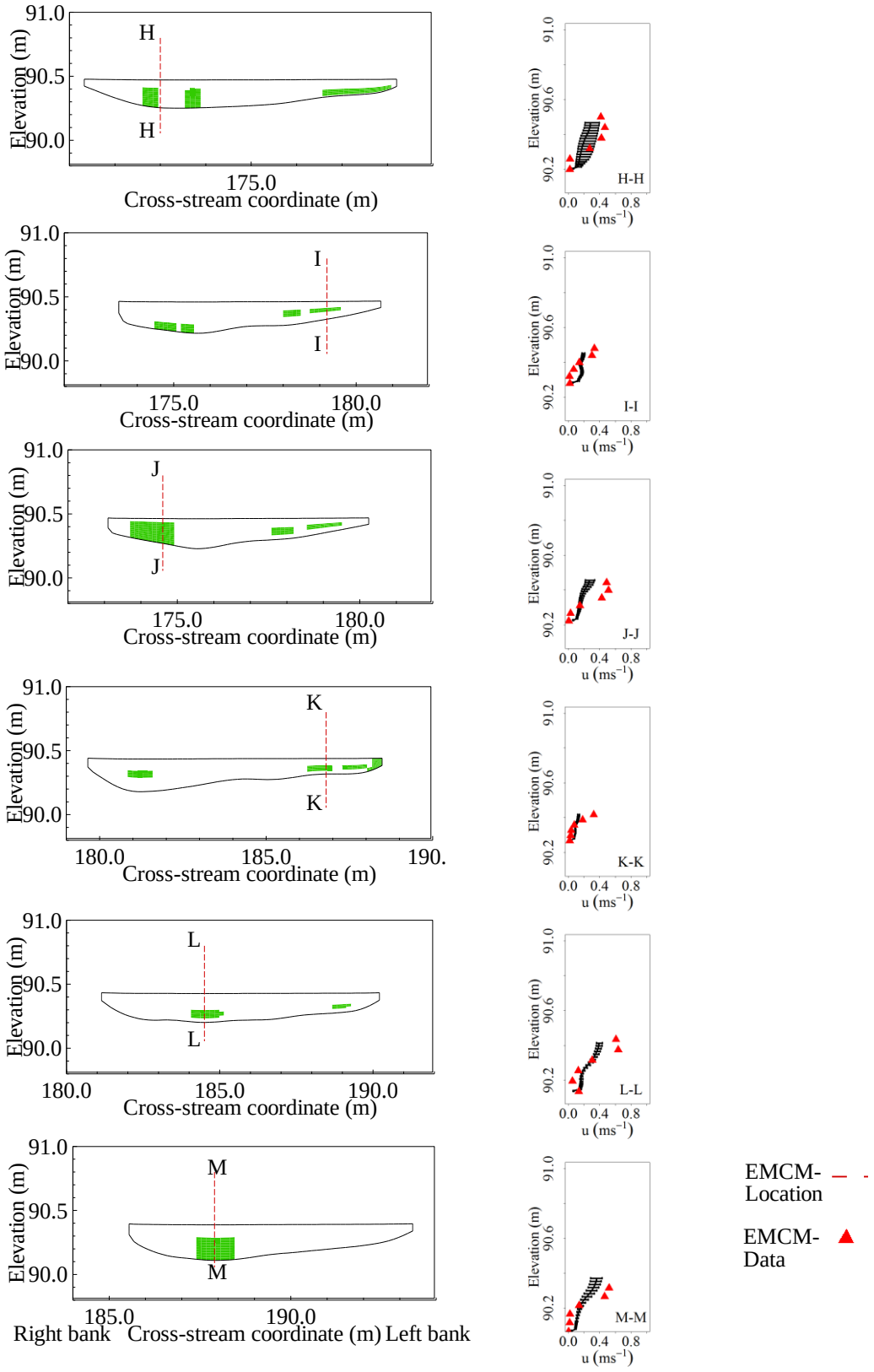

Figure 4: Comparison of model streamwise velocity for November 2010 after cut to field measurements. Profiles H-H to M-M.

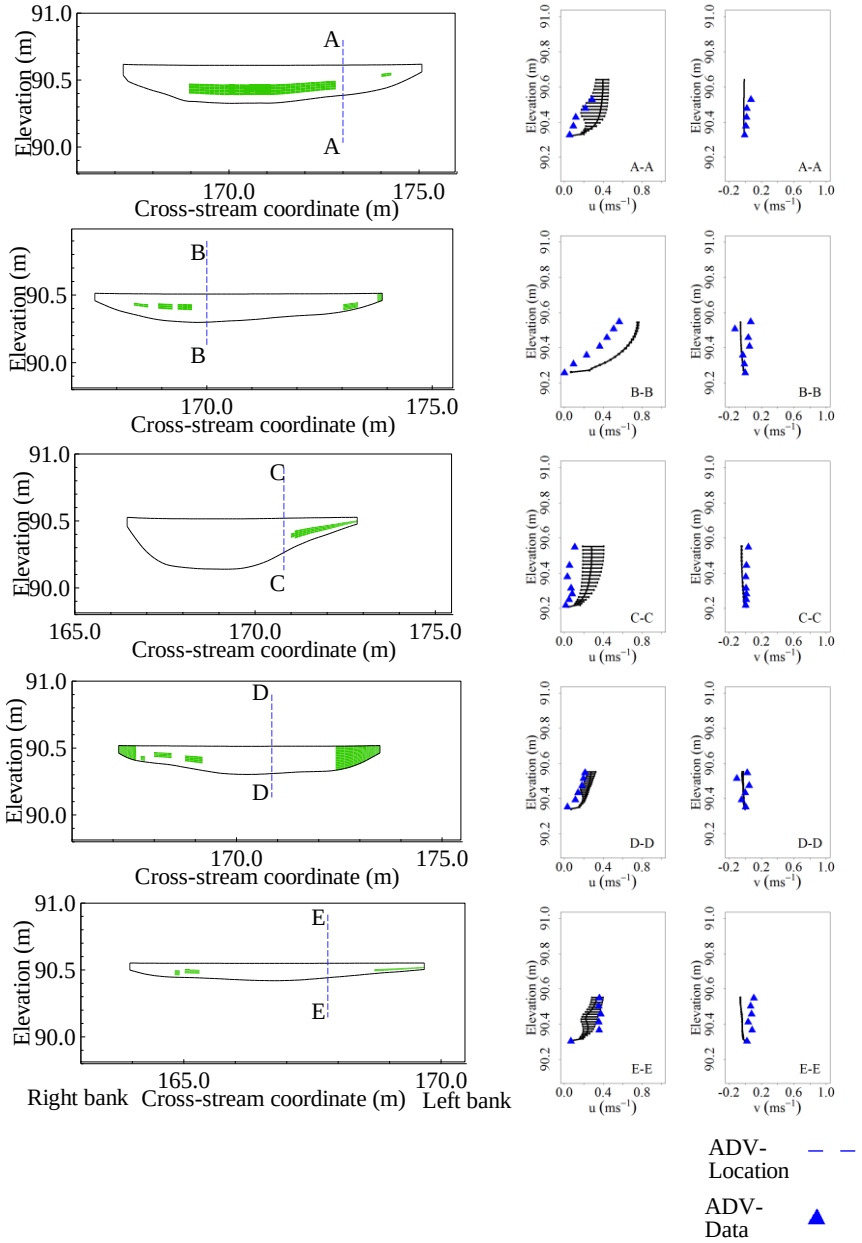

Figure 5: Comparison of model streamwise and lateral velocity to field measurements. Location relative to vegetation shown. A-A shows results for November 2010 before cut. B-B to E-E show results for after cut case.

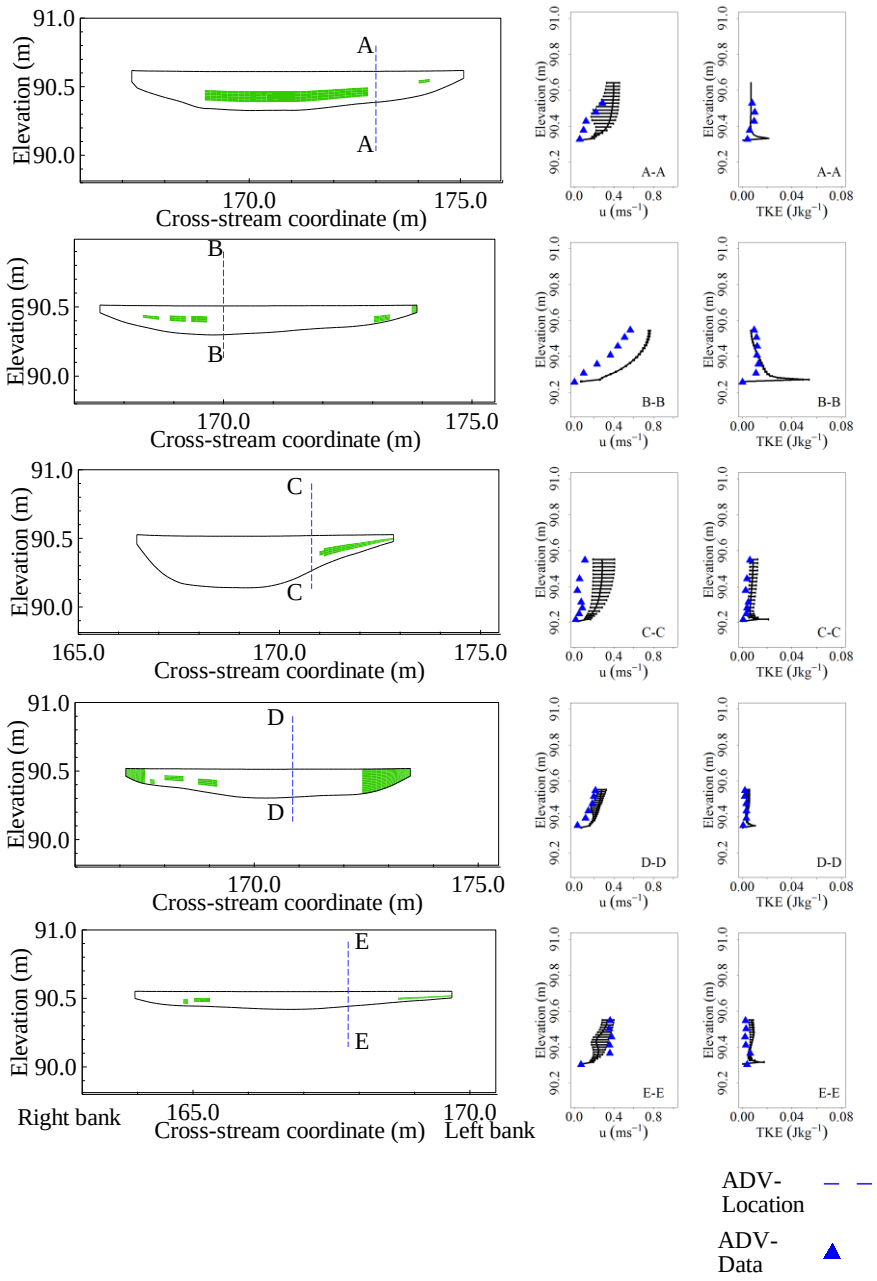

Figure 6: Comparison of model turbulent kinetic energy to field measurements. Location relative to vegetation shown. A-A shows results for November 2010 before cut. B-B to E-E show results for after cut case.